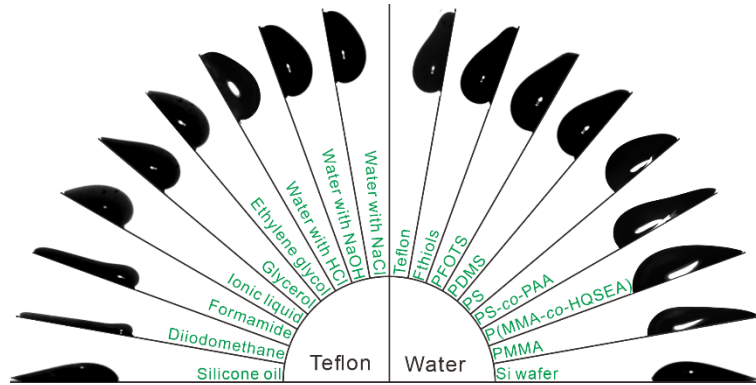# Drop sliding:

Influence of Surface Adaptation and Slide Electrification

Dissertation

zur Erlangung des Grades

"Doktor der Naturwissenschaften"

im Promotionsfach Chemie

am Fachbereich Chemie, Pharmazie, Geographie und Geowissenschaften der Johannes

Gutenberg-Universität Mainz und in Kooperation mit dem Max-Planck-Institut für

Polymerforschung Mainz

Xiaomei Li

Geboren in Nanning / China

Mainz, 2023

This dissertation was undertaken at the Max Planck Institute for Polymer Research from September 2019 until April 2023 under the supervision of Professor Hans-Jürgen Butt and Dr. Rüdiger Berger. To the best of my knowledge and conscience, I assure the reader that original research is presented, and no plagiarism has been committed. Sources are acknowledged to the best of my knowledge. Material originating from other publications has been reproduced with the corresponding permissions.

April, 2023

1. Gutachter in：

2. Gutachter in:

Tag der mündlichen Prüfung:

II

III

Abstract

Drop sliding is omnipresent in daily life and industry, from raindrops on a windshield to printing. Starting with the concept of surface energy, drop kinetics has been studied for over 200 years. Flat and smooth surfaces with lower surface energy normally have higher contact angles. Thus, people normally use contact angle as a characterization of surface wettability. In practice, depending on the roughness, heterogeneity, and history that surfaces have undergone, the contact angle lies between the advancing and receding contact angles. Advancing and receding contact angles are the angles formed when the contact line starts to spread and retract. Their difference is contact angle hysteresis, which indicates the existence of drop friction—the force resisting drop motion. Numerous dissipation channels cause drop friction. How and how much dissipation channels contribute to the drop friction on different surfaces is, however, unclear. Therefore, until today, it is impossible to predict the velocity and hence the position of drops after sliding down a few centimeters on a tilted surface.

One of the dissipation channels that contribute to drop friction is surface adaptation. Surface adaptation namely surface changes its chemical/physical properties when it contacts a liquid or its vapor. In 2018, Butt *et al.* proposed an adaptation model to interpret contact angle hysteresis [*Langmuir* 2018, 34, 11292−11304]. In their model, the change of surface energy/interfacial tension by surface adaptation leads to a change in advancing and receding contact angles and therefore induces contact angle hysteresis. In 2018, the adaptation model was speculative and experimental validation was required. To verify how applicable the adaptation model is, I explored the adaptation of a random copolymer composed of styrene with 11%−25% (in molar) acrylic acid (PS/PAA) to water by a home-built tilted plate setup. By velocity-dependent dynamic contact angle measurement, the advancing contact angle of sliding water drops on the PS/PAA surface decreased from 95° to 87° at velocity < 20 μm/s. I showed that the adaptation model can be fitted to the measured decreasing advancing contact angles. The fitting results indicate a relaxation time of ⩽2 ms for the dry-to-wet process. In order to explore the molecular origin of surface adaptation, we found water diffusion into polymer film by confocal microscopy measurement and polymer reorientation at the interface by sum frequency generation spectroscopy. With this knowledge, I show that the adaptation model is a valid and valuable contribution to

understanding and characterizing the adaptation kinetics of polymer surfaces. The adaptation kinetics of polymers can play an important role in releasing substances, e.g. drugs, upon an external stimulus. In particular, studying release kinetics at a time scale <1s is experimentally challenging owing to the small amounts that are released, the limited sensitivity, and the temporal resolution of NMR or fluorescence methods. By investigating velocity-dependent contact angles of a pH-reactive polymer, I entered new territory. The novelty way to study fast relaxation kinetics by velocity-dependent contact angle measurement in this thesis expands the possible application of the goniometer as a technique. I show that the hydrolysis reaction of active agents takes place at a time scale <1 s. Such a time scale for a hydrolysis reaction is not considered in today's chemistry textbooks.

Another dissipation channel causing drop friction is slide electrification given by the separation of charges for a receding liquid at the three-phase contact line. These charges accumulate at de-wetted surfaces. This effect leads to the charging of the sliding drop as well. In this case, the charging of drops and surfaces is the adaptation process. Both may influence drop motion. However, whether and how slide electrification affects drop motion is still unclear. To answer this, we measured drop velocity, dynamic advancing, and receding contact angle of drops sliding on tilted substrates with different permittivity but the same hydrophobic coating. We discovered the friction force is higher on a low-permittivity substrate (quartz) than one on a high-permittivity substrate (gold/Si wafer). The extra force (higher part) can account for 10% to 50% of all the friction force, depending on slide length and drop number. One origin of the extra force would be the Coulomb interaction owing to charges from slide electrification. Indeed, based on the Coulomb interaction, the electrostatic force from theoretical and numerical computation explains most of the experimental extra force. In addition, charge deposition by slide electrification affects contact angle as well. We observed that the dynamic advancing and receding contact angles were reduced on low-permittivity substrates compared to high-permittivity substrates. We attributed the observed decrease in dynamic contact angles to two effects: An electro-capillary reduction of contact angles caused by drop charging and a change in the free surface energy of the solid due to surface charging.

In addition to surface adaptation such as molecule orientation and slide electrification, hydrodynamic viscous and contact-line friction are two important contributions to drop friction.

Viscous dissipation occurs inside a sliding drop, which is normally divided into wedge and bulk regions. How much viscous dissipation comes from wedge and bulk and how to define the two regions is still unclear. Based on the dissipation from wedge viscous and contact-line friction, the hydrodynamic model and molecular kinetic theory predict how dynamic contact angle changes as velocity accordingly. But theories suffer from unmeasurable parameters such as slip length and molecular equilibrium frequency. Unmeasurable parameters in a model mean that no predictions can be made. By tilted plate experiments, we discovered that the friction force of sliding drops on flat, smooth, rigid, and homogenous surfaces with high-permittivity substrates follows a simple, universal empirical equation. With this equation, only one material-specific parameter is required to describe drop motion. We term this dimensionless parameter "friction coefficient". In contrast to static wetting of sessile drops, which is fully described by the advancing and receding contact angles, dynamic wetting is determined by this friction coefficient. Knowing the friction coefficient, a prediction of drop sliding is feasible.

In conclusion, my findings clarify and enrich the mechanism leading to contact angle hysteresis or drop friction. By opening a new perspective on contact angle hysteresis or drop friction and providing a theoretical scaling and foundation, the present work would inspire a large number of future works relevant to wetting science, material science, soft matter physics, and microfluidics.

Zusammenfassung

Tropfen, die sich über feste Oberflächen bewegen, sind im täglichen Leben und bei industriellen Prozessen allgegenwärtig. Beispiele sind Regentropfen auf Windschutzscheiben und Tinte in Druckmaschinen. Ausgehend vom Konzept der Oberflächenenergie wird Tropfenverhalten seit über 200 Jahren untersucht. So weisen flache Oberflächen mit geringerer Oberflächenenergie höhere Kontaktwinkel auf, als diejenigen mit hoher Oberflächenenergie. Daher werden oft Kontaktwinkel gemessen und zur Bestimmung der Oberflächenenergie verwendet. In der Praxis liegt der Kontaktwinkel je nach Rauheit, Heterogenität und Vorgeschichte der Oberflächen zwischen dem Fortschreit- und dem Rückzugskontaktwinkel. Der Fortschreit-und der Rückzugskontaktwinkel sind die Winkel, die entstehen, wenn die Kontaktlinie beginnt, sich auszubreiten und zurückzuziehen. Ihr Unterschied ist die Kontaktwinkelhysterese. Diese gibt Hinweise auf das Vorhandensein von Tropfenreibung - der Kraft, die der Tropfenbewegung entgegensteht. Zahlreiche Dissipationsprozesse verursachen Tropfenreibung. Es ist jedoch unklar, wie und in welchem Umfang verschiedene Dissipationskanäle zur Tropfenreibung auf verschiedenen Oberflächen beitragen. Daher ist es bis heute nicht möglich, die Geschwindigkeit und damit die Position von bewegten Tropfen vorherzusagen.

Ein Dissipationskanal, der zur Tropfenreibung beiträgt, ist Oberflächenadaption. Oberflächenadaption bedeutet, dass die Oberfläche ihre chemischen/physikalischen Eigenschaften ändert, wenn sie mit einer Flüssigkeit oder deren Dampf in Kontakt kommt. 2018 schlugen Butt und Koautoren ein Adaptionsmodell zur Interpretation der Kontaktwinkelhysterese vor [Langmuir 2018, 34, 11292-11304]. In ihrem Modell führt die Änderung der Oberflächenenergie, hervorgerufen durch Oberflächenadaption, zu einer Änderung der Fortschreit- und Rückzugskontaktwinkel. Somit verursacht Oberflächenadaption eine zusätzliche Kontaktwinkelhysterese. Das Adaptionsmodell beruhte auf hypothetischen Annahmen und deren tatsächlicher Beitrag der Adaption von Oberflächen zur gemessen Kontaktwinkelhysterese war nicht bekannt. Um das Adaptionsmodell auf die Probe zu stellen, untersuchte ich ein statistisches Copolymers, bestehend aus Styrol und 11%-25% (in molaren Anteilen) Acrylsäure (PS/PAA). Mittels eines selbstgebauten experimentellen Aufbaus setze ich Wassertropfen auf die Oberfläche von dünnen Filme des Copolymers, die aufgrund von Gravitationskräften abrollen. Die geschwindigkeitsabhängige Kontaktwinkelmessung ergab

eine Reduktion der Fortschreitkontaktwinkel auf der PS/PAA-Oberfläche von 95° auf 87° bei einer Geschwindigkeit < 20 µm/s. Mit diesen Experimenten konnte ich zeigen, dass das Adaptionsmodell die Reduktion des Kontaktwinkel beschreibt. Somit trägt das Adaptionsmodell wesentlich zum Verständnis der Benetzung von Polymeroberflächen bei.

Ein weiterer Dissipationskanal, der zur Tropfenreibung beiträgt, ist die elektrische Ladungstrennung an der rückwärtigen Dreiphasen-Kontaktlinie. Auf hydrophoben, nicht-leitfähigen Oberflächen werden negative Ladungen auf der Oberfläche deponiert. Dieser Effekt führt zur positiven Aufladung des gleitenden Tropfens. In diesem Fall ist die Ladungstrennung eine Konsequenz der Adaption von Oberfläche und Tropfen. Ob und wie diese Ladungstrennung die Tropfenbewegung beeinflusst, ist jedoch unklar. Daher haben wir die Tropfengeschwindigkeit, den geschwindigkeitsabhängigen Fortschreit- und Rückzugskontaktwinkel von Tropfen systematisch untersucht. Wir haben mittels des oben erwähnten experimentellen Aufbaus Proben derselben hydrophoben Beschichtung aber mit unterschiedlicher Permittivität untersucht. Wir fanden heraus, dass die Reibungskraft auf einem Substrat mit niedriger Permittivität (Quarz) höher ist, als auf einem Substrat mit hoher Permittivität (Gold/Si-Wafer). Der Unterschied der Reibungskraft in beiden Fällen kann 10 % bis 50 % der gesamten Reibungskraft ausmachen. Ursache für die zusätzliche Kraft ist die Coulomb-Wechselwirkung zwischen Ladungen auf dem Substrat und in dem Tropfen. Darüber hinaus beeinflusst die Ladungsseparation auch die Kontaktwinkel. Wir beobachteten, dass die geschwindigkeitsabhängigen Kontaktwinkel auf Substraten mit niedriger Permittivität geringer waren als auf Substraten mit hoher Permittivität. Der beobachtete Rückgang der geschwindigkeitsabhängigen Kontaktwinkel beruht auf zwei Effekten: Es gibt eine elektrokapillare Verringerung des Kontaktwinkels durch Tropfenaufladung und einen Anstieg der Oberflächenenergie des Festkörpers aufgrund der Oberflächenaufladungen.

Zusätzlich zur Oberflächenadaption und Ladungstrennung, tragen hydrodynamische viskose Dissipation und die Reibung an der Kontaktlinie zur Tropfenreibung bei. Die viskose Dissipation findet im Inneren eines gleitenden Tropfens statt. Wieviel Energie nahe der Kontaktlinie und im Volumen dissipiert wird, ist jedoch unbekannt. Bestehende hydrodynamische und die molekularkinetische Theorien sagen vorher, wie sich die Kontaktwinkel mit der entsprechenden Geschwindigkeit ändern. Allerdings basieren beide Theorien auf nicht messbaren Parametern, wie zum Beispiel der Slip-Länge und der Schwingungsfrequenz der Moleküle an der Dreiphasenkontaktlinie. Beide Parameter dienen

dazu die Theorien an die experimentellen Daten zu fitten. Aber sie bedeuten auch, dass keine Vorhersagen für verschiedene Oberflächen und Flüssigkeiten gemacht werden können. Meine Experimente mit Tropfen, die eine schiefe Ebene hinunter gleiten zeigen, dass die Reibungskraft auf flachen, glatten, starren und homogenen Oberflächen mit Substraten hoher Permittivität einer einfachen, universellen empirischen Gleichung folgt. In dieser Gleichung ist nur ein materialspezifischer Parameter erforderlich, um die Tropfenbewegung zu beschreiben. Wir bezeichnen diesen dimensionslosen Parameter als Reibungskoeffizient. Im Gegensatz zur statischen Benetzung von sitzenden Tropfen, die vollständig durch den Fortschreit- und Rückzugskontaktwinkel beschrieben ist, wird die dynamische Benetzung durch diesen Reibungskoeffizienten bestimmt. Mit der Kenntnis des Reibungskoeffizienten ist eine Vorhersage des Tropfengleitens möglich.

Meine Ergebnisse klären und bereichern unser Verständnis über Kontaktwinkelhysterese und Tropfenreibung. Ich hoffe, dass die in dieser Arbeit beschriebenen Ergebnisse neue Perspektiven eröffnet und zu weiteren Untersuchungen inspiriert, die für die Oberflächenforschung, die Materialwissenschaft, die Physik der weichen Materie und die Mikrofluidik relevant sind.

Contents

1. Introduction

1.1. Historical Overview

Wetting phenomena have been studied for almost 400 years, starting with Leonardo da Vinci's discovery of *capillary action* in the late fifteenth century (Figure 1).[1, 2] In the 1600s, more and more scientists observed capillary-raised liquid in a glass tube and tried to explain this phenomenon. For example, Robert Boyle found that vacuum had no observable influence on the height of the liquid in the capillary in 1660.[3] Later on, Honoré Fabri[4] and Jacob Bernoulli[5] explained the liquid raise with pressure difference inside and outside of the tube. While Isaac Vossius,[6] Giovanni Alfonso Borelli,[7] and Louis Carré[8] *et al.* considered the attraction between liquid and liquid molecules or the interaction between liquid and the wall of the tube. In 1751, Johann Andreas von Segner proposed a vital concept of *surface tension* as a natural feature of liquids, accelerating the quantitative treatment of capillary action.[9] Around fifty years later, the idea was utilized in *Young's equation*. The Young–Laplace equation describes the capillary pressure difference sustained at the interface between two static fluids,[10] while the Young-Dupré equation describes the force or energy at the three-phase contact line of an ideal solid surface.[11]

An ideal surface is flat, rigid, inert, perfectly smooth, and chemically homogeneous. When a liquid drop sits on an ideal surface at its equilibrium state, the contact angles along the three-phase contact line are the same. In contrast to the case, Agnes Pockels first noticed the difference in the contact angle when forcing a liquid to advance and retract in 1914.[12] Later on, in the 1920s and 1930s, researchers developed the concept of receding and advancing contact angles for the contact angles formed when the contact line starts to retract and spread respectively.[13-15] The difference between the advancing and the receding contact angles is *contact angle hysteresis.*[16]

The existence of contact angle hysteresis indicates that drop sliding on solid surfaces suffers from *drop friction*. In the 1950s, Birkerman,[17] Kawasaki,[18] and Furmidege[19] *et al.* derived a simple formula to quantify the retention force of drops on tilted surfaces, in which the retention force is proportional to surface tension, drop width, and the difference in cosines between the receding and advancing contact angles. When a drop starts to move, the corresponding critical retention force is the static friction force. Meanwhile, scientists also tried to explain possible effects leading to drop friction. In 1969, considering the activated dynamics of individual molecules near

the contact line lead to energy dissipation and reflect in a change of contact angle, Blake and Haynes proposed the *molecular-kinetic theory (MKT)* [20] to quantify the change of contact angle by contact-line friction. Meanwhile, a competitive model attributes drop friction to hydrodynamic viscous dissipation. Huh and Scriven first stated that shear stress diverges at the contact line with a no-slip boundary condition in 1971.[21] By introducing a cut-off length in molecular scale and considering the viscous stress is balanced by surface tension, Voinov in 1976 [22] and Cox in 1986 [23] succeeded to predict the change of contact angle. That is *Cox–Voinov hydrodynamic model*. In the last decades, researchers have conducted plenty of experiments and simulations to verify the two models. However, neither the Cox-Voinov model nor the MKT describes experimental data universally with reasonable fitting parameters.[24-35]

Later on, people realized that multiple dissipation sources might occur simultaneously. In this case, the change of contact angle can be described by a *combined model*. In the 1990s, Petrov and Petrov considered that activated dynamics in MKT mainly change the microscopic contact angle, and the change of microscopic contact angle further affects the macroscopic contact angle described by the Cox-Voinov model.[25] Brochard-Wyart and de Gennes proposed that total energy dissipation comprises the viscous losses in the wedge plus the losses due to contact-line friction in 1992.[36] While Andreotti *et al.* unified the two dissipative mechanisms by a dynamic crossover from activated dynamics dominated at low capillary numbers to hydrodynamic viscous dominated at high capillary numbers in 2016.[37]

With the development of functional surfaces in the 21st century, the effects leading to drop friction are enriched and become more complex. For example, on soft and deformable surfaces, elasto-capillary deformation of surfaces resist drop motion substantially;[38] on adaptive surfaces, surfaces adapt with changes in interfacial properties when they contact with liquid and its vapor. The change in interfacial tension is reflected in the change of contact angles, which is predicted by the *adaptation model*;[39] on superhydrophobic surfaces, aero-dynamical resistance becomes dominant because the liquid-solid contact area is low and drops slide fast.[40]
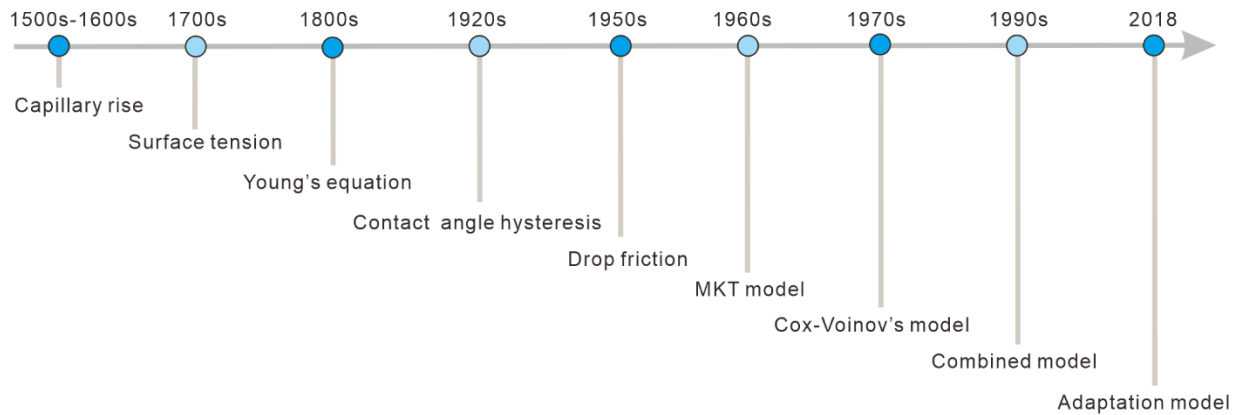
Figure 1. *Development overview of theory describing contact-line behavior.*

1.2. How Liquid Forms a Drop on a Solid Surface?

1.2.1. Surface Tension and Contact Angle

Surface (interfacial) tension (γ) determines the shape of liquid on solid surfaces. The physical origin of surface tension is that surface molecules undergo unbalanced cohesive interaction with adjacent molecules compared to the ones in the bulk (Figure 2a).[41] Although having a molecular origin, surface tension is a macroscopic parameter and is defined on a macroscopic scale. The dimension of surface tension is force per unit length (N/m) or energy per unit area (J/m^2). When using energy per unit area, it is more general to term surface energy. For liquid, surface tension and surface energy are equivalent, while for solid especially elastomer, surface tension is not equal to surface energy due to the Shuttleworth effect.[42]

To minimize the total surface energy, liquids adjust their shape on solid surfaces. When the solid surface energy (γ_S) is higher than the sum of liquid-air (γ_L) and liquid-solid interfacial tension (γ_{SL}), namely $\gamma_S > \gamma_L + \gamma_{SL}$, the liquid spreads and wets the solid surface completely. In contrast, when the solid surface energy (γ_S) is lower than the sum of liquid–air (γ_L) and liquid-solid interfacial tension (γ_{SL}), namely $\gamma_S < \gamma_L + \gamma_{SL}$, the liquid wets the solid surface partially and forms a drop with non-zero contact angle. The contact angle is the angle formed at the three-phase contact line (Figure 2b). Therefore, surface tension is an important property to characterize wettability.
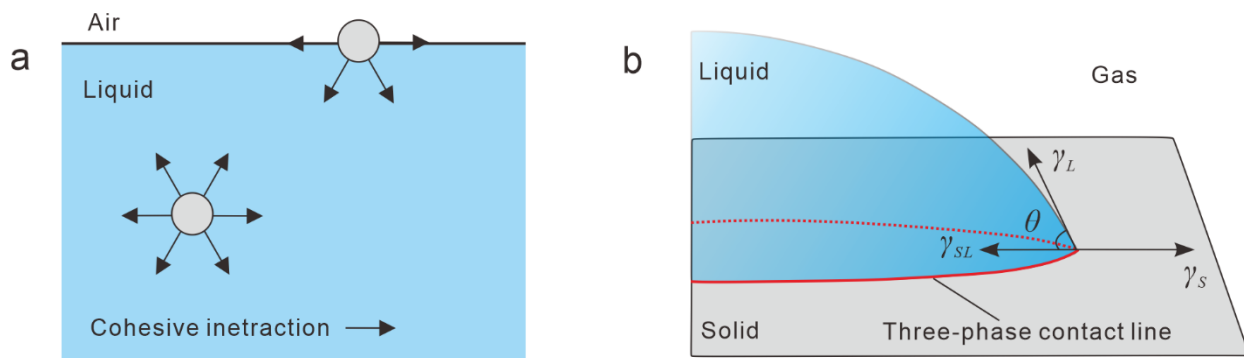
3

Figure 2*. Definitions of surface tension, contact angle, and three-phase contact line.*

The methods to measure liquid surface tension include the Du-Noüy ring method, the Wilhelmy-plate method, the maximum-bubble-pressure method, and the drop-weight method, (Figure 3).[43] In the Du-Noüy ring method, by measuring the force (F) required to detach a ring with an inner radius of r_i and outer radius of r_a from a liquid, the liquid surface tension is calculated with $F = 2\pi (r_i + r_a)\gamma_L$. In the Wilhelmy-plate method, the ring is replaced by a plate with a length of l, and the measured force required to prevent the plate from being drawn down to liquid is $F = 2l\gamma_L$. In the above two methods, the liquid must wet the ring or plate completely. The difference between the two methods is the former is a quasi-static measurement while the latter is a static measurement. In the maximum-bubble-pressure method, liquid surface tension (γ_L) is determined from the pressure (ΔP) which is necessary to push a bubble out of a capillary with a radius of r_c against the Laplace pressure in a liquid bath by $\gamma_L = r_c \Delta P/2$. Similarly, in the drop-weight method, liquid surface tension is determined based on the balance between gravity force (mg) and surface tensional force ($2\pi r_c \gamma_L$) when a drop is detached from a capillary tube. In practice, because a thin neck is formed before drop release, a correction factor (f) is considered, that is $mg = 2\pi f r_c \gamma_L$. The latter two methods are used infrequently but the underlying phenomena are interesting.

Though liquid surface tension can be measured experimentally, solid surface tension is unmeasurable directly until now. It can be calculated by measuring the contact angle. Therefore, the contact angle is a more intuitive and feasible parameter to quantify surface wettability. In general, a surface is hydrophobic with a contact angle over 90° while is hydrophilic with a contact angle below 90°.
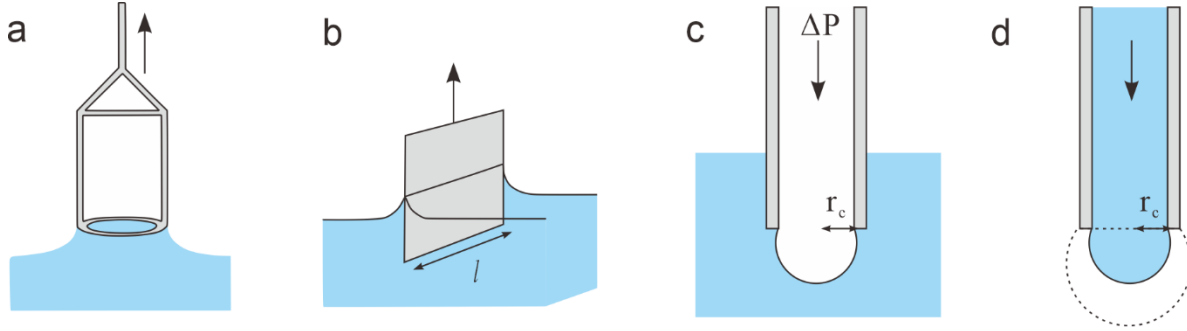
Figure 3. The methods to measure liquid surface tension. (a) Du-Noüy ring method; (b) Wilhelmy plate method. (c)Maximum-bubble-pressure method; (d) drop-weight method.

1.2.2. Young's Model and Modifications

The relationship between surface tensions and contact angle was quantified by the Young–Dupré equation (Figure 4a): [44, 45]

$$\gamma_L \cos\theta_Y = \gamma_S - \gamma_{SL} \tag{1}$$

The Young–Dupré equation can be explained from both a thermodynamic perspective and a mechanical perspective. The former is based on minimizing the system energy when a liquid contacts a solid surface. While the latter considers the balance of interfacial tensions at the contact line in the horizontal direction. The Young–Dupré equation is only valid for an equilibrium drop on an ideal surface, on which the contact angle is only determined by interfacial tensions. That is, a higher contact angle indicates a lower solid surface energy. Therefore, the contact angle in the Young–Dupré equation also terms intrinsic contact angle or Young's angle (θ_Y).

In practice, a contact angle measured by a goniometer is normally determined within a resolution $>10\,\mu m$, which could be different from the intrinsic contact angle (θ_Y). For distinguishing, we called the experimental contact angle measured in a macroscopic scale "apparent contact angle", θ_{app} (Figure 4a).[39]

Considering real surfaces rather than ideal surfaces, there are many modified models existing to adapt intrinsic contact angle with the apparent contact angle. When the surface is physically rough, the deviation of the apparent contact angle from the intrinsic contact angle is estimated by the Wenzel model (Figure 4b):[46]

$$\cos\theta_{app} = r\cos\theta_Y. \tag{2}$$

5

r is the roughness of solid surfaces. When surfaces are rough ($r > 1$), $\theta_Y > 90°$ leads to $\theta_{app} > \theta_Y$. In contrast, $\theta_{app} < \theta_Y$ when $\theta_Y < 90°$. That is, surface roughness always magnifies the underlying wetting properties no matter hydrophobicity or hydrophilicity. The limitation of this model is, when r is large enough, θ_{app} could be over 180° or below 0°, which is not realistic. Thus, the roughness range between which the Wenzel model is applicable is limited.[47]
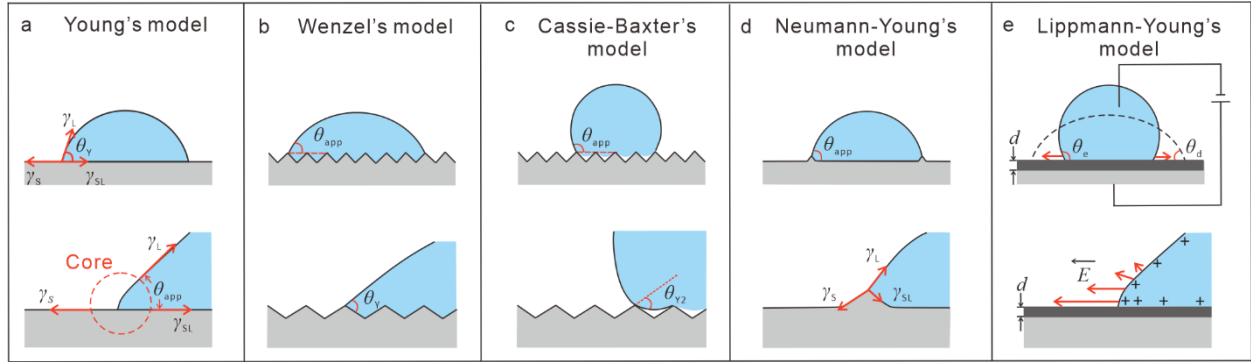

Figure 4. Young's model and its modification.

In addition to physical roughness, real surfaces could be chemically heterogeneous. For example, a surface that is perfectly flat but consists of two different components with intrinsic contact angles of θ_{Y1} and θ_{Y2}. When individual areas of the two components are small compared to the drop size. The apparent contact angle on this two-component surface can be predicted by:

$$\cos\theta_{app} = \varphi_1\cos\theta_{Y1} + \varphi_2\cos\theta_{Y2}, \tag{3}$$

φ_1 and φ_2 are the fractional surface areas occupied by each of these components ($\varphi_1 + \varphi_2 = 1$). When one of the two components is air, the contact angle in the air is 180°, the model can be simplified as:

$$\cos\theta_{app} = \varphi\cos\theta_Y + 1 - \varphi \tag{4}$$

This is the so-called "Cassie-Baxter equation".[48, 49] Nowadays, people also describe liquids sitting upon asperities with air pockets underneath as a Cassie-Baxter state (Figure 4c). Thus, the Cassie-Baxter model paves the road toward understanding superhydrophobic surfaces.

Besides, instead of being rigid, many surfaces are soft and deformable. When a drop sits on a soft surface, the pulling of the contact line causes surface deformation with a wetting ridge (Figure 4d). When the wetting ridge is small compared to the drop size, the contact angle (θ_{app})

still satisfies the Young–Dupré equation. In contrast, the balance between interfacial tensions at the three-phase contact line is applied to a circular system rather than only in the horizontal direction. In this case, the Young–Dupré equation is invalid, and the global balance of interfacial tension is described by the Neumann equation:[50]

$$\gamma_{12}\boldsymbol{t_{12}} + \gamma_{13}\boldsymbol{t_{13}} + \gamma_{23}\boldsymbol{t_{23}} = \boldsymbol{0}, \tag{5}$$

Where γ_{ij} is the interfacial tension between phase i and j, and $\boldsymbol{t_{ij}}$ is the vector pointing along the $i - j$ interface.

A contact angle can also be altered by applying a voltage ΔU between a drop and an electrode submerged in the substrate. In general, a contact angle decreases with the increase of applied voltage. The phenomenon is known as electrowetting (Figure 4e). Microscopically, the change in contact angle is due to the fringe electric field bending liquid surfaces near the contact line. The fringe electric field is localized within a regime with a length scale comparable to the dielectric layer thickness (d). Macroscopically, the effect is equivalent to a reduction of the solid-liquid interfacial tension because of charge accumulation under applied voltage. The dependence of the apparent contact angle on the applied voltage is given by the Young-Lippmann equation:[51]

$$\cos\theta_{app} = \cos\theta_Y + \frac{\varepsilon\varepsilon_0\Delta U^2}{2d\gamma_L} \tag{6}$$

Here, ε is the relative permittivity of substrates and ε_0 is the vacuum permittivity.

1.3. How Liquid Drops Slide on a Solid Surface?

All the above models are derived based on Young's equation. Thus, the drop should be in an equilibrium state. In practice, even static drops are often not at chemical or phase equilibrium. Therefore, the apparent contact angle measured with a static drop is between the advancing contact angle (θ_a) and the receding contact angle (θ_r). When the drop starts to slide, the angle formed at the advancing contact line is the advancing contact angle, while the angle formed at the retracting contact line is the receding contact angle. The difference between the advancing angle and the receding angle is contact angle hysteresis.

The methods to measure advancing and receding contact angles include the Wilhelmy-plate method, in-/deflated drop method, scanning drop friction force microscopy (sDoFFI), and the

tilted-plate method (Figure 5).[16] In the Wilhelmy-plate method, a tested surface with a length of l is forced to immerse into or withdraw from the tested liquid bath. By measuring the force (F) and knowing the liquid surface tension (γ_L), the advancing and receding contact angles are determined indirectly with the equation, $F = l\gamma_L\cos\theta_{a/r}$, which is derived based on the force balance when the meniscus is under equilibrium. In the other three methods, the advancing and receding contact angles are determined by drop shape analysis. Therefore, the accuracy of the measurement depends on the resolution of the camera and the quality of the images. In addition, different fitting models lead to a variation in the contact angle. Therefore, we should provide the fitting model upon mentioning contact angle values. The difference between the three methods is the way to control the contact-line velocity. In the de-/inflated drop method, the contact line is moved with the change of drop volume by pumping liquid in and out of the drop with a syringe. Thus, the contact-line velocity is controlled by a flow rate. Moreover, the position of the syringe needle inside the drop affects the results. To suppress the influence, we normally put the syringe needle in the middle of the drop and close to the solid-liquid interface. In scanning drop friction force microscopy, the contact line is moved by fixing a drop with a spring on a moving surface by a motor. Thus, the contact-line velocity is controlled by the motor. In the tilt-plate method, the contact line is moved by tilting surfaces. After drops start to move, the drop de-/accelerates. In this case, contact-line velocity depends on the drop volume, the tilt angle, and the drop friction.
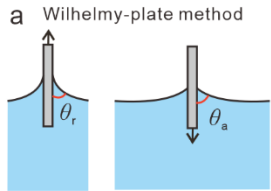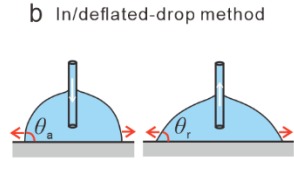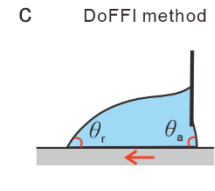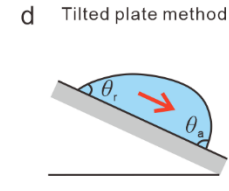

Figure 5. Methods to measure the advancing and receding contact angles.

8

1.4. What Causes Drop Friction?

1.4.1. Contact-Line Friction

One of the dissipative mechanisms that lead to drop friction is contact-line friction, due to the pining/de-pining of the contact line. The energy dissipation by contact-line friction happens directly at the contact line and reflects in changes of dynamic contact angles (θ_d). In the molecular scale, the pining/de-ping occurs because of discontinuous molecular motion on the solid surface. In 1949, Yamold and Mason first suggested that liquid molecules adsorb and desorb near a moving contact line.[52] Later, Blake and coworkers transformed this idea into a quantitative theory called molecular kinetic theory (MKT).[28] In the MKT, liquid molecules discontinuously adsorb/desorb (jump) on a solid surface near the three-phase contact line. When the contact line is moving, the adsorption/desorption equilibrium is disturbed, leading to a local surface tension gradient and a change in contact angle (Figure 6a). This jump is quantified by equilibrium frequency (κ^0) and the average distance between the adsorption/desorption sites on the solid surface (λ). Using the two parameters, the contact-line velocity, $v(\theta)$ is given by

$$v(\theta) = 2\kappa^0 \lambda \sinh\left[\frac{F_w \lambda^2}{2k_B T}\right] \tag{7}$$

k_B is the Boltzmann constant, T is the absolute temperature, F_w is the driving force in unit length for the jump and can be calculated by

$$F_w = \gamma_L(\cos\theta_0 - \cos\theta_d) \tag{8}$$

θ_0 is the equilibrium contact angle. Inserting equation (8) into equation (7), one has:

$$\cos\theta_0 - \cos\theta_d = \frac{2k_B T}{\gamma_L \lambda^2} \sinh^{-1}\left(\frac{v}{2\kappa^0 \lambda}\right) \tag{9}$$

Knowing κ^0 and λ, equation (9) can predict the change in contact angle by the activated dynamics of liquid molecules.

In the nano-/micrometer scale, the pining/de-pining is caused by surface defects or deformation. The contact line is deformed when it faces defects during drop sliding, which leads to a local change in surface tension and a restoring force due to fringe elasticity (Figure 6b). In this case, the friction force depends on the contact-line shape. For an infinitely small defect on a hydrophilic surface withdrawn from a liquid bath, Joanny and de Gennes derived an equation to

quantify the corresponding force based on the shape of the contact line.[53] In 2022, Saal *et al.* verified Joanny and de Gennes's equation experimentally by measuring the pinning forces owing to the contact-line deformation by a single defect. They also found that the pinning force is largely independent of drop size and sliding speed.[54] In addition, pioneering studies have shown that contact-line motion on soft surfaces becomes extremely slow due to surface deformation with a wetting ridge, which leads to a viscoelastic dissipation opposing the contact-line motion (Figure 6c).[55] During drop sliding, the wetting ridge is reoriented by the moving contact line and leads to a change in dynamic contact angles.[56] Zhao *et al.* reported that viscoelastic dissipation increases with increasing elastomer thickness.[57] In addition, the viscoelastic dissipation depends on contact-line velocity. At a low-velocity regime, complex phase separation with the presence of uncross-linked polymer chains at the surfaces or swelling of soft substrates by absorbing the wetting liquid can happen.[58, 59] At a relatively high-velocity regime, the contact line de-pins and slides down the wetting ridge, then forms a new one after a transient, leading to a stick-slip motion.[60]
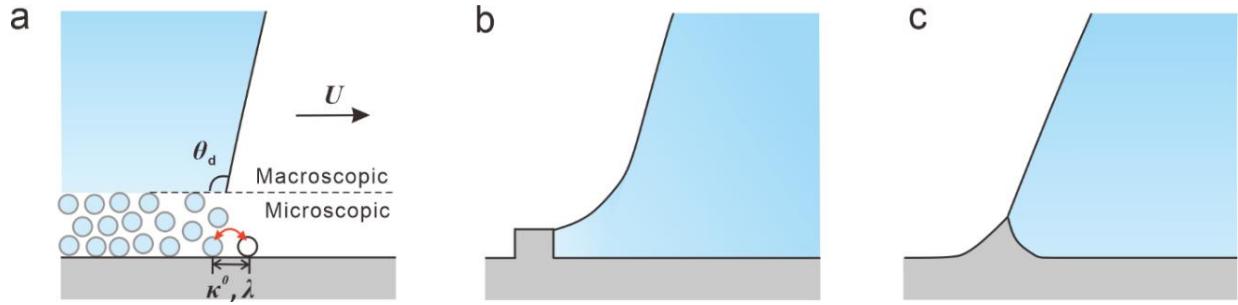

Figure 6. *Schematic of dissipative mechanisms leading to contact-line friction. (a) Activated dynamics of liquid molecules; (b) Surface defects; (c) Surface deformation.*

1.4.2. Viscous Dissipation

The second dissipative mechanism is viscous dissipation due to the shear stress of fluids. One of the fluids is the liquid inside a sliding drop. The hydrodynamic model assumes that viscous dissipation of the liquid dominates the contact-line motion, and is balanced by interfacial energy. The balance can be represented by lubrication theory with the assumption that the flow profile (position-dependent height of the liquid), $h(x)$, is nearly parabolic in the liquid phase:

$$\frac{d^3 h}{dx^3} = -\frac{3Ca}{h^2} \tag{10}$$

$Ca = \frac{\mu v}{\gamma_L}$ is the capillary number, μ is the dynamic viscosity of the liquid, and v is the velocity of the fluid. By assuming the flow profile can be divided into an inner and outer region, Voinov derived the solution of the above equation with:[22]

$$h'(x) \approx \theta(x) \cong [9Ca ln\left(\frac{L_0}{L_S}\right)]^{\frac{1}{3}} \qquad (11)$$

In the outer region, the traditional "no-slip" boundary condition is used within a macroscopic length scale (L_0). People usually take the capillary length as the macroscopic length scale. In the inner region, slip is allowed to remove the singularity at the contact line within a cut-off length (L_S, or called slip length). The cut-off length is normally in a couple of molecular layers scale (Figure 7a). [59,60] Later on, Cox extended Voinov's solution to two fluids (air and liquid) by: [23]

$$g(\theta_d) - g(\theta_0) = Ca ln\left(\frac{L_0}{L_S}\right) \qquad (12)$$

Equation (12) is therefore called the "Cox-Voinov model" today. In 1992,[25] Petrov & Petrov pointed out that for $\theta < 135°$, equation (12) can be simplified to:

$$\theta_d^3 - \theta_0^3 = \pm 9Ca ln(\frac{L_0}{L_S}) \qquad (13)$$

When fitting the velocity-dependent contact angles with equation (13), one normally gets the fitting parameter of slip length (L_S).
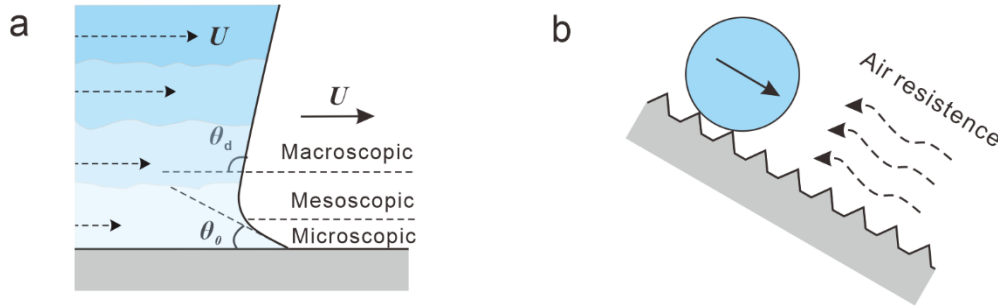

Figure 7. *Schematic of viscous dissipative mechanisms by the shear stress of (a) flowing liquid inside the drop and (b) air around the sliding drop.*

The other fluid is the flowing air around the sliding drop, especially the part facing front to the sliding drop (Figure 7b). Because the viscosity of air is around 2 orders of magnitude lower than the liquid viscosity. The viscous dissipation from the air only becomes dominant for the cases with low liquid viscosity, low liquid-solid contact area, and high drop velocity. According to a

nonlinear relationship between drop friction and drop velocity, Mouterde *et al.* found that the main source of resistance to water drop motion on superhydrophobic surfaces is from the air around it.[40]
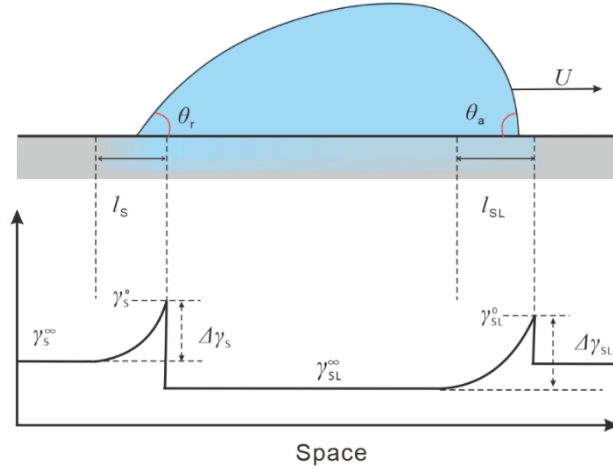
1.4.3. Surface Adaptation

Figure 8. *Schematic of the adaptation model.*

The third dissipative mechanism is surface adaptation—surfaces change their properties when they contact with a liquid or its vapor. Surface adaption is due to polymer reconstruction, reorientation, or swelling; diffusion or ordering of liquid molecules; chemical reaction; water/airborne hydrocarbons/surfactant adsorption; formation of the electric double layer. Surface properties changed by adaptation are equivalent to changes in interfacial tensions and reflect in the change of contact angle. To describe the change in contact angle by surface adaptation quantitatively, Butt *et al.* proposed an adaptation model in 2018.[39] By introducing exponentially relaxing interfacial energies and applying Young's equation locally (Figure 8), they predict a change of advancing contact angle (θ_a) and receding contact angles (θ_r) depending on the contact-line velocity (v):

$$\cos\theta_a = \cos\theta_0 - \frac{\Delta\gamma_{SL}}{\gamma_L} e^{-l/v\tau_{SL}} \tag{14}$$

$$\cos\theta_r = \cos\theta_0 + \frac{\Delta\gamma_S}{\gamma_L} e^{-l/v\tau_S} \tag{15}$$

Here, $\Delta\gamma_{SL}/\Delta\gamma_S$ quantifies the change in solid-liquid/solid-vapor interfacial tensions due to adaption. The relaxation times for the dry-to-wet and wet-to-dry adaptation processes are τ_{SL} and τ_S, respectively. The peripheral thickness l is the width of the contact region, which influences the

contact angle. The fitting parameters of this model are peripheral thickness (l) and relaxation time (τ), which relate the velocity-dependent contact angle to the adaptation kinetics. Therefore, by measuring velocity-dependent contact angle, one can study the adaptation kinetic. One of the limitations in applying the model is the uncertainty in peripheral length, which cannot be measured experimentally yet. In addition, multiple adaptation processes with different relaxation times could happen in a single liquid/solid system. To distinguish them, a good reference is required. Butt *et al.* proposed the model, but its relevance was not experimentally clarified.

1.4.4. Multiple Dissipative Mechanism

In practice, the energy dissipation of sliding drop should be multi-sourced. This argument is supported by the fact that neither the hydrodynamic model nor the MKT solely explains the velocity-dependent contact angle for the whole velocity range. To integrate multiple dissipation channels, some trials have been made. For example, Brochard-Wyart and de Gennes considered that the total energy dissipation in partial wetting comprises both viscous dissipation and non-viscous dissipation at the moving contact line.[36] While Petrov and Petrov emphasized that the equilibrium contact angle in the hydrodynamic model is also velocity dependent, which can be estimated from the molecular kinetic theory.[25] All of them came out with a similar combined model:

$$\theta_d^3 = \left\{\cos^{-1}\left[\cos\theta_0 - \frac{2k_BT}{\gamma_L\lambda^2}\sinh^{-1}\left(\frac{v}{2\kappa^0\lambda}\right)\right]\right\}^3 + 9Caln\left(\frac{L_0}{L_S}\right). \tag{16}$$

Some researchers reported that the combined model fits the experimental data better.[25, 26, 29, 31] However, the combined model is clearly empirical and phenomenological. In particular, we need to pay attention to the outcoming values of fitting parameters (λ, L_S, and k^0) which might be unphysical. In addition, Perrin *et al.* unified the dissipation channels of both viscus dissipation and activate dynamics by a crossover between a low-velocity activated regime and a high-velocity viscous regime.[37] Until now, a combination that includes surface adaptation is still unsolved yet.

1.5. How to Quantify Drop Friction?

Before the dissipative mechanism of moving contact line and its consequence in changing contact angle was studied, people had tried to quantify drop friction. Wet in 1911 [61] and Yarnold in 1938 [62] demonstrated that multiple factors determined the resistance to drop sliding, including the difference between the cosines of the advancing and receding contact angle, the radius of the

tube, and interfacial tension. In 1950, Birkerman proposed that the nature of resistance to drop sliding is the work required for drop elongation or stretching when the drop starts to move [17] and the resistance force (F_s) is proportional to the liquid surface tension (γ_L) and the drop width (w). That is

$$F_s = \beta \gamma_L w \tag{17}$$

Here, β is a constant and depends on the wettability and roughness of solid surfaces. In 1960, Kawasaki verified equation (17) experimentally and found out $\beta \propto (cos\theta_r - cos\theta_a)$.[18] Almost at the same time (1961), Furmidg deduced an equation to quantify the work needed to be done to overcome the resistance force and got:[19]

$$F_s = \gamma_L w(cos\theta_r - cos\theta_a) \tag{18}$$

Which is identical to Birkerman and Kawasaki's finding. In 1983, Dussan and Chow modeled the critical drop shape during motion and came out with the same results as Furmidge's equation (18) as well.[63]

However, the assumption made in Dusaan and Chow's model about constant contact angle might be invalid because contact angle varies around the contact line in reality. Extrand and Gent took this into account and came out with a constant of $4/\pi$ as a pre-factor adding to equation (18) when the drop has a perfect circle shape with a radius r.[64] Later on, ElSherbini and Jacobi generalized the pre-factor as a geometry factor k, which depends on the contact angle distribution along the contact line and the shape of the contact contours. Correspondingly, equation (18) was modified as:

$$F_s = k\gamma_L w(cos\theta_r - cos\theta_a) \tag{19}$$

The equation can also be derived by integrating the unbalance surface tension force over the counter of the drop with contact angle θ (φ) and the radius $r(\varphi)$ depending on the azimuthal angle φ (Figure 9):

$$F_s = - \oint \gamma_L \, cos\theta(\varphi)cos\varphi r(\varphi)d\varphi \tag{20}$$

By finding out an empirical relationship between contact angle and azimuthal angle experimentally, they further calculated $k \approx 0.774$.[65]

In all the above studies, the retention force is quantified before drop sliding. Similar to the

friction between solid-solid interfaces, Gao *et al.* found that drop friction can also be divided into a static and a kinetic regime, corresponding to the cases when a drop starts to slide and has been sliding with a non-zero velocity.[66] To distinguish, we called the friction forces in the two cases "static friction force" and "kinetic friction force", respectively. The maximum retention force mentioned above when the drop starts to slide is the static friction force. Thus, one can use equation (19) to predict static drop friction on the onset of drop sliding. The only uncertainty comes from the k-factor. Because the k-factor depends on the shape of the contact contours and the contact angle distribution along the contact line, determining the k-factor experimentally remains challenging. Laroche *et al.* reported the static friction force can be tuned by over 30% by pre-shaping the drop before moving while the kinetic friction force is independent of the pre-shape.[67] Then the open questions are: can we also use equation (19) to quantify the kinetic friction? If yes, why and how to determine the k-factor? If not, how to quantify kinetic friction force?
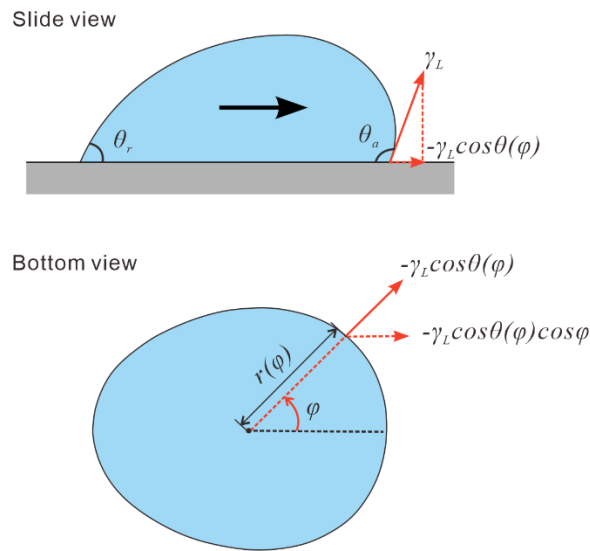

Figure 9. Schematic of unbalanced surface tension along the contact line of a sliding drop.

1.6. Knowledge Gaps and Findings

The main findings toward predicting drop sliding, the development in materials fabrication, and the new methods included in this thesis are described in 11 either published or submitted manuscripts in peer-reviewed scientific journals. An overview of the Ph.D. study and the connection between the 11 manuscripts are shown in Figure 10. Among the 11 manuscripts, I selected six first-author manuscripts to describe in detail in section 2. The main knowledge gaps, results, and conclusions of the six selected manuscripts are summarized below.
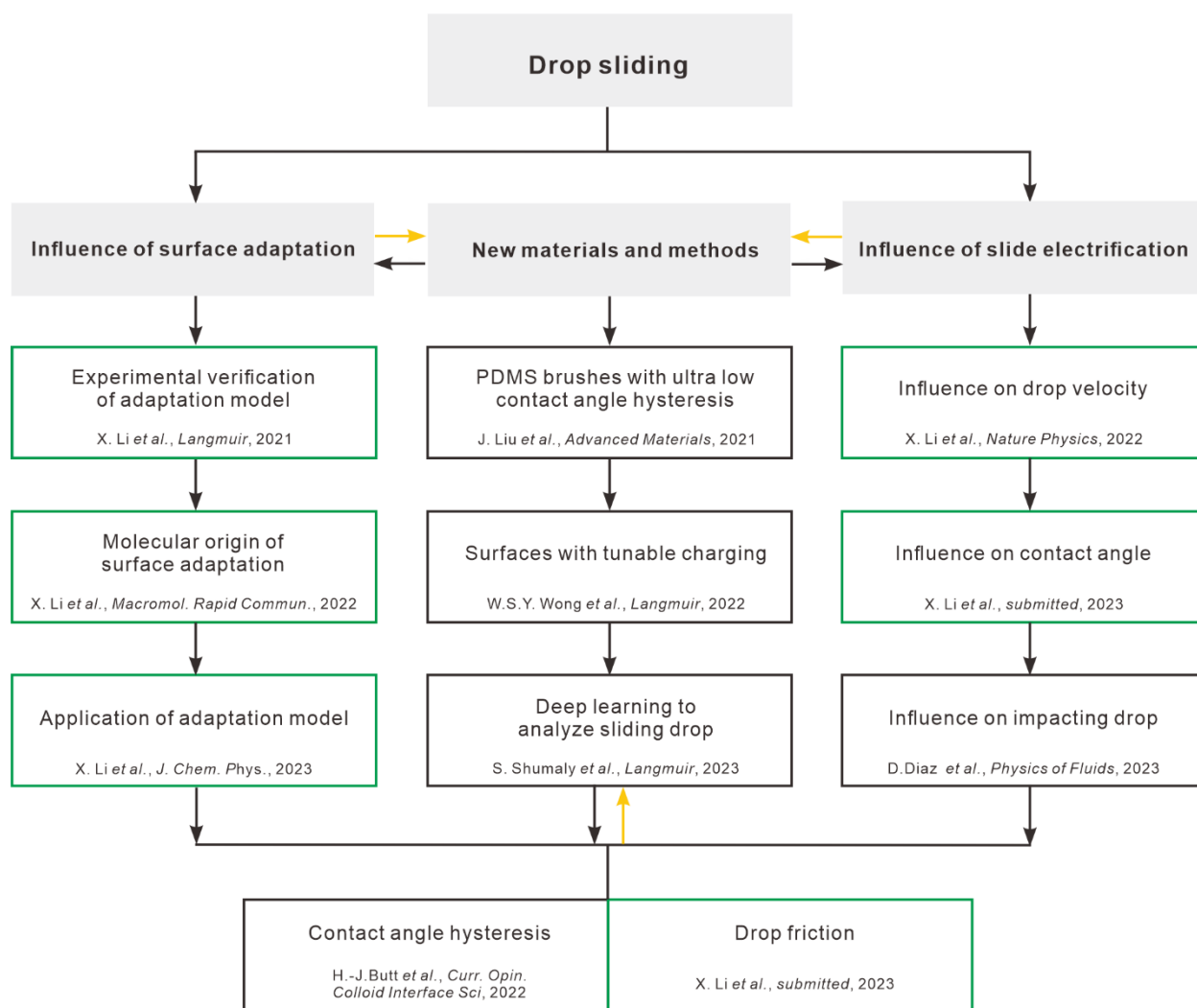

Figure 10. *Towards predicting contact angle hysteresis and drop friction of sliding drops, the Ph.D. projects evolving in three dimensions: (1) Understanding the influence of surface adaptation on drop sliding (left); (2) Understanding the influence of slide electrification on drop sliding (right);*

(3) Related new materials and methods which are developed during the research in the direction of (1) and (2). Green boxes show the main topics of the manuscripts collected in Appendix B. Black boxes show the topics of the co-author manuscripts. Black and yellow arrows indicate the connections between projects.

Experimental verification of the adaptation model

In 2018, Butt *et al.* proposed adaptation as a mechanism of contact angle hysteresis, along with a theoretical framework described in section 1.4.3. However, there was no existing experimental verification of the adaptation model. To verify how applicable the adaptation model is, we explored the adaptation of a random copolymer composed of styrene with 11%−25% (in molar) acrylic acid (PS/PAA) to water by a home-built tilted plate setup. By velocity-dependent dynamic contact angle measurement, we found that the advancing contact angle of sliding water drops on the PS/PAA surface decreased from 95° to 87° when the contact-line velocity is < 20 µm/s. The decreasing advancing contact angle fits the adaptation model well, resulting in a relaxation time of ≤ 2 ms for the dry-to-wet process. This adaptation could occur due to water diffusion into the polymer layer or polymer reorientation at the interface. We further confirmed water diffusion occurs in a few minutes with confocal microscopy measurement. For details, see section 2.1.

Molecular origin of surface adaptation

After verifying the adaptation model by dynamic contact angle measurement (Section 2.1), what causes the adaption of PS/PAA surfaces to water in milliseconds still remained unclear. In addition, we only observed the adaptation process from dry to wet at the advancing sides of sliding drops but did not see the wet-to-dry dynamic on the receding sides. To clarify the above situation, by sum frequency generation (SFG) measurements at the liquid/solid interface, we discovered that the adaptation is also caused by PS segment displacement from the surface and PAA segment enrichment. To recover the adapted PS/PAA surfaces from wet to dry, both drop velocity measurement and SFG measurement indicated that annealing is required. That also explains why we did not observe the spontaneous wet-to-dry process on the receding side of sliding drops. For details, see section 2.2.

Application of the adaptation model

The successful verification of the adaptation model indicates that the adaptation model relates adaptation kinetics to dynamic contact angle. Active agents released from functional polymer surfaces under certain liquid environment is a kind of adaptation. The release kinetics is normally studied by HPLC, NMR, or ultraviolet−visible spectroscopy. However, these techniques cannot offer characterization for a fast release within a time scale <1 s. Thus, up until now, we have only limited knowledge about the release kinetics at shorter time scales. In this project, we implemented dynamic contact angle measurement to study the fact-release kinetics of a pH-responsive copolymer. The copolymer consists of methyl methacrylate and 8-quinolinyl-sulfide-ethyl acrylate, namely P(MMA-*co*-HQSEA). The active agent is 8-hydroxyquinoline (8HQ), which acts as an inhibitor for metal corrosion or proteasome. 8HQ can be released by hydrolysis on the β-thiopropionate groups when coming in contact with aqueous solutions. After releasing 8HQ, the surface becomes more hydrophilic leading to a decrease in contact angle. Thus, dynamic contact angle measurements are a sensitive way to study the release process. We found that both hydrolysis rate and polymer conformation affect the release kinetics which both already take place at a time scale <1 s, indicating that we enter new territory for studying release kinetics. For details, see section 2.3.

Influence of slide electrification on drop velocity

Until now, energy dissipation in a sliding drop has been attributed to viscous dissipation, contact-line friction, and adaptation. However, in this project, by recording drop sliding on tilted surfaces with a high-speed camera, we found the substrate under the polymer coating, which has no contribution to viscous dissipation, contact-line friction, or adaptation influences drop trajectories significantly. After analyzing the forces working on the sliding drops, we found that drops sliding on low-permittivity substrates undergo higher friction force than the ones sliding on high-permittivity substrates, though the coatings on top of the substrates are the same. The extra friction force on low-permittivity substrates can contribute up to 50% of the drop friction, depending on slide length and drop number. Based on the dependencies and measurements of drop charge, we believe the extra force has an electrostatic origin because of slide electrification. We then built a model to quantify the electrostatic force base on the Coulomb interaction between drop charges and surface charges. The theoretical electrostatic force predicts the experimental extra

friction force well. Therefore, we concluded that slide electrification is a new important dissipation channel leading to drop friction and contact angle hysteresis. For details, see section 2.4.

Influence of slide electrification on contact angle

In the above project, we have demonstrated that spontaneous charging of moving drops and surfaces by slide electrification affects drop motion substantially. However, it is still not clear if spontaneous charging changes the contact angle. The field of electrowetting has already demonstrated how contact angles decrease in response to deliberately applied electric fields. In this project, we show that the naturally occurring fields due to deposited charges have a similar effect. We complement our experimental findings with a fundamental theoretical model that expands upon Young's equation. Pivotal to this macroscopic treatment is the occurrence of a microscopic length scale over which the electrostatic Maxwell stress localizes close to the contact line. The universality of the discovered phenomenon is confirmed, as we show that it occurs over a wide range of experimental parameters. Additionally, our theory helps to rationalize experimental accounts from literature. The underlying physical mechanism is very general and the phenomenon is likely to play a role in many dynamic wetting scenarios, both in research and applications. For details, see section 2.5.

Universal law of drop friction

Though we have enriched the dissipation channels leading to drop frictions with surface adaptation and slide electrification, still today, it is still impossible to predict the velocity and hence the position of sliding drop. The reason is that numerous dissipation channels occur spontaneously. How and how much dissipation channels contribute to the drop friction on different surfaces is, however, unclear. With tilted plate experiments, we find that friction forces follow a simple, universal empirical equation. Only one material-specific parameter is necessary to describe drop motion. We term this dimensionless parameter "friction coefficient". In contrast to static wetting of sessile drops, which is fully described by the advancing and receding contact angles, dynamic wetting is determined by the friction coefficient. For details, see section 2.6.

1.7. References

1. Libri, G. History of the mathematical sciences in Italy, from the Renaissance until the end of the seventeenth century. 3, 54 (1840).

2. Wolf, C. On the influence of temperature on phenomena in capillary tubes. *Annalen der Physik und Chemie* 101, 550-576 (1857).

3. Boyle, R. New experiments physico-mechanicall, touching the spring of the air and its effects. 265–270 (1660). URL: http://echo.mpiwg-berlin.mpg.de/MPIWG:SUV5ZB7D

4. Fabri, H. *Dialogi physici quorum*. (1665). URL: https://books.google.com/books?id=zRJ2rQs730QC&pg=PA267

5. Bernoulli, J. *Dissertatio de gravitate Aetheris*. (1683). URL: https://www.jstor.org/stable/i206895

6. Vossius, I. *On the sources of the Nile and other rivers*. (1666).URL: https://books.google.com/books?id=FjoVAAAAQAAJ&pg=PA3

7. Borelli, G. A. *De motionibus naturalibus a gravitate pendentibus*. (1670). URL: http://echo.mpiwg-berlin.mpg.de/ECHOdocuView?highlightQuery=CLXXXV&viewLayer=dict%2Csearch&url=%2Fpermanent%2Farchimedes_repository%2Flarge%2Fborel_demot_010_la_1670%2Findex.meta&highlightElement=s&highlightElementPos=2&pn=385&queryType=fulltextMorph

8. Carré. Experiments on capillary tubes. *Mémoires de l'Académie Royale des Sciences*, 241-254 (1705). URL: http://gallica.bnf.fr/ark:/12148/bpt6k3487x/f409.image

9. Maxwell, J. C. Capillary action. *Encyclopedia Britannica* (1911). URL: https://en.wikisource.org/wiki/1911_Encyclop%C3%A6dia_Britannica/Capillary_Action

10. Laplace, P. S. Traité de mécanique céleste. *L'Imprimerie de Crapelet*: Chez J.B.M. Duprat, 1798. URL: http://archive.org/details/traitdemcaniquec03lapl

11. Young, T. III. An essay on the cohesion of fluids. *Philosophical Transactions of the Royal Society* 95, 65-87, (1805).

12. Pockels, A. Über Randwinkel und Ausbreitung von Flüssigkeiten auf festen Körpern. *Physikalische Zeitschrift* 15, 39-46 (1914).

13. Sulman, H. Hysteresis of contact-angles. *Transactions of the Institution of Mining and Metallurgy* 29, 88-97 (1920).

14. Ablett, R. An investigation of the angle of contact between paraffin wax and water. *Philosophical Magazine and Journal of Science 46*, 244-256 (1923).

15. N. K. Adam, G. J. Angles of contact and polarity of solid surfaces. *Journal of the Chemical Society* 127, 1863-1868 (1925).

16. Butt, H.-J. *et al.* Contact angle hysteresis. *Current Opinion in Colloid & Interface Science*, 101574 (2022).

17. Bikerman, J. J. Sliding of drops from surfaces of different roughnesses. *Journal of Colloid Science* 5, 4, 349-359 (1950).

18. Kawasaki, K. Study of wettability of polymers by sliding of water drop. *Journal of Colloid Science* 15, 5, 402-407 (1960).

19. Furmidge, C. G. L. Studies at phase interfaces. I. The sliding of liquid drops on solid surfaces and a theory for spray retention. *Journal of colloid science* 17, 4: 309-324 (1962).

20. Blake, T. & Haynes, J. Kinetics of liquid-liquid displacement. *Journal of colloid and interface science* 30, 421-423 (1969).

21. Huh, C. & Scriven, L. E. Hydrodynamic model of steady movement of a solid/liquid/fluid contact line. *Journal of colloid and interface science* 35, 85-101 (1971).

22. Voinov, O. Inclination angles of the boundary in moving liquid layers. *Journal of Applied Mechanics and Technical Physics* 18, 216-222 (1977).

23. Cox, R. The dynamics of the spreading of liquids on a solid surface. Part 1. Viscous flow. *Journal of fluid mechanics* 168, 169-194 (1986).

24. Hayes, R. A. & Ralston, J. The molecular-kinetic theory of wetting. *Langmuir* 10, 340-342 (1994).

25. Petrov, P. & Petrov, I. A combined molecular-hydrodynamic approach to wetting kinetics. *Langmuir* 8, 1762-1767 (1992).

26. Sedev, R. V. & Petrov, J. G. Influence of geometry on steady dewetting kinetics. *Colloids and surfaces* 62, 141-151 (1992).

27. Hayes, R. A. & Ralston, J. Forced liquid movement on low energy surfaces. *Journal of colloid and interface science* 159, 429-438 (1993).

28. Blake, T. *et al.* Contact angle relaxation during droplet spreading: comparison between molecular kinetic theory and molecular dynamics. *Langmuir* 13, 2164-2166 (1997).

29. Schneemilch, M. *et al.* Dynamic wetting and dewetting of a low-energy surface by pure liquids. *Langmuir* 14, 7047-7051 (1998).

30. Petrov, J. G. *et al.* Dynamics of partial wetting and dewetting in well-defined systems. *The Journal of Physical Chemistry B* 107, 1634-1645 (2003).

31. Ranabothu, S. R. *et al.* Dynamic wetting: hydrodynamic or molecular-kinetic? *Journal of colloid and interface science* 288, 213-221 (2005).

32. Le Grand, N. *et al.* Shape and motion of drops sliding down an inclined plane. *Journal of Fluid Mechanics* 541, 293-315 (2005).

33. Vega, M. *et al.* Experimental investigation of the link between static and dynamic wetting by forced wetting of nylon filament. *Langmuir* 23, 10628-10634 (2007).

34. Duvivier, D. *et al.* Experimental evidence of the role of viscosity in the molecular kinetic theory of dynamic wetting. *Langmuir* 27, 13015-13021 (2011).

35. Kim, J.-H. *et al.* Dynamic contact angle measurements on superhydrophobic surfaces. *Physics of Fluids* 27, 032107 (2015).

36. Brochard-Wyart, F. & De Gennes, P. Dynamics of partial wetting. *Advances in colloid and interface science* 39, 1-11 (1992).

37. Perrin, H. *et al.* Defects at the nanoscale impact contact line motion at all scales. *Physical review letters* 116, 184502 (2016).

38. Andreotti, B. & Snoeijer, J. H. Statics and dynamics of soft wetting. *Annual review of fluid mechanics* 52, 285-308 (2020).

39. Butt, H.-J. *et al.* Adaptive wetting—adaptation in wetting. *Langmuir* 34, 11292-11304 (2018).

40. Mouterde, Timothée, *et al.* Superhydrophobic frictions. *Proceedings of the National Academy of Sciences* 116, 17, 8220-8223 (2019).

41. De Gennes, P.-G. *et al.* Capillarity and wetting phenomena: drops, bubbles, pearls, waves. Vol. 315, Springer (2004).

42. Shuttleworth, Ro. The surface tension of solids. *Proceedings of the physical society*. Section A 63, 5, 444-457 (1950).

43. Butt, H.-J. *et al.* Physics and chemistry of interfaces. John Wiley & Sons (2023).

44. Dupré, A. & Dupré, P. *Théorie mécanique de la chaleur*. Gauthier-Villars (1869).

45. Schrader, M. E. Young- Dupré revisited. *Langmuir* 11, 3585-3589 (1995).

46. Wenzel, R. N. Resistance of solid surfaces to wetting by water. *Industrial & Engineering Chemistry* 28, 988-994 (1936).

47. Quéré, D. Wetting and roughness. *Annual review of materials research* 38, 71-99 (2008).

48. Cassie, A. B. D. and Baxter, S. Wettability of porous surfaces. *Transactions of the Faraday Society* 40, 546-551 (1944).

49. Cassie, A.B. D. Contact angles. *Discussions of the Faraday Society* 3, 11-16 (1948).

50. Bico, J. *et al.* Elastocapillarity: when surface tension deforms elastic solids. *Annual Review of Fluid Mechanics* 50 (2018): 629-659.

51. Mugele, F. & Heikenfeld, J. Electrowetting: fundamental principles and practical applications. John Wiley & Sons (2018).

52. Yarnold, G. & Mason, B. A Theory of the Angle of Contact. *Proceedings of the Physical Society. Section* B 62, 121 (1949).

53. Joanny, J. F. & De Gennes, P. G. A model for contact angle hysteresis. *The Journal of chemical physics* 81, 1, 552-562 (1984).

54. Saal, A. *et al.* Pinning forces of sliding drops at defects. *Europhysics Letters* 139, 4, 47001 (2022).

55. Carré, A. *et al.* Viscoelastic effects in the spreading of liquids. *Nature* 379, 6564, 432-434 (1996).

56. Karpitschka, S. *et al.* Droplets move over viscoelastic substrates by surfing a ridge. *Nature Communications* 6, 1, 7891-7898 (2015).

57. Zhao, M. *et al.* Geometrical control of dissipation during the spreading of liquids on soft solids. *Proceedings of the National Academy of Sciences* 115, 8, 1748-1753 (2018).

58. Cohen Stuart, M. A. *et al.* Why surfaces modified by flexible polymers often have a finite contact angle for good solvents. *Langmuir* 22, 4, 1722-1728 (2006).

59. Hauer, L. *et al.* Phase separation in wetting ridges of sliding drops on soft and swollen surfaces. *Physical Review Letters* 130, 5, 058205 (2023).

60. Kajiya, T. *et al.* Advancing liquid contact line on visco-elastic gel substrates: stick-slip vs. continuous motions. *Soft Matter* 9, 2, 454-461(2013).

61. West, G. D. On the resistance to the motion of a thread of mercury in a glass tube. *Proceedings of the Royal Society of London. Series A, Containing Papers of a Mathematical and Physical Character* 86, 583, 20-25 (1911).

62. Yarnold, G. D. The motion of a mercury index in a capillary tube. *Proceedings of the Physical Society* 50, 4, 540 (1938).

63. Chow, R. T. P. On the ability of drops or bubbles to stick to non-horizontal surfaces of solids. *Journal of Fluid Mechanics* 137, 1-29 (1983).

64. Extrand, C. W. & Gent, A. N. Retention of liquid drops by solid surfaces. *Journal of Colloid and Interface Science* 138, 2, 431-442 (1990).

65. ElSherbini, A. I. & Jacobi, A. M. Retention forces and contact angles for critical liquid drops on non-horizontal surfaces. *Journal of colloid and interface science* 299, 2, 841-849 (2006).

66. Gao, N. *et al.* How drops start sliding over solid surfaces. *Nature Physics* 14, 2, 191-196 (2018).

67. Laroche, A. *et al.* Tuning static drop friction. *Droplet,* e42 (2023).

2. Selected Publications

2.1. X. Li *et al. Langmuir*, 2021

Adaptation of a styrene-acrylic acid copolymer surface to water

Xiaomei Li, Simon Silge, Alexander Saal, Gunnar Kircher, Kaloian Koynov, Rüdiger Berger,*
Hans-Jürgen Butt

Max Planck Institute for Polymer Research, 55128 Mainz, Germany

Author contributions:

Rüdiger Berger and Hans-Jürgen Butt proposed the project, Xiaomei Li designed and built up the tilted plate setup, prepared the samples, performed measurements of sliding drop by tilted plate setup, static contact angles by a goniometer, surface topography by SFM imaging, and analyzed the data. Simon Silge and Alexander Saal helped to build the setup and wrote a MATLAB code for image processing. Gunnar Kircher synthesized the PS/PAA random copolymer and conducted the GPC and NMR measurements. Dr. Kaloian Koynov conducted the confocal microscopy measurement. All the authors discussed, interpreted the results, and wrote the manuscript.

LANGMUIR

Article

Adaptation of a Styrene−Acrylic Acid Copolymer Surface to Water

Xiaomei Li, Simon Silge, Alexander Saal, Gunnar Kircher, Kaloian Koynov, Rüdiger Berger,* and Hans-Jürgen Butt

Read Online

ACCESS | Metrics & More | Article Recommendations | Supporting Information

ABSTRACT: Solid surfaces, in particular polymer surfaces, are able to adapt upon contact with a liquid. Adaptation results in an increase in contact angle hysteresis and influences the mobility of sliding drops on surfaces. To study adaptation and its kinetics, we synthesized a random copolymer composed of styrene and 11−25 mol% acrylic acid (PS/PAA). We measured the dynamic advancing (θ_A) and receding (θ_R) contact angles of water drops sliding down a tilted plate coated with this polymer. We measured $\theta_A \approx 87°$ for velocities of the contact line <20 μm/s. At higher velocities, θ_A gradually increased to ∼98°. This value is similar to θ_A of a pure polystyrene (PS) film, which we studied for comparison. We associate the gradual increase in θ_A to the adaptation process to water: The presence of water leads to swelling and/or an enrichment of acid groups at the water/polymer interface. By applying the latest adaptation theory (Butt et al. *Langmuir* **2018**, *34*, 11292), we estimated the time constant of this adaptation process to be ≪1 s. For sliding water drops, θ_R is ∼10° lower compared to the reference PS surface for all tested velocities. Thus, at the receding side of a sliding drop, the surface is already enriched by acid groups. For a water drop with a width of 5 mm, the increase in contact angle hysteresis corresponds to an increase in capillary force in the range of 45−60 μN, depending on sliding velocity.
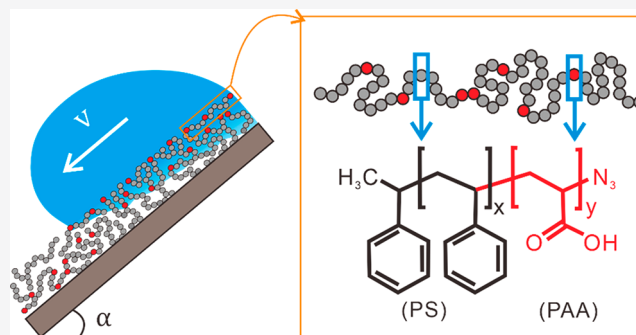
INTRODUCTION

Many surfaces react when they are brought into contact with a liquid. Some polymer surfaces, for example, reconstruct due to a reorientation of side groups or due to selective exposure of specific segments to the liquid interface.[1−4] In addition, polymers swell when liquid diffuses into the polymer.[5−7] Mixed polymer brushes, or block copolymers, expose the more compatible component to the liquid interface.[8−10] Adaptation of the surface typically leads to changes in surface composition upon exposure to a liquid. Consequently, adaptation contributes to contact angle hysteresis and dynamic contact angle changes.[11] These parameters are important in the fields of printing, digital microfluidics, and fiber coatings. Despite the importance in many wetting applications, a quantitative understanding of adaptation is still in its infancy.

When adaptation is nonreversible upon exposure to air, the adaptive kinetics at the solid/liquid interface can be probed by immersing the sample in liquids for different time spans. Subsequently, the surface can be studied by X-ray photoelectron spectroscopy (XPS).[12−17] However, reversible adaptation cannot be studied by XPS as it requires vacuum conditions. In addition, studying adaptation kinetics with a time scale of <1 s is challenging due to the time required to immerse samples into and remove samples from the liquid. Thus, measurements locoated directly at, or close to, the moving three-phase contact line are beneficial.
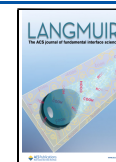
Contact angle measurements[18−20] are an elegant way of measuring adaptation kinetics. Surface adaptation leads to a change in advancing and receding contact angles,[11] which is experimentally easily measurable. Surface adaptation kinetics have been probed by measuring time-dependent dynamic contact angles using the Wilhelmy method, or by using the infused drop method.[21−24] Both methods can reveal changes in contact angles caused by surface adaptation. However, the studied adaptation processes are rather slow; they range in time from several minutes to several days.[22,25−27] To our knowledge, no report of direct contact angle measurements exists that reveals adaptation velocities of surfaces faster than seconds.

A quantitative description of the adaptive wetting phenomena was recently outlined by Butt et al. They introduced exponentially relaxing interfacial energies and applied Young's equation locally. The theory predicts the advancing (θ_A) and receding (θ_R) contact angles of a sliding drop on a surface exhibiting specific adaptation kinetics:[11]

ACS Publications

26

$$\cos \theta_A = \cos \theta^\infty - \frac{\Delta \gamma_{SL}}{\gamma_L^\infty} e^{-l_{SL}/v\tau_{SL}} \quad (1)$$

$$\cos \theta_R = \cos \theta^\infty + \frac{\Delta \gamma_S}{\gamma_L^\infty} e^{-l_S/v\tau_S} \quad (2)$$

θ^∞ is the contact angle in thermodynamic equilibrium (that is, for velocity $v \to 0$), and γ_L^∞ is the liquid surface tension. $\Delta \gamma_{SL}$ and $\Delta \gamma_S$ quantify the change in solid/liquid interfacial energy due to adaptation and the change in solid surface energy due to adaptation after the surface becomes dry, respectively. τ_{SL} and τ_S are relaxation times for the adaptation processes of the solid surface after it comes into contact with the liquid and dries again. l_{SL} and l_S are peripheral thicknesses, which are the spans of the contact region that influence the advancing and receding contact angles, respectively. According to this theory, contact angle measurements allow us to calculate the ratio of the peripheral length and the relaxation time. The kinetics, i.e., relaxation time of adaptation can then be anticipated by assuming a peripheral length value. To date, experimental verification of this adaptation theory is still lacking.

To explore the adaptation kinetics of surfaces upon contact with a liquid at a time scale <1 s, we designed and built a tilted-plate setup allowing us to measure velocity-dependent dynamic contact angles. As an adaptive surface, we used films of a random copolymer consisting of hydrophobic styrene (majority) and hydrophilic acrylic acid (minority) monomers. We studied the adaptation of these films to sliding water drops.

■ METHODS

Substrate Cleaning. Si wafers and cover glass slides were cleaned by ultrasonication in toluene (98%, Sigma), ethanol (99.5%, Sigma), and deionized (DI) water for 10 min, respectively. Then the substrates were dried using a nitrogen stream. Before coating, the substrates were further cleaned or activated for 10 min in a gas plasma made by 100% oxygen.

Preparation of the PS/PAA Surface. To synthesize PS/PAA copolymers, 22 mL of styrene, 2 mL of acrylic acid, and 60 mg of azobis(isobutyronitrile) (98%, Sigma) were dissolved in 30 mL of dimethylformamide (DMF) (99.8%, Sigma). The solution was degassed by three freeze/pump/thaw cycles and then stirred at 70 °C for 48 h. After it was precipitated three times using methanol, we obtained the copolymer.

To fabricate a PS/PAA film, 0.5−1 wt % PS/PAA copolymer in tetrahydrofuran (THF) (99.9%, Sigma) solution was dropped onto the Si wafer. Spinning was performed for 60 s at 1000 rpm. Then, the samples were heated at 150 °C in a vacuum overnight. Films with thicknesses between 30 and 70 nm were obtained.

Preparation of the PS Surface. PS was synthesized by anionic polymerization. The glassware was baked under vacuum, and then 150 mL of cyclohexane (99.8%, Sigma) with dissolved starter (*sec*-butyllithium) was added. Then 20 g of styrene was added. The mixture reacted overnight at room temperature. The polymerization was stopped by adding a few mL of degassed methanol. Subsequently more degassed methanol was added until the PS precipitated. The precipitate was dissolved in THF again and reprecipitated with degassed methanol.

To coat a Si wafer with PS, 2 wt % PS in toluene was dropped onto the Si wafer and then spinning was performed for 60 s at 2000 rpm. Finally, the samples were heated at 120 °C in vacuum overnight.

Preparation of the PS/PAA Surface with pH-Sensitive Dye. After cleaning and activation, cover glass slides were immersed in 2 wt % (3-aminopropyl)triethoxysilane (APTES, 98%, Sigma) anhydrous toluene (99.8%, Sigma) solutions for 4 h to form an APTES monolayer as a precursor. The slides were then sonicated twice in toluene for 10 min to remove physisorbed APTES. After drying in a

stream of nitrogen gas, the pH-sensitive dye (pHrodo iFL STP EATER, ThermoFisher) was grafted onto the APTES slides by immersing them in a mixture of 0.1 M sodium bicarbonate buffer (pH 8.2) and 5 wt % dimethyl sulfoxide (99.7%, Sigma) at a dye concentration of 100 μg/mL for 3 h. Afterward, the slides were sonicated twice in deionized water for 10 min and dried with nitrogen gas. Finally, the 8.7/1 PS/PAA copolymer was spin-coated onto the slides with a dye layer using 0.8 wt % THF solution and a spinning speed of 1000 rpm for 60 s.

Contact Angle Measurement Using the Sessile Drop Method. Contact angles were measured in the sessile drop configuration (Dataphysics contact angle measurement system, OCA35). An 8 μL water drop was deposited on the surface. Then 16 μL of DI water was pumped into the drop by a Hamilton syringe (100 μL) with a hydrophobic needle. Then 16 μL of water was sucked out of the drop (flow rate = 0.5 μL/s, mean contact line velocity = (8 $\pm$ 0.5) $\times$ 10^{-5} m/s). The process was repeated five times without interruption. Inflation and deflation were imaged using a high-speed camera taking side images. The advancing and receding contact angles were calculated by fitting an elliptical model to the images recorded in side view.

Dynamic Contact Angle Measurement Using the Tilted-Plate Setup. A 33 $\pm$ 1 μL water drop was pipetted onto the tilted surface using a syringe pump (KD Scientific, Legato 100 Syringe Pump). The tilt angles of the surface were varied from 33° to 70° for an 8.7/1 PS/PAA surface to adjust the drop velocity. In addition, different sliding velocities of drops were accomplished by measuring the drop at different distances from the position where the drop was released. The interval between drops was 10 min for PS surfaces. PS/PAA surfaces were annealed to 150 °C for 10 min between measurements.

To check if the interval between drops was long enough to dry the surface, a series of 40 drops with a volume of 33 $\pm$ 1 μL was pipetted onto the 67 nm 8.7/1 PS/PAA surface and the PS surface using the syringe pump. We set the interval between individual drops to 1 min for PS surfaces. For the PS/PAA surface, we set it to 10 min as it includes a heating step at 150 °C. The inclination angle was kept constant: $\alpha = 30°$ for the PS/PAA surface, and $\alpha = 16°$ for the PS surface. The distance between the pipet and the camera's field of view ranges from 3 to 6 cm. To prevent the results being affected by surface inhomogeneity, the contact angle was always measured at the same spot on the samples.

Confocal Laser Scanning Microscopy Measurement. Confocal laser scanning microscopy (CLSM) experiments were performed on a commercial confocal microscope, LSM 510 (Carl Zeiss, Jena, Germany) equipped with a C-Apochromat 40/1.2 W water-immersion objective. For excitation, the 488 nm line of an argon laser fiber-coupled to the microscope was used. Emitted fluorescence light was collected with the same objective and then passed through a confocal pinhole and a LP530 long pass emission filter to reach a photomultiplier detector. A stainless-steel chamber Attofluor (Thermo Fisher Scientific) holding the 25 mm round coverslip was used as a sample cell. A glass coverslip functionalized with pHrodo dye and covered (or not) with a polymer film was mounted in the sample holder, and a droplet of buffer solution with pH = 9.0 (ROTI Calipure) was added. For CLSM experiments, the functionalized glass surface was positioned in the middle of the confocal volume (in a vertical direction), and horizontal scans of different regions of the droplet contact line were acquired.

■ RESULTS AND DISCUSSION

As an adaptive surface, a random PS/PAA copolymer surface was prepared on Si wafers by spin-coating. Subsequently, we annealed the samples at 150 °C for 10 min in an oven (Figure 1a). The average roughnesses of the films were 0.2 $\pm$ 0.02 nm on a 500 $\times$ 500 nm^2 scale (Figure S1). The thicknesses of the films were 38 $\pm$ 1 and 67 $\pm$ 1 nm, respectively, as measured by a profilometer (KLA-Tencor Stylus-Profiler model P7). By annealing, we expected the hydrophobic styrene side groups to
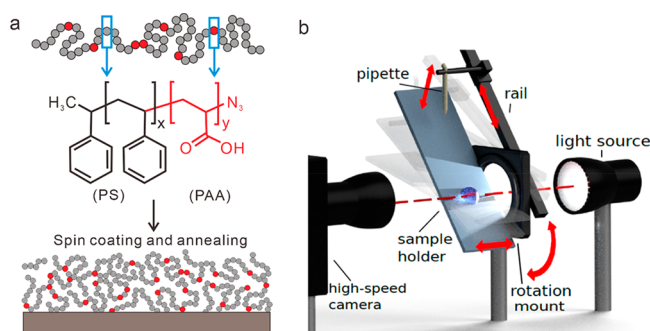
Figure 1. (a) Schematics of the PS/PAA copolymer surface. (b) Schematics of the tilted-plate setup. The corresponding data-processing process is explained in the Supporting Information (S4).

enrich at the surface to lower the surface energy. When the PS/PAA films were exposed to water, they were able to change their wetting properties by swelling and by reorientation of the polymer chain segments at the surface.

We synthesized PS/PAA surfaces with three different styrene/acrylic acid molar ratios: 8.7/1, 4.2/1, and 2.9/1 (details are in the Methods section). The ratios were revealed by NMR (Figure S2). The glass transition temperature T_g of all three PS/PAA copolymers was measured to be between 100 and 130 °C (Figure S3).

When measuring the contact angles of films by the traditional sessile drop method, the advancing contact angles of PS and all PS/PAA copolymers were in the range from 95° to 98°. However, the receding contact angle decreased by 21° when increasing the acrylic acid content from 8.7/1 to 2.9/1 (Table 1). Compared to pure PS, the receding angle for 2.9/1

Table 1. Dynamic Contact Angles of Copolymer Surfaces with Different PS-to-PAA Ratios[a]

polymer (PS/PAA)	θ_A (deg)	θ_R (deg)	$\Delta\theta$ (deg)
10/0	97 ± 1	70 ± 1	27 ± 2
8.7/1	98 ± 1	66 ± 1	32 ± 2
4.2/1	96 ± 1	50 ± 1	46 ± 2
2.9/1	95 ± 1	45 ± 1	50 ± 2

[a]The advancing and receding angles were measured using the sessile drop method.

(PS/PAA) even decreased by 25°. Accordingly, the contact angle hysteresis varies between 27° and 50°. In this contact angle measurement, the advancing side of the drop always wets a dry surface. In contrast, when measuring the receding contact angles, the surface stayed in contact with water for seconds. Thus, the response of the receding contact angle may indicate that the PS/PAA copolymer surfaces have already started to adapt to water.

The PS/PAA surfaces with a molar ratio of 8.7/1 (PS/PAA) had the highest advancing and receding contact angles. In addition, these films exhibited the lowest contact angle hysteresis (32° ± 2°). According to[28−30]

$$\sin \alpha_c = \frac{w\gamma_L^\infty k}{V\rho g}(\cos\Theta_R - \cos\Theta_A) \tag{3}$$

they also show the lowest roll-off angle α_c. The roll-off angle is the critical angle of a tilted plate at which a drop of volume V starts to move downward. Here, w is the width of the contact area of the drop, ρ is the density of the liquid, $g = 9.81$ m/s²,

and $k \approx 1$ is a geometrical factor, which depends on the shape of the drop.[31−34] Thus, the PS/PAA surface with a molar ratio of 8.7/1 (PS/PAA) allows us to measure the largest velocity range of drops by varying the tilting angle. Therefore, we mainly used an 8.7/1 PS/PAA copolymer surface to measure the velocity-dependent contact angle hysteresis on our tilted-plated setup.

We applied the tilted-plate setup to measure the velocity-dependent dynamic contact angles (Figure 1b). The dynamic contact angles were always measured along the same track on the sample. Between measuring subsequent drops, we annealed the sample for 10 min at 150 °C to ensure a reproducible dry surface. Before being measured again, the samples were quickly cooled down to room temperature by making a contact to a marble slab for 1 min (Figures S4 and S5).

We first consider a water drop with a length of L that slides down the PS/PAA surface with a tilted angle α at a velocity v (Figure 2a). During the sliding process, the surface stays in contact with water for $t = L/v$. This contact time can be controlled by adjusting the drop velocity (v), which depends on the tilt angle (α) of the substrate and the distance from the position where the drop was released. The scenarios of both adaptation processes are illustrated at the advancing and receding sides of the drop with a symbolistic view of the orientation of the phenol rings and the carbonic acid groups (Figure 2a). For a sliding drop, we obtain two scenarios for the adaptation of the dynamic contact angle.

(1) When $v \geq l_{SL}/\tau_{SL}$, the drop slides too fast to allow adaptation of the surface, and phenol rings remain on the surface. Assuming that this is correct, no change in the contact angle can be measured at higher sliding velocities of the drop. Indeed, for the PS/PAA surface, we measured a constant advancing contact angle of 96° at the velocity range of 10^{-4} up to 0.1 m/s (red symbols in Figure 2b). In this velocity range, we did not observe a significant difference to the PS reference sample (blue symbols in Figure 2b). We conclude that annealed PS/PAA films mostly exhibit styrene at the surface.

(2) However, for a drop velocity of 7×10^{-5} m/s and below, the advancing contact angle decreased to 87° for a PS/PAA surface compared to 95° for a PS surface ($v \leq l_{SL}/\tau_{SL}$). We interpret this contact angle decrease at very low velocity as an indication of the enrichment of carbonic acid groups at the surface. This enrichment is driven by the contact with water at the advancing side of the sliding drop. It has to take place in a narrow region around the contact line, which influences the contact angle, called the peripheral thickness. Notably, the contact angle decrease at a low sliding velocity does not depend on the thickness of the sample (Figure 2b). Thus, only the surface of the PS/PAA films is involved. The surface can restructure and expose acrylic acid groups or water can penetrate, leading to an increasing dielectric constant of the topmost surface.

To estimate the order of the relaxation time τ_{SL} for this process, we fitted eq 1 to the measured advancing angles of the PS/PAA surface.[11] For the fit, we used $\theta_a^\infty = 87°$, $\Delta\gamma_{SL} = 0.013$ N/m, and $\gamma_L^\infty = 0.072$ N/m in the velocity range of 5×10^{-6} to 0.1 m/s (red continuous line in Figure 2b). The fit revealed a ratio of $\frac{l_{SL}}{\tau_{SL}} = (5 \pm 2) \times 10^{-5}$ m/s. Assuming a peripheral thickness on the order of $l_{SL} = 10$ nm results in a relaxation time τ_{SL} of ~0.2 ms. With $l_{SL} = 100$ nm, one would estimate $\tau_{SL} = 2$ ms.
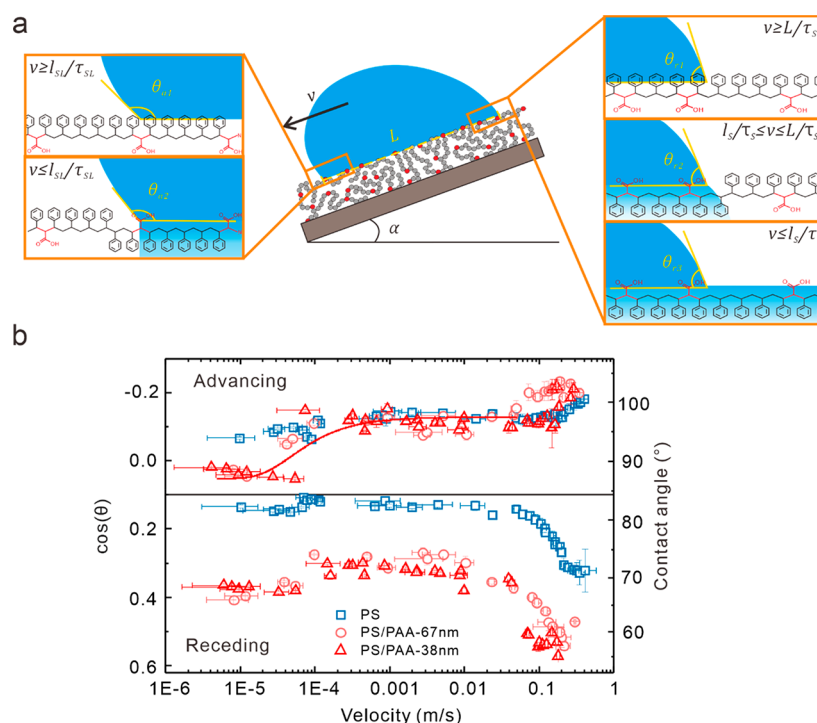
Figure 2. (a) Schematic drawing of the relationship between drop velocity and the change in dynamic contact angles caused by surface adaptation. (b) Contact angles (θ) and $\cos(\theta)$ vs velocity on the PS and PS/PAA (8.7/1) surfaces with thicknesses of 38 and 67 nm, respectively. Each symbol stands for a measurement of an individual drop. The solid line is according to the adaptation theory. The R-square of the fit is 0.87, in which

$$R^2 = 1 - \frac{\sum_1^n (y_i - f_i)^2}{\sum_1^n \left(y_i - \frac{1}{n}\sum_1^n y_i\right)^2} \quad (y_i, \text{ experimental data}; f_i, \text{ fitting data}).$$

The presence of acid groups at the surface may be correlated with a diffusion of water into the polymer film. Assuming a diffusion constant D for the PS/PAA film on the order of 10^{-13} m^2/s,[35] we obtained a diffusion depth of ~4−40 nm ($\tau_d = h^2/2D$). Thus, a likely scenario is that water diffuses into the copolymer, swelling occurs, and the topmost side groups of the copolymer reorient.

Our next step was to demonstrate that the adaptation of the surface to water was also visible at the receding side of the drop. We used a 33 ± 1 μL drop volume in the tilted-plane experiment. This volume resulted in a drop length of 8.1 mm, when the drops slid at a maximum velocity of 0.35 m/s in our setup. Thus, the drop stayed in contact with the surface for ~23 ms. This contact time is ~10−100 times the relaxation time for the PS/PAA surface. Thus, the surface was able to adapt during all the different velocities applied in our measurement setup. The adaptation was reflected in the ~10° lower receding contact angles of the PS/PAA surface compared to the reference PS surface for all velocities measured (Figure 2b). Thus, contact angle hysteresis was larger for the PS/PAA surface compared to the pure PS surface. Despite the offset in the receding contact angle, the characteristics of velocity-dependent receding contact angles of PS surface and 8.7/1 PS/PAA surface were quite similar (Figure 2b). This indicates that the reverse adaptation time at the receding side of the drop, τ_s, was much larger compared to τ_{SL}. Thus, the topmost side groups of the copolymer did not return to their original positions before contact with water, and it is possible that water stayed partially in the films. We attribute the slight decrease of the receding angles of the PS/PAA copolymer at a velocity of $\leq 1 \times 10^{-4}$ m/s to the prolonged time that the surface was in contact with water (~80

s). For such contact times, the surface became more and more hydrophilic, as we will report later. The increase in advancing angles and decrease in receding angles observed for PS and PS/PSA surfaces at a velocity of ≥ 0.1 m/s were both caused by viscous dissipation and the Marangoni effect.[36]

When surfaces adapt to a liquid, the contact angle hysteresis and dynamic contact angles change. Accordingly, the mobility of the drop is affected due to changes in the capillary force,

$$F_{capillary} = kw\gamma_L^\infty(\cos\theta_R - \cos\theta_A) \qquad (4)$$

Exemplarily, we calculate the capillary force for a drop volume of 33 μL, corresponding to a drop width of 5 mm. In comparison to a pure PS surface, the decrease in receding angle on PS/PAA surfaces leads to an increase in capillary force from ~87 to ~148 μN at 0.2 mm/s $\leq v \leq$ 20 mm/s. At lower velocity, ≤ 20 μm/s, where the advancing and receding contact angles adapt, the capillary force increases from ~87 to ~132 μN. That is, the adaptation of the PS/PAA copolymer surface with a water drop leads to the increase in contact angle hysteresis of 22°−25°, corresponding to an increase in capillary force in the range of 45−60 μN, depending on the sliding velocity.

The receding contact angles decreased with decreasing PS-to-PAA ratio (Table 1). We measured the velocity-dependent dynamic contact angles on a PS/PAA surface made by a copolymer with a ratio of 4.2/1 (Figure S6). Then we also fitted eq 1 to the measured advancing angles, leading to $l_{SL}/_{SL}$ = 0.04 m/s. Again, assuming $l_{SL} \approx 10-100$ nm, we obtained a relaxation time of $\tau_{SL} \approx 0.25-2.5$ μs. Thus, in comparison to the 8.7/1 PS/PAA the 4.2/1 PS/PAA copolymer surfaces, it required less time to adapt to water. For the sliding drop, the magnitude of the advancing contact angle change is similar for
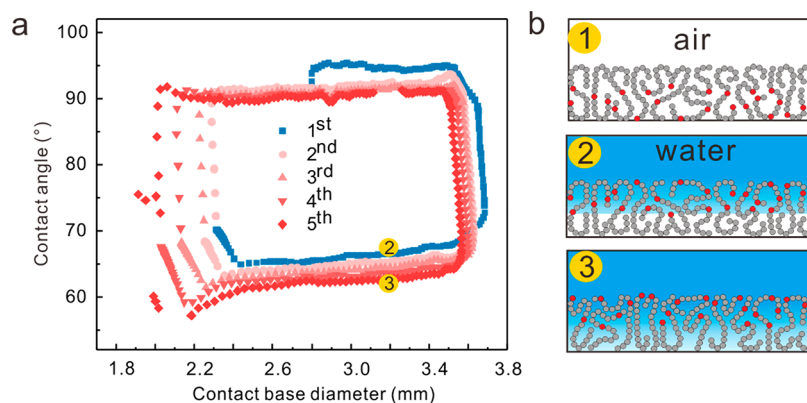
Figure 3. (a) Contact angle vs contact base diameter on the 67 nm PS/PAA (8.7/1) surface. The cycle's orders of repeated inflating and deflating processes are represented by 1st−5th. The 5 repeated tests required 4 ± 0.5 min, corresponding to 50 ± 1 s for each cycle. (b) Possible arrangement of the PS/PAA copolymer at the interface corresponding to positions 2 and 3 in (a). In particular, state 1 in air is the original state of the copolymer before a drop was deposited on the surface.
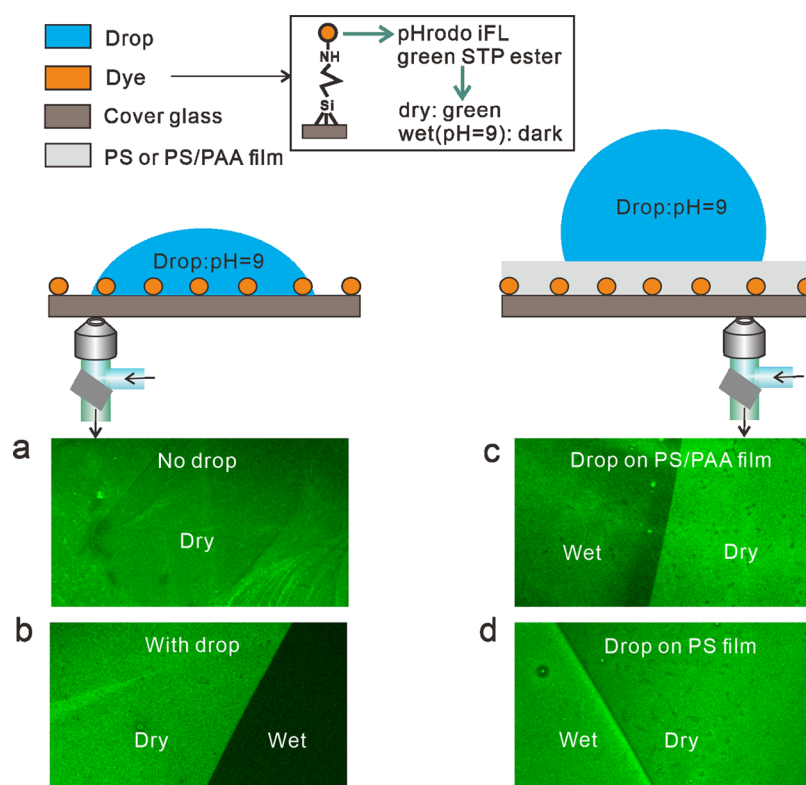

Figure 4. Schematic drawing of water penetration into the copolymer film using confocal microscopy. The images show fluorescence intensity maps (a) before a drop (pH = 9) was deposited on a glass surface grafted with a pH-sensitive dye, (b) after a drop (pH = 9) was deposited on the dye-grafted glass surface, (c) after a drop (pH = 9) was deposited on a 8.7/1 PS/PAA film spin-coated above the dye-grafted glass surface, and (d) after a drop (pH = 9) was deposited on a PS film spin-coated above the dye-grafted glass surface. The detected area for (b), (c), and (d) was a three-phase area.

the surfaces made from 8.7/1 and 4.2/1 PS/PAA copolymers. Thus, we conclude that water diffuses faster into the copolymer that has more acrylic acid content. For the receding side, the 4.2/1 PS/PAA surface has also already completely adapted to the water. We measured a receding angle of 55° ± 2°, which is almost 15° lower than that of the 8.7/1 PS/PAA surface (Figure S6).

To study the adaptation upon contact with water over a longer time scale, we measured the advancing and receding contact angles of PS/PAA films by repeatedly inflating and deflating a water drop. The flow rate used during the measurement was 0.5 μL/s (this is the lowest flow rate that our instrument could achieve), corresponding to a contact line velocity of $(8 \pm 1) \times 10^{-5}$ m/s (beginning with small drop volumes) to $(6 \pm 1) \times 10^{-5}$ m/s (ending with the maximum inflated drop volume). The first contact angle measurement was performed on a pristine PS/PAA surface, as used in the sliding drop experiments (blue data points in Figure 3a). In the first cycle of the contact angle measurement during inflation, the advancing angle was 95° ± 1°. The receding contact angle measured during deflation was 66° ± 1°. This contact angle slightly decreased during deflation of the drop. We inflated the

drop again (red, round symbols in Figure 3a). In the second cycle, the advancing contact angle decreased to 92° ± 1°. The corresponding receding contact angle decreased to 64° ± 1°. Subsequently, the drop was inflated again three more times. In the 3rd−5th cycles, the advancing contact angle only slightly decreased to 90° ± 1°. The corresponding receding contact angles kept decreasing continuously for each cycle by ∼1°. At the fifth cycle, a receding contact angle of 62° ± 1° was measured (Figure 3a).

We attributed the decrease in advancing and receding contact angles to water penetrating into the PS/PAA film and staying in the film for the subsequent cycles. Thus, in the 2nd−5th cycles, the surface appears more hydrophilic. In addition, the presence of water in the film allows the hydrophilic PAA segment to move to the interface (Figure 3b, states 2 and 3). Therefore, the advancing angles and receding angles gradually decreased after every cycle.

It is worth mentioning that during successive inflations of the drop the advancing contact angle never reached the value of the pristine sample. Thus, τ_s is longer than the time for one measurement cycle, which is 50 ± 5 s. For comparison, we used pure PS surfaces as a reference. Both the advancing and receding angles on the PS surfaces remained almost constant ($\theta_A = 97°$, $\theta_R = 73°$) even after five inflation/deflation cycles (Figure S7). The small differences in the contact angles measured by sliding drop and sessile drop for the same samples at their original state and final state can be caused by the different measuring methods and fitting models. We used a polynomial model for sliding drop and an elliptical model for sessile drop experiments.

To determine whether water molecules are able to diffuse in the PS/PAA film and if they can reach the SiO_2 substrate interface, we grafted a pH-sensitive fluorophore (pHrodo iFL STP eater, ThermoFisher) to the surface of a glass coverslip. This fluorophore emits green light with an emission maximum at a wavelength of 525 nm after excitation by a 488 nm laser. Fluorescence decreases when it comes into contact with basic water (pH = 9). To confirm the activity of the pH-sensitive dye, we deposited a drop with pH = 9 on the surface of a dye-grafted glass surface and recorded the fluorescence intensity using a confocal microscope. The fluorescence intensity of the dry area is higher than that in the wet area (Figure 4a and b).

We used this fluorophore to verify the presence of water at the PS/PAA/substrate interface. We spin-coated the PS/PAA polymer film (thickness = 45 nm) on a dye-grafted glass surface and added a drop (pH = 9) onto the polymer surface. The fluorescence image recorded ∼1 min after adding the drop showed a slight decrease in fluorescence (Figure 4c). Thus, we concluded that water had penetrated through the polymer film and reached the dye layer grafted on the glass surface. In comparison, the pure PS film showed no decrease in fluorescence (Figure 4d). The latter rules out optical artifacts due to the presence of a water drop on top of the surface, which could also lead to changes in the intensity of the backscattered light.

CONCLUSION

The surface of a PS/PAA copolymer film adapts upon contact with water. Most likely, water penetrates in the uppermost layer and acrylic acid groups become exposed to the water interface. On the basis of a recently proposed theory, we estimated the time scale of the swelling and reorganization process to be ≪1 s. For a 8.7/1 PS/PAA surface and for sliding

velocities of drops $\geq 7 \times 10^{-4}$ m/s, the advancing contact line "sees" a styrene-dominated surface. For a sliding velocity $\leq 7 \times 10^{-4}$ m/s, the acrylic acid groups have sufficient time to get exposed so that the advancing contact line of the drop can be influenced by the acrylic acid groups. This adaptation gradually leads to the decrease of advancing angle. In the case of a 4.2/1 PS/PAA surface, the critical sliding velocity increases to 3×10^{-2} m/s. In both cases, at the receding contact line, the surface has adapted and more acid groups are exposed. In particular, the adaptation time scale could depend on phase separation of PAA and PS moieties. The latter would be even more pronounced for block copolymer morphologies. The adaptation processes of the surface influence the mobility of drops by increasing the capillary force in the range of 45−60 μN in comparison to a pure PS reference surface.

■ ASSOCIATED CONTENT

ⓢ Supporting Information

The Supporting Information is available free of charge at https://pubs.acs.org/doi/10.1021/acs.langmuir.0c03226.

> Surface morphology characterization by scanning force microscopy; copolymer composition characterization by NMR; T_g of PS, PAA, and PS/PAA copolymers; data processing of sliding drops; evidence of drying "wet" surfaces by annealing; adaptation on 4.2/1 PS/PAA surface by sliding drops; and dynamic contact angles of PS surface measured by sessile drop (PDF)

■ AUTHOR INFORMATION

Corresponding Author

 Rüdiger Berger − *Max Planck Institute for Polymer Research, 55128 Mainz, Germany;* ⓞ orcid.org/0000-0002-4084-0675; Email: berger@mpip-mainz.mpg.de

Authors

 Xiaomei Li − *Max Planck Institute for Polymer Research, 55128 Mainz, Germany*

 Simon Silge − *Max Planck Institute for Polymer Research, 55128 Mainz, Germany*

 Alexander Saal − *Max Planck Institute for Polymer Research, 55128 Mainz, Germany*

 Gunnar Kircher − *Max Planck Institute for Polymer Research, 55128 Mainz, Germany*

 Kaloian Koynov − *Max Planck Institute for Polymer Research, 55128 Mainz, Germany;* ⓞ orcid.org/0000-0002-4062-8834

 Hans-Jürgen Butt − *Max Planck Institute for Polymer Research, 55128 Mainz, Germany;* ⓞ orcid.org/0000-0001-5391-2618

Complete contact information is available at:
https://pubs.acs.org/10.1021/acs.langmuir.0c03226

Notes

The authors declare no competing financial interest.

■ ACKNOWLEDGMENTS

■ REFERENCES

(1) Lavielle, L.; Schultz, J. Surface properties of graft polyethylene in contact with water: I. Orientation phenomena. *J. Colloid Interface Sci.* **1985**, *106* (2), 438−445.

(2) de Crevoisier, G.; Fabre, P.; Corpart, J.-M.; Leibler, L. Switchable tackiness and wettability of a liquid crystalline polymer. *Science* **1999**, *285* (5431), 1246−1249.

(3) Grundke, K.; Pöschel, K.; Synytska, A.; Frenzel, R.; Drechsler, A.; Nitschke, M.; Cordeiro, A. L.; Uhlmann, P.; Welzel, P. B. Experimental studies of contact angle hysteresis phenomena on polymer surfaces—Toward the understanding and control of wettability for different applications. *Adv. Colloid Interface Sci.* **2015**, *222*, 350−376.

(4) Sui, X.; Zapotoczny, S.; Benetti, E. M.; Memesa, M.; Hempenius, A. M.; Vancso, G. J. Grafting mixed responsive brushes of poly(N-isopropylacrylamide) and poly(methacrylic acid) from gold by selective initiation. *Polym. Chem.* **2011**, *2*, 879−884.

(5) Liu, C.; Lopes, M. C.; Pihan, S. A.; Fell, D.; Sokuler, M.; Butt, H.-J.; Auernhammer, G. K.; Bonaccurso, E. Water diffusion in polymer nano-films measured with microcantilevers. *Sens. Actuators, B* **2011**, *160* (1), 32−38.

(6) Yoon, J.; Cai, S.; Suo, Z.; Hayward, R. C. Poroelastic swelling kinetics of thin hydrogel layers: comparison of theory and experiment. *Soft Matter* **2010**, *6* (23), 6004−6012.

(7) Zhang, H.; Gao, X.; Chen, K.; Li, H.; Peng, L. Thermo-sensitive and swelling properties of cellouronic acid sodium/poly (acrylamide-co-diallyldimethylammonium chloride) semi-IPN. *Carbohydr. Polym.* **2018**, *181*, 450−459.

(8) Ionov, L.; Minko, S. Mixed polymer brushes with locking switching. *ACS Appl. Mater. Interfaces* **2012**, *4* (1), 483−489.

(9) Ochsmann, J. W.; Lenz, S.; Lellig, P.; Emmerling, S. G. J.; Golriz, A. A.; Reichert, P.; You, J.; Perlich, J.; Roth, S. V.; Berger, R.; Gutmann, J. S. Stress-Structure Correlation in PS-PMMA Mixed Polymer Brushes. *Macromolecules* **2012**, *45* (7), 3129−3136.

(10) Lee, S.; Flores, S. M.; Berger, R.; Gutmann, J. S.; Brehmer, M.; Conrad, L.; Funk, L.; Theato, P.; Yoon, D. Y. Sheeting, Temperature dependence of surface reorganization characteristics of amphiphilic block copolymer in air and in water studied by scanning force microscopy. *J. Plast. Film Sheeting* **2015**, *31* (4), 434−448.

(11) Butt, H. J.; Berger, R.; Steffen, W.; Vollmer, D.; Weber, S. A. L. Adaptive Wetting-Adaptation in Wetting. *Langmuir* **2018**, *34* (38), 11292−11304.

(12) Dupont-Gillain, C. C.; Adriaensen, Y.; Derclaye, S.; Rouxhet, P. G. Plasma-oxidized polystyrene: wetting properties and surface reconstruction. *Langmuir* **2000**, *16* (21), 8194−8200.

(13) Vaidya, A.; Chaudhury, M. K. Synthesis and surface properties of environmentally responsive segmented polyurethanes. *J. Colloid Interface Sci.* **2002**, *249* (1), 235−45.

(14) Honda, K.; Morita, M.; Sakata, O.; Sasaki, S.; Takahara, A. Effect of Surface Molecular Aggregation State and Surface Molecular Motion on Wetting Behavior of Water on Poly(fluoroalkyl methacrylate) Thin Films. *Macromolecules* **2010**, *43* (1), 454−460.

(15) Honda, K.; Yamamoto, I.; Morita, M.; Yamaguchi, H.; Arita, H.; Ishige, R.; Higaki, Y.; Takahara, A. Effect of α-substituents on molecular motion and wetting behaviors of poly(fluoroalkyl acrylate) thin films with short fluoroalkyl side chains. *Polymer* **2014**, *55* (24), 6303−6308.

(16) Zhao, J.; Wang, M.; Gleason, K. K. Stabilizing the Wettability of Initiated Chemical Vapor Deposited (iCVD) Polydivinylbenzene Thin Films by Thermal Annealing. *Adv. Mater. Interfaces* **2017**, *4* (18), 1700270.

(17) Neto, C.; James, M.; Telford, A. M. On the Composition of the top layer of microphase separated thin PS-PEO films. *Macromolecules* **2009**, *42*, 4801−4808.

(18) Inutsuka, M.; Tanoue, H.; Yamada, N. L.; Ito, K.; Yokoyama, H. Dynamic contact angle on a reconstructive polymer surface by segregation. *RSC Adv.* **2017**, *7*, 17202.

(19) Crowe, J. A.; Genzer, J. Creating responsive surfaces with tailored wettability switching kinetics and reconstruction reversibility. *J. Am. Chem. Soc.* **2005**, *127* (50), 17610−17611.

(20) Farris, S.; Introzzi, L.; Biagioni, P.; Holz, T.; Schiraldi, A.; Piergiovanni, L. Wetting of biopolymer coatings: contact angle kinetics and image analysis investigation. *Langmuir* **2011**, *27* (12), 7563−74.

(21) Holly, F. J.; Refojo, M. F. Wettability of hydrogels I. Poly (2-hydroxyethyl methacrylate). *J. Biomed. Mater. Res.* **1975**, *9* (3), 315−326.

(22) Yasuda, H.; Sharma, A. K.; Yasuda, T. Effect of orientation and mobility of polymer molecules at surfaces on contact angle and its hysteresis. *J. Polym. Sci., Polym. Phys. Ed.* **1981**, *19* (9), 1285−1291.

(23) Lee, S. H.; Ruckenstein, E. Surface restructuring of polymers. *J. Colloid Interface Sci.* **1987**, *120* (2), 529−536.

(24) Wong, W. S. Y.; Hauer, L.; Naga, A.; Kaltbeitzel, A.; Baumli, P.; Berger, R.; D'Acunzi, M.; Vollmer, D.; Butt, H. J. *Langmuir* **2020**, *36* (26), 7236−7245.

(25) Bartell, F. E.; Bjorklund, C. W. Hysteresis of contact angles. *J. Phys. Chem.* **1952**, *56* (4), 453−457.

(26) Ruckenstein, E.; Gourisankar, S. V. Surface restructuring of polymeric solids and its effect on the stability of the polymer—water interface. *J. Colloid Interface Sci.* **1986**, *109* (2), 557−566.

(27) Sedev, R. V.; Budziak, C. J.; Petrov, J. G.; Neumann, A. W. Dynamic contact angles at low velocities. *J. Colloid Interface Sci.* **1993**, *159* (2), 392−399.

(28) Furmidge, C. G. L. Studies at phase interfaces. I. The sliding of liquid drops on solid surfaces and a theory for spray retention. *J. Colloid Sci.* **1962**, *17* (4), 309−324.

(29) Olsen, D. A.; Joyner, P. A.; Olson, M. D. The sliding of liquid drops on solid surfaces. *J. Phys. Chem.* **1962**, *66* (5), 883−886.

(30) Wolfram, E. Liquid drops on a tilted plate, contact angle hysteresis and the Young contact angle. *Wetting, Spreading Adhes.* **1978**, 213−222.

(31) Dussan V, E. B. On the ability of drops or bubbles to stick to non-horizontal surfaces of solids. Part 2. Small drops or bubbles having contact angles of arbitrary size. *J. Fluid Mech.* **1985**, *151*, 1−20.

(32) Extrand, C. W.; Gent, A. N. Retention of liquid drops by solid surfaces. *J. Colloid Interface Sci.* **1990**, *138* (2), 431−442.

(33) ElSherbini, A. I.; Jacobi, A. M. Retention forces and contact angles for critical liquid drops on non-horizontal surfaces. *J. Colloid Interface Sci.* **2006**, *299* (2), 841−849.

(34) Antonini, C.; Carmona, F. J.; Pierce, E.; Marengo, M.; Amirfazli, A. General methodology for evaluating the adhesion force of drops and bubbles on solid surfaces. *Langmuir* **2009**, *25* (11), 6143−6154.

(35) Fike, L. R. *Transport properties of polystyrene above and below the glass transition temperature*; Texas Tech University: 1983.

(36) Henrich, F.; Fell, D.; Truszkowska, D.; Weirich, M.; Anyfantakis, M.; Nguyen, T.-H.; Wagner, M.; Auernhammer, G. K.; Butt, H.-J. Influence of surfactants in forced dynamic dewetting. *Soft Matter* **2016**, *12* (37), 7782−7791.

Supporting information for

"Adaptation of a styrene-acrylic acid copolymer surface to water"

Xiaomei Li, Simon Silge, Alexander Saal, Gunnar Kircher, Kaloian Koynov, Rüdiger

Berger*, Hans-Jürgen Butt

Max Planck Institute for Polymer Research, Ackermannweg 10, 55128 Mainz,

Germany

S1: Surface morphology characterization by Scanning Force Microscopy (SFM)

S2: Copolymer composition characterization by NMR

S3: Tg of PS, PAA and PS/PAA copolymers

S4: Data processing of sliding drops

S5: Evidence of drying "wet" surfaces by annealing

S6: Adaptation on 4.2/1 PS/PAA surface by sliding drops

S7: Dynamic contact angles of PS surface measured by sessile drop

S1: Surface morphology characterization by Scanning Force Microscopy (SFM)

The morphologies of the polymer surfaces were studied with SFM (Dimension Icon, Bruker) in the tapping mode. SFM tips with a nominal resonance frequency of 300 kHz and a spring constant of 26 N/m were used (OPUS 160AC-NA). The root means square roughness (rms) was determined on $0.5 \times 0.5 \ \mu m^2$ for each sample. Notably, the film thickness for 2.9/1, 4.2/1, 8.7/1 PS/PAA surfaces and PS surface used for the measurement are 30 ± 5 nm, 32 ± 5 nm, 38 ± 5 nm and 98 ± 5 nm, respectively.
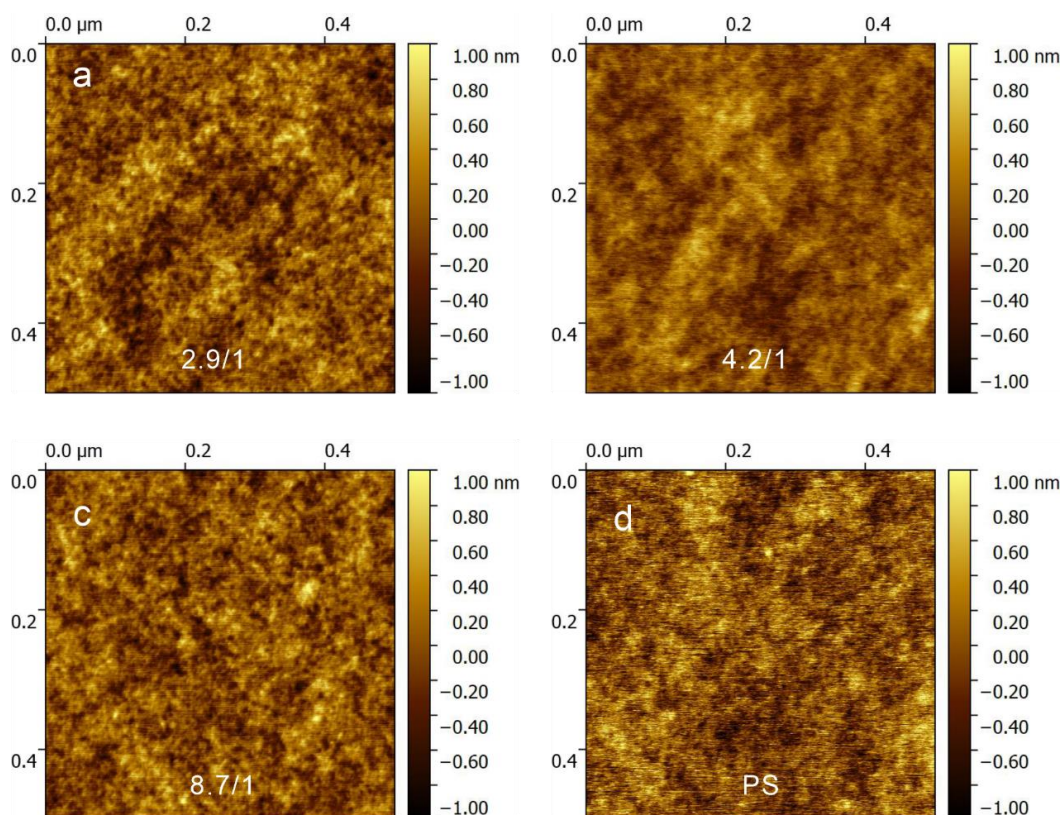
Figure S1. *SFM images of (a) 2.9/1 PS/PAA copolymer surface, (b) 4.2/1 PS/PAA copolymer surface, 8.7/1 PS/PAA copolymer surface, and (d)PS surface.* The Rms roughness for 2.9/1, 4.2/1, 8.7/1 PS/PAA copolymer and PS surfaces, are 0.2 nm, 0.2 nm, 0.2 nm and 0.3 nm.

S2: Copolymer composition characterization by NMR

The composition of copolymer was checked by 1H-NMR. The 1H-NMR spectra were measured with a Bruker Spectrospin NMR spectrometer (300MHz) at 25 °C.
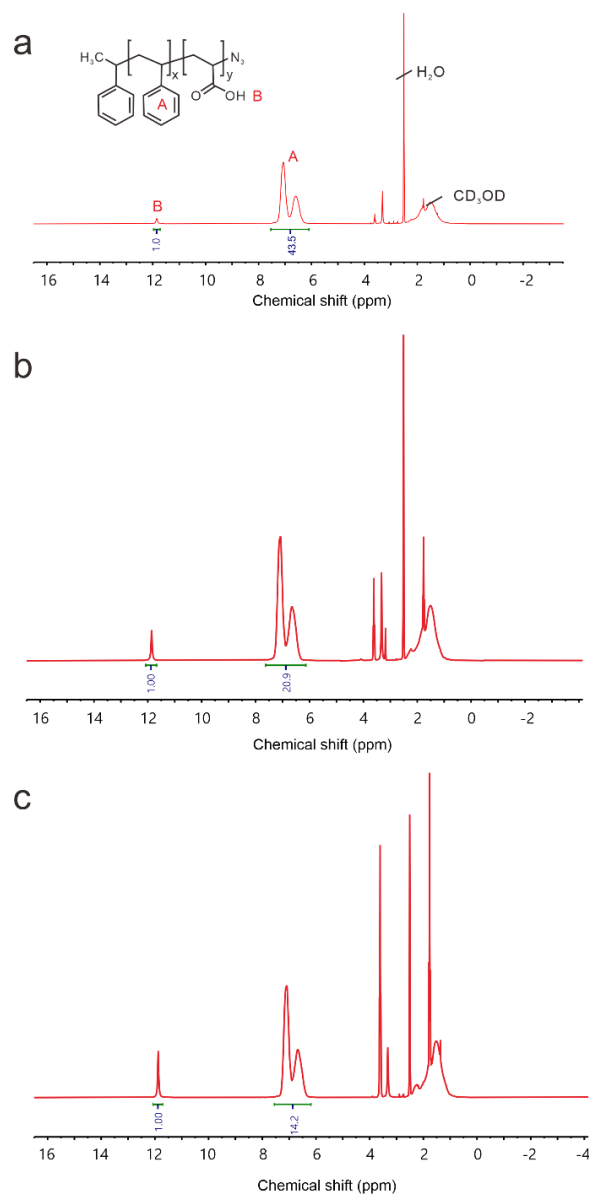
Figure S2. 1H-NMR spectrum of PS/PAA copolymer with a ratio of (a) (PS/PAA)8.7/1, (b) 4.2/1 and (c) 2.9/1.

S3: Tg of PS, PAA and PS/PAA copolymers

Glass transition temperature (Tg) were measured by DSC (Mettler Toledo, DSC-822), and obtained from the second heating run with a rate of 10 K/min. In particular, pure PAA for Tg measurement was purchased (Sigma-Aldrich, 181285) and used as received. All Tg of the tested copolymers are smaller than 150°C, ~133°C for 2.9/1, ~120°C for 4.2/1 and ~110°C for 8.7/1 PS/PAA copolymers, respectively. In particular, Tg for all the PS/PAA copolymers are slightly higher than the Tg of both pure PS (~103°C) and pure PAA (~109°C). We attributed the phenomenon to specific interactions, e.g. hydrogen bonding which produces some kind of local "network" that inhibits free rotational motions of the segments and hence increases Tg.[1,2]

The molecular weight and density of PS and PS/PAA copolymers were measured by gel permeation chromatography (GPC, Water Alliance 2000), DMF was used as the eluent.
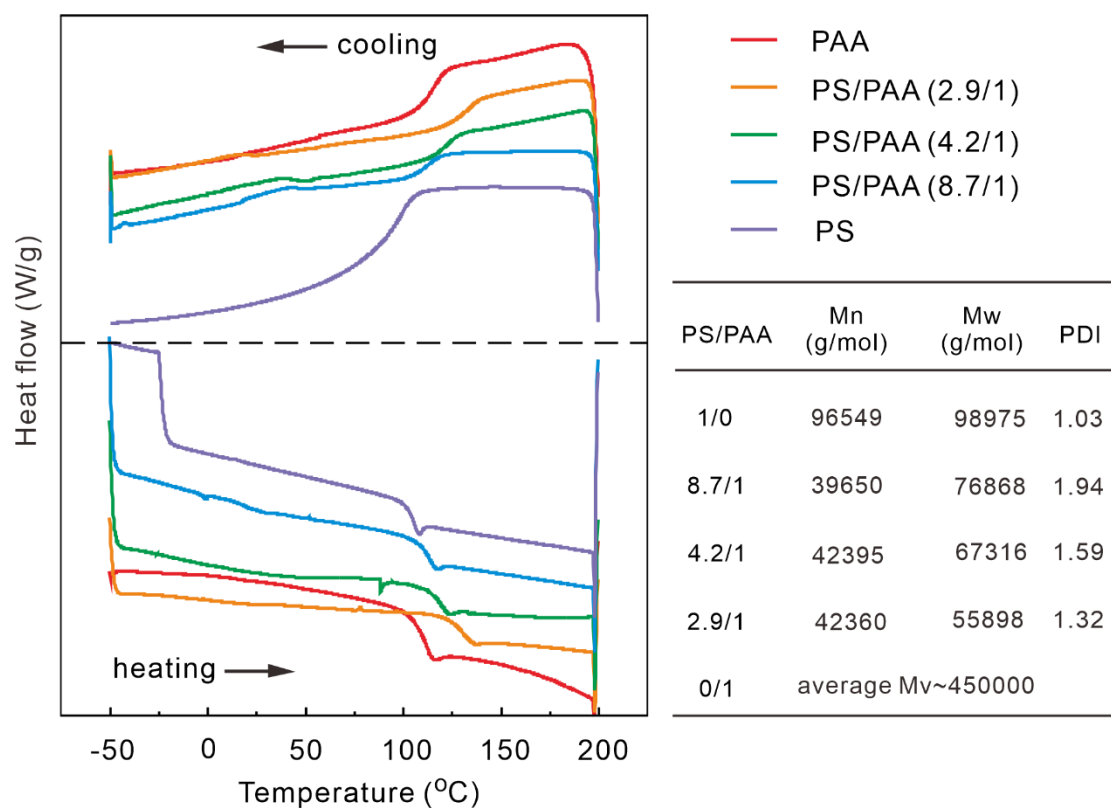
Figure S3. *Glass transition temperature (Tg), molecular weight (Mn, Mw Mv) and polydispersity index(PDI) of PS, PS/PAA and PAA.*

PS/PAA	Mn (g/mol)	Mw (g/mol)	PDI
1/0	96549	98975	1.03
8.7/1	39650	76868	1.94
4.2/1	42395	67316	1.59
2.9/1	42360	55898	1.32
0/1	average Mv~450000		

S4: Data processing of sliding drops

In order to extract the contact angles from the videos, we used and adapted the openly available script collection for drop shape analysis from MATLAB (DSAfM). It was originally developed by Andersen et al.[3] The processing details are: the script first filters out the images without a drop and the images with complete drops (Figure S4a, step 1). The images without a drop are used as a reference, by which the exact tilt angle of the sample is calculated (Figure S4a, step 2). The images with a complete drop were corrected by subtracting the background and then rotating into a horizontal drop (Figure S4a, step 3). Then the contour and edge position of the drops were detected with sub-pixel precision. After that, the edge was divided into the left and right part of the drop for a different angle and velocity calculation on both sides (Figure S4a, step 4). Based on these contours, the velocity was calculated by the pixel rate and the dynamic contact angles were estimated by applying a "polyfit" in each image (Figure S4a, step 5). Finally, the average velocity and average dynamic contact angles of every frame in a video were used as a final result for one sliding drop.

The accuracy of the processing is verified by an artificial drop. We simulated a drop with its contact angle changing from 60° to 120° in 105-frame image serials. In addition, the drop moved on a plate with a tilted angle of 3° and a frame rate of 14 pixels per frame. Then we analyzed the artifact drop with our MATLAB code and compared the fitting results with the setting parameters. The comparisons between the fitting results and setting parameters (Figure S4b and S4c) including the tilted angle of the plate, the

average velocities of the drops, the advancing and receding angles of the drops indicate that the processing process was accurate. Expect the case when the contact angle of the drop is around 90°, because it's hard to defined the contact line position of drop automatically. Therefore, we set the contact line position hand-made in this case.
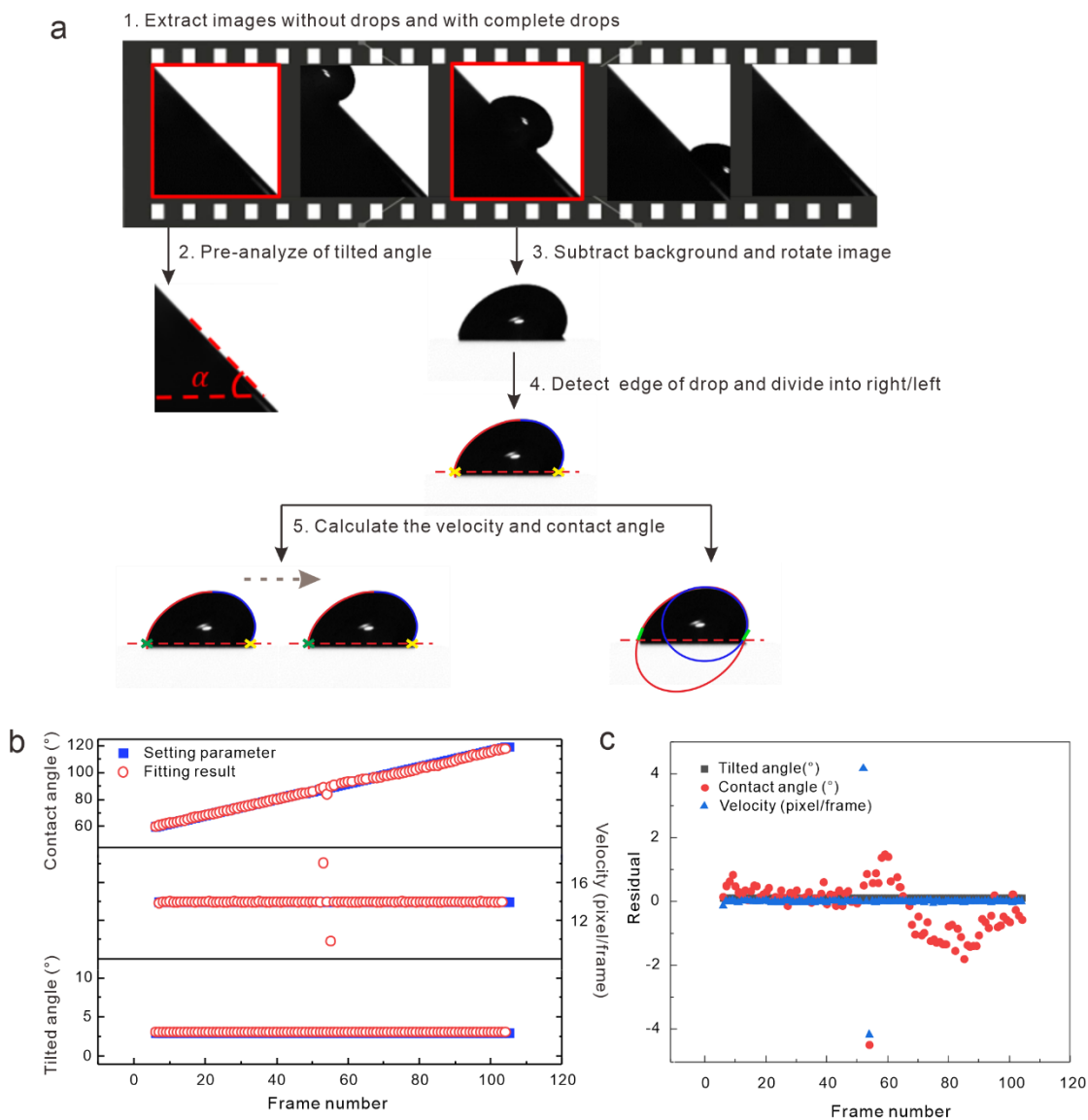
Figure S4. (a) Schematic of sliding drop processing of video recorded by tilted-plate setup. (b) Comparison between fitting results by DSAfM and setting parameter. (c)The residual of the fitting results by DSAfM.

39

S5: Evidence of drying "wet" surface by annealing

In order to dry the "wet" copolymer surface after adaptation, we annealed the copolymer surface at 150 ℃ (over Tg, Figure S3) for 10 min between every measurement, i.e. between every drop. Since there is no adaptation on a PS surface, we only had to wait 1 min between drops. Then we recorded a series of drops sliding down the surface under the same conditions, but at different intervals (Details in S1, Dynamic contact angles measurement of a tilted-plate setup). The velocities of sliding drops on the PS surface was stable at about 0.045 m/s, advancing angles ($\theta_A \approx 92°$) and receding angles ($\theta_A \approx 76°$) also did not change with drop number, indicating no adaptation for a PS surface when in contact with a water drop (Figure S5a and S5b). In the case of the PS/PAA copolymer surface (8.7/1) the velocity of the sliding drop decreased from 0.015 m/s to 2×10^{-5} m/s, advancing angles and receding angles also decreased by around 10° as the increase of sliding drops when the interval between drops is 1 min (Figure S5c). These decreases were caused by the adaptation of the PS/PAA surface with the water drop, waiting 1 min di not let the surface dry again. However, the velocity, advancing and receding angles stayed almost constant when a heating interval of 10 min at 150 ℃ (Figure S5c, d) is applied, demonstrating that heating the PS/PAA surface to 150 ℃ dries it again after adaptation.
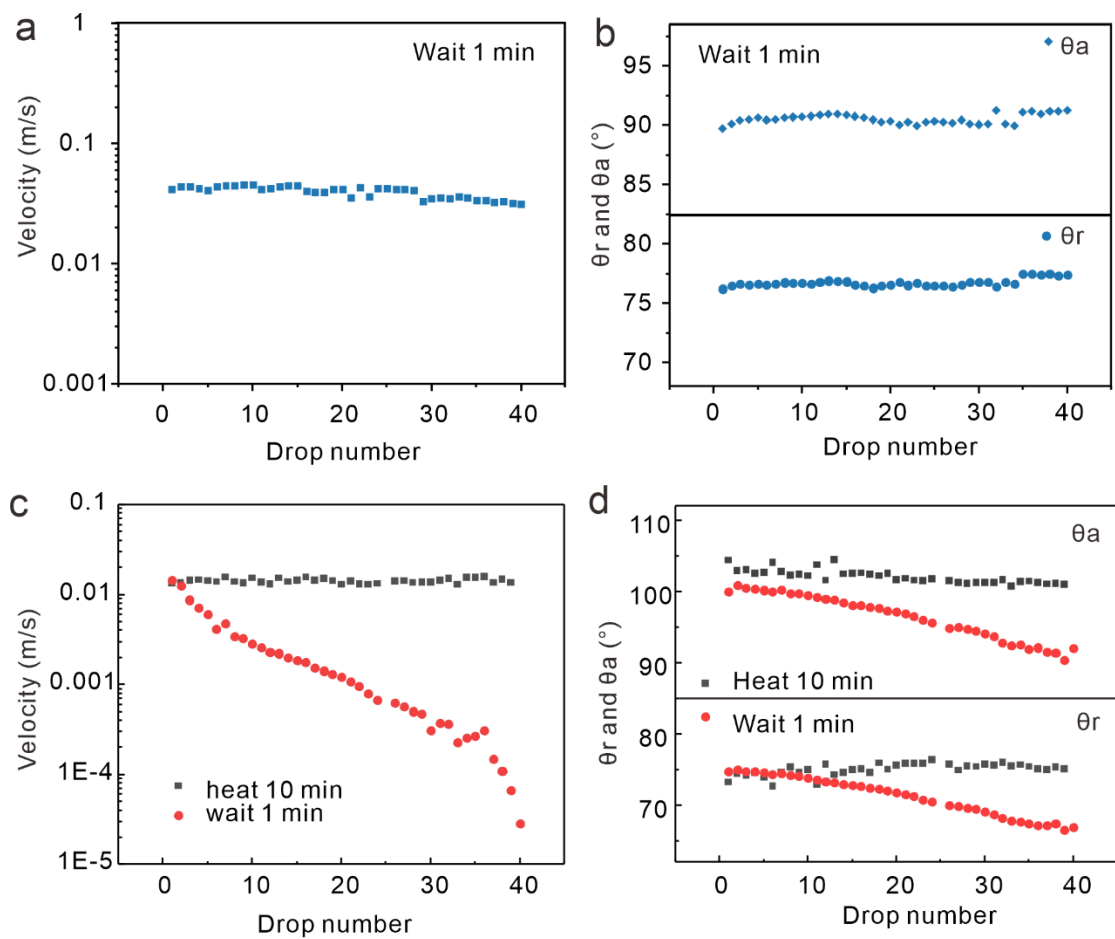
Figure S5. *Velocity, advancing angles and receding angles vs. drop number on the PS*

surface (a), (b) and on the 67 nm PS/PAA (8.7/1) surface (c), (d) using the dropwise-

dependent test.

S6: Adaptation on 4.2/1 PS/PAA surface by sliding drops

For the advancing side, the advancing angles increase from 85° to 97° at velocity of $\geq$ 0.001 m/s (Figure S6). Then we also fit the experimental data using equation (1). For the fit, we used $\theta_a^\infty = 87°$, $\Delta\gamma_{SL}$=0.015 N/m and $\gamma_L^\infty = 0.072$ N/m in the velocity range of 1×10^{-5} to 0.2 m/s, leading to a fitting parameter of $\frac{l_{SL}}{\tau_{SL}} = 0.04$ m/s. If assuming $l_{SL} = 10\sim100$ nm, we can also get the relaxation time of $\tau_{SL} \approx$ 0.25~2.5 μs. For the receding side, the 4.2/1 PS/PAA surface has also already completely adapted with water drop, leading to a receding angle of $(55 \pm 2)°$, which is almost 15° lower than that of 8.7/1 PS/PAA surface.
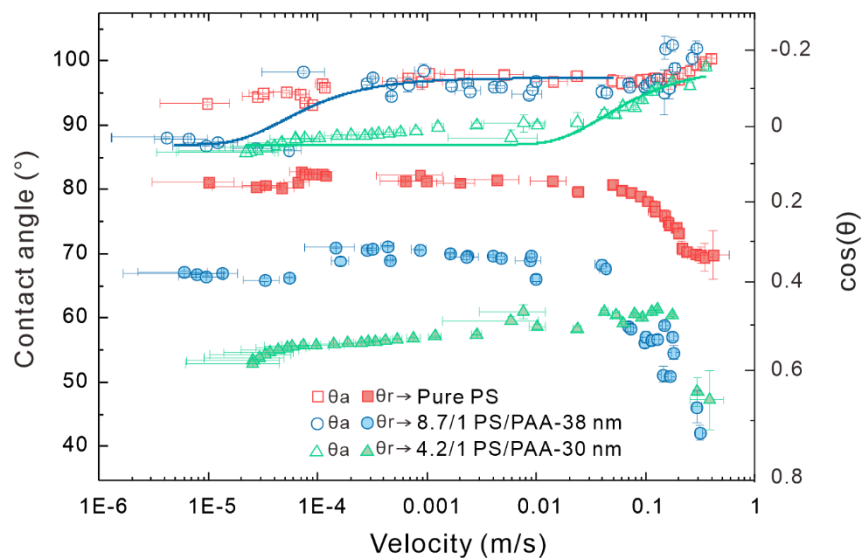
Figure S6. *Contact angles (θ) and cos(θ) vs velocity on 4.2/1 PS/PAA surfaces (green triangle) with a thickness of 30 nm. Solid lines are the fitting line according to the adaptation theory, the R-square for the fit (green line) is 0.81. Each symbol stands for an measurement of an individual drop.*

S7: Dynamic contact angles of PS surface measured by sessile drop
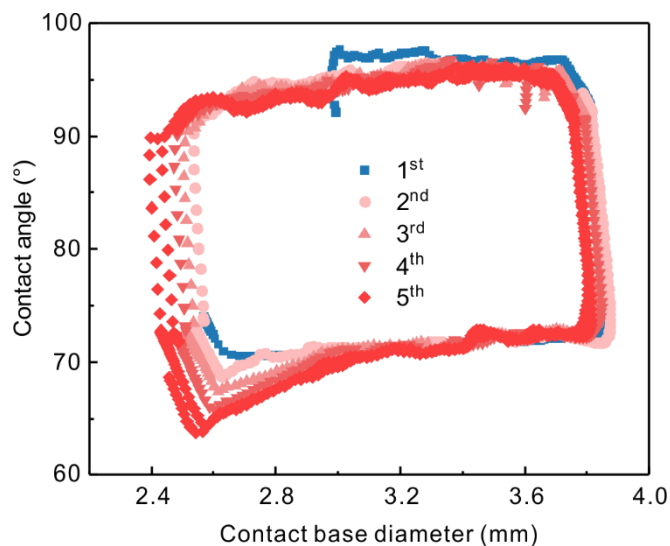
Figure S7. *Contact angle vs. contact base diameter on the PS surface. 1ˢᵗ to 5ᵗʰ represents the orders of repeated inflating and sucking back processes.*

References

(1) Lessard, B.; Schmidt, S. C.; Marić, M. Styrene/acrylic acid random copolymers synthesized by nitroxide-mediated polymerization: effect of free nitroxide on kinetics and copolymer composition. *Macromolecules* 2008, **41**, 3446-3454.

(2) Zhang, J.; Li, J.; Huang, L.; Liu, Z. Gradient copolymers of styrene–methyl acrylate and styrene–acrylic acid by organostibine-mediated controlled/living radical polymerization and their glass transition behaviors. *Polym. Chem.* 2013, **4**, 4639-4647.

(3) Andersen, N. K.; Taboryski, R. Drop shape analysis for determination of dynamic contact angles by double sided elliptical fitting method. *Meas Sci Technol* 2017, **28**, 047003.

2.2. X. Li *et al. Macromol. Rapid Commun.*, 2022

Adaptation and recovery of a styrene-acrylic acid copolymer surface to water

Xiaomei Li[1], Mirela Encheva[2], Hans-Jürgen Butt[1], Ellen H. G. Backus[2], and Rüdiger Berger[1*]*

1. Max Planck Institute for Polymer Research, Ackermannweg 10, Mainz 55128, Germany
2. Department of Physical Chemistry, University of Vienna, Währinger Straße 42, Vienna 1090, Austria

Published in:

Author contributions:

Xiaomei Li and Mirela Encheva contributed equally. Rüdiger Berger and Xiaomei Li proposed the project. Xiaomei Li designed and built up the tilted plate setup, prepared the samples by spin coating, performed measurements of sliding drop by the tilted plate setup, static contact angles by a goniometer, surface topography by SFM imaging, and analyzed the data. Mirela Encheva performed the SFG measurement. Mirela Encheva and Ellen Backus analyzed the SFG results. All the authors of this paper discussed, interpreted the results, and wrote the manuscript.

Adaptation and Recovery of a Styrene-Acrylic Acid Copolymer Surface to Water

Xiaomei Li, Mirela Encheva, Hans-Jürgen Butt, Ellen H. G. Backus, and Rüdiger Berger*

Drops sliding down an adaptive surface lead to changes of the dynamic contact angles. Two adaptation processes play a role: 1) the adaptation of the surface upon bringing it into contact to the drop (wetting) and 2) the adaptation of the surface after the drop passed (dewetting). In order to study both processes, the authors investigate samples made from random styrene (PS)/acrylic acid (PAA) copolymers, which are exposed to water. Sum-frequency generation spectroscopy and tilted-plate measurements indicate that during wetting, the PS segments displace from the interface, while PAA segments are enriched. This structural adaptation of the PS/PAA random copolymer to water remains after dewetting. Annealing the adapted polymer induces reorientation of the PS segments to the surface.

1. Introduction

Surfaces can change their chemical-physical properties when coming into contact with liquids. The umbrella term for those processes is surface adaptation.[1,2] Adaptation processes can be reversible, like swelling of polymers by diffusion of molecules.[3–5] Mixing of two polymers may result in selective swelling of one of them. In some cases, the swelling process leads to a preferential enrichment of the more compatible component to the selected liquid.[6–10] Then the adaptation process may become nonreversible. Both, reversible and nonreversible adaptation processes provide potential to create smart surfaces for sensors[11] and biomedical applications.[12]

When a drop is sliding over an adaptive surface, two phenomena play a role: 1) the adaptation of the surface upon bringing it in contact with the liquid on the advancing side of the drop (wetting

X. Li, H.-J. Butt, R. Berger
Max Planck Institute for Polymer Research
Ackermannweg 10, Mainz 55128, Germany
E-mail: berger@mpip-mainz.mpg.de
M. Encheva, E. H. G. Backus
Department of Physical Chemistry
University of Vienna
Währinger Straße 42, Vienna 1090, Austria
E-mail: ellen.backus@univie.ac.at

process) and 2) the adaptation of the surface after the drop passed (dewetting process). In this context, measuring drop velocity-dependent dynamic contact angles is an elegant way to understand the wetting and dewetting kinetics. In a previous study,[13] we investigated the wetting process by measuring velocity dependent dynamic contact angles on a random copolymer composed of styrene and 11–25 mol% acrylic acid (PS/PAA). Both, the advancing and the receding contact angles decreased when the PS/PAA surface adapted to water. This adaptation could occur due to water diffusion into the polymer layer and/or PAA enrichment at the surface (**Figure 1**). We have verified the presence of water diffusion by fluorescence microscopy measurement, but we had no direct proof of water induced PAA enrichment at the interface. Here, we address the questions: Does the copolymer surfaces enrich with one component of the PS/PAA upon wetting with water? Is such an enrichment permanent after dewetting? Does the enrichment change with the number of sliding water drops?

2. Results and Discussions

2.1. Sum-Frequency Generation Spectroscopy (SFG)

In order to probe the adaptation and recovery of the PS/PAA copolymer surface, we used sum-frequency generation spectroscopy (SFG). SFG is a technique that provides a vibrational spectrum of interfacial molecules. In SFG an infrared (IR-ω_{IR}) and a visible (VIS-ω_{VIS}) laser pulse are overlapped in space and time to generate a third beam (SF), the frequency of which results from the addition of the previous two ($\omega_{SFG} = \omega_{IR} + \omega_{VIS}$). This third beam (SF) can only be produced in noncentrosymmetric environments, making SFG stand out as a powerful tool for analyzing interfaces (**Figure 2**A).[14] If the IR-beam is in resonance with the vibrational modes of the surface molecules, the SFG signal will be enhanced producing a vibrational spectrum of the interfacial molecules.[14] The intensity of the resulting spectrum is proportional not only to the density of the molecular groups but also to their orientation, leading to higher intensity values for ordered systems than for randomly organized ones.

In order to perform SFG experiments, the PS/PAA copolymer was spin-coated on CaF_2 windows. Before the SFG measurements, the resulting layers were annealed in an oven at 150 °C for 60 min. In order to determine a restructuring of the PS/PAA copolymer, vibrational spectra were acquired before and after wetting the sample. To assure that the spectra obtained before and

**ADVANCED
SCIENCE NEWS**

www.advancedsciencenews.com

Ⓜ acro-
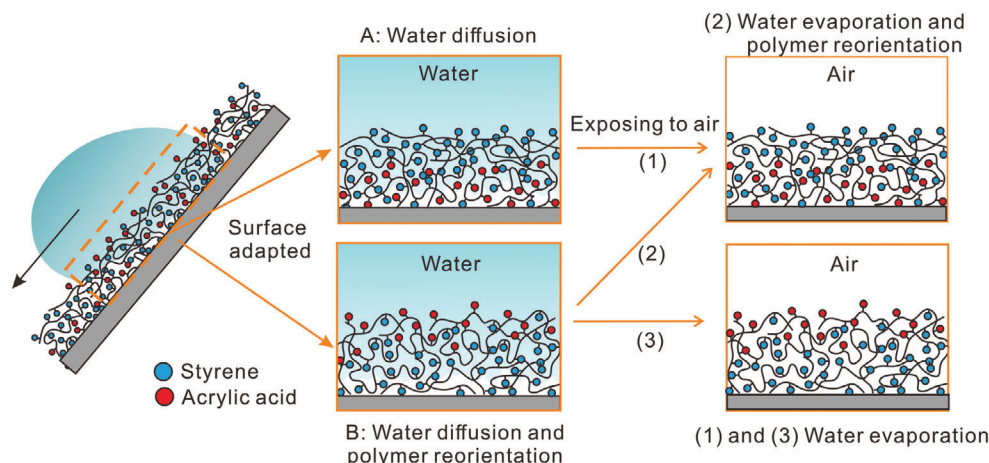molecular
Rapid Communications

www.mrc-journal.de

Figure 1. A,B) Possible adaptation and 1–3) recovery processes of a PS/PAA copolymer surface upon wetting.
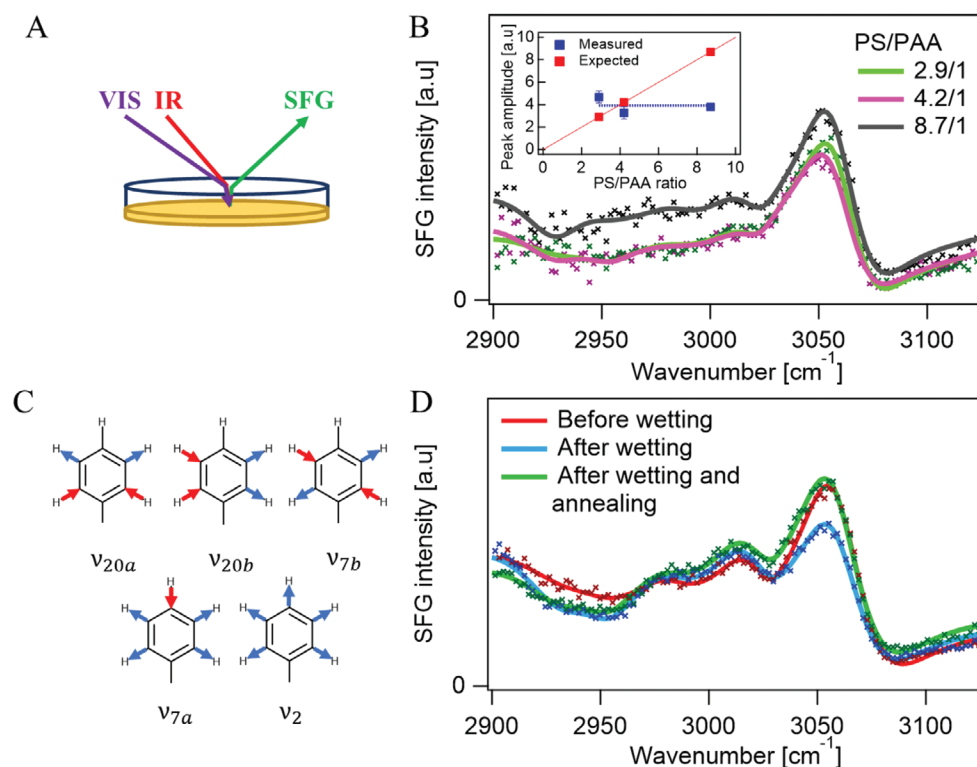

Figure 2. A) Working principle of sum frequency generation; B) SFG spectra of different PS/PAA ratios after annealing and their correspondent fits. The inset shows the measured and expected (based on PS fraction) peak amplitude as function of PS/PAA ratio; C) Phenyl ring C–H stretching vibrational modes; D) SFG spectrum of 130 nm 8.7/1 PS/PAA in SSP polarization before contact with water (red), after (blue) contact with water, and after annealing again (green) with their corresponding fit.

after wetting were measured on exactly the same spot at the interface, the surface was wetted using a flow cell. The IR and VIS beams transmit through the CaF_2 window before hitting the polymer layer (Figure 2A). Our sample entails the CaF_2–PS/PAA and the PS/PAA–air interface, both of which can contribute to the SFG-signal. We are interested in the PS/PAA–air interface, since it is the one that can be directly exposed to water. Therefore, we have adjusted the PS/PAA film thickness in order to obtain

an SFG-signal dominated by the PS/PAA–air interface (Sections SI1 and SI2, Supporting Information).[15]

Figure 2B shows SFG spectra of spin coated and annealed films made from polymers that have different ratios of PS/PAA: 8.7/1, 4.2/1, and 2.9/1. All three spectra show a dominating signal at ∼3060 cm^{-1}. To quantify the signal intensity, we fit the SFG data with a sum of Lorentzian line-shapes representing each resonance.[16] A minimum of nine Lorentzian peaks, assigned ac-

**ADVANCED
SCIENCE NEWS**

www.advancedsciencenews.com

**｜M｜acro-
molecular**

Rapid Communications

www.mrc-journal.de

Table 1. Assignments for PS/PAA SFG spectra.

Wave number [cm^{-1}]	FWHM [cm^{-1}]	Relative sign of amplitude	Assignment
2907	100	+	CH$_2$ as
2931	36	−	CH$_3$ Fermi
2956	28	−	CH$_3$ as
2980	30	+	Combination mode
3016	34	+	ν_{20b}
3030	19	−	ν_{7a}
3057	40	+	ν_{7b} and ν_2
3076	55	−	ν_{20a}
3693	250	+	OH

cording to literature, are needed in order to describe the spectrum correctly (**Table 1**).[17–20] The different ring modes are schematically depicted in Figure 2C.

The assignment shows that the phenyl rings of the PS part of the copolymer produce several CH stretching vibrations (3016, 3030, 3057, and 3076 cm^{-1}). The resonances below 3000 cm^{-1} can be either from PS or from PAA. As the 3057 cm^{-1} peak is by far the most intense, we decided to use it as a marker of the PS surface contribution. The blue squares in the inset in Figure 2B show that the amplitude of the 3057 cm^{-1} band is independent of the PS/PAA ratio. In principle, one might expect that the amplitude of this band scales linear with the amount of PS in the layer schematically represented by the red data-points in the inset of Figure 2B. Thus, we conclude that independently of the PS/PAA ratio indicated, the same amount of PS groups is present at the polymer–air interface after annealing.

Upon wetting with water, the surface adapts and the contact angle reduces.[13] However, it is unclear if this adaption will lead to a permanent reorientation of the PS even after drying the surface. Here we use SFG to determine the surface structure of the PS/PAA 8.7/1 sample after the wetting and dewetting process. The corresponding samples were wetted with water. After 3 min, the water was removed and the samples were dried by blowing dry air. Right after that, an SFG spectrum was acquired from the same measuring spot as the first one. Clearly, the intensity of the 3057 cm^{-1} band, used as a marker of the phenyl side chain of the PS segments, reduces upon wetting (Figure 2D, blue curve). From the spectra in the OH stretch region (see Figure S6 in Section SI3, Supporting Information), we have no indication that water remains in the surface region of the layer. Fitting the spectra reveals that the amplitude of the 3057 cm^{-1} peak decreases by 16 ± 7%. This decrease of the signal could originate from a displacement of the PS rings from the surface or from a reorientation of the rings. Experiments under different polarization combinations could provide information about orientational changes of molecular groups. As upon wetting the SSP, SPS, and PSS signal decrease, the SFG data indicate that the decrease of the signal is due to displacement of the PS rings from the surface (see Section SI1, Supporting Information). Moreover, as the signal for a pure PS film shows in contrary a small increase before and after wetting (see Figure S7 in Section SI4, Supporting Information), possibly due to a small reorientation, the observed decrease for

the PS/PAA layer is assigned to a displacement of the PS rings from the surface, reducing the hydrophobicity of the resulting surface. Thus, the wetting and dewetting process of the PS/PAA sample surface results in a permanent restructuring of molecular groups on the interface. However, after annealing the sample at 150 °C for 1 h the SFG spectrum is similar to the one before wetting (Figure 2D, green curve). Therefore, we can affirm that annealing reverses the adaptation of the surface into a state very similar to the pristine sample.

The SFG results indicate that the PS segments are displaced from the interface after being exposed to water. We attribute this displacement to a movement of the PS segments away from the interface and enrichment of the PAA segments toward the surface. Unfortunately, we were unable to detect the C=O vibration of the PAA segment with SFG to support this conclusion, as we lack sensitivity to the PS/PAA–air interface for this vibration (see Figure S4 in Section SI2, Supporting Information). However, as mentioned above, the decrease in different polarizations already points to a removal of phenyl rings at the surface.

2.2. Contact angle dependence

In order to quantify the fraction of PS segments (ϕ) at the interface, we measured the advancing contact angles of PS/PAA surfaces after being wetted and annealed at temperature from 50 to 150 °C. All advancing contact angles of PS/PAA surfaces with different ratios are between 94° and 98° after annealing the samples at 150 °C (**Figure 3**A). These values are only a little bit lower than the advancing contact angle of a surface made from pure PS, θ_{PS}, which is around 100°. Therefore, the contact angle measurements are consistent with the interpretation of the SFG signals, which revealed that the amount of air-exposed PS groups is independent of the PS/PAA ratio. Surfaces of pure PAA are soluble in water and therefore hydrophilic. Due to this, we assume an advancing contact angle θ_{PAA} of 0°. According to the Cassie model,[21]

$$\cos\theta_{PS/PAA} = \varphi\cos\theta_{PS} + (1 - \varphi)\,\cos\theta_{PAA} \tag{1}$$

we calculated the PS fraction at the interface of the PS/PAA surfaces with different ratios. After covering the surface with a water drop for 30 min, the advancing angle of 8.7/1 PS/PAA surfaces decreased from 99° to 88°. Correspondingly, the PS-fraction decreases from 98% to 82% at the interface, which is consistent with the decrease of the SFG intensity. After annealing the adapted PS/PAA surface at 50, 75, and 100 °C for 30 min each, the advancing contact angles increased gradually (Figure 3A). This conclusion is supported by SFG experiments performed after annealing at different temperatures showing an increasing recovery with increasing annealing temperature (see Figure S8 in Section SI5, Supporting Information). PS/PAA surfaces with ratios of 4.2/1 and 2.9/1 PS/PAA follow a similar trend with advancing angles 1–5° lower compared to 8.7/1 PS/PAA surfaces. Correspondingly, we obtain 1.5–7.5% less PS at the interface. Also for poly(α-hydroxymethyl-n-butylacrylate) and poly(methyl methacrylate) films, a change in the contact angle and SFG signal has been observed and assigned to a larger exposure of the hydrophilic groups to the interface.[22,23] For the butylacrylate film, annealing in water above the T_g enhances the restructuring.[22]

**ADVANCED
SCIENCE NEWS**

www.advancedsciencenews.com

[M] acro-
molecular
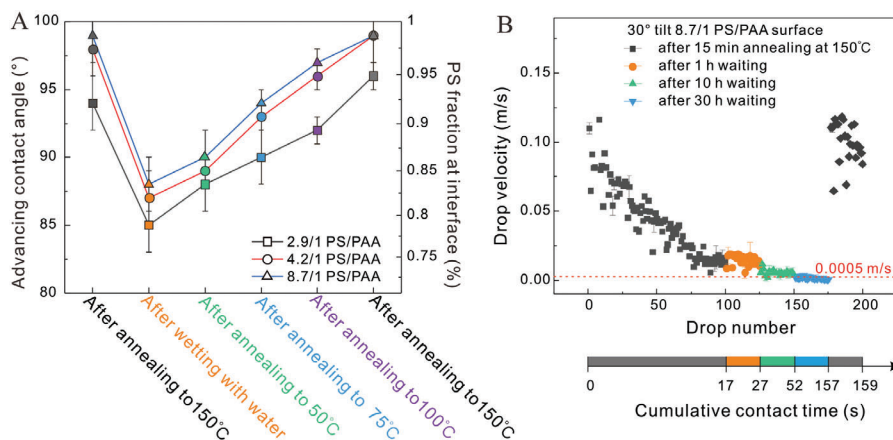Rapid Communications

www.mrc-journal.de

Figure 3. A) Advancing contact angles and corresponding PS fractions at the interfaces of 2.9/1, 4.2/1, and 8.7/1 PS/PAA after being covered with a water drop for 30 min and annealing at temperatures of 50, 75, 100, and 150 °C for 30 min, respectively. The errors were determined by averaging over three experiments. B) Drop velocities versus drop number. Measurements were performed at a tilt angle of 30° on an 8.7/1 PS/PAA surface with drop interval of 1 min after surface annealing at 150 °C for 15 min (drop 1–drop 100, drop 176–drop 200), waiting for 1 h (drop 101–drop 125), 10 h (drop 126–drop 150), and 30 h (drop 151–drop 175). Note: cumulative contact time $= \sum_{n} \frac{\text{Drop length}}{\text{drop velocity}}$ (n is drop number).

Subsequently, we measured how the PS/PAA copolymer surfaces adapt owing to a sliding drop. We measured the velocity of sliding drops with a drop interval of 1 min. For the first 100 drops the velocity decreased with increasing drop number (Figure 3B). Thus, the surface adapts more and more for subsequent drops. In order to test if there would be a partial recovery of the surface for longer waiting times, that is, exposure to air, we stopped the drop deposition and waited for 1 h. The velocity of the 101th drop didn't increase and subsequent drops exhibited a further slight decrease in drop velocity (Figure 3B). We even extended the waiting time to 30 h; the drop velocity remained constant (Figure 3B). Thus, at room temperature the surface does not recover. However, annealing the surface at temperature of 150 °C for 15 min, led to an increase in drop velocity to the same level of the first drop. For subsequent drops, the drop velocity decreased at a similar trend like the first 100 drops (Figure 3B). The latter indicates that the surface recovered by annealing, consistent with the SFG results (Figure S8 in Section SI5, Supporting Information) and contact angle measurements (Figure 3A and Figure S9 in Section SI6, Supporting Information). The observation that the adapted PS/PAA surface cannot recover at room temperature, but only after being annealed is attributed to the memory effect of polymers.[24–26]

3. Summar and Conclusions

In summary, annealed PS/PAA copolymer surfaces adapt nonreversibly to wetting by water. The SFG measurements indicated that the PS segments are displaced from the interface and PAA segments enrich at the surface. The latter results in the observed decrease in the advancing contact angles. Thus, adaptation of PS/PAA copolymer surfaces is given by both water diffusion into the sample (swelling)—as previously proven by fluorescence microscopy—and polymer reorientation at the surface. To which extend swelling and reconstruction contribute to the decrease in sliding velocity, respectively, is not yet clear. We exclude plastic

deformation of the surface, because the surface roughness remains constant. Additionally, elastic deformation of the sample surface may happen near the three-phase contact line[27] and contribute to the decrease in sliding velocity. Both, the analysis of the SFG and contact angle measurements suggest a decrease of the PS content at the surface by about 16% after wetting with water for the 8.7/1 PS/PAA copolymer. This decrease is not considerably influenced by increasing the PAA content in the copolymer (Figure 3A). Therefore, the contact angles are still dominated by styrene and a transition to a fully PAA dominated surface does not take place. Interestingly, in the sliding drop experiment the enrichment of acrylic acid groups at the surface increases with drop number. Thus, the contact time of the surface with water corresponds to 50 ms for a drop velocity of 0.1 m s^{-1} and a drop length of 5 mm. Therefore, by controlling the contact time (e.g., using the tilt angle) and the drop number, the enrichment of acrylic acid at the surface can be controlled. A saturated state is observed after about 150 drops have passed. The accumulated contact time in this case corresponds to 157 s (Figure 3B). The time the water was kept in contact with the sample in the SFG-experiment was 180 s. Thus, the SFG measurement corresponds to the saturated state.

4. Experimental Section

Preparation of PS/PAA Copolymer Surfaces: For details, the authors referred to their previous work.[13] The characteristics of the synthesized PS/PAA random copolymer is summarized in Section S7, Supporting Information. Briefly, after synthesis, the PS/PAA random copolymer was dissolved in THF (1.5 wt%). Then the solution was spin-coated onto a Si wafer at 1300 rpm for 60 s. Before each measurement, the surfaces were annealed at 150 °C in an oven under vacuum overnight. For SFG experiments, 1.5% PS/PAA in THF solution was spin-coated (1300 rpm, 60 s) on the top CaF$_2$ windows (Ø 25 ± 0.1 mm × 2 ± 0.1 mm) purchased from CRYSTAL GmbH, resulting in a thickness of 130 ± 10 nm as measured with a profilometer (P-7 Stylus Profiler, KLA-Tencor). The resulting samples were annealed at 150 °C for 1 h in an oven before their usage. The aver-

age roughness of the surface after annealing corresponded to ≈0.27 nm. Then, the authors placed a 10 µL water drop on the surface for 30 min and measured afterward the roughness again. They obtained an average value of ≈0.28 nm, which was similar to the value before contact with water (Section S8, Supporting Information).

Static Advancing Contact Angle Measurement: A 10 µL water drop was deposited on the surface after annealing at different temperatures and after contacting with water for 30 min each. Then 20 µL of DI water was pumped into the drop by a Hamilton syringe (100 µL) with a hydrophobic needle. The process was repeated on three different positions of the surfaces. Inflation was imaged using a camera from side view. The advancing contact angles were calculated by fitting an elliptical model to the images recorded.

Sliding Drop Measurement: 33 µL water drops were deposited on 30° tilted 8.7/1 PS/PAA surfaces at intervals of 1 min by a syringe pump (KD Scientific, Legato 100 Syringe Pump). After 1, 10, and 30 h of exposing to air subsequently, 25 drops were deposited at the same position after every exposing to air. To ensure the surface could recover, the surface was finally annealed at 150 °C for 10 min and 25 drops were deposited on the surface again. The sliding drops were recorded after they had slid on the surfaces for 1 cm by a high-speed camera (Photron, FASTCAM MINI UX100, 1000 fps, with 1× SilverTL Telecentric Lens, Edmund Optics). The recorded slide length of the drop was 1 cm. The velocity of every drop was an average velocity of 1 cm sliding. The details regarding calculating the drop velocity, dynamic advancing and receding contact angles from the recorded video can be found in the authors' previous work.[13]

SFG Measurement: The SFG spectra were measured with a setup based on a femtosecond Ti:sapphire amplified laser. (Coherent Libra, ≈800 nm, ≈50 fs, 1 kHz, 5.2 W). The narrowband (full width of half maximum [FWHM], 20 cm^{-1}) VIS beam was produced by passing part of the laser output through a Fabry–Perot etalon. The broadband (FWHM: 260 cm^{-1}) IR beam was generated by pumping an optical parametric amplifier (TOPAS) in combination with a non-collinear difference frequency generator with a part of the laser output. Both beams (IR: 6.5 mW and VIS: 21 mW) were overlapped spatially and temporally at the surface of the sample with angles of $\theta_{IR} \approx 40°$ and $\theta_{VIS} \approx 60°$ with respect to the surface normal. This produced an SFG signal detected by an electron multiplied charge-coupled device camera (Newton EMCCD) after being dispersed in a spectrometer (Andor Shamrock 303i). All spectra reported in the main text were recorded in SSP (s-polarized SFG, s-polarized VIS, and p-polarized IR) polarization combination during 1 min. Spectra for different polarization combinations and in different frequency regions can be found in the Supporting Information.

Sample Wetting during SFG Experiments: The samples were kept in the flow cell mounted into a stage. For wetting the sample, demineralized water (18.2 mΩ cm) was pumped inside the flow cell by means of tubes (Versilon AE30012 3/16″ inner diameter, 5/16″ out diameter) and a manually controlled peristaltic pump (Masterflex L/S Model: 07559-07). The water was introduced with a flow rate of ≈1 mL s^{-1} (laminar flow) until the tube system was filled up. The water was kept in contact with the sample for 3 min and then removed with the same flow rate used for its introduction. After water removal, the tubes were dried under a dry airflow until no water droplets were visualized inside the cell.

SFG Data Processing: An SFG spectrum of a buried gold sample was used to correct the frequency dependence of the authors' IR beam. A background was acquired for all spectra (gold and samples) by measuring with a blocked IR beam. For normalizing the data, every background was subtracted from its corresponding spectrum and the result was divided by the background-corrected gold spectrum. The calibration of the wavelengths was performed by using a PS foil introduced in the IR path during gold signal measurements. The resulting spectrum had dips corresponding to the PS infrared absorption that could be used to calibrate the wavelength.

Supporting Information

Supporting Information is available from the Wiley Online Library or from the author.

[1] H.-J. Butt, R. Berger, W. Steffen, D. Vollmer, S. A. L. Weber, *Langmuir* **2018**, *34*, 11292.

[2] W. S. Y. Wong, L. Hauer, A. Naga, A. Kaltbeitzel, P. Baumli, R. Berger, M. D'Acunzi, D. Vollmer, H.-J. Butt, *Langmuir* **2020**, *36*, 7236.

[3] R. Zhang, K. Graf, R. Berger, *Appl. Phys. Lett.* **2006**, *89*, 223114.

[4] I. Tokarev, S. Minko, *Soft Matter* **2009**, *5*, 511.

[5] S. Minko, M. Müller, M. Motornov, M. Nitschke, K. Grundke, M. Stamm, *J. Am. Chem. Soc.* **2003**, *125*, 3896.

[6] S. Lee, S. M. Flores, R. Berger, J. S. Gutmann, M. Brehmer, L. Conrad, L. Funk, P. Theato, D. Y. Yoon1, *J. Plast. Film Sheeting* **2015**, *31*, 434.

[7] L. Ionov, S. Minko, *ACS Appl. Mater. Interfaces* **2012**, *4*, 483.

[8] S. Minko, D. Usov, E. Goreshnik, M. Stamm, *Macromol. Rapid Commun.* **2001**, *22*, 206.

[9] J. A. Crowe, J. Genzer, *J. Am. Chem. Soc.* **2005**, *127*, 17610.

[10] G. D. Crevoisier, P. Fabre, J.-M. Corpart, L. Leibler, *Science* **1999**, *285*, 1246.

[11] B. K. Crone, A. Dodabalapur, R. Sarpeshkar, A. Gelperin, H. E. Katz, Z. Bao, *J. Appl. Phys.* **2002**, *91*, 10140.

[12] H. Kuroki, I. Tokarev, S. Minko, *Annu. Rev. Mater. Res.* **2012**, *42*, 343.

[13] X. Li, S. Silge, A. Saal, G. Kircher, K. Koynov, R. Berger, H.-J. Butt, *Langmuir* **2021**, *37*, 1571.

[14] Y. R. Shen, *Nature* **1989**, *337*, 519.

[15] C. Cai, M. S. Azam, D. K. Hore, *J. Phys. Chem. C* **2021**, *125*, 12382.

[16] A. G. Lambert, P. B. Davies, D. J. Neivandt, *Appl. Spectrosc. Rev.* **2005**, *40*, 103.

[17] X. Li, X. Lu, *Macromolecules* **2018**, *51*, 6653.

[18] H. Tsuruta, Y. Fujii, N. Kai, H. Kataoka, T. Ishizone, M. Doi, H. Morita, K. Tanaka, *Macromolecules* **2012**, *45*, 4643.

[19] K. A. Briggman, J. C. Stephenson, W. E. Wallace, L. J. Richter, *J. Phys. Chem. B* **2001**, *105*, 2785.

[20] P. Balzerowski, K. Meister, J. Versluis, H. J. Bakker, *Phys. Chem. Chem. Phys.* **2016**, *18*, 2481.

[21] A. B. D. Cassie, *Discuss. Faraday Soc.* **1948**, *3*, 11.

[22] N. Dhopatkar, E. Anim-Danso, C. Peng, S. Singla, X. Liu, A. Joy, A. Dhinojwala, *Macromolecules* **2018**, *51*, 5114.

[23] A. Horinouchi, H. Atarashi, Y. Fujii, K. Tanaka, *Macromolecules* **2012**, *45*, 4638.

[24] I. Luzinov, S. Minko, V. V. Tsukruk, *Prog. Polym. Sci.* **2004**, *29*, 635.

[25] S. Schubotz, C. Honnigfort, S. Nazari, A. Fery, J.-U. Sommer, P. Uhlmann, B. Braunschweig, G. K. Auernhammer, *Adv. Colloid Interface Sci.* **2021**, *294*, 102442.

[26] S. Santer, A. Kopyshev, J. Donges, H.-K. Yang, J. Rühe, *Langmuir* **2006**, *22*, 4660.

[27] L. Chen, E. Bonaccurso, T. Gambaryan-Roisman, V. Starov, N. Koursari, Y. Zhao, *Curr. Opin. Colloid Interface Sci.* **2018**, *36*, 46.

Supporting Information

Adaptation and Recovery of a Styrene-Acrylic Acid Copolymer Surface to Water

Xiaomei Li, Mirela Encheva, Hans-Jürgen Butt, Ellen H. G. Backus* and Rüdiger Berger*

Supporting information for

Adaptation and Recovery of a Styrene-Acrylic Acid Copolymer Surface to Water

Xiaomei Li[1#], Mirela Encheva[2#], Hans-Jürgen Butt[1], Ellen H.G. Backus[2*] and Rüdiger Berger[1*]

1 Max Planck Institute for Polymer Research, Ackermannweg 10, 55128 Mainz, Germany

2 Department of Physical Chemistry, University of Vienna, Währinger Straße 42, 1090 Vienna, Austria

(# Xiaomei Li and Mirela Encheva contributed equally to this work)

Email address of corresponding authors:

Ellen H.G. Backus: ellen.backus@univie.ac.at

Rüdiger Berger: berger@mpip-mainz.mpg.de

Content:

SI 1. Fresnel factors calculation and sensitivity to different interfaces

SI 2. Interface sensitivity at different polarization combinations

SI 3. O-H stretch signal on 8.7/1 PS/PAA surfaces

SI 4. SFG measurement on the pure PS surfaces

SI 5. SFG amplitude recovery as a function of annealing temperature

SI 6. Drop number dependent advancing and receding contact angles

SI 7. Characteristics of the copolymers made from styrene and acrylic acid

SI 8. Morphology of the surfaces

SI 1. Fresnel factors calculation and sensitivity to different interfaces

Fresnel coefficients for both interfaces (CaF$_2$-polymer (interface$_{12}$) and polymer-air (interface$_{23}$)) were calculated as a function of thickness for wavenumbers of 3060 cm^{-1} IR and 12500 cm^{-1} VIS. We assumed a three-layer system with multiple reflections in the middle layer supposing that: $n_{interface_{12}} = n_{interface_{23}} = n_{PS/PAA} = n_{PS}$ for the IR and VIS beams, and $n_{interface_{12}} = n_{CaF_2}$, $n_{interface_{23}} = n_{air}$ for the SFG [1, 2]. The results from these calculations are plotted in Figures S1 and S2. The values of the y-axis from these figures were calculated as described below:

$$Fresnel\ Factor\ SSP \rightarrow |L_{yy}(\omega_{SFG})L_{yy}(\omega_{VIS})L_{zz}(\omega_{IR})\sin\theta_{IR}|^2$$

$$Fresnel\ Factor\ SPS \rightarrow |L_{yy}(\omega_{SFG})L_{zz}(\omega_{VIS})L_{yy}(\omega_{IR})\sin\theta_{VIS}|^2$$

$$Fresnel\ Factor\ PSS \rightarrow |L_{zz}(\omega_{SFG})L_{yy}(\omega_{VIS})L_{yy}(\omega_{IR})\sin\theta_{SFG}|^2$$

$$Fresnel\ Factor\ PPP\ (xxz) \rightarrow |L_{xx}(\omega_{SFG})L_{xx}(\omega_{VIS})L_{zz}(\omega_{IR})\cos\theta_{SFG}\cos\theta_{VIS}\sin\theta_{IR}|^2$$

$$Fresnel\ Factor\ PPP\ (zzz) \rightarrow |L_{zz}(\omega_{SFG})L_{zz}(\omega_{VIS})L_{zz}(\omega_{IR})\sin\theta_{SFG}\sin\theta_{VIS}\sin\theta_{IR}|^2$$

$$Fresnel\ Factor\ PPP\ (xzx) \rightarrow |L_{xx}(\omega_{SFG})L_{zz}(\omega_{VIS})L_{xx}(\omega_{IR})\cos\theta_{SFG}\sin\theta_{VIS}\cos\theta_{IR}|^2$$

$$Fresnel\ Factor\ PPP\ (zxx) \rightarrow |L_{zz}(\omega_{SFG})L_{xx}(\omega_{VIS})L_{xx}(\omega_{IR})\sin\theta_{SFG}\cos\theta_{VIS}\cos\theta_{IR}|^2$$
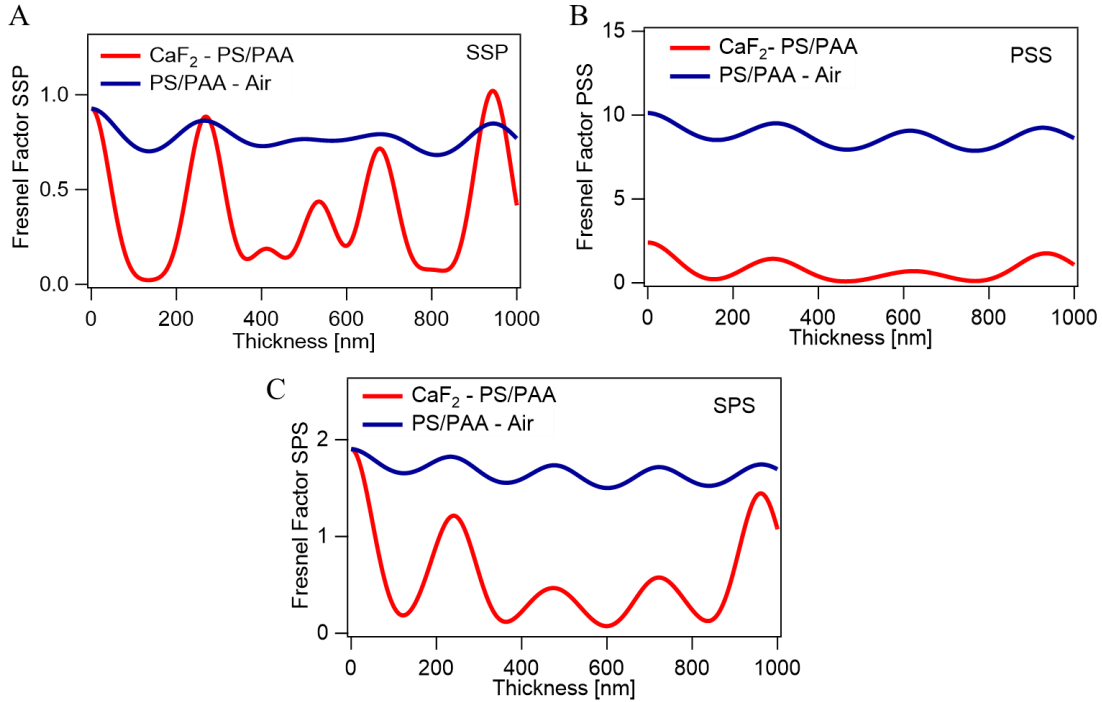
Figure S1 *Fresnel factor calculations for the CaF$_2$-polymer and polymer-air interfaces for SSP, PSS and SPS polarization combination.*
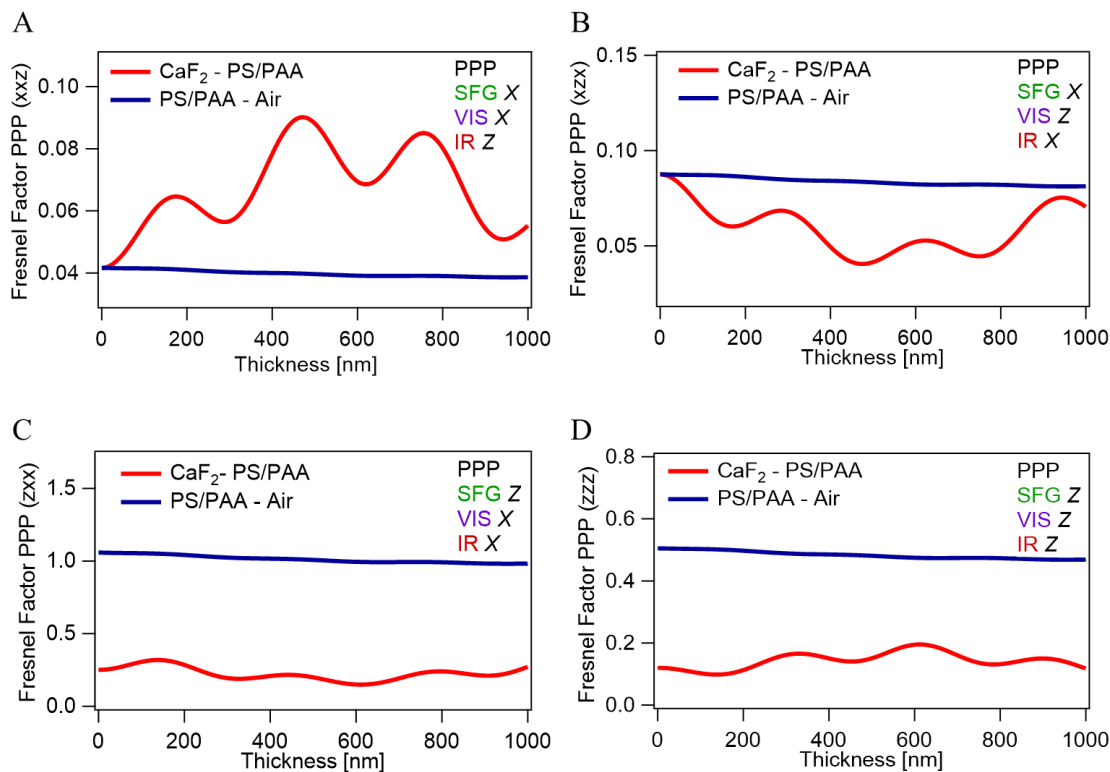
Figure S2. *Fresnel factor calculation for CaF₂-polymer and polymer-air interfaces for the different PPP contributions A) (xxz), B) (xzx), C) (zxx) and D) (zzz).*

SI 2. Interface sensitivity at different polarization combinations

For SSP polarization combination, the Fresnel coefficients (Figure S1A) of the CaF₂-polymer interfaces show a pronounced thickness dependence with a maximum at 271 nm and a minimum at 136 nm, whereas the Fresnel coefficients for the polymer-air interface show a much weaker thickness dependence. In order to determine the interface that we are measuring, we compared the response of two samples that have different thicknesses (130±10 nm and 260±10 nm) (Figure S3).

We observe a weak intensity change between the two spectra, which does not match with the pronounced thickness dependence expected for the CaF₂-polymer interface case. However, it fits good with the less marked thickness dependence of the polymer-air interface. We thus conclude that the SFG signal in SSP polarization in the C-H/O-H spectral range originates mainly from the polymer/air interface. Apparently, the SFG signal from the CaF₂/polymer interface in the C-H/O-H spectral region is very low.
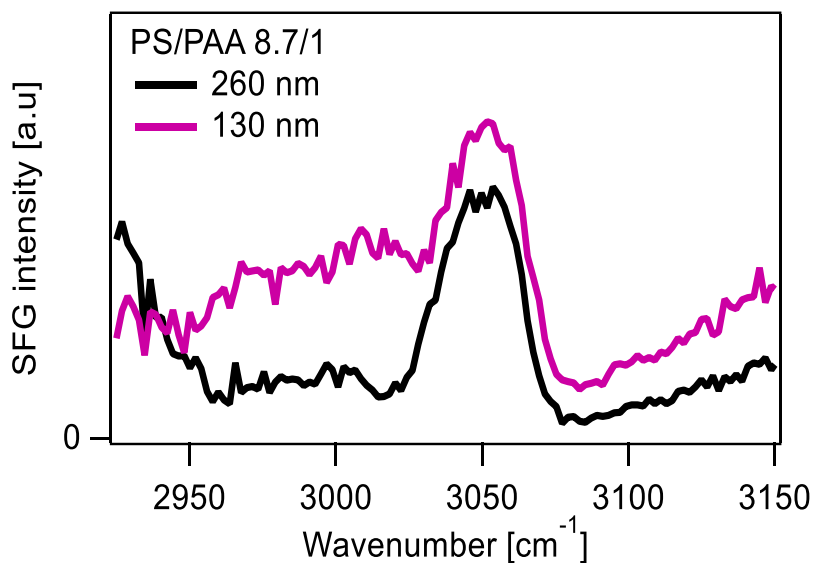
Figure S3. *SFG spectra in SSP of PS/PAA 8.7/1 films with thicknesses of 130 nm and 260 nm in the CH spectral region acquired for 1 min.*
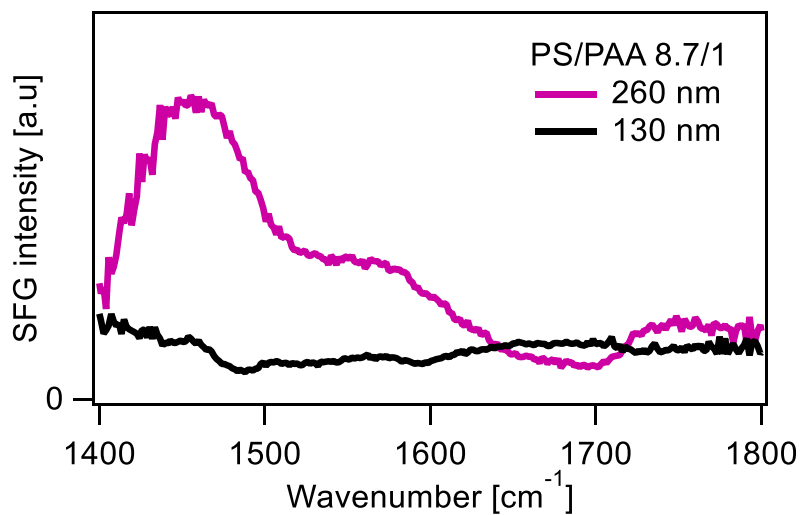
Figure S4. *SFG spectra of PS/PAA 8.7/1 films with thicknesses of 130 nm (acquired for 7 min) and 260 nm (acquired for 2 min) in the CO spectral region. The spectra on the plot are time normalized.*

For the C=O spectral region, this does not occur, since the 130 nm and 260 nm samples show very different spectra (Figure S4), making it impossible to extract any conclusions from the measurements performed in this frequency range.

SFG spectra were also obtained for the four possible polarization combinations in the samples: SPS, PSS, PPP and SSP. When switching polarization, it is important to ensure

that we still maintain the sensitivity to the polymer-air interface. For this reason, we measured the two different thickness samples to check if the detected vibrations were the same (behaviour expected if mainly the polymer-air interface is measured).

Of the four polarization combinations, only the PPP showed different vibrations in the two samples. This, together with the fact that there are four electrical susceptibility terms related to this polarization, each with their corresponding Fresnel factor, made us consider that the interpretation of data obtained in this polarization combination would be too complex.

This result is supported by Fresnel factor calculations since, as it can be seen in Figure S1, the Fresnel factors for the polymer-air interface are higher than the one of the CaF_2-polymer interfaces for SPS, PSS and SSP polarization combinations. This is not the case for PPP where we have to consider four different Fresnel factors showing different behaviour for each component (Figure S2). Therefore, we focus on the SPS, PSS, and SSP polarization combinations and show the spectra before and after exposing the samples to water (Figure S5).
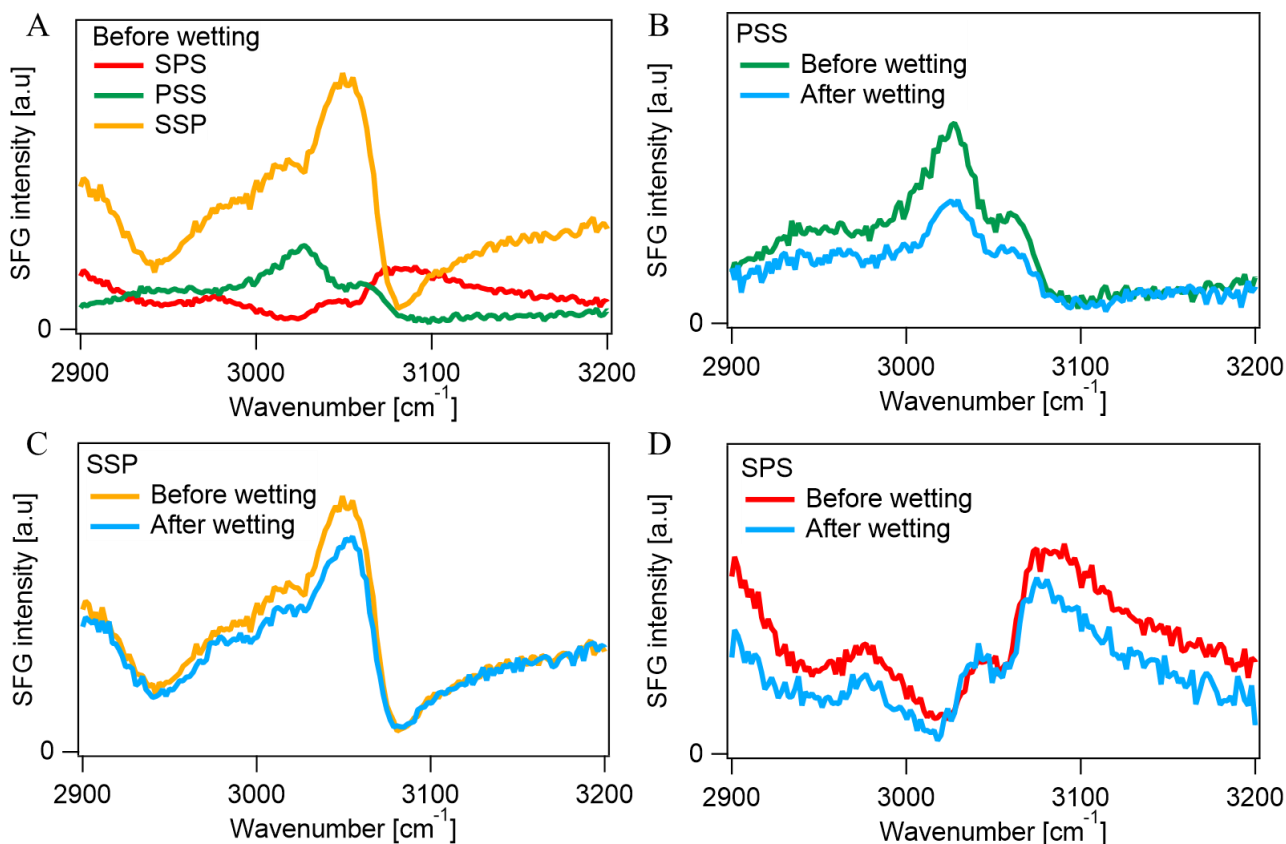
Figure S5*. PS/PAA 8.7/1 SFG spectra measured for the 130 nm thickness at A) SPS (acquired for 4 min), PSS (acquired for 4 min) and SSP (acquired for 2 min) polarization combinations before wetting. The spectra of this figure are time normalized. B) PSS polarization before (green) and after wetting (blue) C) SSP polarization before (yellow) and after wetting (blue) and D) SPS polarization before (red) and after wetting (blue).*

All three polarization combinations show a decrease in the aromatic bands. In case only a slight change in the orientation of the phenyl rings was happening, one would expect to see a decrease in one polarization together with an increase in another, since different polarizations are probing different oriented vibrations. However, since a general decrease is observed in all of them, we conclude that most likely the PS is hiding from the water, decreasing in this way the amount of phenyl rings on the interface, and therefore also our SFG intensity.

SI 3. O-H stretch signal on 8.7/1 PS/PAA surfaces

The signal in the O-H stretch region between 3100 and 3500 cm^{-1} is the same before and after wetting as is clear from the figure below (Figure **S6**). The spectrum in this frequency region contains contributions from the non-resonant signal and from resonances. As the signal does not change, we conclude that no water remains in the surface region. As SFG is not sensitive to centrosymmetric water, we cannot exclude that water remains in the bulk of the polymer film.
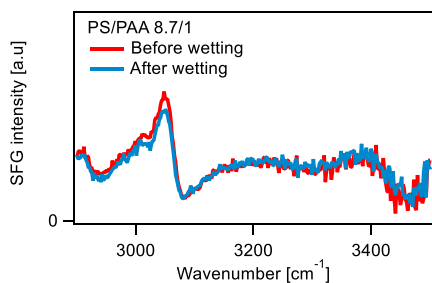
Figure S6. *SFG spectrum of PS/PAA 8.7/1 with 130 nm thickness (acquired for 2 min) between 2900 cm^{-1} and 3500 cm$^{-1,}$ before (red) and after wetting (blue).*

SI 4. SFG measurement on the pure PS surfaces

A small increase was observed in the pure PS samples after wetting.
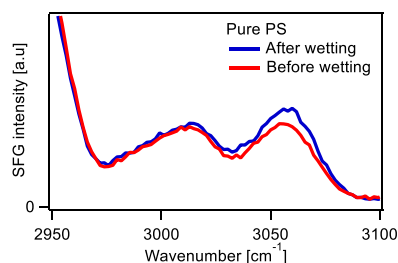
Figure S7. *SFG spectra of pure PS sample with 130 nm thickness (acquired for 2 min) before water exposure (red), and after water exposure (blue).*

SI 5. SFG amplitude recovery as a function of annealing temperature

Figure S8 shows a recovery of the 3057 cm^{-1} PS band as a function of annealing temperature in analogue with Figure 3A. The SFG spectra were all measured at room temperature.
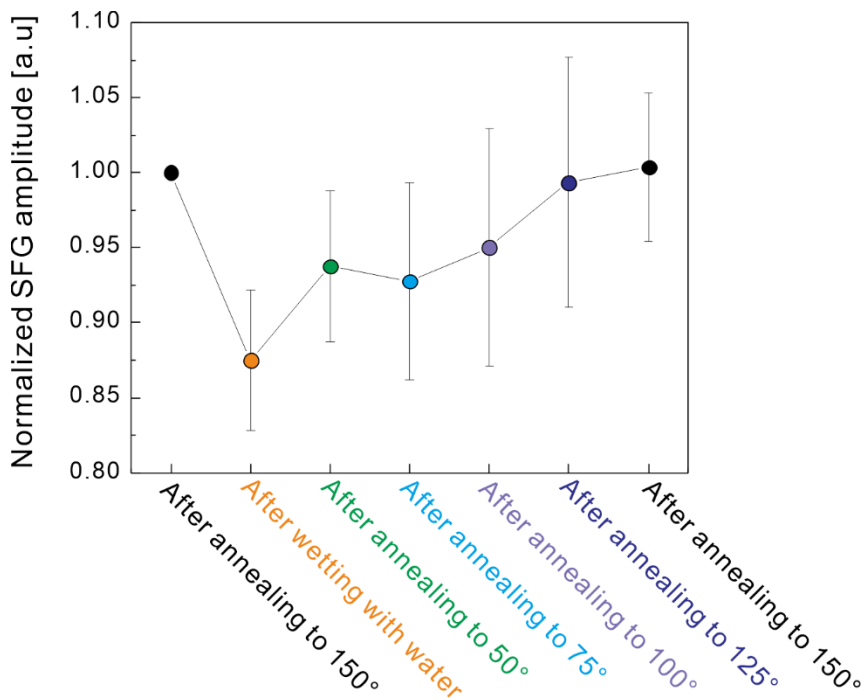
Figure S8. Amplitude of the 3057 cm^{-1} band at different states, after annealing, wetting, and subsequent annealing at different temperatures: 50ºC, 75ºC, 100ºC, 125ºC, 150ºC. The amplitude was measured for a PS/PAA 8.7/1 sample with 130 nm thickness. All SFG spectra were measured at room temperature.

SI 6. Drop number dependent advancing and receding contact angle

In addition to the drop velocity decrease versus drop number (Figure 3B), we analysed the corresponding dynamic contact angles of the sliding drops as well. The dynamic advancing contact angle decreases with drop number from 100° to 96° (Figure S9). The dynamic receding contact angle remained constant. The decrease in advancing contact angles is consistent with the decrease of drop velocity, which was caused by the PS/PAA surface adaptation to the sliding water drop.

59
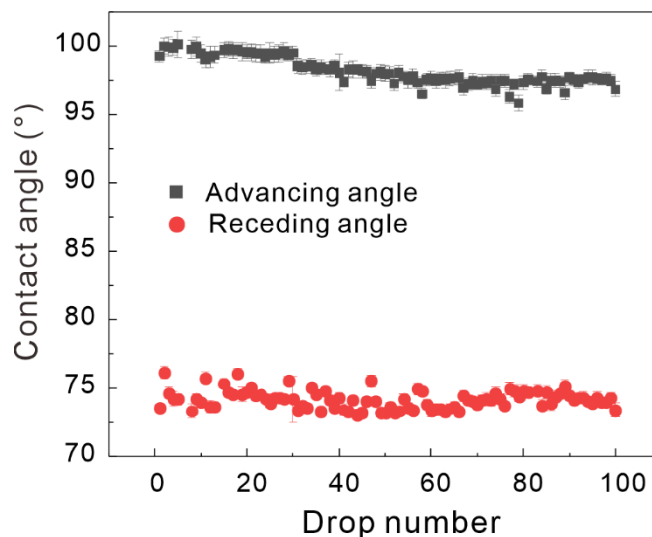
Figure S9. *Drop number dependent advancing and receding contact angles.*

SI 7. Characteristics of the copolymers made from styrene and acrylic acid

Table S1. *Characteristics of the copolymers made from styrene and acrylic acid.*

sample	PS/PAA molar ratio		Reaction time (h)	M_w (g/mol)	M_n (g/mol)	M_w /M_n	T_g (°C)
	In monomer	In copolymer					
1	6.6/1	8.7/1	48	76868	39650	1.94	118±3
2	3.0/1	4.2/1	48	67316	42395	1.59	122±3
3	1.6/1	2.9/1	48	55898	42360	1.32	130±3

SI 8. Morphology of the surfaces

The morphology of copolymer surfaces may change upon contact with water [3, 4]. We measured the morphology of our samples by SFM in tapping mode (Dimension Icon, Bruker, OTESPA, 300 kHz, 26 N/m) before and after covering the surface with a water drop for 30 min. The SFM measurements indicated a root mean square roughness on an area of 1 μm^2 for all samples < 0.3 nm (Figure S10), indicating that there are no significant changes in morphology.
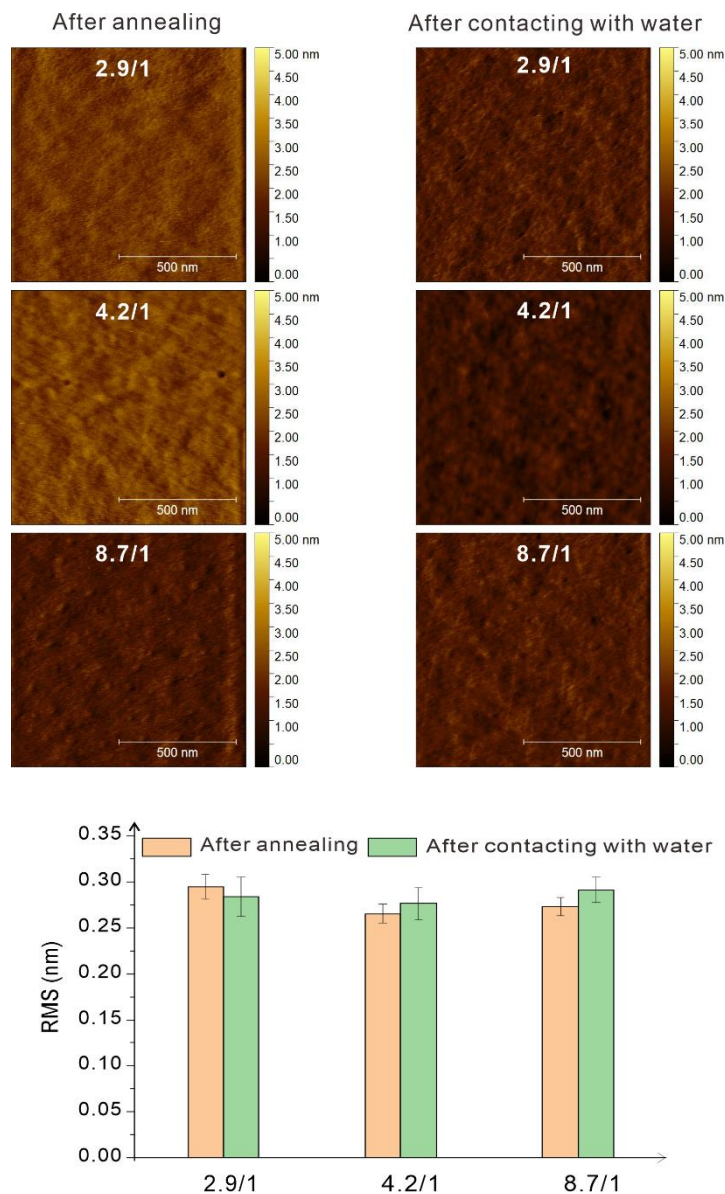
Figure S10. *Morphology and root mean square (RMS) of roughness of the copolymer surface with PS/PAA ratio of 2.9/1, 4.2/1, 8.7/1 after annealing and after contacting with water. The error bar comes from three measurements on different positions and different samples.*

Reference

[1] E. H. G. Backus, N. Garcia-Araez, M. Bonn, H. J. Bakker, *The Journal of Physical Chemistry C* **2012**, 116(44), 23351-23361.

[2] C. Cai, M. S. Azam, D. K. Hore, *The Journal of Physical Chemistry C* **2021**, 125, 12382.

[3] J. Peng, Y. Han, W. Knoll, D. Kim, *Macromol. Rapid Commun*. **2007**, 28, 1422–1428.

[4] M.R. Tomlinson and J. Genzer, *Langmuir* **2005**, 21, 11552-1155.

2.3. X. Li *et al. J. Chem. Phys.*, 2023

Fast-release kinetics of a pH-responsive polymer detected by dynamic contact angles

Xiaomei Li[1#], Krisada Auepattana-Aumrung[2#], Hans-Jürgen Butt[1], Daniel Crespy[2]*, Rüdiger Berger[1]*

1. Max Planck Institute for Polymer Research, Mainz, Germany

2. Department of Materials Science and Engineering, School of Molecular Science and Engineering, Vidyasirimedhi Institute of Science and Technology (VISTEC), Rayong 21210, Thailand

Published in:

Author contributions:

Xiaomei Li and Krisada Auepattana-Aumrung contributed equally to this work. Rüdiger Berger and Daniel Crespy conceived and supervised the project. Xiaomei Li and Krisada Auepattana-Aumrung planned, conducted the experiments, and analyzed the data. All the authors discussed, reviewed, wrote, and approved the manuscript.

Fast-release kinetics of a pH-responsive polymer detected by dynamic contact angles EP

View Online   Export Citation   CrossMark

Xiaomei Li,[1] iD Krisada Auepattana-Aumrung,[2] iD Hans-Jürgen Butt,[1] iD Daniel Crespy,[2,a] iD
and Rüdiger Berger[1,a] iD

AFFILIATIONS

[1] Max Planck Institute for Polymer Research, Mainz, Germany

[2] Department of Materials Science and Engineering, School of Molecular Science and Engineering, Vidyasirimedhi Institute
of Science and Technology (VISTEC), Rayong 21210, Thailand

Note: This paper is part of the JCP Special Topic on Chemical Physics of Controlled Wettability and Super Surfaces.
[a] Authors to whom correspondence should be addressed: daniel.crespy@vistec.ac.th and berger@mpip-mainz.mpg.de

ABSTRACT

Polymers conjugated with active agents have applications in biomedicine, anticorrosion, and smart agriculture. When the active agent is used as a drug, corrosion inhibitor, or pesticide, it can be released upon a specific stimulus. The efficiency and the sustainability of active agents are determined by the released kinetics. In this work, we study the fast-release kinetics of 8-hydroxyquinoline (8HQ) from a pH-responsive, random copolymer of methyl methacrylate and 8-quinolinyl-sulfide-ethyl acrylate [P(MMA-*co*-HQSEA)] by hydrolysis of the β-thiopropionate groups. We used contact angle measurements of sliding drops as an elegant way to characterize the release kinetics. Based on the results gained from ^{1}H nuclear magnetic resonance measurement, fluorescent intensity measurement, and velocity-dependent contact angle measurement, we found that both the hydrolysis rate and polymer conformation affect the release kinetics of 8HQ from a P(MMA-*co*-HQSEA) film. Polymer chains collapse and further suppress the release from the inner layer in acidic conditions, while polymer chains in a stretched condition further facilitate the release from the inner layer. As a result, the cumulative release rate of 8HQ is higher in the basic condition than in the acidic condition.

INTRODUCTION

Polymers conjugated with active agents are already being applied in biomedicine, to prevent corrosion, and in smart agriculture.[1–4] Active agents such as drugs, corrosion inhibitors, and pesticides are released from polymers upon a specific stimulus, depending on the type of cleavable bond, the substituents around the bond, and the affinity to the surrounding medium.[3,5] To unravel and control the release kinetics of active agents from polymers to the environment is vital for the success of their applications. A rapid release provides high availability in the short term, while a slow, long-term release maintains a certain level of the active agent.[6,7] Therefore, understanding the release kinetics at all time scales is essential for further specific applications.

Polymer release kinetics depends on the contact time and contact medium. In the case of active agents released from a free polymer chain in a good solvent by a chemical reaction [Fig. 1(a)], the release kinetics is determined by the reaction rate itself. When multiple free polymer chains form a nanoparticle [Fig. 1(b)], the release from the outer layer of the nanoparticle is mainly affected by the reaction rate, while the release from the inner layer is influenced by the conformation of the polymer chains.[8–11] Polymer chains in a collapsed state prevent liquid from penetrating into the inner layer, which, in turn, suppresses the release from the inner layer. In contrast, polymer chains in a stretched state allow liquid penetration, which facilitates release from the inner layer. The release from a condensed polymer film on a substrate is also affected by the polymer conformation, namely, the collapsed state or the stretched state [Fig. 1(c)]. However, the release kinetics is probably different for polymer films and nanoparticles, given their different geometries. To distinguish the influence of reaction rate and polymer conformation, studying the fast-release kinetics is required.
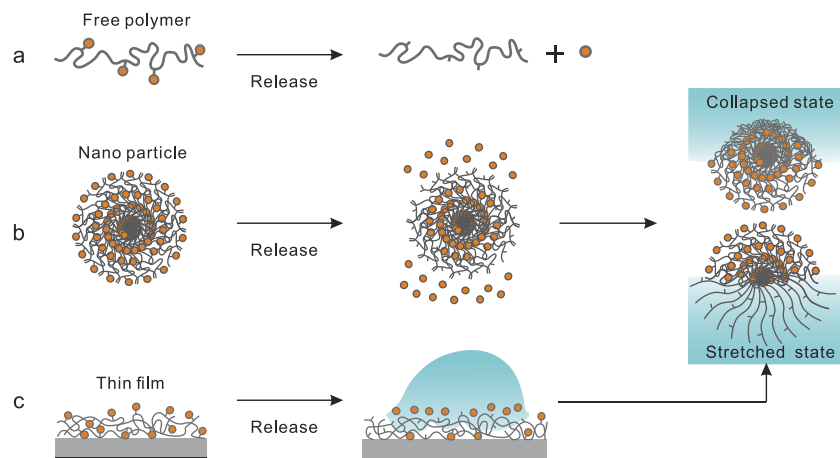
FIG. 1. Schematics showing active agents (orange circles) attached to polymer chains. The active agent is released from a polymer by exposure to a liquid. The polymer forms different states: (a) a free polymer chain, (b) a polymer nanoparticle, and (c) a thin polymer film on a substrate.

To characterize the release kinetics of active agents from polymers, typically ultraviolet–visible spectroscopy, nuclear magnetic resonance spectroscopy (NMR), and high-performance liquid chromatography (HPLC) are applied.[12,13] The latter two techniques require an experimental time for a quantitative analysis of at least a few minutes or even longer. In these cases, a burst release with high errors usually appears in the release profiles, because a large quantity of molecules is released in a very short time. Thus, until now, only very limited knowledge about the release kinetics at shorter time scales is available. Here, we propose to use contact angle measurements directly near the three-phase contact line of sliding drops as a way to characterize the release kinetics.

The relationship between the release kinetics and the dynamic contact angles can be described by the adaptation model proposed by Butt *et al.* in 2018.[14] In the adaptation model, surface adaptation causes a change in the chemical/physical properties of the surfaces. The chemical/physical properties of the surfaces later lead to a change of the interfacial energies and the contact angle. For example, liquid diffusion and polymer reorientation at the interface change the contact angle.[15,16] We assume that the changes in surface energy due to the hydrolysis reaction follow first-order kinetics. Then, the exponentially relaxing interfacial energies are described by

$$\gamma(t) = \gamma^{\infty} + \Delta\gamma e^{-t/\tau}, \quad (1)$$

where τ is the relaxation time correlated with the release, γ^{∞} is the equilibrium interfacial energy, and $\Delta\gamma$ is the change in interfacial energy due to surface adaptation. The peripheral length (l) is defined as the width in the contact region, which determines the contact angles. By replacing the time t by the ratio between the peripheral length and the contact-line velocity (v), we can rewrite Eq. (1) as

$$\gamma(t) = \gamma^{\infty} + \Delta\gamma e^{-l/v\tau}. \quad (2)$$

Assuming that Young's model is still valid locally and with the surface energies in Young's model described by Eq. (2), the advancing angle (θ_A) and the receding angle (θ_R) can be quantified by the two equations

$$\cos\theta_A = \cos\theta_A^{\infty} - \frac{\Delta\gamma_{SL}}{\gamma_L^{\infty}} e^{-l/v\tau_{SL}}, \quad (3)$$

$$\cos\theta_R = \cos\theta_R^{\infty} + \frac{\Delta\gamma_S}{\gamma_L^{\infty}} e^{-l/v\tau_S}. \quad (4)$$

Here, θ_A^{∞} and θ_R^{∞} are the static advancing and receding contact angles that are valid for $v \to 0$. The subscripts "S," "L," and "S/L" correspond to the solid/air, liquid/air, and solid/liquid interfaces. Measurements of the dynamic advancing and receding contact angles can be performed, e.g., by tilted plate experiments.[15–17] The relaxation time can be calculated by fitting the measured dynamic contact angles vs velocity with Eqs. (3) or (4). A general unknown parameter is the peripheral length. Here, we assume a peripheral length to be around 10 nm, which is a typical length scale for surface force and surface stress.[14] Generally, multiple adaptation processes can lead to changes in contact angles. To distinguish them, a reference surface is required, to attribute change of surface energy (chemical composition or topography) to hydrolysis of the surface. Then, the adaptation model can be used to fit the experimental data.

In this work, we investigate the release kinetics of active agents in solution and from thin polymer films. We explore the release kinetics of 8-hydroxyquinoline (8HQ) from a pH-reactive, random copolymer of methyl methacrylate (MMA) and 8-quinolinyl-sulfide-ethyl acrylate (HQSEA) [P(MMA-*co*-HQSEA)]. P(MMA-*co*-HQSEA) is a random pH-responsive copolymer, with 8-hydroxyquinoline (8HQ) as the active agent. The 8HQ groups are linked to the polymer chains with β-thiopropionate groups and can be released by a hydrolysis reaction. Due to the electron-withdrawing sulfide on the β-thiopropionate groups, the hydrolysis reaction is sensitive to the presence of acids or bases.[7,18–23] The released 8HQ groups can work as inhibitors for metal corrosion or proteasome; therefore, β-thiopropionate polymers with the active agent of 8-hydroxyquinoline (8HQ) have potential applications in the fields of anticorrosion and biomedicine.[24–26] Thus, P(MMA-*co*-HQSEA) is a representative polymer for studying the release kinetics of active agents.

EXPERIMENTAL SECTION

1. **Materials:** methyl methacrylate (MMA, 99%, Acros Organics) was purified by distillation before use. 8-quinolinyl-sulfide-ethyl acrylate (HQSEA) was synthesized according to a previously reported method.[25] *N,N*-Dimethylformamide extra dry (DMF, 99.8%, Acros Organics), 1,1′-azobis (cyclohexanecarbonitrile) (ABCN, 98%, Sigma-Aldrich), diisopropyl ether (99%, Carlo Erba), dichloromethane (DCM, 99.9%, Honeywell), aluminum chloride (AlCl$_3$, 99%, Acros Organics), 1,4-dimethoxybenzene (>99%, Tokyo Chemical Industry), chloroform-d$_1$ (CDCl$_3$, 99.8%, Cambridge Isotope Laboratories, Inc.), deuterium oxide (D$_2$O, 99.96%, Cambridge Isotope Laboratories), dimethyl sulfoxide-d$_6$ (99.9%, Cambridge Isotope Laboratories), hydrochloric acid (HCl, 37%, Carlo Erba), potassium hydroxide (KOH, 85%, Carlo Erba), sodium hydroxide (NaOH, 97%, Carlo Erba), di-sodium tetraborate (99.5%, QReC), boric acid (99.8%, Carlo Erba), monosodium phosphate (98%, Carlo Erba), glacial acetic acid (99.5%, Carlo Erba), pH 3 citric buffer solution (citric/sodium hydroxide/sodium chloride, Fluka), pH 3 phosphate buffer solution (Fisher Chemical), pH 4 buffer solution (citric/sodium hydroxide/sodium chloride, Fluka), pH 5.5 buffer solution (sodium acetate, AmBion), pH 7 buffer solution (Sodium phosphate, Alfa Aesar), pH 8 buffer solution (Sodium phosphate, Alfa Aesar), and pH 10 buffer solution (Borax/sodium hydroxide, Fluka) were used without further purification. Deionized water was used throughout this experimental work.

2. **Polymer synthesis:** HQSEA (1660.45 mg, 5.00 mmol) and MMA (500.60 mg, 5.00 mmol) were dissolved in 6 ml of DMF in a 25-ml, round-bottom flask. After adding ABCN (24.43 mg, 0.1 mmol) as the reaction's initiator, the liquid was bubbled with nitrogen gas for 5 min. The reaction flask was then placed in an oil bath at 80 °C in a nitrogen atmosphere for 20 h. After polymerization and cooling to room temperature, the products were precipitated into 200 ml cold diisopropyl ether. Then, the products were dissolved in 10 ml dichloromethane and re-precipitated in cold diisopropyl ether two more times. Finally, the product was dried under a vacuum.

3. **Preparation of surfaces:** We used pure poly(methyl methacrylate) (PMMA) as a reference surface for the dynamic contact angle measurement. Both PMMA surfaces and P(MMA-*co*-HQSEA) surfaces were prepared by a home-made dip-coating machine at a dipping speed of 90 mm/min from a solution of 1 wt. % PMMA or P(MMA-*co*-HQSEA) in tetrahydrofuran. After coating, the surfaces were dried under vacuum at room temperature for 10 h. The thickness of the polymer film was ≈18 nm, as measured by scanning force microscopy (Fig. S1).

4. **Scanning Force Microscopy (SFM):** The topography and the thickness of the surfaces were measured by SFM (Dimension Icon, Bruker) in the tapping mode (Fig. S2). SFM tips with a nominal spring constant of 26 N/m and a nominal resonance frequency of 300 kHz were utilized (160AC-NA, OPUS).

5. **^{1}H NMR spectroscopy measurements:** ^{1}H NMR spectra of products dissolved in CDCl$_3$, D$_2$O, and DMSO-d$_6$ were recorded at room temperature with a 600 MHz Bruker NMR spectrometer. To study the release kinetics of 8HQ, 2.5 mg P(MMA-*co*-HQSEA) and 0.5 mg 1,4-dimethoxybenzene were dissolved in a mixture of 700 μl of DMSO-d$_6$ with 70 μl of D$_2$O (neutral condition), 70 μl of 0.5M HCl solution in D$_2$O (acidic condition) or 70 μl of 0.5M KOH solution in D$_2$O (basic solution). The different solutions were then transferred to NMR tubes, which were placed in a shaking incubator (NB-205, N-Biotek), at 30 °C, applying a shaking rate of 100 rpm. The solutions in the NMR tubes were then measured by ^{1}H NMR spectroscopy at different time intervals.

5. **Fluorescence spectroscopy measurements:** The fluorescence intensity of 8HQ was measured by fluorescence spectroscopy (Edinburgh Instruments FLS980 spectrometer). We monitored the temporal evolution of the fluorescence intensity of the released 8HQ from P(MMA-*co*-HQSEA) surfaces. The coated glass substrates were immersed in a 15 ml solution at pH 3, in a solution at pH 7, and in a solution at pH 10 in shaking incubators (NB-205, N-Biotek, 30 °C, 100 rpm). At different time intervals, 2 ml of the buffer solution, including released molecules, was removed for measurements and replaced by 2 ml of fresh buffer solution. A solution at pH 3 was prepared by adding 0.3 g of glacial acetic acid to 225 ml of deionized water, followed by the gradual addition of a 1N HCl aqueous solution, to control the pH value. The volume was then adjusted to 500 ml with deionized water. A solution at pH 7 was prepared by adding 0.6 g of monosodium phosphate to 225 ml of deionized water, followed by the gradual addition of a 1N NaOH aqueous solution, to control the pH value. The volume was then adjusted to 500 ml with deionized water. A solution at pH 10 was prepared by adding 3.1 g of boric acid and 2.5 g of di-sodium tetraborate to 225 ml of deionized water, followed by the gradual addition of a 1N NaOH aqueous solution, to control the pH value. The volume was then adjusted to 500 ml with deionized water. To increase the fluorescence, we added 200 μl of 20 mg/ml AlCl$_3$ aqueous solution to the aliquots taken from the release media. The concentration of 8HQ in the released media was then determined from the measured fluorescence intensity (λ_{ex} = 360 nm and λ_{em} = 530 nm). The calibration curves are provided in the supplementary material (Fig. S2). The cumulative release percentage was calculated using[27]

$$C_n = C_{n\_measured} + \frac{A}{V} \sum_{s=1}^{n-1} C_{s\_measured}. \tag{5}$$

Here, C_n is the expected *n*th sample concentration, $C_{n\_measured}$ is the measured concentration, A is the volume of the withdrawn aliquot, V is the volume of the dissolution medium, $n - 1$ is the total volume of all the previously withdrawn samples before measuring the current sample, and $C_{s\_measured}$ is the total concentration of all previously measured samples taken before the current sample was measured.

6. **Dynamic contact angle measurement:** The experimental setup and procedure were described previously.[15,17] Briefly, ≈35 μl drops were deposited onto a tilted surface by a peristaltic pump (MINIPULS 3, Gilson) at a height of 5 mm. The movement of the drop was recorded by a high-speed camera (FASTCAM Mini UX100, Photron) using a 1.0x SilverTL™

Telecentric Lens from the side. The recorded length was around 1 cm. The video was processed by an adapted drop-shape analysis code from MATLAB (open source DSAfM) version 9.5.0.944 444 (R2018b). The contact-line velocity and the contact angles on the advancing and the receding sides were then calculated automatically using a polynomial fit. The average velocity of the advancing and receding contact lines is defined as drop velocity. The drop velocity was varied by changing the tilt angle from 30° to 70°. Pristine samples were used for every measurement at varying tilt angles. All the buffer solutions for the tilted plate setup were bought and used directly. The influence of the different compositions of buffer solutions is investigated by measuring the dynamic contact angles of a citrate buffer solution and of a phosphate solution at pH 3 on the P(MMA-co-HQSEA) surfaces—the nearly identical results for the two cases indicate that the influence of the buffer solution composition is low see Fig. S5 of the supplementary material.

RESULTS AND DISCUSSION

To study the release kinetics of 8HQ under different conditions, we synthesized a random P(MMA-co-HQSEA) polymer. The molar ratio between methyl methacrylate and 8-quinolinyl-sulfide-ethyl acrylate units in the copolymer was 1:1, as measured by ^{1}H NMR spectroscopy in CDCl$_3$ [Fig. 2(a)].

The release kinetics of 8HQ from P(MMA-co-HQSEA) under neutral, acidic, and basic conditions was investigated by monitoring the ^{1}H NMR spectra in the solutions at different time intervals at 25 °C. The release of 8HQ from P(MMA-co-HQSEA) was investigated by comparing the signal of aromatic protons in 8HQ with the signal of protons of 1,4-dimethoxybenzene used as an internal standard [Fig. 2(b) and Fig. S2]. Under neutral conditions [green triangles in Fig. 2(c)], we detected no significant signal from 8HQ. Thus, under neutral conditions, 8HQ was not released or the released amount was too low to be detected. In contrast, more than 70% of 8HQ was released in acidic conditions after 480 h [red squares in Fig. 2(c)]. Moreover, all 8HQ had been released from P(MMA-co-HQSEA) in basic conditions within 5 min before the first ^{1}H NMR measurement [blue circles in Fig. 2(c)]. Hydrolysis of β-thiopropionate groups under the acidic and basic conditions was, therefore, faster than that under neutral conditions, confirming previous reports.[4,28] However, the release kinetics of 8HQ on a very short time scale (for example, in basic solution) could not be detected by ^{1}H NMR spectroscopy because of the relatively low sensitivity and long measuring time.

To slow down the release kinetics of 8HQ, we used a dense, 18-nm-thick P(MMA-co-HQSEA) film on a glass substrate, immersed in solutions with different pH values. 8HQ is a weakly fluorescent molecule due to intramolecular proton transfer from the hydroxyl group to the nitrogen atom in the excited state. However, chelation of metal cations can prevent this transfer, rendering the 8HQ complex highly fluorescent.[25,29,30] For this reason, a measurement of fluorescent intensity is also a normal way to explore the release kinetics of 8HQ after adding 20 mg/ml AlCl$_3$ to the solution. Upon light excitation at 360 nm, the chelated 8HQ displayed a fluorescence emission at 530 nm. The cumulative amount of released 8HQ could be calculated based on the calibration curves see Fig. S3 of the supplementary material.

We measured an increasing fluorescence intensity over time after immersing the film in the basic solution at pH 10 [Fig. 3(a)]. The cumulative release percentages of 8HQ in acidic and basic conditions were 7.5% and 7.8%, respectively, after 72 h of immersion [Fig. 3(b)]. Consistent with the NMR results, the P(MMA-co-HQSEA) film in neutral conditions did not display measurable fluorescence. At the early stage of immersion (1–6 h), the release of 8HQ from the coating in the basic condition was faster than that in the acidic condition, also in line with the NMR results. Since the fluorescence intensity of the released 8HQ in the first 1 h after immersing the samples was low, the release kinetics on a time scale of up to 1 h could not be resolved [Fig. 3(a)].

To study the release kinetics of 8HQ on a time scale ≤1 s and to distinguish the influence of hydrolysis rate from that of polymer conformation, we measured the velocity-dependent contact angles of sliding drops on P(MMA-co-HQSEA) films. Even on non-adaptive surfaces, the dynamic advancing contact angles increased, while the dynamic receding contact angles decreased, with increasing contact-line velocity. This effect is known and originates from viscous energy dissipation and contact-line friction.[31–33] To exclude the influence of non-adaptive energy dissipation and to consider only the changes in dynamic contact angles by surface adaptation due to the release of 8HQ and the presence of carboxyl acid groups, a non-hydrolyzed PMMA surface was used as a reference. On the PMMA surfaces, the dynamic advancing contact angles increased slightly from 76° to 82°. The dynamic receding contact angles decreased from 60° to 35° at a contact-line velocity of 0.3 m/s for a buffer solution at pH 3 [Fig. 4(a), gray].

The relevant contact time between a sliding drop and a P(MMA-co-HQSEA) surface on the advancing side is different from that on the receding side, giving us different time windows during which we could study the release kinetics. On the advancing side of a sliding drop, the relevant time scale is $\tau_{SL} = l/v$. At pH 3, the dynamic advancing contact angle on the P(MMA-co-HQSEA) surface was almost constant (~82°) and the same as the dynamic advancing contact angle of the PMMA surface for velocities >2 cm/s [Fig. 4(a), red]. Then, it decreased from 80° to 60° for velocities <2 cm/s. At a velocity U → 0, the static advancing contact angle (θ_a^∞ = 66°) was 10° lower than the one on the PMMA surface (θ_a^∞ = 76°). This result indicates that the copolymer surfaces became more hydrophilic compared to the PMMA surface after contact with an acidic drop. That means that the P(MMA-co-HQSEA) surface adapts when it contacts the sliding drop at low velocity. Fitting the velocity-dependent dynamic advancing contact angles to Eq. (3), we obtained the fitting parameter of the peripheral length divided by relaxation time [Fig. 4(b)]. Using 10 nm as the peripheral length, we calculated the relaxation times for drops at pH 3 to be around 3 μs. The relaxation time indicates the time needed to reduce the solid/liquid interfacial energies to 37% of their initial value. Varying the pH value of the sliding drop changes the critical contact-line velocities at which the dynamic advancing contact angles start to increase with velocity [Fig. 4(a) and Fig. S4, circles]. This observation indicates that the relaxation time of surface adaptation for solutions at different pH values varies. The relaxation time increased from around 1 to 5 μs when the pH value increased from 3 to 7, and when pH > 7, it saturated at around 5 μs [Fig. 4(c)]. In the
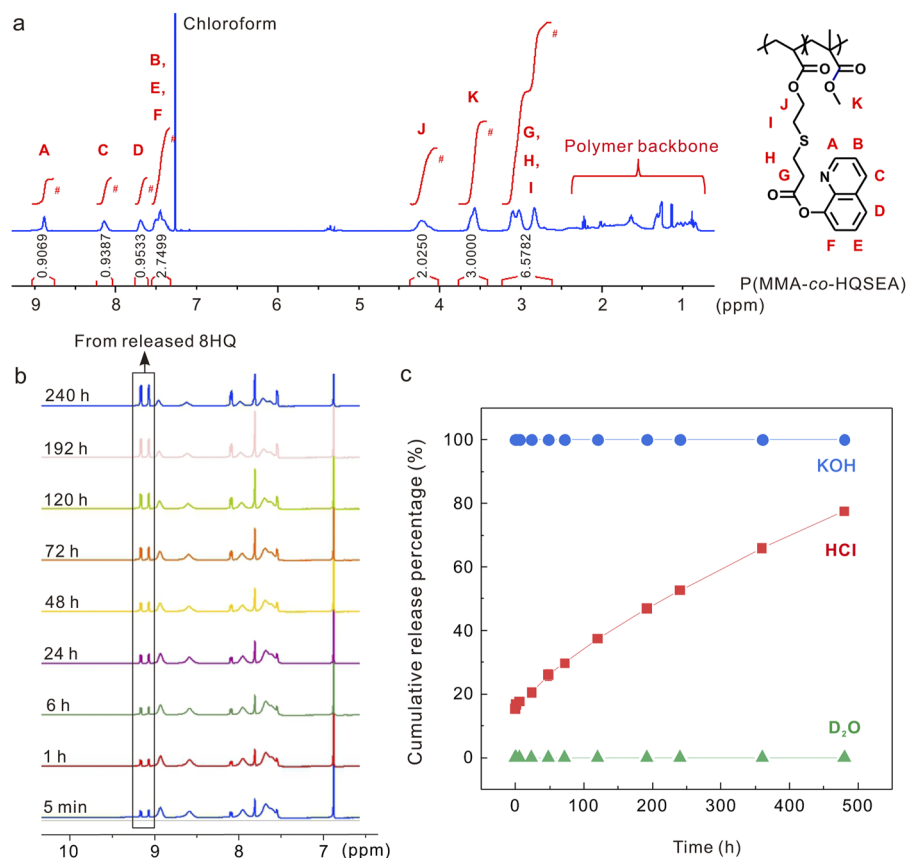
FIG. 2. Representative results of ^1H NMR measurements. (a) ^1H NMR spectrum of P(MMA-*co*-HQSEA) in CDCl$_3$. (b) Temporal evolution of the ^1H NMR spectra of a solution of P(MMA-*co*-HQSEA) in an acidic condition. (c) Temporal evolution of the cumulative release percentage of 8HQ from P(MMA-*co*-HQSEA) in neutral, acidic (pH $\approx$ 0.3), and basic (pH $\approx$ 13.7) conditions.
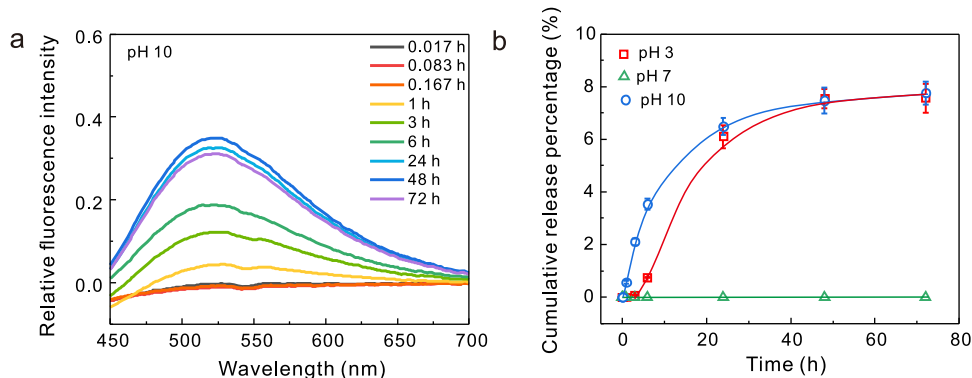
FIG. 3. The results of fluorescence microscopy measurements. (a) The typical change in the fluorescence spectrum of 8HQ over time in the solution at pH 10. (b) Temporal evolution of the release of 8HQ from P(MMA-*co*-HQSEA) solutions at pH 3, pH 7, and pH 10, measured by fluorescence spectroscopy.

literature, the time needed for protonation/deprotonation of the nitrogen atom at the quinolinyl group is microseconds.[34] Thus, one possible explanation for the adaptation of the P(MMA-*co*-HQSEA) surface could be protonation in acidic conditions, which makes the surface hydrophilic. However, the protonation effect does not explain why the P(MMA-*co*-HQSEA) surface also becomes hydrophilic in the basic condition. Based on the above-mentioned ^1H NMR measurements, an alternative explanation for the adaptation of the P(MMA-*co*-HQSEA) surface would be hydrolysis of the β-thiopropionate group on the advancing side of the drop. Hydrolysis leads to the presence of carboxyl groups after releasing 8HQ, which makes the surface more hydrophilic. In this case, the

hydrolysis time would be a few microseconds, which is surprisingly short.

The diffusion coefficient (D) for water in PMMA or in PAA polymer film is around 10^{-12} to 10^{-13} m^2/s.[35,36] The time needed for water to diffuse 10 nm deep (Δz) into a polymer film is ($\tau = \frac{\Delta z^2}{D}$) $\approx$ 10 ms, which is longer than a few microseconds.[14–16] According to the time scale, hydrolysis would only affect the outer layer of the sample on the advancing side. Lower advancing contact angles [Fig. 4(b)] and shorter relaxation time [Fig. 4(c)] of drops at pH 3 indicate that the hydrolysis reaction would be faster in the acidic solution than in the basic solution (drops at pH 10). The shorter relaxation time is consistent with the hypothesized hydrolysis
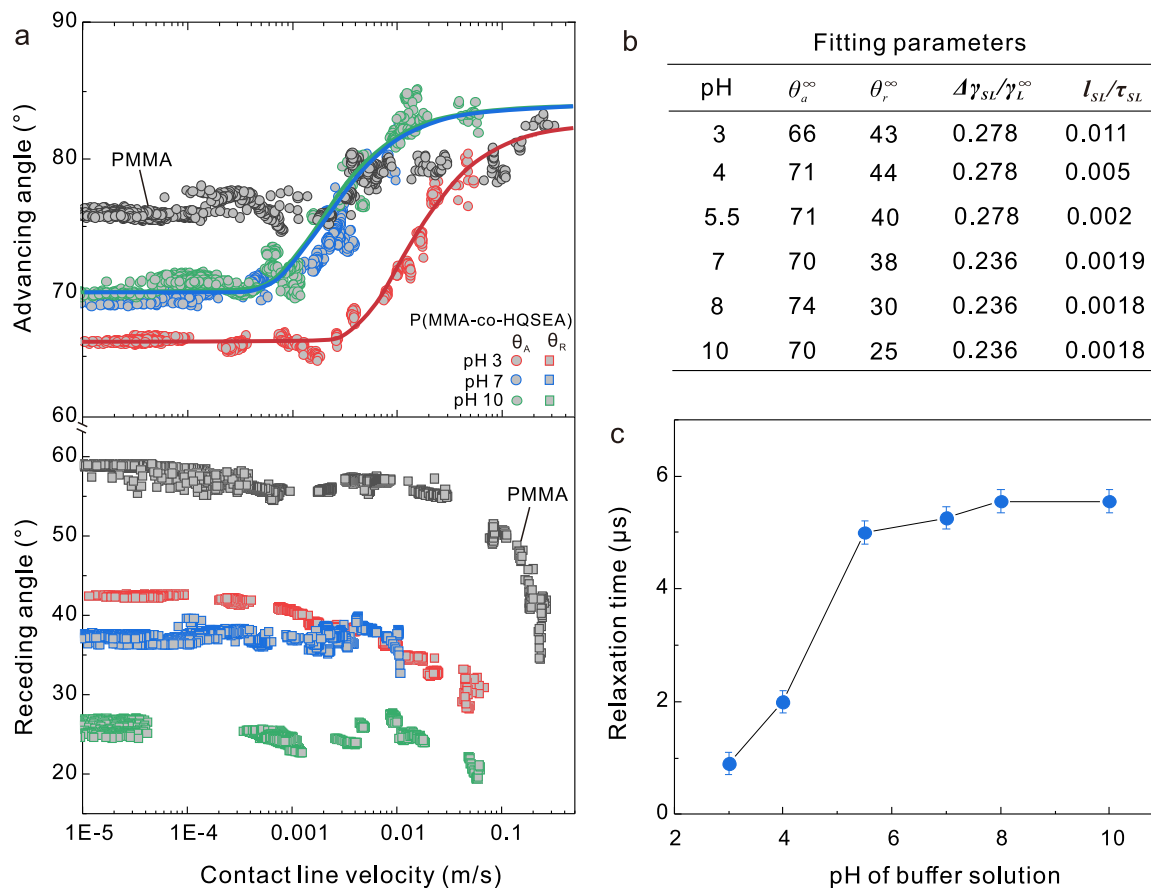
FIG. 4. The results of the dynamic contact angle measurements of pristine samples. Dynamic contact angles were measured for drops with a volume of 35 μl which slid down a tilted plate at different tilt angles. (a) Velocity-dependent contact angles of drops at different pH values, sliding down the P(MMA-*co*-HQSEA) surfaces and inert PMMA surfaces. Circles represent the dynamic advancing angles, while rectangles represent the dynamic receding contact angles. (b) Fitting parameters for the fitting curves are given in Fig. 4(a) and Fig. S4. (c) Evolution of the relaxation time with the pH values of the drops.

mechanism of the β-thiopropionate groups.[4,23] In the acidic solutions, sulfur atoms are protonated, which increases the positive charge on the carbon atom of the ester group and makes the formation of a six-membered ring intermediate easier (Fig. 5). Therefore, the hydrolysis in acidic conditions could be faster than the hydrolysis in basic conditions.

However, our observation and hypothesis that the hydrolysis reaction is faster in acidic solutions seem to contradict the lower cumulative release rate of 8HQ measured by NMR and fluorescent microscopy [Figs. 2(c) and 3(b)]. In fact, the measurements of NMR and fluorescence intensity only reveal the cumulative release rate. In addition to the hydrolysis rate, the cumulative release rate is affected by the polymer conformation. The influence of polymer conformation is visible on the receding side of the drop in our sliding drop experiments on polymer films. Sliding drops have a contact length of around 5 mm. On the receding side, the contact time between a sliding drop and a P(MMA-*co*-HQSEA) surface is in the range 0.05–500 s at a contact line velocity ranging from 0.1 to 10^{-5} m/s. Even the shortest contact time on the receding side of the drop

(50 ms) is already longer than the hypothetical hydrolysis reaction time (5 μs) on the advancing side. In addition, 50 ms is long enough to allow water to diffuse deeper into the polymer film. Thus, the 8HQ could be released from the inner layer of the film. After releasing 8HQ from the outer layer, the remaining moiety polyacrylate (PAA) is a kind of polyelectrolyte with *pKa* of 4.5.[37] In the acidic solution with pH < 4.5, the functional group (–COOH) in polymer chains is primarily un-dissociated and protonated. Because of the inter-/intra-molecular H-bonding attraction between fully protonated carboxyl groups, the liquid tends to be excluded from the polymer mesh, leading to a collapsed conformation of the polymer [Figs. 1(b) and 5]. In this case, the 8HQ in the inner layer is protected by the collapsed polymer chains. Release from the inner layer is suppressed. However, in a basic solution with pH $\gg$ 4.5, the functional group (–COOH) in the polymer chains manifests as a carboxylate anion (–COO$^-$). Because of electrostatic repulsion between neighboring chains and the same chain, the polymer chains show stretched conformation [Figs. 1(b) and 5]. As a result, the liquid penetrates the inner layer and facilitates the release of 8HQ from
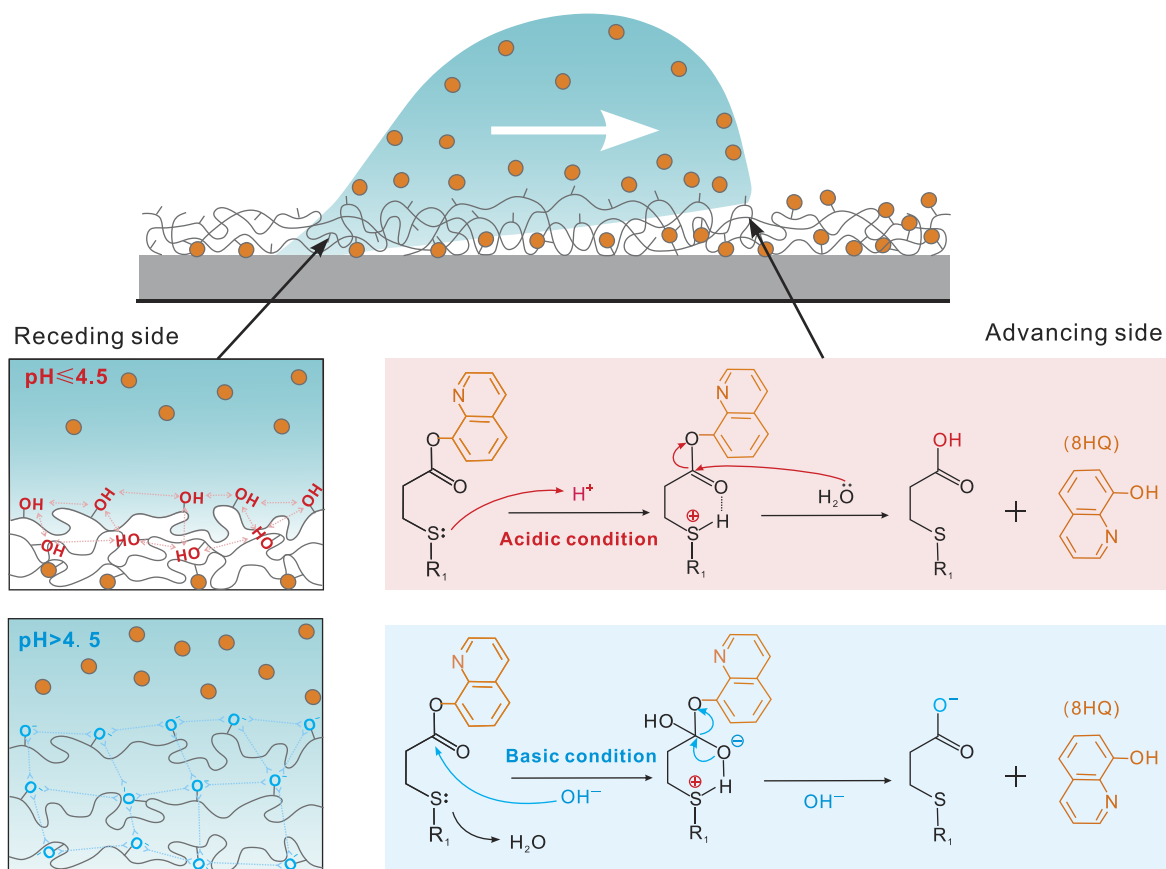
FIG. 5. The schematic of release steps of 8HQ from the P(MMA-*co*-HQSEA) surfaces when the surfaces are in contact with the drops.

the inner layer, leading to a higher cumulative release percentage and lower receding contact angles. In fact, the static receding contact angles of the low-velocity regime (<0.01 m/s) decrease with the increase of pH [Fig. 4(a) and Fig. S4 in the supplementary material, rectangles], in line with above expectations and with the cumulative released percentage measured by NMR and fluorescence microscopy.

CONCLUSIONS

In summary, the release of active agents (8HQ) from pH-responsive P(MMA-*co*-HQSEA) thin films was affected by the hydrolysis rate and polymer conformation. The release kinetics in the outer layer of thin films is dominated by the hydrolysis rate, whereas the release kinetics in the inner layer is influenced by both the hydrolysis rate and polymer conformation. After partially releasing 8HQ from the outer layer, the polymer chains assumed a collapsed state in the acidic condition, while taking on a stretched state in the basic solution. Therefore, the cumulative release rate of 8HQ is higher in the basic solution than in the acidic solution. Using velocity-dependent contact angle measurements, we were able

to study the fast-release kinetics at a time scale <1 s, which paves the way to release kinetics at very short time scales.

SUPPLEMENTARY MATERIAL

The supplementary material includes the surface morphology characterization by scanning force microscopy; ^{1}H NMR spectra of P(MMA-*co*-HQSEA) in the acidic, neutral, and basic conditions; calibration curves of 8HQ concentration in solutions of pH 3, pH 7, and pH 10; velocity-dependent dynamic contact angles of drops at pH 4, pH 5.5, and pH 8 on the P(MMA-*co*-HQSEA) surfaces, and velocity-dependent dynamic contact angles of a citrate buffer solution and a phosphate buffer solution at pH 3 on the P(MMA-*co*-HQSEA) surfaces.

ACKNOWLEDGMENTS

AUTHOR DECLARATIONS

Conflict of Interest

The authors have no conflicts to disclose.

Author contributions

X.L. and K.A.-A. contributed equally to this work. R.B. and D.C. conceived and supervised the project. X.L. and K.A.-A. planned, conducted the experiments, and analyzed the data. All the authors discussed, reviewed, wrote, and approved the manuscript.

Xiaomei Li: Data curation (equal); Investigation (equal); Writing – original draft (equal). **Krisada Auepattana-Aumrung**: Data curation (equal); Investigation (equal); Writing – original draft (equal). **Hans-Jürgen Butt**: Project administration (equal); Writing – review & editing (equal). **Daniel Crespy**: Conceptualization (equal); Writing – review & editing (equal). **Rüdiger Berger**: Conceptualization (lead); Writing – review & editing (equal).

DATA AVAILABILITY

The data that support the findings of this study are available within the article and its supplementary material.

REFERENCES

[1] G. Kocak, C. Tuncer, and V. Bütün, Polym. Chem. **8**, 144 (2017).
[2] N. Dararatana, F. Seidi, and D. Crespy, Polym. Chem. **11**, 4723 (2020).
[3] Y. Xue et al., Chem. Soc. Rev. **50**, 4872 (2021).
[4] F. Seidi, R. Jenjob, and D. Crespy, Chem. Rev. **118**, 3965 (2018).
[5] F. Seidi et al., Chem. Soc. Rev. **51**, 6652 (2022).
[6] P. Phoungtawee et al., ACS Macro Lett. **10**, 365 (2021).
[7] K. Auepattana-Aumrung, T. Phakkeeree, and D. Crespy, Prog. Org. Coat. **163**, 106639 (2022).
[8] O. Azzaroni, A. A. Brown, and W. T. S. Huck, Adv. Mater. **19**, 151 (2007).
[9] F. Zhou and W. T. S. Huck, Chem. Commun. **48**, 5999 – 6001 (2005).
[10] Q. Wei et al., Macromolecules **46**, 9368 (2013).
[11] T. Chen et al., Prog. Polym. Sci. **35**, 94 (2010).
[12] N. Kamaly et al., Chem. Rev. **116**, 2602 (2016).
[13] N. Dararatana et al., Polym. Chem. **11**, 1752 (2020).
[14] H.-J. Butt et al., Langmuir **34**, 11292 (2018).
[15] X. Li et al., Langmuir **37**, 1571 (2021).
[16] X. Li et al., Macromol. Rapid Commun. **43**, 2100733 (2022).
[17] X. Li et al., Nat. Phys. **18**, 713 – 719 (2022).
[18] K. Dan and S. Ghosh, Angew. Chem. **125**, 7441 (2013).
[19] S. Lv et al., J. Controlled Release **194**, 220 (2014).
[20] M. R. Molla et al., Biomacromolecules **15**, 4046 (2014).
[21] P. Pramanik et al., Macromol. Rapid Commun. **37**, 1499 (2016).
[22] B. Klahan, F. Seidi, and D. Crespy, Macromol. Chem. Phys. **219**, 1800392 (2018).
[23] N. Kongkatigumjorn et al., Chem. Mater. **34**, 2842 (2022).
[24] F. Chiter et al., Phys. Chem. Chem. Phys. **17**, 22243 (2015).
[25] N. Dararatana, F. Seidi, and D. Crespy, ACS Appl. Mater. Interfaces **10**, 20876 (2018).
[26] K. Auepattana-Aumrung and D. Crespy, Chem. Eng. J. **452**, 139055 (2023).
[27] I. H. Ali, I. A. Khalil, and I. M. El-Sherbiny, ACS Appl. Mater. Interfaces **8**, 14453 (2016).
[28] B. J. Crielaard et al., Angew. Chem. **124**, 7366 (2012).
[29] E. Bardez et al., J. Phys. Chem. B **101**, 7786 (1997).
[30] H. Zhang et al., Org. Lett. **7**, 4217 (2005).
[31] H.-J. Butt et al., Curr. Opin. Colloid Interface Sci. **59**, 101574 (2022).
[32] J. H. Snoeijer and B. Andreotti, Annu. Rev. Fluid. Mech. **45**, 269 (2013).
[33] T. D. Blake, J. Colloid Interface Sci. **299**, 1 (2006).
[34] S.-I. Lee and D.-J. Jang, J. Phys. Chem. **99**, 7537 (1995).
[35] A. Arce et al., Phys. Chem. Chem. Phys. **6**, 103–108 (2004).
[36] P. P. Roussis, J. Membr. Sci. **15**, 141 (1983).
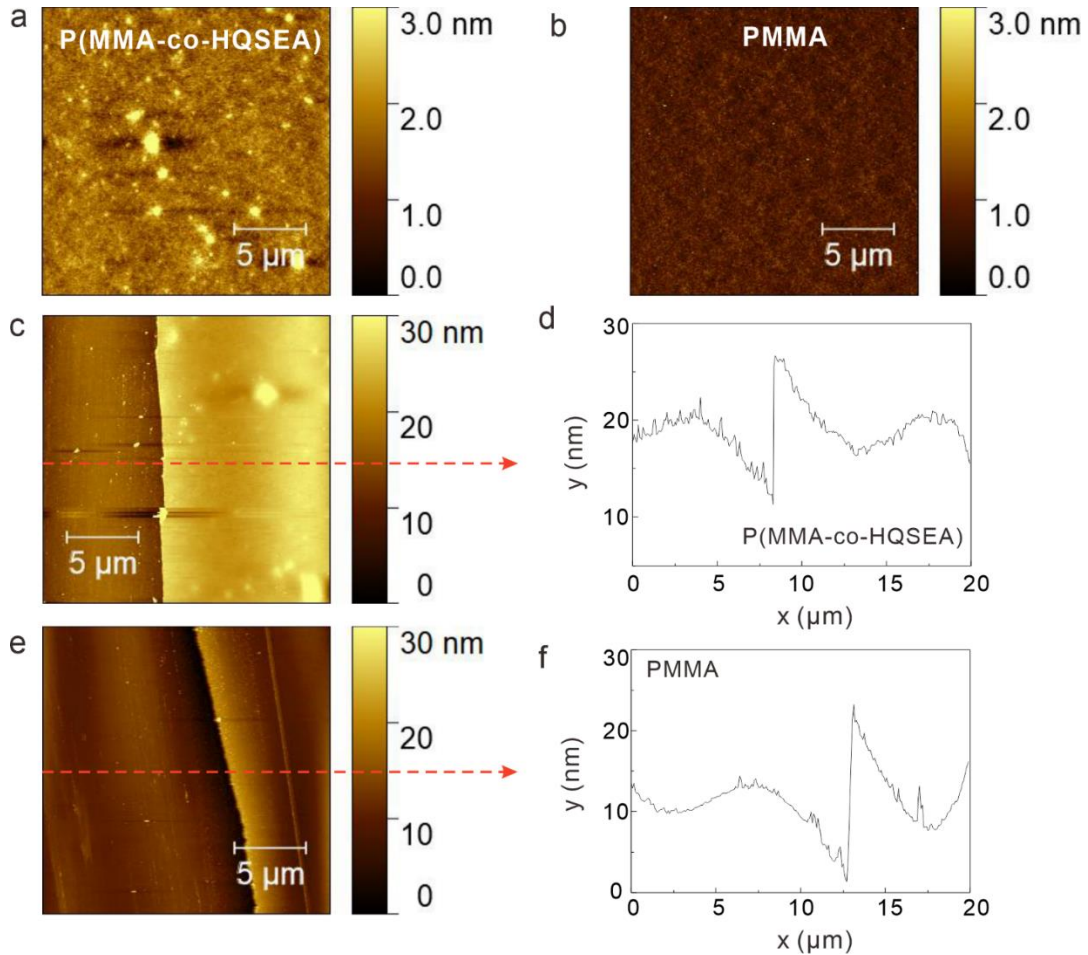[37] A. S. Michaels and O. Morelos, Ind. Eng. Chem. **47**, 1801 (1955).

Figure S1. *Surface roughness and film thickness of the P(MMA-co-HQSEA) surface and the PMMA surface measured by AFM. (a) The topography of the P(MMA-co-HQSEA) surface with an average RMS of 0.4±0.05 nm in an area of 20 μm x20 μm. (b) The topography of the PMMA surface with an average RMS of 0.2±0.05 nm in an area of 20 μm x 20 μm. (c, d) The thickness of the P(MMA-co-HQSEA) surface is 15±2 nm. (e, f) The thickness of the PMMA surface is 18±2 nm.*
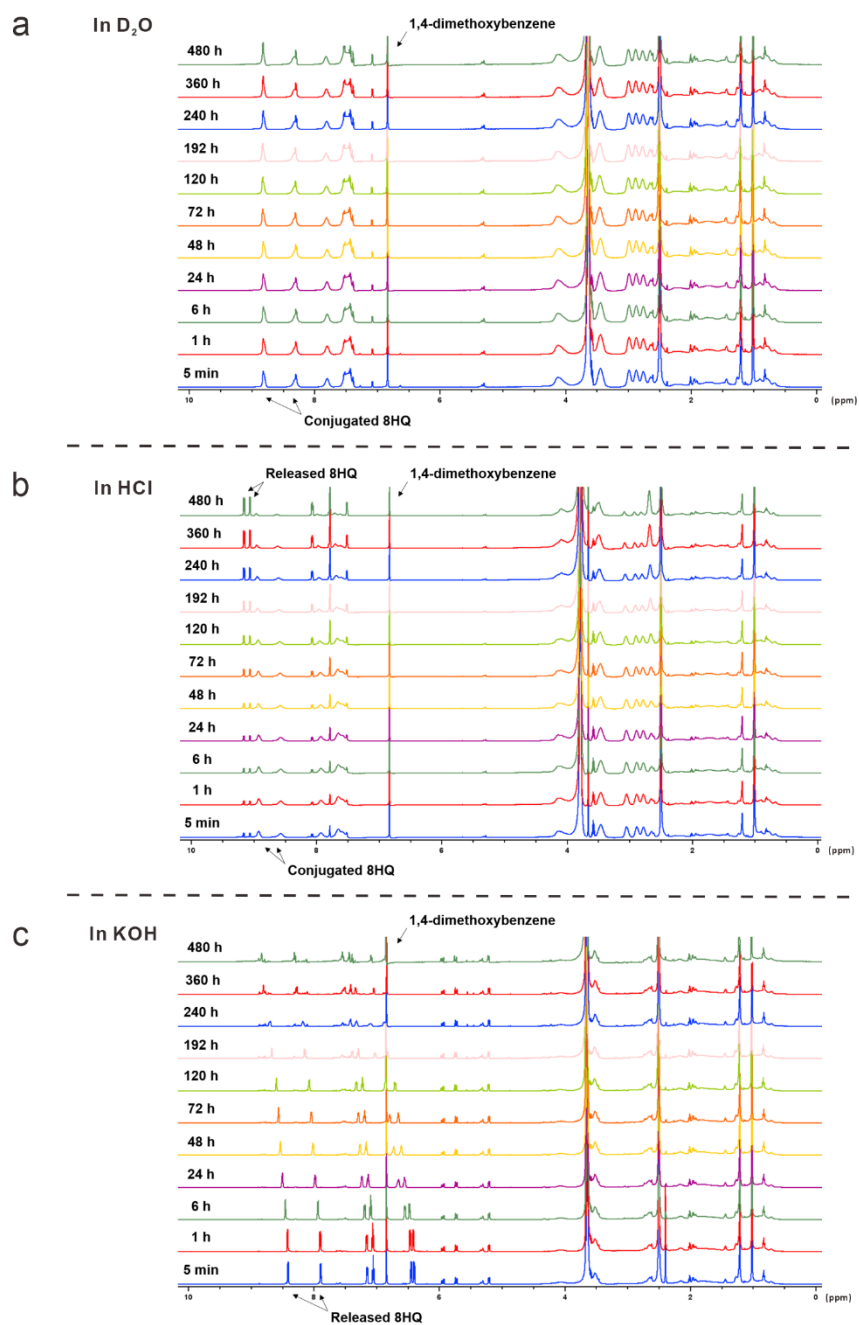
Figure S2. *The stacked ^{1}H NMR spectra of P(MMA-co-HQSEA) in the neutral (a), acidic (b), and basic conditions (c) at different time intervals.*
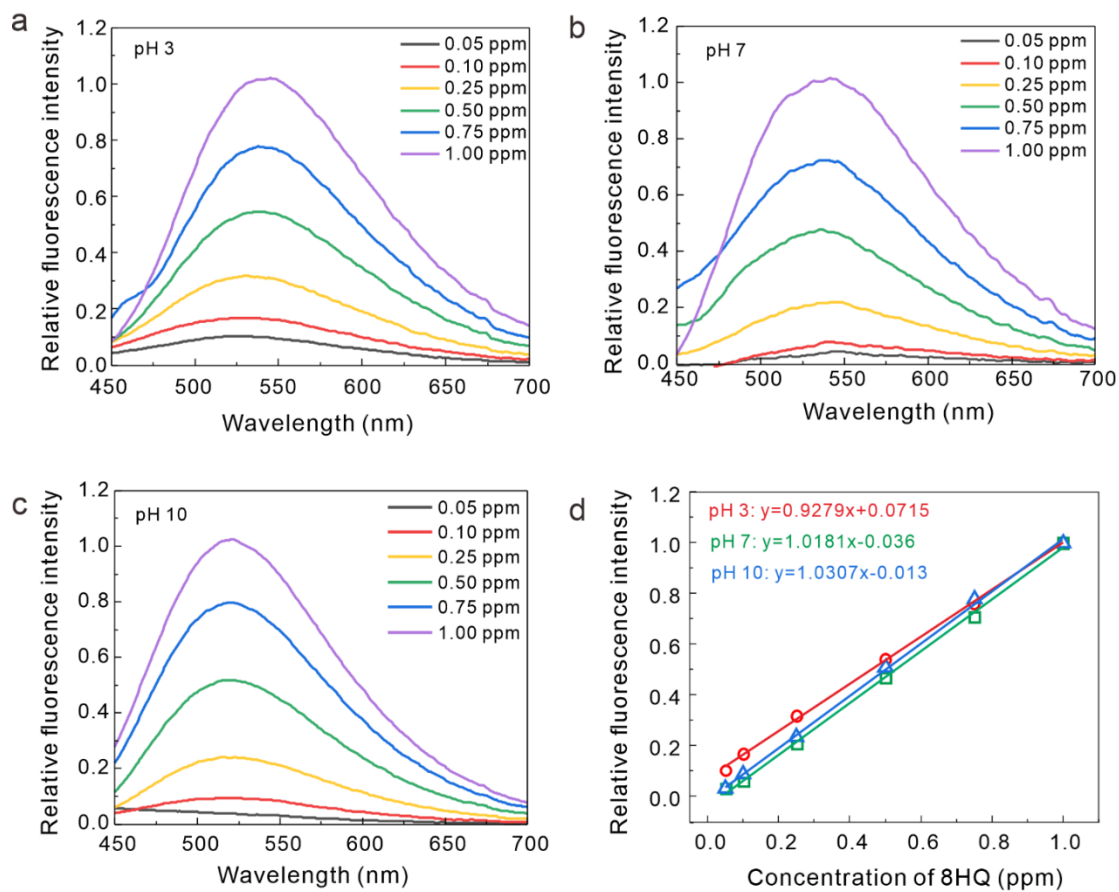
Figure S3. *The calibration curves of 8HQ in solutions of pH 3, 7, and 10. (a, b, and c) The fluorescence spectrums of 8HQ with concentration from 0.05 ppm to 1 ppm in solutions of h pH 3, pH 7, and pH 10. (d) The calibration curves in buffer solution with different pH values, which were calculated based on the fluorescence intensity shown in the (a-c).*
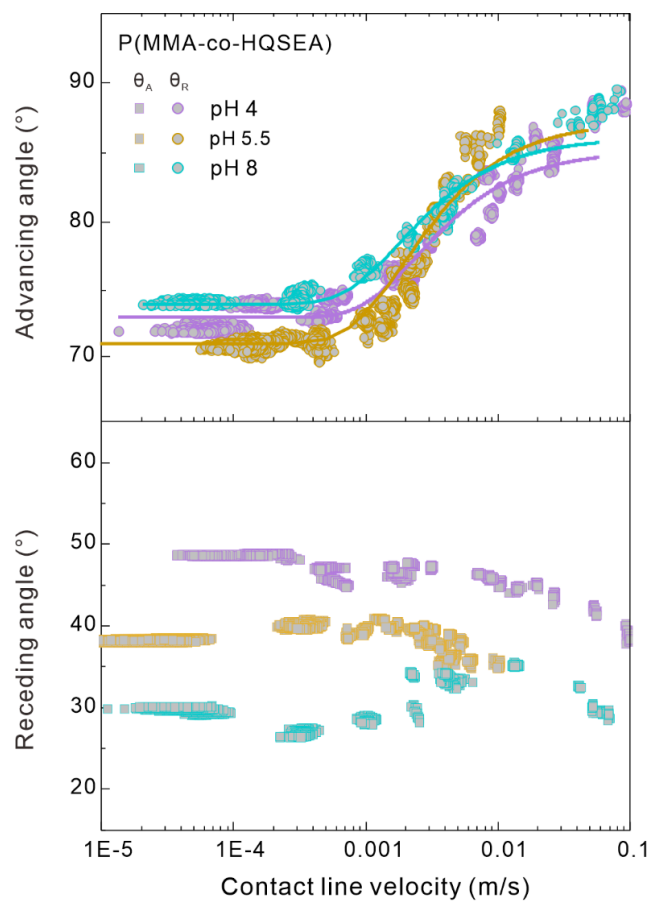
Fitting parameters				
pH	θ_a^∞	θ_r^∞	$\Delta\gamma_{SL}/\gamma_L^\infty$	l_{SL}/τ_{SL}
4	71	44	0.278	0.005
5.5	71	40	0.278	0.002
8	74	30	0.236	0.0018

Figure S4. *Velocity-dependent dynamic contact angles of drops with buffer solutions of pH 4, pH 5.5, and pH 5 sliding on the P(MMA-co-HQSEA) surfaces. Circles represent the dynamic advancing angles while rectangles represent the dynamic receding contact angles.*

74
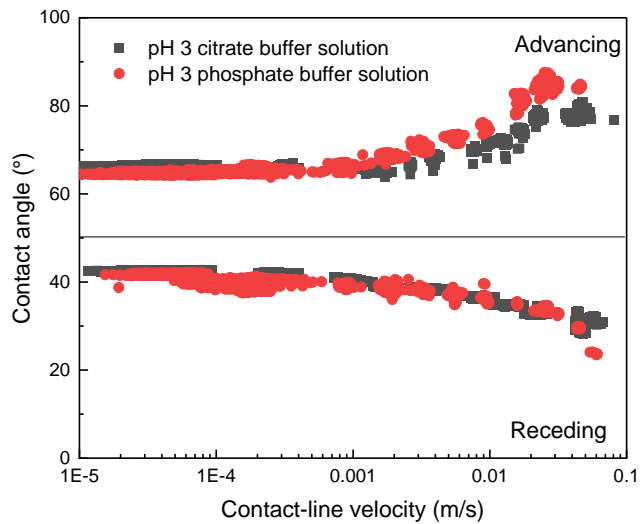
Figure S5. *Dynamic advancing and receding contact angles versus contact-line velocities for drops of a citrate buffer solution and a phosphate buffer solution at pH 3 on the P(MMA-co-HQSDEA) surfaces.*

2.4. X. Li *et al. Nature Physics*, 2022

Spontaneous charging affects the motion of sliding drops

Xiaomei Li[1], Pravash Bista[1], Amy Z. Stetten[1], Henning Bonart[1,2], Maximilian T. Schü[2], Steffen Hardt[2], Francisco Bodziony[3], Holger Marschall[3], Alexander Saal[1], Xu Deng[4], Rüdiger Berger[1], Stefan A. L. Weber[1,5] and Hans-Jürgen Butt[1]

1. Max Planck Institute for Polymer Research, Mainz, Mainz, Germany
2. Institute for Nano- and Microfluidics, Technische Universität Darmstadt, Darmstadt, Germany
3. Computational Multiphase Flows, Technische Universität Darmstadt, Darmstadt, Germany
4. Institute of Fundamental and Frontier Sciences, University of Electronic Science and Technology of China, China
5. Institute of Physics, Johannes Gutenberg University, Mainz, Germany

Author contributions:

Xiaomei Li prepared the samples, performed the tilted-plate experiments and analysed the data. Xiaomei Li, Alexander Saal and Rüdiger Berger designed the tilted-plate setup. Pravash Bista and Amy Z. Stetten measured the drop charges. Hans-Jürgen Butt and Stefan Weber numerically calculated the electrostatic force on a drop. Francisco Bodziony and Holger Marschall carried out the numerical diffuse-interface simulations of drop motion. Stefan Weber, Steffen Hardt, Maximilian Schü and Hans-Jürgen Butt derived the analytical theory. Hans-Jürgen Butt derived the concept of extracting the electrostatic force from the equation of motion. All the authors discussed and interpreted the results and wrote the manuscript.

Check for updates

OPEN

Spontaneous charging affects the motion of sliding drops

Xiaomei Li [1], Pravash Bista [1], Amy Z. Stetten[1], Henning Bonart [1,2], Maximilian T. Schür [2],
Steffen Hardt[2], Francisco Bodziony[3], Holger Marschall[3], Alexander Saal[1], Xu Deng [4], Rüdiger Berger [1],
Stefan A. L. Weber [1,5 ✉] and Hans-Jürgen Butt [1 ✉]

Water drops moving on surfaces are not only an everyday phenomenon seen on windows but also form an essential part of many industrial processes. Previous understanding is that drop motion is dictated by viscous dissipation and activated dynamics at the contact line. Here we demonstrate that these two effects cannot fully explain the complex paths of sliding or impacting drops. To accurately determine the forces experienced by moving drops, we imaged their trajectory when sliding down a tilted surface, and applied the relevant equations of motion. We found that drop motion on low-permittivity substrates is substantially influenced by electrostatic forces. Our findings confirm that electrostatics must be taken into consideration for the description of the motion of water, aqueous electrolytes and ethylene glycol on hydrophobic surfaces. Our results are relevant for improving the control of drop motion in many applications, including printing, microfluidics, water management and triboelectric nanogenerators.

Water drops moving on surfaces are a common phenomenon. The lateral adhesion of drops can be a nuisance; for example, nature developed sophisticated surface structures to keep feathers, fur or plant leaves dry. Science and technology have adopted these surface modifications to keep drops from sticking on textiles, in microfluidics, or to keep window screens and glasses clear in the rain[1–4]. In other applications, the resistance of sessile drops to sliding motion is essential, for example, in coating, painting, flotation and deposition of insecticides and herbicides[5,6]. Still, a full description of forces acting on moving drops remains elusive. Closing this gap of knowledge has become more imperative due to the recent endeavour to generate electricity from moving drops[7–15]. This direct form of harvesting hydrovoltaic energy without moving parts promises to expand the range of hydroelectricity generation to small-scale devices applicable in remote and off-grid areas, or as emergency generators. The efficiency of energy conversion, however, is still too low. Here the poor understanding of moving drops still hampers the development of useful hydrovoltaic generators.

In accepted studies in the literature, drop motion is determined by viscous dissipation due to hydrodynamic flow in the drop and by activated processes, in which the contact line has to overcome local energy barriers leading to contact-line friction[6,16–22]. The viscous force of a sliding drop is commonly split in two components. Both are, to the first order, proportional to slide velocity U. One component comes from the viscous dissipation in the bulk, F_b, and the other from the wedge of the drop, F_w (refs. [23–25]). Viscous dissipation in the wedge and contact-line friction change the macroscopically observed advancing and receding contact angles, namely, $\Theta_a(U)$ and $\Theta_r(U)$, respectively. As a result, the capillary force acting on a sliding drop[4,26,27]

$$F_c = w\gamma k \left(\cos \Theta_r - \cos \Theta_a\right) \tag{1}$$

depends on the velocity. Here w is the width of the contact area of the drop, γ is the surface tension of the liquid and $k \approx 1$ is a geometrical factor that depends on the detailed shape of the drop[24,27–30]. Bulk viscous dissipation, which is much lower than viscous dissipation in the wedge, can be approximated by $F_b \approx \eta \frac{\pi l w}{2H} U$ (Supplementary Section 1). Here η denotes the dynamic viscosity of the liquid, l is the length of the drop and H is its height.

Here by a simple tilted-plate experiment, we demonstrate that the motion of drops cannot be accurately predicted by these forces. In a tilted-plate experiment, a defined gravitational force $F_g = mg\sin\alpha$ is acting in the lateral direction[21,25,31–36]. Here m is the mass of the drop, $g = 9.81$ m s^{-2} is the standard acceleration of gravity and α is the tilt angle.

Two observations demonstrate that the trajectories of the sliding drops require more than hydrodynamics and activated processes. First, on surfaces with identical surface chemistry but different substrate conductivities and substrate thicknesses, we see different average velocities. For example, in Fig. 1a–d, we show surfaces coated with perfluorooctadecyltrichlorosilane (PFOTS): a silicon wafer with ~2 nm oxide layer, a 1-mm-thick SiO$_2$ plate and a 5-mm-thick SiO$_2$ plate. The first drop on each surface had an average velocity of 0.25 m s^{-1} (Fig. 1a), 0.18 m s^{-1} (Fig. 1b) and 0.06 m s^{-1} (Fig. 1c), respectively. When substrate conductivity was higher than that in the wafer, we observed even faster drop motion. Gold surfaces coated with a monolayer of perfluorodecanethiol (Fig. 1e) and Teflon (Fig. 1f) films have surface chemistry comparable to PFOTS, yet with average velocities of 0.42 and 0.48 m s^{-1}, respectively. Water drops move faster on these surfaces than on PFOTS-coated SiO$_2$ surfaces. This simple experiment alone demonstrates that there is an important contribution missing in the description of drop motion.

Our second piece of evidence is that for a series of drops, sliding speeds become dependent on the drop number and thus dependent

[1]Max Planck Institute for Polymer Research, Mainz, Germany. [2]Institute for Nano- and Microfluidics, Technische Universität Darmstadt, Darmstadt, Germany. [3]Computational Multiphase Flows, Technische Universität Darmstadt, Darmstadt, Germany. [4]Institute of Fundamental and Frontier Sciences, University of Electronic Science and Technology of China, Chengdu, China. [5]Institute of Physics, Johannes Gutenberg University, Mainz, Germany. ✉e-mail: webers@mpip-mainz.mpg.de; butt@mpip-mainz.mpg.de
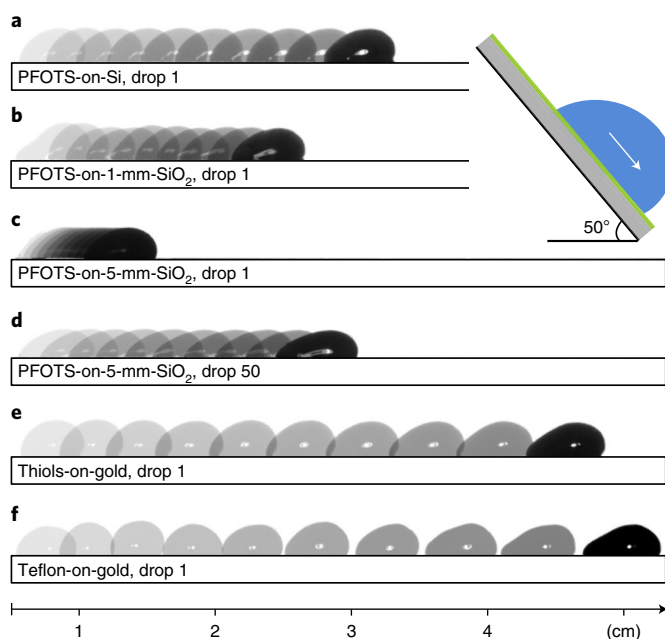
Fig. 1 | Movement of drops on different surfaces. Water drops (33 µl) sliding down a plate tilted by 50° after detaching from a grounded electrode and imaged every 10 ms with a side-view camera.

on surface history. For example, the drop 50 sliding down a PFOTS-on-5-mm-SiO$_2$ plate is faster than the drop 1 (Fig. 1d). The surface chemistries of the three samples mentioned are identical and thus one expects identical capillary and viscous forces; however, the sliding speed of the drops varied by more than a factor of two, both between samples and between successive drops.

We believe that one logical explanation for this missing force is electrostatics. It is known that on bulk Teflon samples, fluorinated insulators and superhydrophobic surfaces, sliding water drops deposit negative electric charges, whereas the drops acquire a positive charge[8,9,11,37–42]. It is commonly believed that the surface charges behind sliding water drops are remnants of interfacial charges generated spontaneously at the water–solid interface[8,11,37,43,44]. Hydrophobic surfaces usually charge negatively in water. The reason for this charge is still debated[45]. The most popular explanation is an enrichment of hydroxyl ions at the interface. Alternative hypotheses speculate the origin of interfacial charge in the asymmetry of the hydrogen-bond network[46], adsorption of bicarbonate/carbonate ions[47] or the flow of electrons from water to the polymer[15].

Surface charges generate an electric field in the air above the surface. A charge q on top of an infinitely extending dielectric half-space with a relative permittivity ε_S generates an electric field

$$E = \frac{q}{2\pi\varepsilon_0 (\varepsilon_S + 1) r^2}. \qquad (2)$$

Here, ε_0 is the vacuum permittivity and r is the distance from the charge. If we now place a charged drop atop this charged surface, the drop will experience a Coulomb force that scales with $1/(1 + \varepsilon_S)$.

Given the importance of moving drops in our daily lives, we will address the following questions: is it possible to quantitatively measure electrostatic forces on moving drops? How? Can electrostatic forces explain the measured drop trajectories? Specifically, why and how does the substrate influence drop motion? Why is the motion of a drop influenced by previous drops? To answer these questions and to directly measure the forces acting on moving drops, we

developed a new method to analyse tilted-plate experiments (Fig. 2a and Supplementary Section 2).

We prepared smooth, hydrophobic surfaces with receding and advancing contact angles ranging within 77–110° and 93–122°, respectively (Fig. 2b and Supplementary Section 3). All the surfaces had a root-mean-squared roughness of ≤1 nm, as determined by scanning force microscopy (SFM; Supplementary Section 4). To find out how strong the electrostatic forces are, we varied the substrate and its thickness d with respect to a grounded metal back-electrode. We chose SiO$_2$ plates ($\varepsilon_S = 3.7$; Supplementary Section 5) as a low-permittivity substrate and Si wafers with only a natural oxide layer as a high-permittivity sample ($\varepsilon_S = 11.7$; data from the supplier, Silicon Materials). The stability of the coatings was confirmed by measuring the drop velocity, advancing and receding contact angles, and morphology before and after 1,000 water drops sliding down the reference surfaces. None of the parameters had changed (Supplementary Section 6). In the presence of the grounded metal back-electrode, the field is screened by image charges. The distance to the grounded metal layer defines the screening length.

To describe the results and analysis, we first concentrate on PFOTS-coated samples (Fig. 3a and Supplementary Section 7). For the PFOTS-on-Si sample, the first, second and subsequent drops showed similar velocity profiles (Fig. 3a, green symbols). In contrast to common expectation, on 1-mm- and 5-mm-thick SiO$_2$ substrates (Fig. 3a, blue and red symbols), the velocity profiles of the first, second and subsequent drops were distinctly different, although all the samples have similar contact angles. First, the velocities tended to be lower on SiO$_2$ than the silicon wafer. Second, often, rather complex traces occurred. Although complex, these traces are systematic and reproducible. For example, on the PFOTS-on-5-mm-SiO$_2$ sample, the first drop shows a monotonically increasing velocity (Fig. 3a, red squares). However, for drop number 100 (Fig. 3a, red stars), the velocity increased for the first 3 cm, but then decreased again.

We draw two conclusions. First, the drop motion is not simply determined by viscous dissipation and activated dynamics at the contact line. Second, there is a fundamental difference between static and dynamic wetting. The static shape of a drop is largely determined by the properties of the top-most 1 nm of the surface; the substrate underneath has little influence (except in the case of strong externally applied electric fields such as in electrowetting[48]). In contrast, the dynamic properties such as the sliding speed are influenced by the substrate down to a thickness of the order of 1 mm.

To quantify the extra force, we analyse the equation of the motion of a drop:

$$m^* \frac{dU}{dt} = mg \sin\alpha - F_r(U) - F_e^n(U, L). \qquad (3)$$

In the acceleration term ($m^* \frac{dU}{dt}$), we take into account the rolling components in drop motion[6,16,21,36,49,50]. Therefore, we used the effective mass m^*, which was determined by the direct numerical diffuse-interface simulations of the flow pattern inside sliding drops (Supplementary Section 8). These simulations gave an estimate of $m^*/m = 1.05$ as a good mean value for the velocity range covered by our experiments.

All the forces acting on the drop in the absence of electrostatic effects are summarized in the reference force, $F_r(U)$. The reference force depends on the velocity U but not on the slide length L, because the surfaces are homogeneous. For the extra force F_e, the subscript 'e' indicates 'extra' or presumably 'electrostatic'. It may depend on the velocity, slide length and drop number n.

To obtain the reference force, we assume that on Si wafers, electrostatic forces are negligible. This assumption is in line with the
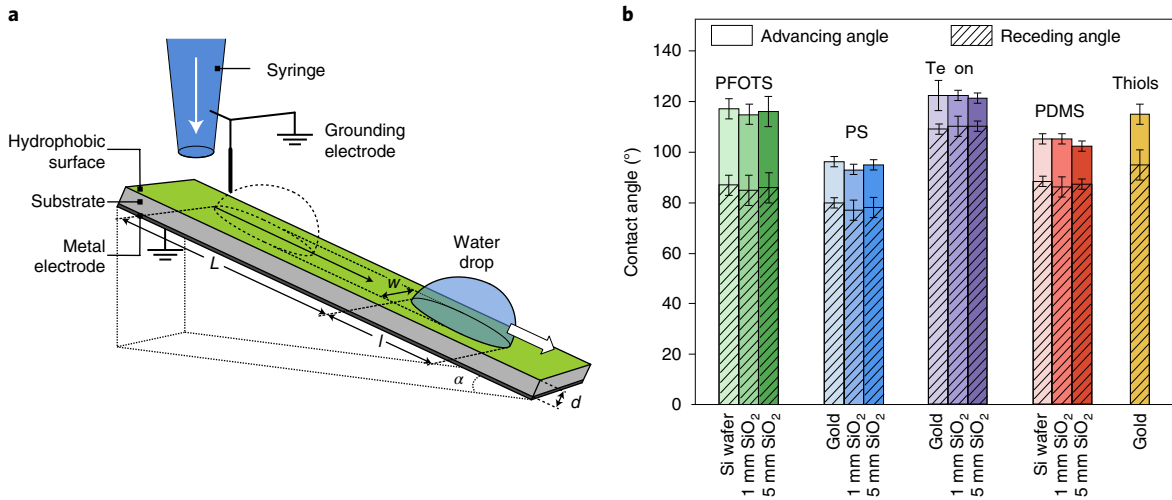
Fig. 2 | Experimental design. a, Schematic of the experimental setup (Supplementary Section 2). **b**, Hydrophobic samples under investigation. The 'static' advancing and receding contact angles Θ_a^0 and Θ_r^0 were measured with sessile water drops as they slowly inflated and deflated, and imaged in the side view (Supplementary Section 3). The errors arise due to repeated measurements on different positions and samples.

fact that no differences in velocity were observed between successive drops (Fig. 3a). With equation (3), we obtain $F_r = mg\sin\alpha - m^*\frac{dU}{dt}$. The acceleration is obtained from the measured velocity traces, $U(t)$. The reference forces increase linearly in the velocity range up to $0.4\,\text{m s}^{-1}$ (Fig. 3b). This increase is correlated with an increase in length and decrease in width of the drops (Supplementary Section 9).

By inserting the respective drop widths as well as the advancing and receding contact angles into equation (1), we calculated the capillary force with $k = 1$ (Supplementary Fig. 9, red symbols). The capillary forces, which include wedge viscous forces (Supplementary Section 1), make up for most of the measured reference forces (Supplementary Fig. 9, black symbols). The bulk viscous forces (Supplementary Fig. 9, blue symbols) contribute less than 10% to the reference force (Supplementary Section 10).

With the reference force $F_r(U)$ obtained from the experiments on Si wafers, we use $U(t)$ curves measured on SiO_2 to calculate the extra force using equation (3) as $F_e^n = mg\sin\alpha - m^*\frac{dU}{dt} - F_r$ (Fig. 3c and Supplementary Section 11). These extra forces are substantial, they depend on the drop number, n and they show complex distance dependency. Usually, the first and second drops experienced a strong force of 60–100 μN (up to 50% of the reference force), which then decayed over the observation range of 4 cm. The force is positive, hindering the drop motion. After around five drops, the initially high, decaying force gradually changed to an initially low, increasing extra force. Drop 100 showed almost an inverted profile of drop 1: starting at around 30 μN, it typically increased to 60 μN after 4 cm slide length.

To determine the origin of the extra force, we measured the drop charges (Supplementary Section 12). In agreement with earlier results[39], on SiO_2 substrates, the drops gained a positive charge and left behind a negative surface charge. For the first drop, the charge was typically $Q_1 = 1.0$–1.5 nC on 1 mm and 5 mm SiO_2 (Fig. 3d and Supplementary Table 2). It decreased with subsequent drops until it reached a saturation value of the order of 0.4 nC. In contrast, on silicon wafers, the drop charges were typically 5–10 times lower. We used these values of drop charges to model the electrostatic force.

Modelling the electrostatic force allowed us to explain the shapes and magnitudes of the measured extra force. We derive the electric field by integrating the field strength (equation (2)) for the surface charge density $\sigma_n(x)$. We then multiply it with the drop charge $Q_n(x)$ to obtain the electrostatic force of the nth of drop:

$$F_e^n(L) = -\frac{wQ_n(L)}{2\pi\varepsilon_0(\varepsilon_S+1)}$$
$$\left(\int_0^L \frac{\sigma_n(x)}{(L+a-x)^2}dx - \int_{L+l}^{L_{end}} \frac{\sigma_{n-1}(x)}{(x-L-a)^2}dx\right). \quad (4)$$

Here, x is a coordinate along the path of the drop itself and the path of previous drops. The first integral represents the interaction of the drop with surface charges behind the drop. The second integral represents the interaction with charges deposited by previous drops ahead of the current drop (Supplementary Section 13). The parameter a characterizes the centre position of the charge of the drop; it is the horizontal distance to the rear rim (Supplementary Section 13 and Supplementary Fig. 13). Its value was obtained from numerical calculations of the electric-field distribution and electrostatic force (Supplementary Section 13).

We use a previously derived model to obtain plausible expressions for $\sigma_n(x)$ and $Q_n(x)$ (ref. [39]). Briefly, surface charges behind a sliding drop are the remnants of interfacial charges spontaneously generated at the water–solid interface[8,11,37,43] (Fig. 4a). Hydrophobic surfaces usually charge negatively in water, probably by the adsorption of hydroxyl ions. Some of these charges fail to neutralize at the rear of the sliding drop and remain on the surface. As a result, the drop becomes positively charged. However, the transfer of charges to the solid–air surface decreases with an increasing drop potential[39]. As a result, the density of the deposited surface charges decreases with distance: $\sigma_1 = \sigma_0 e^{-x/\lambda}$. Here σ_0 is the initial surface charge density and λ is the decay length (Supplementary Section 14). In addition, we allow the neutralization of surface charges with time. It is not yet clear which processes dominate surface neutralization, for example, flow of electrons through the grounded substrate or via the surface, ions in the air, or the ejection of electrons[8,42]. Neutralization is characterized by an exponential process with a relaxation time constant τ of typically 10 s. Based on the independent parameters σ_0, λ and τ (Supplementary Section 12 and Supplementary Table 2), the surface charge density can be written as a function of the position and drop number.

Using equation (4), we obtain an analytical expression for the electrostatic force on the first drop (equation (14) in the Supplementary Information) and for higher drop numbers ($n \to \infty$; equation (21) in the Supplementary Information). The calculated electrostatic force yields the same order of magnitude as the experimental
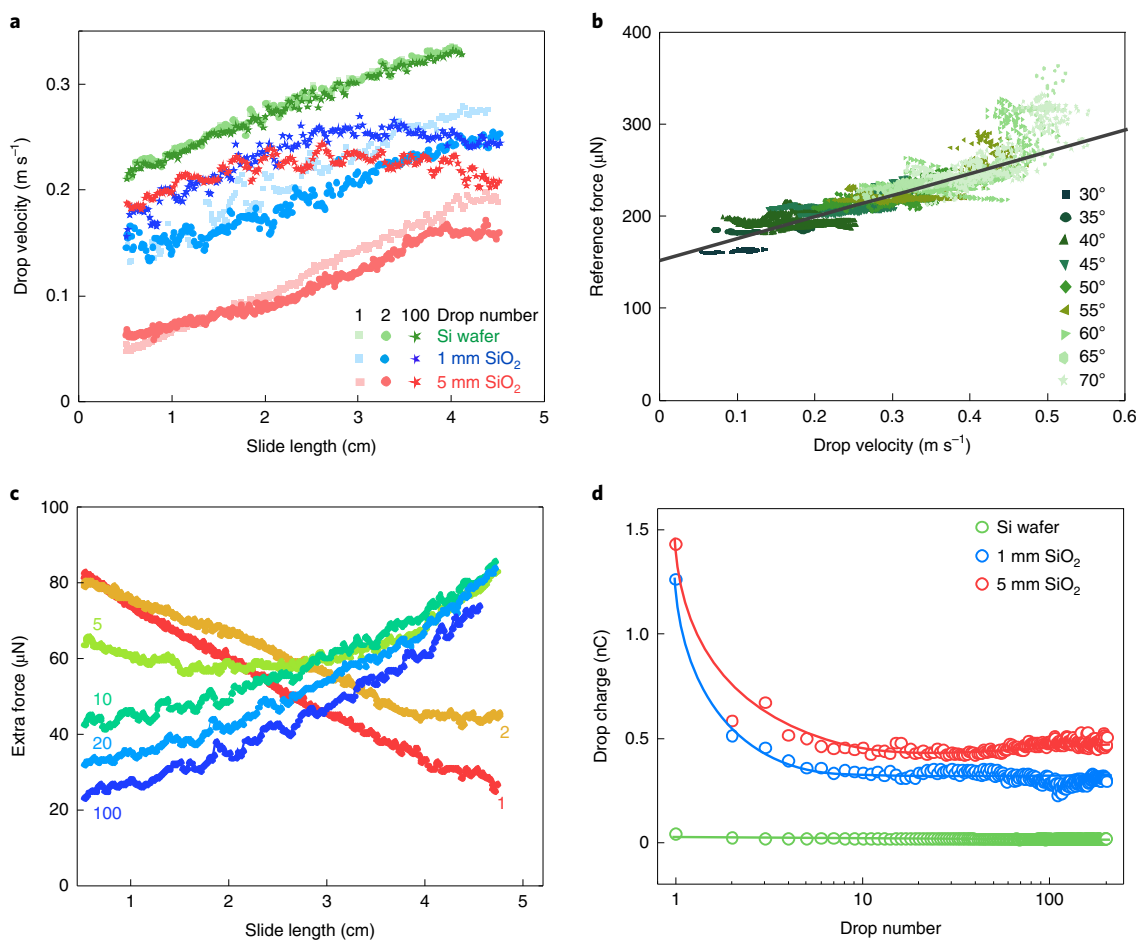
Fig. 3 | Results obtained with 33 µl water drops on PFOTS-coated samples. a, Velocity versus slide length for PFOTS-on-Si (green symbols), 1 mm SiO_2 (blue) and 5 mm SiO_2 (red) sliding down at an inclination of $\alpha = 50°$. Supplementary Section 7 provides data for other tilt angles. **b**, Reference forces measured on four PFOTS-on-Si samples. Fitting the results for $U \leq 0.4$ m s⁻¹ (grey lines) led to $F_r = 156$ µN $+ (218$ µN s m⁻¹$)U$. **c**, Extra forces acting on the 1st, 2nd, 5th, 10th, 20th and 100th drop sliding down 50°-tilted PFOTS-on-5-mm-SiO_2 sample at 1.3 s intervals. Intervals greater than 1 s were chosen to ensure that an adsorbed water film or nanodroplets behind a drop had time to equilibrate with the vapour phase. Forces were calculated with equation (3) with the PFOTS-on-Si sample as the reference. **d**, Measured drop charge versus drop number on PFOTS-coated samples. The results were measured at 50° tilt, 1.5 s intervals between the deionized water drops of 45 µl volume after 4 cm slide length. The lines are guides for the eye. Supplementary Section 12 provides additional details.

results (Fig. 4b), and it explains the observed flip in the slope of F_e versus L curves when going from the first to subsequent drops with $n \geq 10$.

All the drops start with zero charge and thus zero electrostatic force. The first drop deposits a negative charge on the neutral surface and acquires a positive charge within a distance of $L \approx \lambda$ (Fig. 4b, top-left schematic). The increase in drop and surface charges leads to a steep increase in the retarding electrostatic force, with a peak at $L \approx 0.8\lambda$. As a result of drop charging, the drop potential increases, which hinders further charge deposition, and the drop charge saturates. As the drop reaches saturation and moves further from the strongly charged region of the surface, the retarding electrostatic force decreases (Fig. 4b, bottom-right schematic).

The maximum value predicted by the analytical solution at the beginning was missing in the experiments (Fig. 4b, red symbols). This could be the effect of an additional negative surface charge deposited right after the drop impacts the surface before touching the first grounded electrode. As a result, the maximum value would be outside our observation range. It was observed on other substrates described below.

For higher drop numbers (Fig. 4b, blue line, and Supplementary Fig. 15), the electrostatic retardation increases with slide distance

because of two effects. First, the surface charge density is already high from previous drops. As a result, the drop needs to cover a larger distance to reach its saturation charge (Fig. 4b, top-right schematic). Thus, the increase in force (for the first drop, it happens in the first 1 cm) is stretched to a distance of ≥ 4 cm. Second, the surface charges in front of the drop that are left behind by previous drops lead to an acceleration. At the end of the path, the electrostatic force increases even more steeply because there are no more attractive charges ahead since the sample ends.

The good agreement between experiment and electrostatic theory indicates that on PFOTS-coated insulators, the extra forces are predominantly caused by electrostatic charging. To find out how ubiquitous electrostatic forces are, we performed experiments on other hydrophobic samples. When using conductive substrates or high-permittivity substrates (polystyrene (PS)-on-gold, Teflon-on-gold, polydimethylsiloxane (PDMS)-on-Si and thiols-on-gold substrates), the first, second and subsequent drops showed similar velocity profiles (Supplementary Section 15 and Supplementary Fig. 18). Thus, electrostatic effects are negligible. In contrast, on 1-mm- and 5-mm-thick SiO_2 coated with PS, Teflon or PDMS, the velocity profiles of the first, second and subsequent drops were distinctly different (Supplementary Section 15
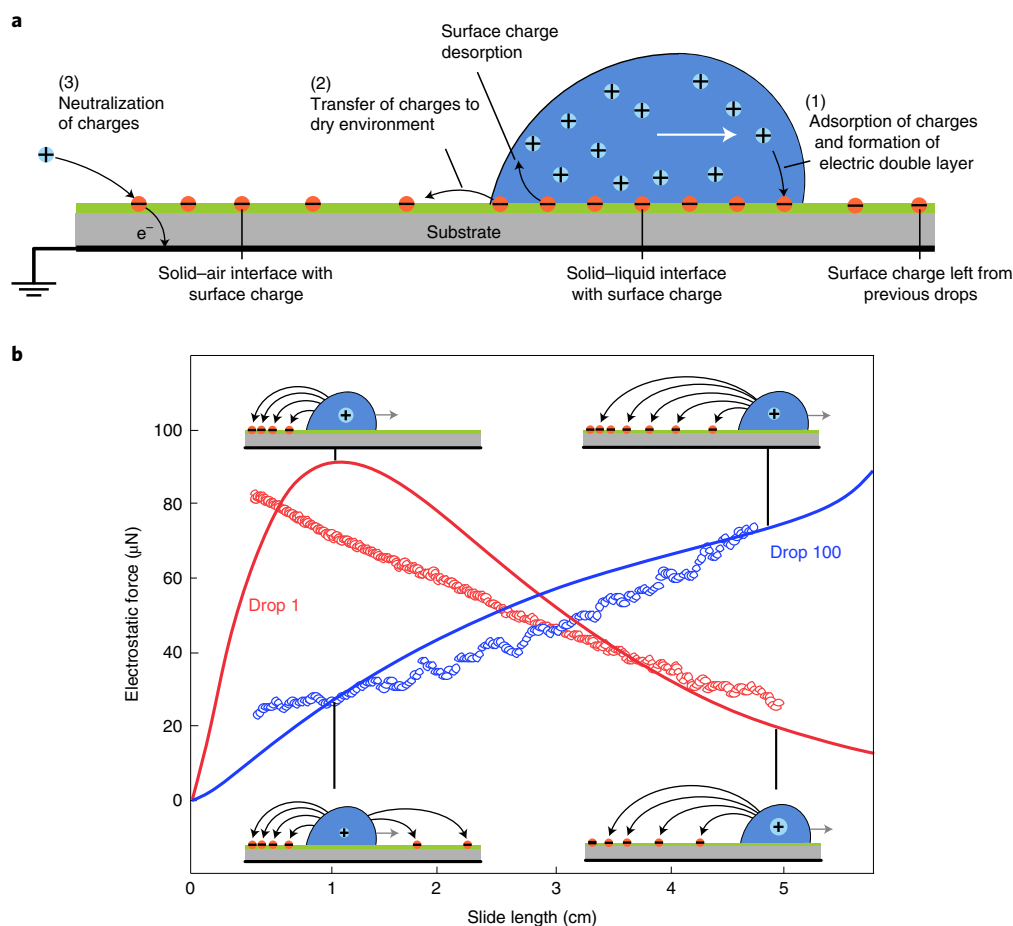
Fig. 4 | Comparison between experimental results and the theoretical model. a, Model applied to calculate the electrostatic forces versus slide length for a series of drops. Step (1): surface charges are generated when water comes into contact with the surface at the front of the drop, for example, by the adsorption of OH⁻, leaving H_3O^+ in the solution. Step (2): at the rear side of the drop, most surface charges are neutralized, for example, by the desorption of OH⁻. A fraction of the surface charges, however, transfers to the solid–air interface. Step (3): charges are neutralized. **b**, Calculated electrostatic force acting on the first drop (red line; equation (14) in the Supplementary Information) and after a large number of drops (blue line; equation (21) in the Supplementary Information). For comparison, we plotted the experimental results (symbols) for the 1st and 100th drop sliding down the PFOTS-on-5-mm-SiO$_2$ sample (Fig. 3c). The parameters were chosen as determined from the measurements of drop charges (Supplementary Table 2; $\sigma_0 = 2 \times 10^{-5}$ µC m⁻², $\lambda = 1.5$ cm, $\tau = 7$ s), the experimental conditions ($w = 4$ mm, $l = 5$ mm, $\Delta t = 1.3$ s, $L_{end} = 6$ cm), and the numerical computations for 5-mm-thick substrates ($a = 1$ mm $= 0.2l$; Supplementary Section 14).

and Supplementary Fig. 19). This observation indicates that drop motion is substantially influenced by electrostatic forces. The charging of drops was detected on all the hydrophobic surfaces on SiO$_2$ (Supplementary Section 12 and Supplementary Fig. 12). In contrast, for the PS-on-gold, Teflon-on-gold and PDMS-on-Si samples, charging was at least ten times lower.

A complex variety of F_e^n versus L graphs were observed, depending on the drop number, tilt angle and substrate thickness. Two typical examples are plotted in Fig. 5; a full set of results is shown in Supplementary Sections 16 and 17. On several samples, such as the Teflon-on-1-mm-SiO$_2$ sample, we observed the maximum in the force versus slide length curves predicted by the electrostatic theory for the first drop (Fig. 5a). We assume that a slight increase in decay length (λ) shifts the maximum value into our observation window. The charge measurements confirmed that indeed on Teflon, $\lambda = 2.5$ cm (compared with $\lambda = 1.5$ cm on PFOTS; Supplementary Table 2). For higher drop numbers, the maximum value became weaker and for drop numbers $n \geq 10$, an increasing extra force started to dominate at larger slide lengths, in agreement with equation (21) in the Supplementary Information.

Figure 5a, however, also shows the limits of the simple model. It does not predict the minimum value in the electrostatic force for $n \geq 10$ at shorter slide lengths. This deficit could be related to the assumption that charge deposition is independent of the slide velocity. Since the deposition of charges is a non-equilibrium process, it most likely depends on the velocity. At a low velocity, charge deposition is probably less pronounced than assumed. A velocity dependence of charge deposition is most likely also the reason for the oscillating electrostatic forces observed, for example, on the PS-on-5-mm-SiO$_2$ sample (Fig. 5b). The oscillation period was not related to drop vibrations, which were at 50 Hz or faster. Thus, a future refinement of the description of charge deposition needs to include the velocity of the receding contact line.

Electrostatic retardation is not restricted to pure water. In aqueous drops containing 0.1–1,000.0 mM NaCl, electrostatic forces made up to 50% of the total force when sliding down the PFOTS-on-1-mm-SiO$_2$ sample (Supplementary Section 18 and Supplementary Fig. 24). For drops of ethylene glycol ($\varepsilon_s = 37$, $\gamma = 0.048$ N m⁻¹, $\eta = 0.016$ Pa s, $V = 18.6$ µl) on the Teflon-on-1-mm-SiO$_2$ sample, the electrostatic forces for the first and second drops were of the order
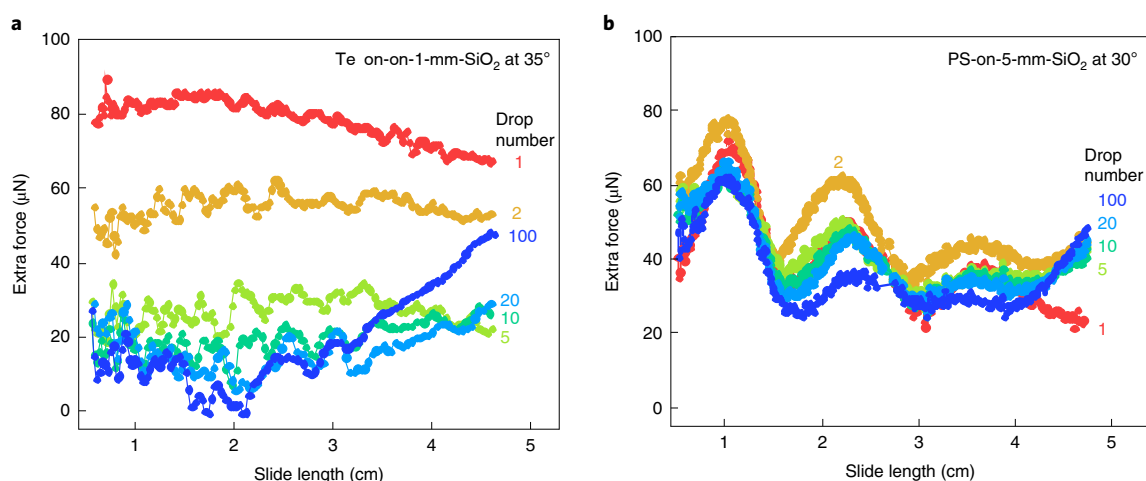
Fig. 5 | Examples of extra forces acting on water drops sliding down. a, Teflon-on-1-mm-SiO$_2$ sample at 35° tilt. **b**, PS-on-5-mm-SiO$_2$ sample at 30° tilt. The results are plotted for the 1st, 2nd, 5th, 10th, 20th and 100th drop. Extra forces were calculated with equation (3), and $F_r = 48\,\mu N + (175\,\mu N\,s\,m^{-1})U$ obtained with the Teflon-on-gold sample and $F_r = 74\,\mu N + (398\,\mu N\,s\,m^{-1})U$ measured on the PS-on-gold sample as reference forces (Supplementary Fig. 20).

of 100 μN; they were even stronger than those for water despite the high viscosity and slow motion of drops (Supplementary Section 18 and Supplementary Fig. 25).

One additional consequence of electrostatic retardation is that impacting drops rebound differently depending on the conductivity and permittivity of the substrates. For example, 20 μl water drops falling from a height of 2.5 cm fully rebound from the Teflon-on-gold substrate. In contrast, the same drops stick on the Teflon-on-SiO$_2$ substrate (Supplementary Section 19). When tilting the surface by 10°, drops rebound on the Teflon-on-gold substrate and roll off completely. On SiO$_2$, drops do not rebound but split apart and stick to the surface. In particular, in printing and coating applications, for the production of window screens and glasses or in heat exchangers, this variation in electrostatic force may control whether impacting drops rebound from or stick to a surface. In general, the insight that surface permittivity influences drop motion opens new avenues towards engineering surfaces with desired wetting properties.

Online content

Any methods, additional references, Nature Research reporting summaries, source data, extended data, supplementary information, acknowledgements, peer review information; details of author contributions and competing interests; and statements of data and code availability are available at https://doi.org/10.1038/s41567-022-01563-6.

References

1. Tuteja, A. et al. Designing superoleophobic surfaces. *Science* **318**, 1618–1622 (2007).
2. Wang, L. M. & McCarthy, T. J. Covalently attached liquids: instant omniphobic surfaces with unprecedented repellency. *Angew. Chem. Int. Ed.* **55**, 244–248 (2016).
3. Huhtamaki, T., Tian, X. L., Korhonen, J. T. & Ras, R. H. A. Surface-wetting characterization using contact-angle measurements. *Nat. Protoc.* **13**, 1521–1538 (2018).
4. Tadmor, R. Open problems in wetting phenomena: pinning retention forces. *Langmuir* **37**, 6357–6372 (2021).
5. Gao, N. et al. How drops start sliding over solid surfaces. *Nat. Phys.* **14**, 191–196 (2017).
6. Backholm, M. et al. Water droplet friction and rolling dynamics on superhydrophobic surfaces. *Nat. Commun. Mater.* **1**, 64 (2020).
7. Lin, Z. H., Cheng, G., Lee, S., Pradel, K. C. & Wang, Z. L. Harvesting water drop energy by a sequential contact-electrification and electrostatic-induction process. *Adv. Mater.* **26**, 4690–4696 (2014).
8. Sun, Y. J., Huang, X. & Soh, S. Using the gravitational energy of water to generate power by separation of charge at interfaces. *Chem. Sci.* **6**, 3347–3353 (2015).
9. Park, J. et al. Identification of droplet-flow-induced electric energy on electrolyte–insulator–semiconductor structure. *J. Am. Chem. Soc.* **139**, 10968–10971 (2017).
10. Boamah, M. D. et al. Energy conversion via metal nanolayers. *Proc. Natl Acad. Sci. USA* **116**, 16210–16215 (2019).
11. Helseth, L. E. A water droplet-powered sensor based on charge transfer to a flow-through front surface electrode. *Nano Energy* **73**, 104809 (2020).
12. Xu, W. H. et al. A droplet-based electricity generator with high instantaneous power density. *Nature* **578**, 392–396 (2020).
13. Wu, H., Mendel, N., van den Ende, D., Zhou, G. F. & Mugele, F. Energy harvesting from drops impacting onto charged surfaces. *Phys. Rev. Lett.* **125**, 078301 (2020).
14. Wang, K. Q. & Li, J. J. Electricity generation from the interaction of liquid–solid interface: a review. *J. Mater. Chem. A* **9**, 8870–8895 (2021).
15. Zhang, J. Y., Lin, S. Q., Zheng, M. L. & Wang, Z. L. Triboelectric nanogenerator as a probe for measuring the charge transfer between liquid and solid surfaces. *ACS Nano* **15**, 14830–14837 (2021).
16. de Gennes, P. G. Wetting: statics and dynamics. *Rev. Mod. Phys.* **57**, 827–863 (1985).
17. Suzuki, S., Nakajima, A., Kameshima, Y. & Okada, K. Elongation and contraction of water droplet during sliding on the silicon surface treated by fluoroalkylsilane. *Surf. Sci.* **557**, L163–L168 (2004).
18. Starov, V. M., Velarde, M. G. & Radke, C. J. *Wetting and Spreading Dynamics* (CRC Press, 2007).
19. Bonn, D., Eggers, J., Indekeu, J., Meunier, J. & Rolley, E. Wetting and spreading. *Rev. Mod. Phys.* **81**, 739–805 (2009).
20. Snoeijer, J. H. & Andreotti, B. Moving contact lines: scales, regimes, and dynamical transitions. *Ann. Rev. Fluid Mech.* **45**, 269–292 (2013).
21. Olin, P., Lindstrom, S. B., Pettersson, T. & Wagberg, L. Water drop friction on superhydrophobic surfaces. *Langmuir* **29**, 9079–9089 (2013).
22. Perrin, H., Lhermerout, R., Davitt, K., Rolley, E. & Andreotti, B. Defects at the nanoscale impact contact line motion at all scales. *Phys. Rev. Lett.* **116**, 184502 (2016).
23. Marsh, J. A., Garoff, S. & Dussan, E. B. Dynamic contact angles and hydrodynamics near a moving contact line. *Phys. Rev. Lett.* **70**, 2778–2781 (1993).
24. Kim, H. Y., Lee, H. J. & Kang, B. H. Sliding of liquid drops down an inclined solid surface. *J. Colloid Interface Sci.* **247**, 372–380 (2002).
25. Le Grand, N., Daerr, A. & Limat, L. Shape and motion of drops sliding down an inclined plane. *J. Fluid Mech.* **541**, 293–315 (2005).
26. Furmidge, C. G. L. Studies at phase interfaces. I. The sliding of liquid drops on solid surfaces and a theory for spray retention. *J. Colloid Sci.* **17**, 309–324 (1962).
27. Wolfram, E. & Faust, R. in *Wetting, Spreading and Adhesion* (ed Padday, J. F.) 213–222 (Academic Press, 1978).
28. Extrand, C. W. & Kumagai, Y. Liquid drops on an inclined plane: the relation between contact angles, drop shape, and retentive force. *J. Colloid Interface Sci.* **170**, 515–521 (1995).

29. Antonini, C., Carmona, F. J., Pierce, E., Marengo, M. & Amirfazli, A. General methodology for evaluating the adhesion force of drops and bubbles on solid surfaces. *Langmuir* **25**, 6143–6154 (2009).

30. Semprebon, C. & Brinkmann, M. On the onset of motion of sliding drops. *Soft Matter* **10**, 3325–3334 (2014).

31. Macdougall, G. & Ockrent, C. Surface energy relations in liquid/solid systems. I. The adhesion of liquids to solids and a new method of determining the surface tension of liquids. *Proc. R. Soc. Lond. A* **180**, 151–173 (1942).

32. Dimitrakopoulos, P. & Higdon, J. J. L. On the gravitational displacement of three-dimensional fluid droplets from inclined solid surfaces. *J. Fluid Mech.* **395**, 181–209 (1999).

33. ElSherbini, A. & Jacobi, A. Retention forces and contact angles for critical liquid drops on non-horizontal surfaces. *J. Colloid Interface Sci.* **299**, 841–849 (2006).

34. Sakai, M. et al. Direct observation of internal fluidity in a water droplet during sliding on hydrophobic surfaces. *Langmuir* **22**, 4906–4909 (2006).

35. Richard, D. & Quéré, D. Viscous drops rolling on a tilted non-wettable solid. *Europhys. Lett.* **48**, 286–291 (1999).

36. Yilbas, B. S., Al-Sharafi, A., Ali, H. & Al-Aqeeli, N. Dynamics of a water droplet on a hydrophobic inclined surface: influence of droplet size and surface inclination angle on droplet rolling. *RSC Adv.* **7**, 48806–48818 (2017).

37. Yatsuzuka, K., Mizuno, Y. & Asano, K. Electrification phenomena of pure water droplets dripping and sliding on a polymer surface. *J. Electrost.* **32**, 157–171 (1994).

38. Shahzad, A., Wijewardhana, K. R. & Song, J. K. Contact electrification efficiency dependence on surface energy at the water-solid interface. *Appl. Phys. Lett.* **113**, 023901 (2018).

39. Stetten, A. Z., Golovko, D. S., Weber, S. A. L. & Butt, H. J. Slide electrification: charging of surfaces by moving water drops. *Soft Matter* **15**, 8667–8679 (2019).

40. Sun, Q. et al. Surface charge printing for programmed droplet transport. *Nat. Mater.* **18**, 936–941 (2019).

41. Zhang, W. L., Sun, Q. Q., Butt, H. J., Wang, Z. K. & Deng, X. Surface charges as a versatile platform for emerging applications. *Sci. Bull.* **65**, 1052–1054 (2020).

42. Lin, S. Q., Xu, L., Wang, A. C. & Wang, Z. L. Quantifying electron-transfer in liquid-solid contact electrification and the formation of electric double-layer. *Nat. Commun.* **11**, 399 (2020).

43. Choi, D. et al. Spontaneous electrical charging of droplets by conventional pipetting. *Sci. Rep.* **3**, 2037 (2013).

44. He, B. & Darhuber, A. A. Electrical surface charge patterns induced by droplets sliding over polymer and photoresist surfaces. *J. Micromech. Microeng.* **29**, 105002 (2019).

45. Nauruzbayeva, J. et al. Electrification at water–hydrophobe interfaces. *Nat. Commun.* **11**, 5285 (2020).

46. Poli, E., Jong, K. H. & Hassanali, A. Charge transfer as a ubiquitous mechanism in determining the negative charge at hydrophobic interfaces. *Nat. Commun.* **11**, 901 (2020).

47. Yan, X. B. et al. Central role of bicarbonate anions in charging water/hydrophobic interfaces. *J. Phys. Chem. Lett.* **9**, 96–103 (2018).

48. Mugele, F. & Heikenfeld, J. *Electrowetting: Fundamental Principles and Practical Applications* (Wiley-VCH, 2019).

49. Yarnold, G. D. The motion of a mercury index in a capillary tube. *Proc. Phys. Soc.* **50**, 540–552 (1938).

50. Shikhmurzaev, Y. D. The moving contact line on a smooth solid surface. *Int. J. Multiph. Flow* **19**, 589–610 (1993).

83

Methods

Tilted-plate experiments. To measure the forces acting on sliding drops, 33 μl drops of distilled water ($<1\,\mu S\,cm^{-1}$; Gibco, Thermo Fisher Scientific), 1 M NaCl solution (Carl Roth), 0.1 mM NaCl solution (made from 10 μl M NaCl solution and 100 ml distilled water) and ethylene glycol (99.8%; Sigma-Aldrich) were deposited at intervals of 1.3 s at the top of a tilted sample by a grounded syringe needle (1.5 mm outer diameter, Dosiernadel Vollmetal), which was connected to a peristaltic pump (MINIPULS 3, Gilson) (Supplementary Fig. 1). Before every series of drops, the surfaces were neutralized by an ionizing air blower for 10 min (Aerostat PC ionizing air blower, Simco-Ion). The drops fell ~5 mm, just enough so that they detached from the syringe before touching the surface. To make sure the drops start sliding without any initial charge, they were neutralized by a 0.025-mm-diameter grounded tungsten wire, right after they landed on the surface. The position where the drops detach from the grounded wire corresponds to the zero slide length ($L = 0$). The observation range starts where the full drop has detached from the grounded wire and the wire is not in the image anymore, that is, at $L = 0.5$ cm. Then, we imaged the drop with a frame rate of 1,000 frames per second in the side and front views over a length of typically 4.5 cm with a high-speed camera (FASTCAM Mini UX100 (Photron) with a TitanTL telecentric lens, ×0.268, one inch, C-mount (Edmund Optics)). By applying two parallel mirrors ($25 \times 36\,mm^2$ protected silver mirror; PFR10-P01, Thorlabs) on both sides of the sample to guide the backlight from the telecentric backlight illuminator (138 mm; Edmund Optics), we also imaged the front view of the sliding drops at the same time. After typically $L_{end} = 6$ cm, the rim of the sample was reached and the drops fell off. To access a wide velocity range, we varied the tilt angle (Supplementary Fig. 6a). On longer samples, we verified that after a slide length of ~10–15 cm, the drops reach a steady-state velocity (Supplementary Fig. 6b). From video images, we extract slide length L, drop velocity U, contact angles at the front (advancing contact angle, Θ_a) and rear (receding contact angle, Θ_r), and length and width of the drop. All the parameters vary with time and thus with position. To extract $\Theta_a(U)$ and $\Theta_r(U)$ from the videos, we adapted the open drop-shape analysis from MATLAB (DSAfM) version 9.5.0.944444 (R2018b). The dynamic contact angles were determined by applying a polynomial fit to every contour image (Supplementary Section 2). All the measurements were conducted at a temperature of $20 \pm 1\,°C$ and a humidity of 15–30%.

Sample preparation. Five types of surface were prepared. (1) PFOTS monolayers on Si wafer, 1-mm-thick and 5-mm-thick SiO_2 slides were prepared by chemical vapour deposition. After O_2-plasma cleaning at 300 W for 10 min (Femto low-pressure plasma system, Diener electronic), the Si wafer (native oxide layer of 1.6 ± 0.3 nm as measured by ellipsometry; resistivity, $<0.005\,\Omega\,cm$; thickness, $525 \pm 25\,\mu m$; Silicon Materials) and the SiO_2 slides were placed in a vacuum desiccator containing a vial with 0.5 ml 1H,1H,2H, 2H-perfluorooctadecyltrichlorosilane (97%; Sigma-Aldrich). We used 1-mm-thick SiO_2 slides ($76.2 \times 25.4 \times 1.0\,mm^3$; Thermo Fisher Scientific) and 5-mm-thick SiO_2 slides ($75.0 \times 25.0 \times 5.0\,mm^3$; Präzisions Glas & Optik). The desiccator was evacuated to less than 100 mbar, closed, and the reaction was allowed to proceed for 30 min. Before measurement, the PFOTS surfaces were rinsed with ethanol to remove any unbound silanes. (2) PS films on gold, 1-mm-thick and 5-mm-thick SiO_2 slides were prepared by dip coating. To get gold substrates, 30 nm gold was sputtered onto $75 \times 25\,mm^2$ glass slides that had been precoated with 5 nm chromium to improve adhesion. The solution consisted of 1 wt% PS (molecular weight, $192\,kg\,mol^{-1}$, $\varepsilon = 2.6$; Sigma-Aldrich) in toluene. After moving down the substrates at a speed of $90\,mm\,min^{-1}$ into the solution and waiting for 10 s, the substrates were moved up again at a speed of $90\,mm\,min^{-1}$. Finally, the films were annealed in an oven at 120 °C under a vacuum for 24 h. The PS films were 20 nm thick measured by a profiler (P-7 stylus profiler, KLA-Tencor). (3) Teflon AF1600 (Teflon) films on gold, 1-mm-thick and 5-mm-thick SiO_2 slides were prepared by dip coating. Sputter-coated gold glass slides (see above) or SiO_2 slides were immersed into 1 wt% Teflon AF1600 ($\varepsilon = 1.9$; Sigma-Aldrich) in FC-75(97% Fisher scientific) at a speed of $90\,mm\,min^1$. After being immersed for 10 s, the substrates were withdrawn from the solution at a constant speed of $10\,mm\,min^{-1}$. Finally, the films on the substrates were annealed at 160 °C in a vacuum for 24 h. Teflon AF1600 films were 60 nm thick to avoid dewetting. We determined that the roughness increased with an increase in film thickness (Supplementary Section 20). (4) PDMS polymer brushes on Si wafers, 1-mm-thick and 5-mm-thick SiO_2 slides were prepared as described elsewhere[51]. After O_2-plasma cleaning (see above), few PDMS drops (molecular weight, $6\,kg\,mol^{-1}$; Alfa Aesar) were deposited on a Si wafer or SiO_2. After the PDMS drop spread and covered the substrates, the samples were kept at 22−23 °C and 30−60% relative humidity for 24–48 h. Then, they were rinsed with toluene and sonicated in toluene, ethanol and deionized water for 10 min each to wash away any unbound PDMS. The brushes were ~3 nm

thick[1]. (5) 1H,1H,2H,2H-perfluorodecanethiol (thiols) monolayers on gold: directly after the preparation of the gold-coated glass slide (see above), the surfaces were immersed in a 1 mM ethanolic thiol (≥96.0%; Sigma-Aldrich) solution for 24 h. Then, the surfaces were rinsed by pure ethanol and dried by Ar_2 blowing.

SFM imaging. All the hydrophobic surfaces were studied using SFM (Dimension Icon, Bruker) in the tapping mode (Supplementary Fig. 2). The SFM tips with a nominal resonance frequency of 300 kHz and spring constant of $26\,N\,m^{-1}$ were used (160AC-NA, OPUS). The root-mean-squared roughness was determined on the areas of $0.5 \times 0.5\,\mu m^2$ for each sample. The error was around 0.1 nm, except for the thiols-on-gold and PFOTS samples, where it was 0.2 nm. The errors were determined from variations observed at different positions on the samples and variations in the different samples.

Static contact angle measurements. 'Static' advancing and receding contact angles, namely, Θ_a^0 and Θ_r^0, respectively, were measured with sessile water drops (OCA 35, DataPhysics Instruments). An 8 μl water drop was deposited on the surface. Then, 16 μl deionized water was pumped into the drop and subsequently sucked out at the rate of $0.5\,\mu l\,s^{-1}$ by a Hamilton syringe connected to a hydrophobic needle. The process was repeated three times without interruption. During inflation and deflation, the drops were imaged in the side view. Then, Θ_a^0 and Θ_r^0 were calculated by fitting an ellipse model to the contour images.

Data availability
Source data are provided with this paper. All other data that support the plots within this paper and other findings of this study are available from the corresponding authors upon reasonable request.

References
51. Teisala, H., Baumli, P., Weber, S. A. L., Vollmer, D. & Butt, H. J. Grafting silicone at room temperature—a transparent, scratch-resistant nonstick molecular coating. *Langmuir* **36**, 4416–4431 (2020).

Author contributions
X.L. prepared the samples, performed the tilted-plate experiments and analysed the data. X.L., A.S. and R.B. designed the tilted-plate setup. P.B., A.Z.S. and S.A.L.W. measured the drop charges. H.B. and S.A.L.W. numerically calculated the electrostatic force on a drop. F.B. and H.M. carried out the numerical diffuse-interface simulations of drop motion. S.A.L.W., S.H., M.T.S. and H.-J.B. derived the analytical theory. H.-J.B. derived the concept of extracting the electrostatic force from the equation of motion. All the authors discussed and interpreted the results and wrote the manuscript.

Competing interests
The authors declare no competing interests.

Additional information
Supplementary information The online version contains supplementary material available at https://doi.org/10.1038/s41567-022-01563-6.

Correspondence and requests for materials should be addressed to Stefan A. L. Weber or Hans-Jürgen Butt.

Peer review information *Nature Physics* thanks Matthew Gebbie and the other, anonymous, reviewer(s) for their contribution to the peer review of this work.

Reprints and permissions information is available at www.nature.com/reprints.

Supplementary information

Spontaneous charging affects the motion of sliding drops

In the format provided by the
authors and unedited

Supplementary information for

Spontaneous charging affects the motion of sliding drops

Xiaomei Li[1], Pravash Bista[1], Amy Z. Stetten[1], Henning Bonart[1,2], Maximilian T. Schür[2], Steffen Hardt[2], Francisco Bodziony[3], Holger Marschall[3], Alexander Saal[1], Xu Deng[4], Rüdiger Berger[1], Stefan A.L. Weber[1,5]*, Hans-Jürgen Butt[1]*

[1] Max Planck Institute for Polymer Research, Ackermannweg 10, 55128 Mainz, Germany

[2] Institute for Nano- and Microfluidics, Technische Universität Darmstadt, Alarich-Weiss-Straße 10, 64287 Darmstadt, Germany

[3] Computational Multiphase Flows, Technische Universität Darmstadt, Alarich-Weiss-Straße 10, 64287 Darmstadt, Germany

[4] Institute of Fundamental and Frontier Sciences, University of Electronic Science and Technology of China, Chengdu, China.

[5] Institute of Physics, Johannes Gutenberg University, Staudingerweg 7, 55128 Mainz, Germany.

Email address of corresponding authors:
Hans-Jürgen Butt: butt@mpip-mainz.mpg.de
Stefan A.L. Weber: webers@mpip-mainz.mpg.de

This PDF file includes:

SI 1. Viscous dissipation due to hydrodynamic flow in the drop

The total viscous force of a sliding drop is commonly split in two components. One comes from the viscous dissipation in the bulk, F_b, the other is concentrated at the wedge, F_w. An upper limit for bulk viscous dissipation can be estimated by replacing a drop with its real 3D shape by drop with vertical side having a base area of $\pi lw/2$ and a height H. We assume that the bottom area of the drop is stationary (no slip) and that the top area at height H is sliding with $2U$. Twice the velocity to ensure that the center moves with U. Then, the bulk viscous force is:

$$F_b \approx \eta \frac{\pi lw}{2H} U \tag{S1}$$

This is more an upper limit. Le Grand, Daerr & Limat use $F_v = \eta UV^{1/3}$ [1]. Kim, Lee & Kang apply $F_v = \eta \pi r_d^2 U/H$ [2]. Here, V is the volume of the drop and r_d is the radius of the contact area of a drop, which, for simplicity, is assumed to have a circular contact radius.

In addition to bulk viscous dissipation, there is viscous dissipation in the wedge region [2-10]. Since we observe the shape of drops with a camera at a resolution of $\approx$10 µm, we detect macroscopic contact angles $\Theta_a(U)$ and $\Theta_r(U)$. Viscous dissipation in the wedge happens at a shorter length scale and manifests itself in an increase of $\Theta_a(U)$ and a decrease of $\Theta_r(U)$. Therefore, it has been already included in Eq. (1).

SI 2. Experimental setup and image analysis

The experimental setup is shown in Figure S1. To extract L, $\Theta_a(L)$, $\Theta_r(L)$, and w from the videos, we used and adapted the freely available drop shape analysis from MATLAB (DSAfM) originally developed by Andersen & Taboryski [11] (for details see [12]). In a first step, images without a drop and the images with complete drops are identified. The images without a drop are used to extract the tilt angle. The images with a complete drop were corrected by subtracting the background and then rotating into a horizontal drop. Then the contour, front edge position and rear edge position of the drops were detected with sub-pixel precision. By the distance between rear edge and front edge, we calculated the length of the drop from side view and the width of the drop from front view. Afterwards, the image was divided into the front half and the rear half of the drop to further analyse the advancing and receding contact angles and the respective velocity. The velocities of both sides were calculated by the rear and front edge point moving distance in each frame, and we use the average value of the velocities of both sides as the final drop velocity. Dynamic contact angles were determined by applying a 4th order polynomial fit to the counter of drop in each image. To get the height of drops, we employ a free software named "Tracker" (https://github.com/OpenSourcePhysics/tracker). By defining the distance between the above drop edges and the highest point of the drop as the drop height, then setting the highest point of a drop as the tracking point, we got the real-time height of drops. All measurements were conducted at a temperature of 20±1°C and a humidity of 15-30%.
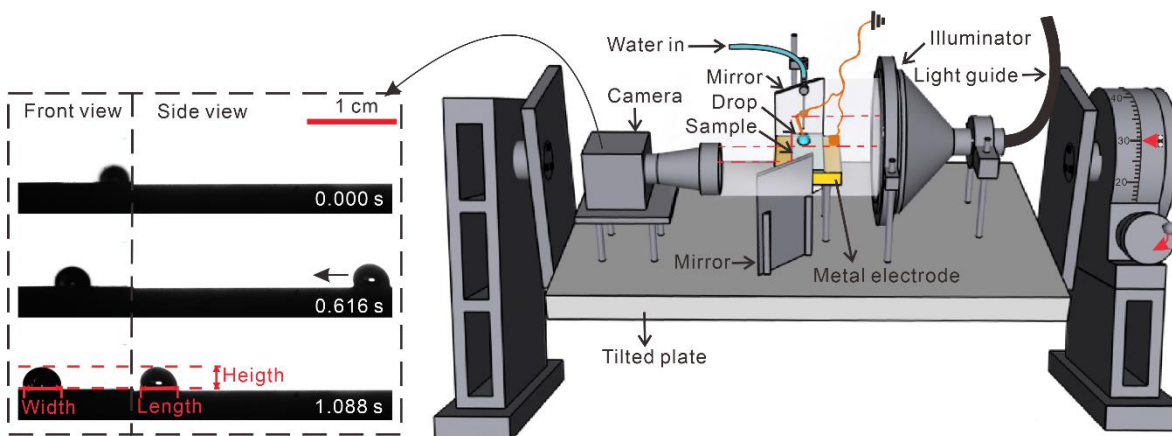

Figure S1. Experimental setup. Water drops were automatically placed from a grounded syringe needle which was connected to a peristaltic pump onto the top of the tilted plate at fixed time intervals of 1.3 s. They contacted a grounded electrode and then started to move down the plate. The slide length and time were set to zero when drops detached from the electrode. At this point they unavoidably already had a velocity U_0. Sliding drops were imaged with a camera in side and front view by using two parallel mirrors. From side-view images, the positions of the front and rear contact lines, drop velocity, dynamic advancing Θ_a, receding contact angles Θ_r and the length of the drops were determined. For details about data processing, we refer to [12].

SI 3. Static advancing and receding contact angles

Table S1. *Receding Θ_r^0 and advancing contact angles Θ_a^0 and contact angle hysteresis, $\Delta\Theta = \Theta_a^0 - \Theta_r^0$ for the hydrophobic samples studied.*

Coating	Substrates	Name of surfaces	Θ_r^0 (°)	Θ_a^0 (°)	$\Delta\Theta$ (°)
PFOTS	Si	PFOTS-on-Si	87±2	117±2	30
	1 mm SiO$_2$	PFOTS-on-1mm-SiO$_2$	85±3	115±2	30
	5 mm SiO$_2$	PFOTS-on-5mm-SiO$_2$	86±3	116±3	30
Polystyrene (20 nm)	Gold	PS-on-gold	80±1	97±1	17
	1 mm SiO$_2$	PS-on-1mm-SiO$_2$	77±2	93±1	16
	5 mm SiO$_2$	PS-on-5mm-SiO$_2$	78±2	95±1	17
Teflon AF 1600 (60 nm)	Gold	Teflon-on-gold	109±3	122±2	13
	1 mm SiO$_2$	Teflon-on-1mm-SiO$_2$	110±2	122±1	12
	5 mm SiO$_2$	Teflon-on-5mm-SiO$_2$	110±1	121±1	11
PDMS brushes	Si	PDMS-on-Si	88±1	105±1	17
	1 mm SiO$_2$	PDMS-on-1mm-SiO$_2$	86±2	105±1	19
	5 mm SiO$_2$	PDMS-on-5mm-SiO$_2$	87±1	102±1	15
Perfluoro-decanethiols	Gold	Thiols-on-gold	95±2	115±3	20

SI 4. Scanning force microscope imaging
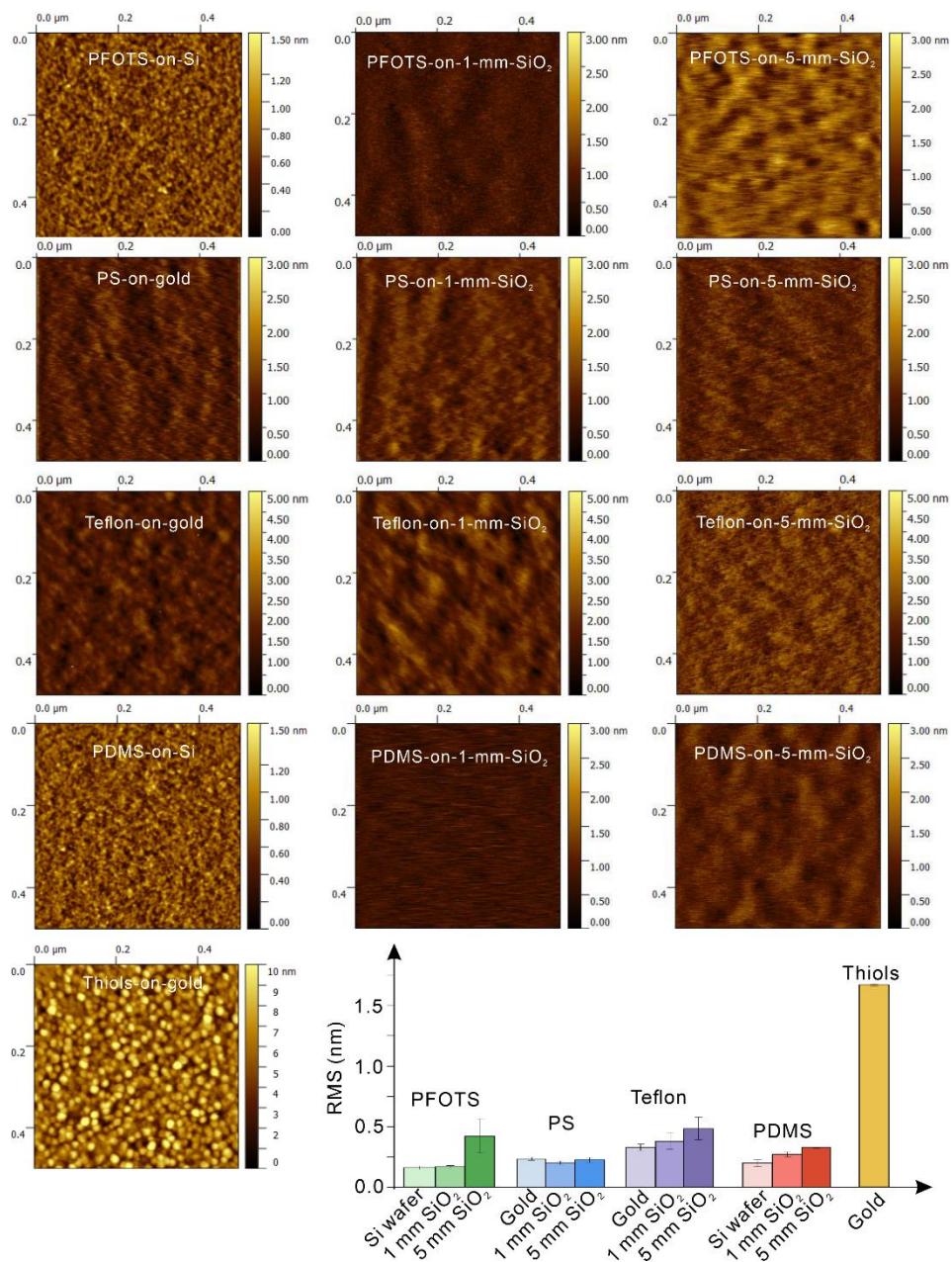
Figure S2. *SFM tapping mode images of all hydrophobic surfaces. Note: The RMS errors come from three measurement on different positions and different samples.*

SI 5. The relative permittivity of the surfaces

To check how the polymer coating on the substrate affects the permittivity, we measured the capacitance (C) of a 1 mm SiO_2 substrate and 1 mm SiO_2 with 20 nm PS, 200 nm PS and 60 nm Teflon AF in a defined area (A) of 0.0005 m^2 and 0.001 m^2 (figure S3 A). We measured two samples for each surface and 10 different positions on the samples to obtain the average capacitance of each sample at 1 kHz with 1 V amplitude. By equation of $\varepsilon_s = \frac{Cd}{A\varepsilon_0}$ (d is the substrate thickness; $\varepsilon_0 = 8.85 \times 10^{-12}\ F/m$ is the vacuum permittivity), we calculated the relative permittivity of the surfaces. From figure S3 B, we infer that the measured permittivity of 1 mm SiO_2 with PS and Teflon AF coating is the same as the one without coating, within the uncertainty given by the error bars. That was 3.7±0.2, which is also similar to the value reported by the supplier. Thus, the polymer films have no influence on the overall capacitance is, however, not surprising, since the thickness of the coating is at least by a factor of 5000 lower than the substrate thickness.
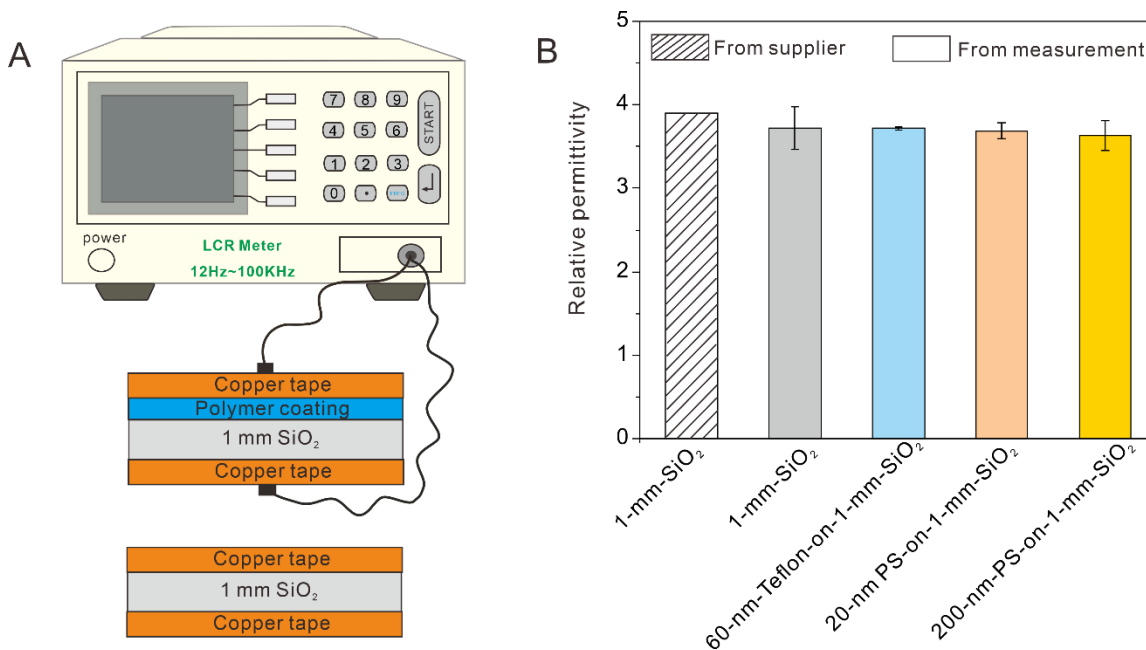
Figure S3. *Relative permittivity of the surfaces. (A) Schematic of the method to measure the capacitance of the substrates. (B) The relative permittivity of 1 mm SiO_2 and 1 mm SiO_2 with coatings of 20 nm PS, 200 nm PS and 60 nm Teflon AF.*

SI 6. Stability of the surfaces

To quantify the stability of the hydrophobic surfaces, we carried out ellipsometry measurements (Ellipsometer: Nanofilm EP3). We checked the film thickness before and after drops sliding. Since the difference in index of refraction between SiO_2 and the silane layer is quite low, the experiments were done on Si wafers. The natural oxide layers on our wafers were 1.9±0.3 nm thick. After silanation with PFOTS and rinsing with ethanol to remove unbound silane layers, the thickness increased to 2.9±0.5 nm, indicating that the silanes formed a mono- or bilayer, but no multilayer. After 1000 drops had slit on the surface, we did not see the change on thickness.

We also tried X-ray photoelectron spectroscopy (XPS: Kratos AXIS Ultra[DLD]) measurements before and after exposition to water. We failed to detect any significant difference.

A much more sensitive test are the tilted plane experiments themselves. Thus, we measured drop velocity, $U(L)$, advancing contact angle, $\Theta_a(L)$, and receding contact angle, $\Theta_r(L)$, of 1000 drops sliding on the reference surfaces with a drop interval of 1.3 s; U, Θ_a and Θ_r are the relevant parameters for force calculations. The results show that $U(L)$, $\Theta_a(L)$, and $\Theta_r(L)$ are indistinguishable for the first and all following drops (Figure S4). Thus, all coatings on Si wafers or gold have stable wettability properties even after 1000 water drops.
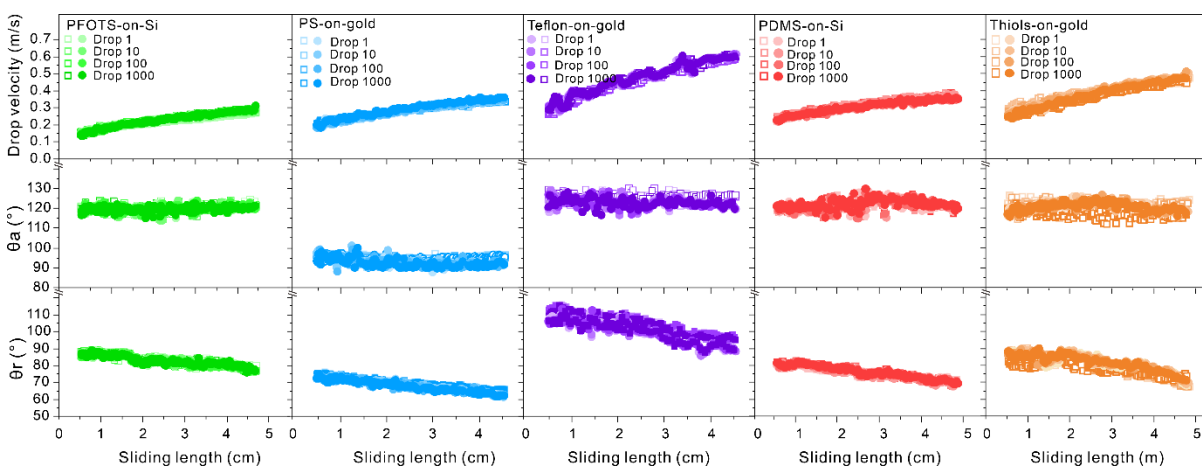
Figure S4. *Drop velocities, advancing contact angles (θ_a) and receding contact angles (θ_r) versus slide length of drop 1, 10, 100, and 1000 drops sliding on 50° tilted PFOTS-on Si, PS-on-gold, Teflon-on gold, PDMS-on-Si and thiols-on-gold surfaces. Note: Rectangles and circles represent the repeated measurement on two samples.*

We also measured the morphology of samples by AFM in tapping mode before and after 1000 sliding drops (Figure S5). We did not observe changes in morphology. Furthermore, the RMS change of all the surfaces before and after drops sliding were all lower than 1 nm, which further supports our conclusion that the surfaces did not change.
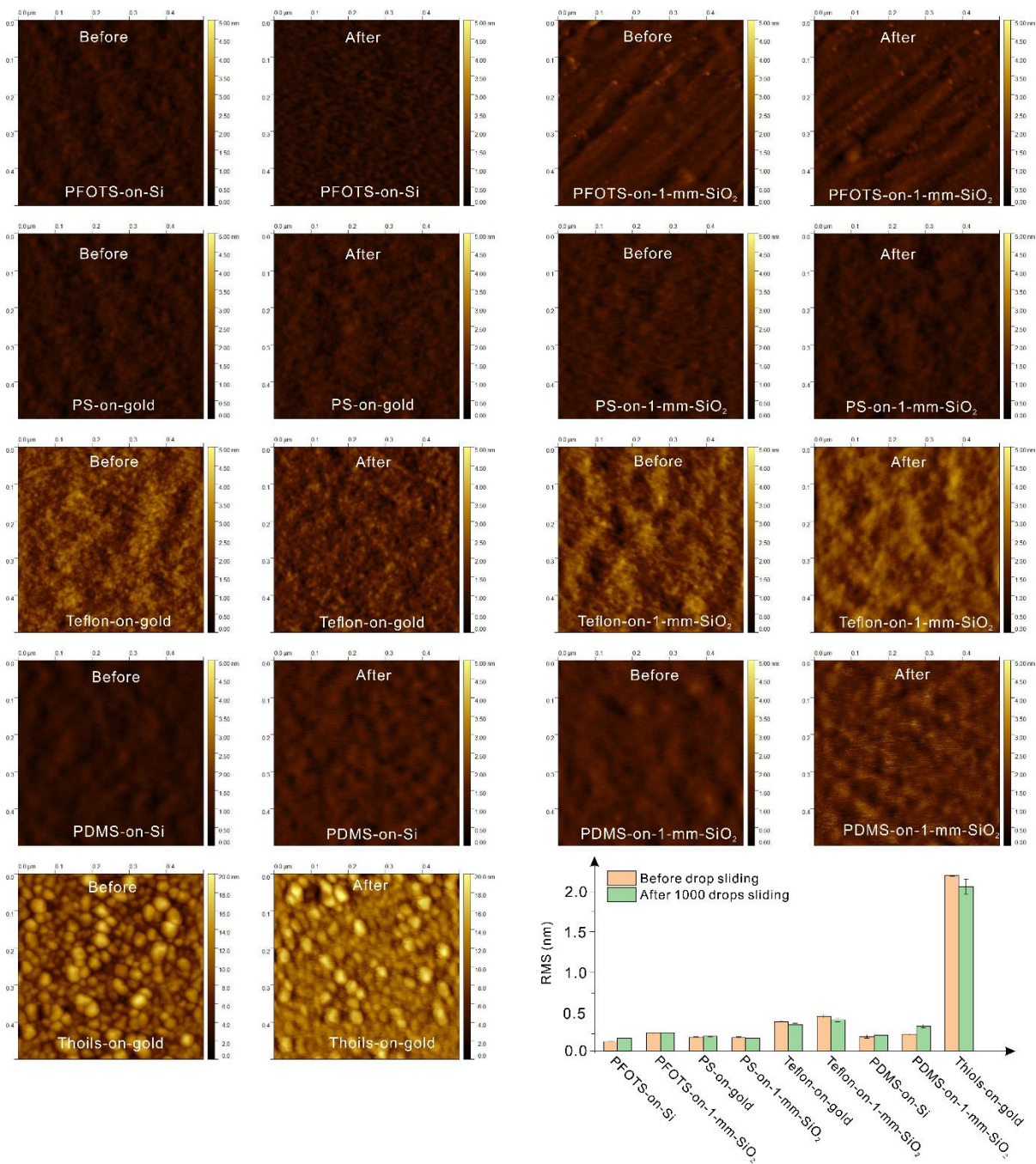
Figure S5. *AFM tapping mode images of the drop path on hydrophobic surfaces made on Si wafer, gold, and 1 mm SiO₂ substrates before and after sliding of 1000 drops. In addition, the root-mean-square (RMS) roughness measured on an area of 0.5×0.5 μm² is plotted as a histogram.*

SI 7. Drop velocity-versus-slide length for PFOTS-coated surfaces at different tilt angles
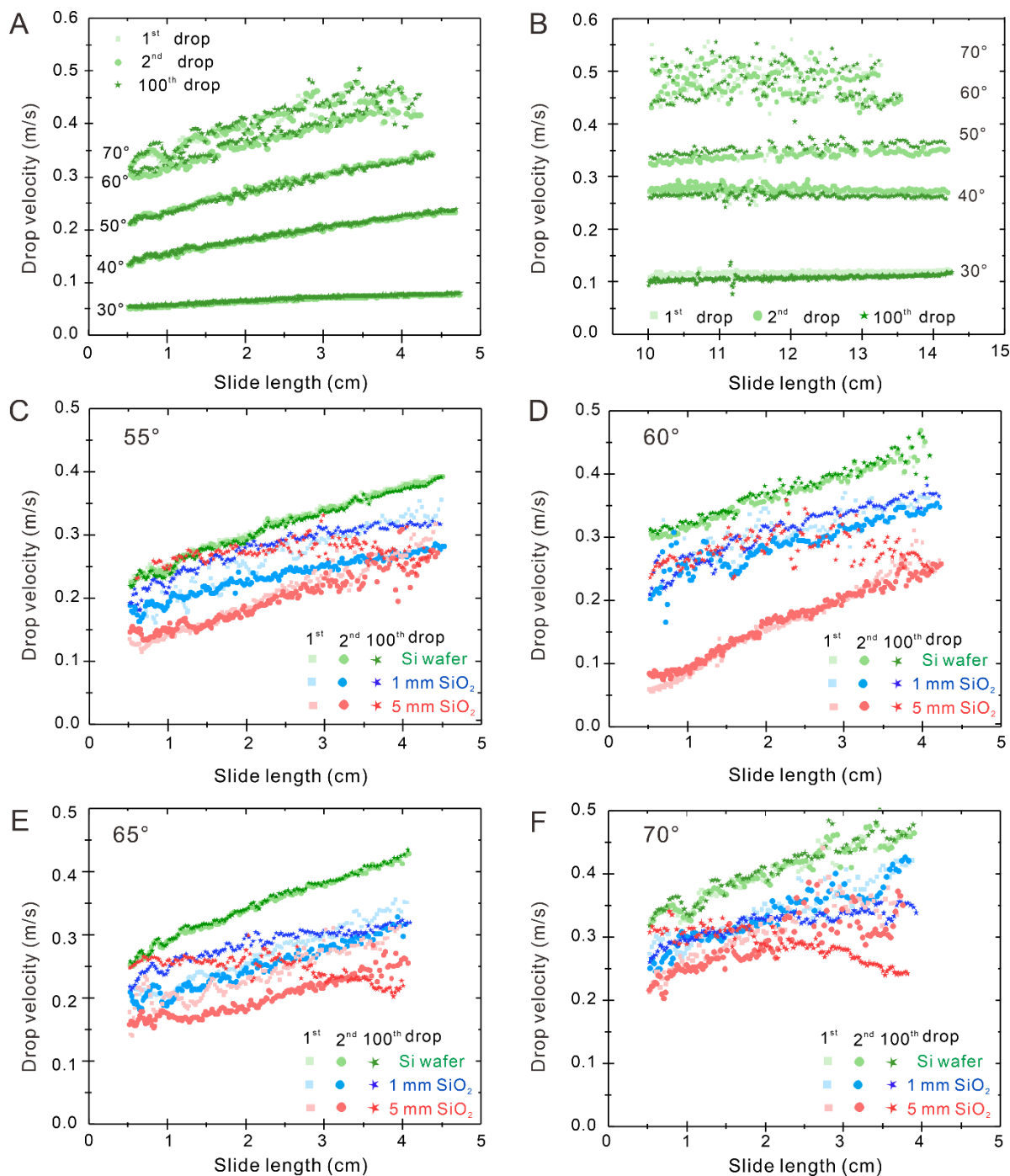

Figure S6. *Representative results for drop velocity-versus-slide length for 33 μL water drops on PFOTS-coated samples. Drops sliding on PFOTS-on-Si the first 5 cm (A) and after having already moved 10 cm (B) at different tilt angles. (C-F) Drops on PFOTS on Si wafer (green symbols), 1 mm SiO₂ (blue symbols) and 5 mm SiO₂ (red symbols) deposited at a rate of one drop per 1.3 s measured at 55° (C), 60° (D), 65° (E), and 70° (E) tilt angles. For comparison also the results obtained on Si wafers are plotted as green symbols. Results for drop number 1 (rectangles), 2 (circles), and 100 (stars) are plotted. Note: due to noise, the U(t) curves were either*

smoothened before differentiation or the whole curve was fitted by a 1st to 4th order polynomial and the derivative of that polynomial was inserted.

SI 8. Direct numerical diffuse interface simulations of drop motion

Due to the no-slip boundary condition on solid surfaces drops show a rolling component in their motion [13-19]. To quantify the effective mass of the rolling drop, Direct Numerical Simulations (DNS) [20] deploying a diffuse interface phase-field method were performed. The effective mass is defined by $m^* = 2E_{kin}/U^2$, where E_{kin} is the kinetic energy of the drop. In our DNS, the interface was treated as a diffuse layer through which the fluid properties vary steeply but continuously. On the mesoscopic scale, the motion of the contact line occurs naturally as diffusion across the interface driven by gradients of the chemical potential. In contrast, the conventional sharp-interface model suffers from a non-integrable stress singularity at the sliding contact line [21,22].

The results of simulations for three-dimensional droplets on an inclined wall were obtained with phaseFieldFoam, a diffuse interface phase-field solver developed within the OpenFOAM C++ library for computational continuum physics [23,24]. The solver has also been enhanced to use a sliding reference-frame technique, to follow the droplet's centre-of-mass, effectively reducing the computational effort.

The following properties of the air-water system were used for the simulations: Water density ρ = 1000 kg/m^3, water dynamic viscosity η = 10^{-3} Pas, air density ρ_a = 1 kg/m^3, air dynamic viscosity η_a = 10^{-5} Pas, surface tension of water γ = 0.072 N/m. A no-slip boundary condition is applied at the bottom boundary with free-slip boundary conditions being applied on every other boundary.

For initialization, a hemispherical drop with radius R = 2.5 mm (V = 32.7 µL, contact angle of 90°) was placed on a 25×10 mm^2 rectangular domain at (0.0125, 0) m, on a smooth inclined wall. For various inclination angles, the droplet's barycentre position and velocity have been tracked and its kinetic energy density field has been measured. This allowed to calculate both contributions to the total kinetic energy – the translational and rotational kinetic energies.

The factor m^*/m slightly changed as a function of barycentre velocity (Figure S7). Initially, the so-called sliding acceleration is greater than the rotational one, leading to a slow increase of m^*/m since the main contribution to the total kinetic energy is from the sliding. The change in slope is more pronounced for lower inclination angles since the sliding acceleration is also lower, when compared to larger inclination angles. After some time, the droplet's sliding acceleration starts to decrease but its angular acceleration is still increasing. Therefore, a steeper increase of m^*/m was observed. Since our calculations of the electrostatic force did not depend sensitively on the precise value of m^*/m, we applied the value of 1.05 throughout our analysis.
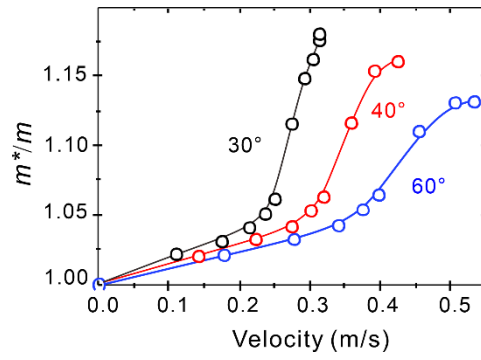
Figure S7. *Effective mass m* divided by real mass m of the drop versus velocity of a 32.7 µL water drop with an initial contact angle of 90° at tilt angles of 30°, 40°, and 60°.*
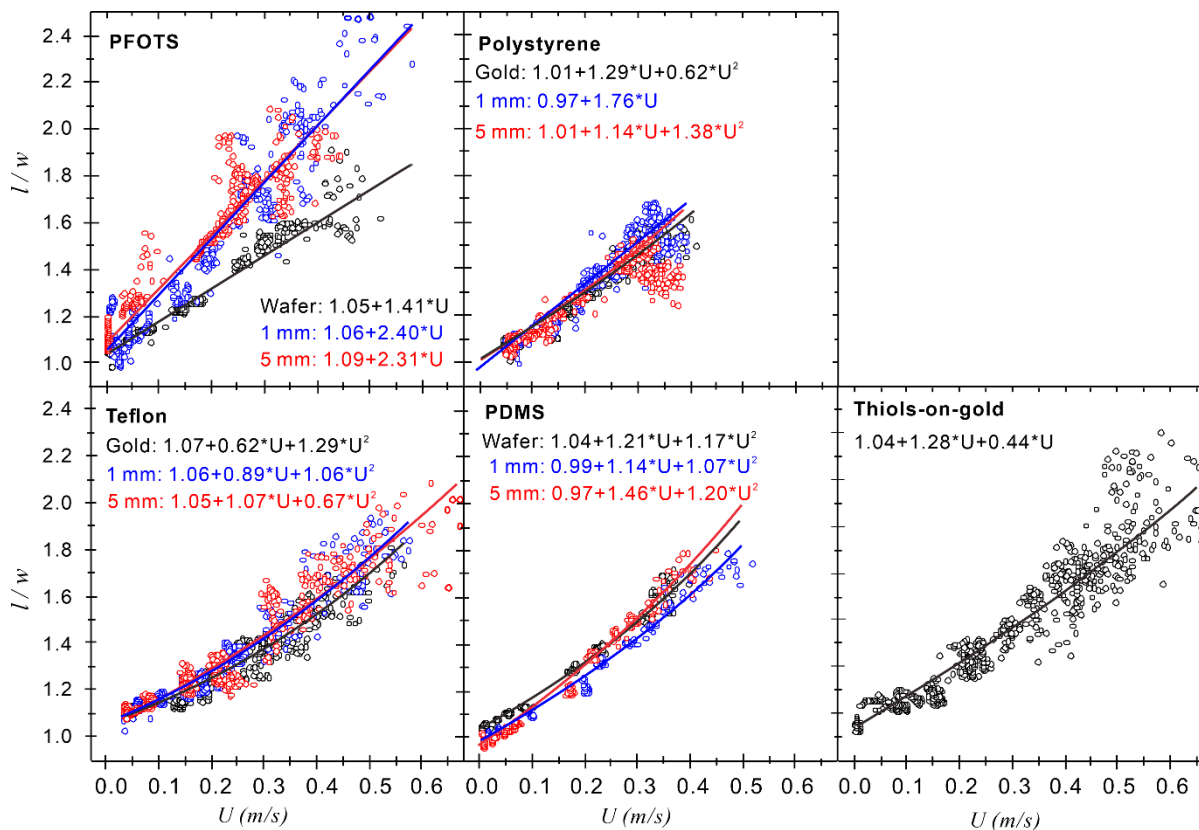
SI 9. Aspect ratio of drops

Figure S8. *Ratio of length-to-width of the contact area of sliding water drops l/w* versus *drop velocity U on different surfaces. The corresponding experiments were carried out at different tilt angles to span a large velocity range. The equations give the best fits. In some cases, linear fits were sufficient. In others we used 2nd order polynomial fits.*

SI 10. Contribution of capillary and bulk viscous force

Although for the analysis of electrostatic force we do not need to know the origin of the reference force, it is still instructive to see how significantly capillary and bulk viscous forces contribute. Therefore, we inserted the respective drop widths, advancing, and receding contact angles into Eq. (1) with $k = 1$, calculated the capillary force (Figure S9, red symbols) and compared it to measured reference forces (Figure S9, black symbols). Capillary forces, which include wedge viscous forces (see SI1), dominate over bulk hydrodynamic viscous forces calculated with Eq. (S1) (Figure S9, blue symbols).
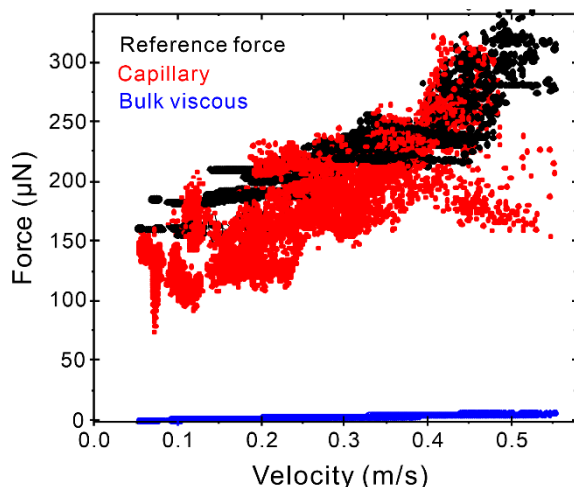
Figure S9. *Force acting on 33 µL water drops sliding down PFOTS-on-Si versus velocity. Reference forces were calculated with $mg\sin\alpha - m^*\frac{dU}{dt}$ (black symbols) for the respective 2nd and 10th drop for tilt angles ranging from 30° to 70°. Capillary forces were calculated with Eq. (1) and k=1. Bulk viscous forces calculated with Eq. (S1) (blue). Results of three experiments are plotted. To complete the graphs in particular at high velocity we added results obtained from 10-14 cm slide length, where the drops were close to their steady-state velocity.*

SI 11. Measured extra force on PFOTS-coated substrates
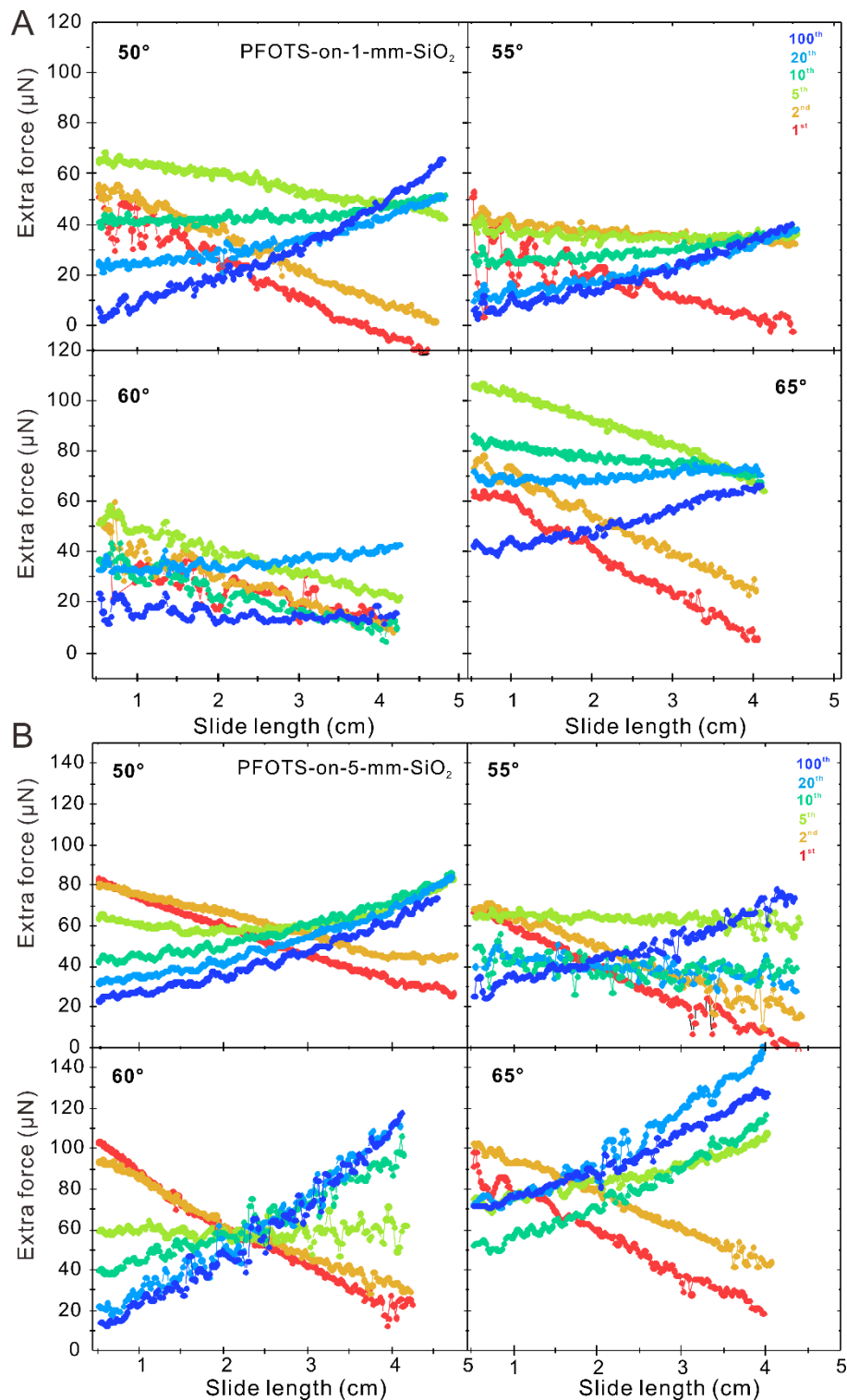

Figure S10. Representative extra force acting on water drops on PFOTS-on-1mm-SiO₂ (A) and PFOTS-on-5mm-SiO₂ (B) measured at different tilt angles. Plotted are results for the 1st, 2nd, 5th, 10th, 20th, 50th and 100th drop. 33 μL drops were deposited at an interval of 1.3 s. Forces were calculated with Eq. (3) with m^*/m=1.05 and $F_r(U) = 156\mu N + 218\frac{\mu Ns}{m}U$.

SI 12. Measurement of drop charges

Drop charges were measured with a tilted plate setup at fixed tilt angle of 50° (details in [25]). Right after deposition, water drops were discharged by touching a grounded electrode at the beginning of their slide path at $L = 0$. After sliding 4 cm, a second electrode measured the drop discharge current via a variable gain sub femto current amplifier (response time: 0.8 ms, DDPCA-300, FEMTO). To reduce noise, the setup was placed in a Faraday cage. Care was taken that the drop disconnected from the electrode before rolling over the end of the sample into a collection dish. Data was recorded using a National Instruments data acquisition card (NI USB-6366 X-Series) and the accompanying LabVIEW software. 45 µL drops were run successively over the surface. A current spike was recorded when each drop touched the electrode (Figure S11). The drop charge was calculated by integrating the current signal over the first 2 ms. Experiments were carried out at a temperature of 21±1°C and a relative humidity of 15-30%.

The charge of the first drop in a series Q_1 was the highest (Figure S12). For the following drops, we measured monotonically decreasing charges. After typically 10-50 drops a saturation charge Q_∞ was reached (table S2). Q_1 and Q_∞ depend on the specific sample and varied by 30%-50% from sample to sample. A possible reason for this variation could be the surface quality of a particular batch, lab temperature, or humidity on the day of the experiment. To get a first estimate of the initial surface charge density σ_0, the decay length λ, and the neutralization time τ, we used the methods and the charging model developed in [25]. The uncertainty from the charge measurement propagated to the estimation of drop charging parameters. We refined these parameters by comparing the experimental first and 100th drop force-vs-slide length curves with predictions by Eqs. (S14) and (S21), respectively.
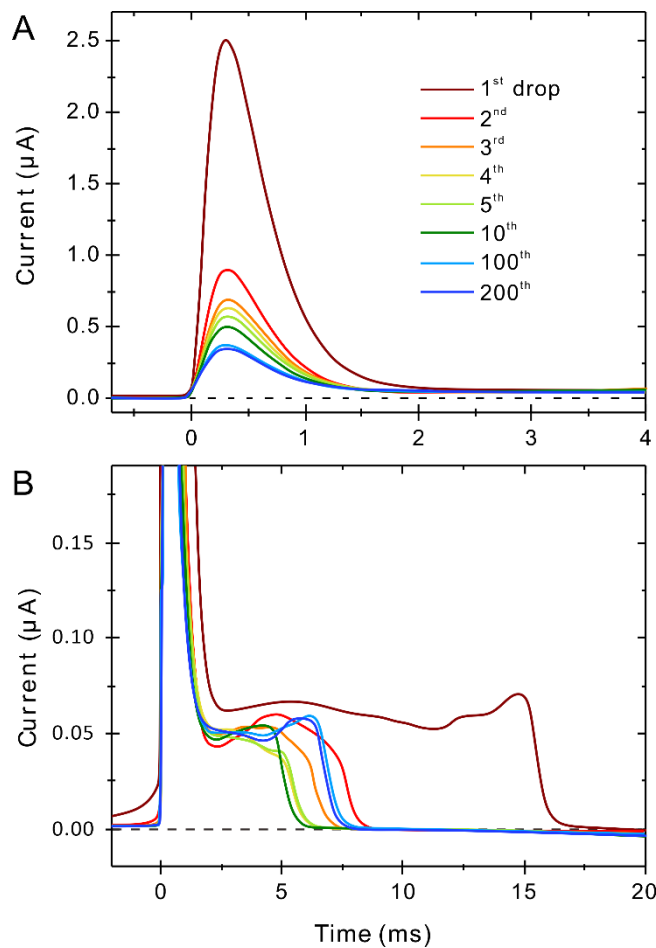
Figure S11. *Typical current traces detected for a series of 45 μL water drops on PFOTS-on-1mm-SiO$_2$ after sliding 4 cm. Currents are plotted at different scales. As the probe electrode touches a sliding drop at $t = 0$, it discharges the accumulated drop charge within 2 ms, causing a positive current peak. This positive peak is due to the flow of electrons towards the positively charged drop, which also implies a negatively charged surface. The total accumulated drop charge was calculated by integrating the initial current peak of 2 ms. While the drop passes the probe electrode, a steady-state current of ≈0.05 μA is generated (B).*
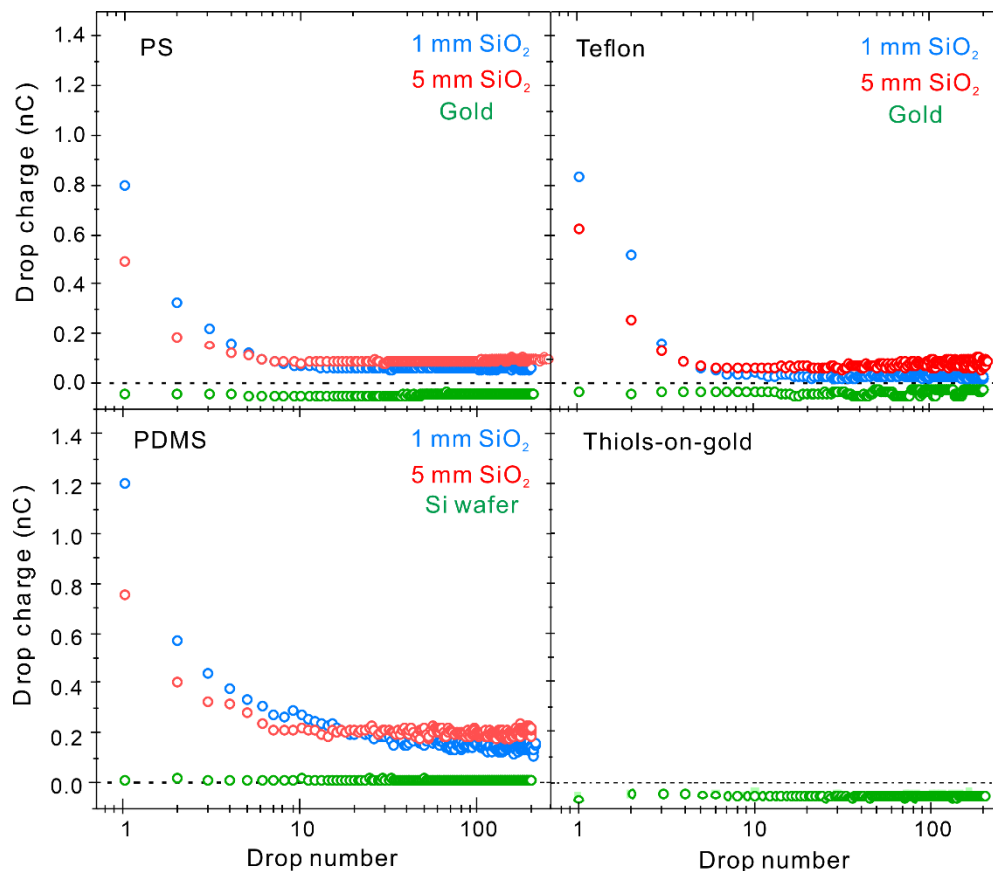
Figure S12. *Measured drop charge-versus-drop number on 20 nm polystyrene films, 60 nm Teflon films, PDMS-brushes on different substrates and monolayers of Perfluorodecanethiol on gold. Results were measured at 50° tilt, 1.5 s intervals between deionized water drops of 45 μL volume after 4 cm slide length.*

On all SiO_2 substrates drops gained a positive charge and deposited a negative charge on the surfaces. In contrast, on silicon wafers or gold, drop charges were much lower. Charge separation was highest on PFOTS-coated SiO_2 followed by PDMS and the polymer films. The saturated drop charge, Q_∞ increased between the 1 mm and 5 mm SiO_2 substrates. This effect was most pronounced on PFOTS. On silicon wafers charging was ≈10 times lower. On gold, the drop charge was even negative. The measured charge values agree well with earlier experiments on PFOTS-coated glass slides [25] and other hydrophobic surfaces.

Table S2. Mean charge of the first drop and drops in steady state in series with 1.5 s time interval between them. V = 45 µl, α = 50°, 4 cm slide length, T = 21±1°C, RH = 15-30%.

Surfaces	Q_1 (nC)	Q_∞ (nC)	τ (s)	λ (cm)	σ_0 ($\mu C/m^2$)
PFOTS-on-Si	0.18±0.04	0.09±0.01			
PFOTS-on-1 mm-SiO$_2$	1.4±0.2	0.26±0.05	12±5	2±0.01	-20±2
PFOTS-on-5 mm-SiO$_2$	1.4±0.09	0.45±0.02	7±5	1.5±0.01	-20±4
PS-on-gold	-0.03±0.01	-0.04±0.01			
PS-on-1 mm-SiO$_2$	0.7±0.2	0.05±0.02	30±7	2.5±0.04	-10±3
PS-on-5 mm-SiO$_2$	0.5±0.01	0.07±0.02	17±7	2±0.012	-7±2
Teflon-on-gold	-0.03±0.01	-0.02±0.001			
Teflon-on-1 mm-SiO$_2$	0.7±0.1	0.03±0.003	70±20	2.8±0.01	-10±3
Teflon-on-5 mm-SiO2	0.7±0.04	0.07±0.02	30±15	3±0.01	-7±1
PDMS-on-Si	0.02±0.001	0.02±0.001			
PDMS-1 mm-SiO$_2$	1.2±0.5	0.15±0.01	12±9.0	4±0.02	-12±5.6
PDMS-5 mm-SiO$_2$	0.6±0.1	0.2±0.02	8±2.1	0.9±0.01	-12±1
Thiols-on-gold	-0.05±0.001	-0.05±0.001			

SI 13. Analytical approximation of the electrostatic force on a drop
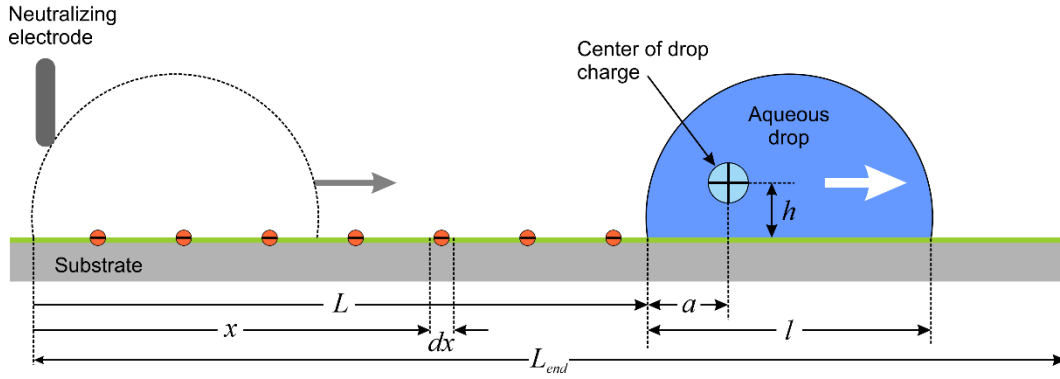
Figure S13. *Parameters used to calculate the electrostatic force.*

We derive an expression for the force between a drop bearing a charge Q interacting with a stripe of surface charges σ distributed over its track of slide length L. Here, we only consider the direct action of the Coulomb force. Charging may also have an effect on contact angles and thus influence drop motion via Eq. (1). For surface potentials up to 800 V such a change of the dynamic advancing contact angle has already been observed [26]. We assume the center of charge of the drop to be at a distance a from the rear side and at a height h (Figure S13). To obtain the electrostatic force we consider the electric field generated by a charge deposited at the solid-air interface on top of an infinitely extending solid half space (eq. 2). A surface charge dq at position x generates an electric field with lateral component

$$dE(x,h) = \frac{dq}{2\pi\varepsilon_0(\varepsilon_S+1)} \frac{L+a-x}{[(L+a-x)^2+h^2]^{3/2}} \qquad . \tag{S4}$$

This is the field strength at a position $L + a$ along the surface and a height h above the solid surface. Along its path, the drop deposits a certain surface charge density $\sigma(x)$. Since the local charge density may vary in a direction perpendicular to the slide direction, σ is taken to be the mean charge density at position x. The deposited charge can be related to the surface charge density on the free solid surface by $dq = \sigma w dx$, where w is the width of the contact area of the drop. Integrating the Coulomb forces of all infinitesimal charge elements dq gives the total lateral force on the drop:

$$F_e^n(L) = \frac{wQ(L)}{2\pi\varepsilon_0(\varepsilon_S+1)}\left[\int_0^L \frac{(L+a-x)\sigma(x)}{((L+a-x)^2+h^2)^{3/2}}dx - \int_{L+l}^{L_{end}} \frac{(x-L-a)\sigma\prime(x)}{((x-L-a)^2+h^2)^{3/2}}dx\right] \tag{S5}$$

Assuming that $h \ll L+a-x$ we get Eq. (5). Here, the sign convention is that a positive force is decelerating the drop. The second term in (S5) takes into account surface charges $\sigma\prime(x)$ situated ahead of the drop which is different from the charge distribution $\sigma(x)$ behind the drop.

To evaluate Eq. (S5), we need to make an assumption about the surface charge distribution. The simplest case is to assume that the drop only interacts with charges deposited by itself. This is the case for the first drop in a series. We further assume that the surface charge density

106

is constant and that no charge on the surface and inside the drop is neutralized. Then, the charge of the first drop is $Q_1 = -Lw\sigma_1$, leading to an electrostatic force of

$$F_e^1(L) = -\frac{Lw^2\sigma_1^2}{2\pi\varepsilon_0(\varepsilon_S+1)}\left[\frac{1}{\sqrt{a^2+h^2}} - \frac{1}{\sqrt{(L+a)^2+h^2}}\right] \qquad . \tag{S6}$$

We used the superscript "1" to indicate that this is the first drop sliding down an initially neutral surface. σ_1 is the surface charge density deposited by the first drop.

A constant surface charge density is, however, not realistic. More realistic is a charge density that saturates exponentially with slide length [25]. Again, considering the first drop and assuming that a drop only interacts with charges deposited by itself, the corresponding surface charge density and total charge of the drop can be parametrized as

$$\sigma_1 = \sigma_0 e^{-x/\lambda} \text{ and } Q_1 = -w\lambda\sigma_0\left(1 - e^{-L/\lambda}\right) \tag{S7}$$

Here we assumed that a possible neutralization of the surface is very slow compared to the sliding time of the drop. Inserting these two expressions into the first term of Eq. (5) leads to

$$F_e^1(L) = -\frac{w\lambda\sigma_0\left(1-e^{-L/\lambda}\right)w\sigma_0}{2\pi\varepsilon_0(\varepsilon_S+1)}\int_0^L \frac{e^{-x/\lambda}}{(L+a-x)^2}dx = -C\left(1 - e^{-L/\lambda}\right)\int_0^L \frac{e^{-x/\lambda}}{(L+a-x)^2}dx \tag{S8}$$

The second term in Eq. (5) was not considered because we only take the charge deposited by the drop into account; thus, there is no charge ahead of the drop. Here, the constant $C = w^2\sigma_0^2\lambda/[2\pi\varepsilon_0(\varepsilon_S + 1)]$ summarizes all slide length-independent parameters. Partial integration yields

$$F_e^1(L) = -C\left(1 - e^{-L/\lambda}\right)\left\{\left[-\frac{e^{-x/\lambda}}{L+a-x}\right]_0^L - \frac{1}{\lambda}\int_0^L \frac{e^{-x/\lambda}}{L+a-x}dx\right\} \tag{S9}$$

Substitution with $t = \frac{L+a-x}{\lambda}$ gives

$$F_e^1(L) = C\left(1 - e^{-L/\lambda}\right)\left\{\frac{1}{a}e^{-\frac{L}{\lambda}} - \frac{1}{L+a} - \frac{1}{\lambda}e^{-\frac{L+a}{\lambda}}\int_{(L+a)/\lambda}^{a/\lambda} \frac{e^t}{t}dt\right\} \tag{S10}$$

The integral in Eq. (S10) has the form of the exponential integral function:

$$Ei(z) = \int_{-\infty}^z \frac{e^t}{t}dt \qquad \text{for } z > 0 \tag{S11}$$

With this function, we can calculate the force as

$$F_e^1(L) = C\left(1 - e^{-L/\lambda}\right)\left\{\frac{1}{a}e^{-\frac{L}{\lambda}} - \frac{1}{L+a} - \frac{1}{\lambda}e^{-\frac{L+a}{\lambda}}\left[Ei\left(\frac{a}{\lambda}\right) - Ei\left(\frac{L+a}{\lambda}\right)\right]\right\} \tag{S12}$$

To evaluate this expression, the series representation of the exponential integral can be employed,

$$Ei(z) = 0.5772 + \ln(|z|) + \sum_{n=1}^\infty \frac{z^n}{n!\,n}, \tag{S13}$$

where 0.5772 is the Euler-Mascheroni constant. Using Eq. (S13), we can write

$$F_e^1(L) = \frac{C}{\lambda}\left(1 - e^{-L/\lambda}\right)\left\{\frac{\lambda}{a}e^{-\frac{L}{\lambda}} - \frac{\lambda}{L+a} - e^{-\frac{L+a}{\lambda}}\left[\ln\left(\frac{a}{L+a}\right) + \sum_{k=1}^{\infty}\frac{a^k - (L+a)^k}{\lambda^k k!k}\right]\right\} \qquad \text{(S14)}$$

For large arguments, convergence of this series can be slow. For example, to reach an accuracy of 5% and 1% at $z = 5$ one needs to take $n = 8$ and 10 terms, respectively. For $z = 10$ the series needs to be considered up to $n = 14$ and 16, respectively. Many modern mathematical programs, such as Wolfram Alpha or IgorPro (Wavemetrics) provide built-in functions for the effective numerical computation of the exponential integral function.

The slide length-dependent part of Eq. (S14) (Dimensionless force) is plotted in figure S14A. A maximum is observed at $L/\lambda \approx 0.8$. The force decreases with increasing a/λ; thus, the more the center of charge is shifted towards the rear of the drop, the stronger the electrostatic retardation becomes. This strong dependence on a/λ results from interactions with surface charges in the close vicinity of the drop, for which the analytical model is not realistic. To better quantify these near-field interactions, we have developed the numerical model described in the following section. In terms of the analytical model, a is regarded as a parameter that describes the near-field interactions in an effective manner.
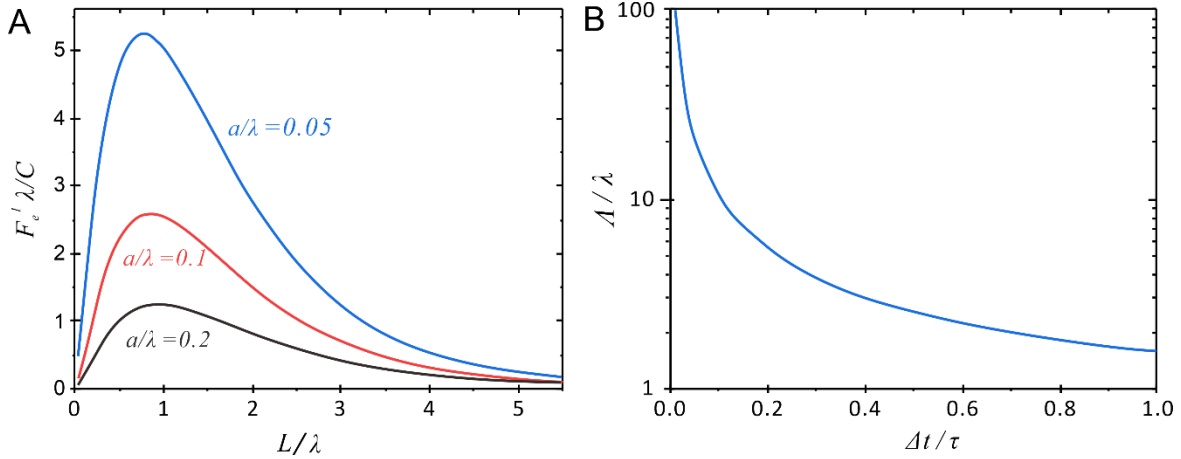
Figure S14. *(A) Plot of dimensionless force $F_e^1\lambda/C$ versus L/λ for $a/\lambda = 0.05$, 0.1 and 0.2 calculated with Eq. S14. (B) Ratio of Λ/λ-versus-$\Delta t/\tau$ calculated with Eq. (S15).*

For a succession of drops sliding over the surface at time intervals of Δt, the charge distribution and the drop charge are altered by the presence of surface charges of previous drops. Once deposited, the surface charge is neutralized with a characteristic neutralization time of τ. To calculate the charge distribution for following drops, a recursive approach is required. Thus, a closed analytical description for the electrostatic force on successive drops is difficult. Nevertheless, a relatively simple analytical description is possible for the saturated drop charge distribution after a large number ($n \to \infty$) of drops. Here, the surface charge density and the drop charge are given by [25]:

$$\sigma_\infty(x) = \sigma_0 e^{-x/\Lambda}, \quad Q_\infty(L) = -\sigma_0\lambda w\left(1 - e^{-L/\Lambda}\right) \text{ with } \Lambda = \frac{\lambda}{1 - e^{-\Delta t/\tau}} \qquad . \qquad \text{(S15)}$$

For short time intervals the modified saturation slide length, Λ, is much larger than the initial saturation slide length, λ (Figure S14B). With increasing drop interval time, $\Delta\tau$, Λ decreases and eventually approaches the initial λ for $\Delta t/\tau \gg 1$.

Using these expressions, we calculate the electrostatic force caused by the charges behind the drop in analogy to Eq. (S14):

$$F_{eb}^\infty(L) = \frac{C}{\Lambda}\left(1 - e^{-L/\Lambda}\right)\left\{\frac{\Lambda}{a}e^{-\frac{L}{\Lambda}} - \frac{\Lambda}{L+a} - e^{-\frac{L+a}{\Lambda}}\left[Ei\left(\frac{a}{\Lambda}\right) - Ei\left(\frac{L+a}{\Lambda}\right)\right]\right\}$$

$$= \frac{C}{\Lambda}\left(1 - e^{-L/\Lambda}\right)\left\{\frac{\Lambda}{a}e^{-\frac{L}{\Lambda}} - \frac{\Lambda}{L+a} - e^{-\frac{L+a}{\Lambda}}\left[\ln\left(\frac{a}{L+a}\right) + \sum_{k=1}^\infty \frac{a^k-(L+a)^k}{\Lambda^k k!k}\right]\right\} \quad \text{(S16)}$$

In addition, surface charges ahead of the drop are accelerating the drop. Their contribution is given by

$$F_{eb}^\infty(L) = \frac{\sigma_0^2 w^2 \lambda}{2\pi\varepsilon_0(\varepsilon_S+1)}e^{-\Delta t/\tau}\left(1 - e^{-L/\lambda}\right)\int_{L+l}^{L_{end}}\frac{\sigma}{(x-L-a)^2}dx$$

$$= Ce^{-\Delta t/\tau}\left(1 - e^{-L/\Lambda}\right)\int_{L+l}^{L_{end}}\frac{e^{-x/\Lambda}}{(x-L-a)^2}dx . \quad \text{(S17)}$$

The factor $e^{-\Delta t/\tau}$ takes into account that after the time interval Δt the charge left by the previous drop has been partially neutralized.

Partial integration and substitution with $t = -(x - L - a)/\Lambda$ gives

$$F_{eb}^\infty(L) = Ce^{-\Delta t/\tau}\left(1 - e^{-L/\lambda}\right)\left\{\left[\frac{e^{-x/\lambda}}{x-L-a}\right]_{L+l}^{L_{end}} + \frac{1}{\Lambda}e^{-\frac{L+a}{\Lambda}}\int_{-(l-a)/\Lambda}^{-(L_{End}-L-a)/\Lambda}\frac{e^t}{t}dt\right\} \quad \text{(S18)}$$

Here, the argument of the exponential integral as defined in Eq. (S11) is negative. We therefore have to use the following function

$$Ei(-z) = -E_1(z) = -\int_z^\infty \frac{e^{-t}}{t}dt \quad \text{for } z > 0 \quad \text{(S19)}$$

Where $E_1(z)$ is defined as

$$E_1(z) = -0.5772 - \ln(|z|) - \sum_{n=1}^\infty \frac{(-z)^n}{n!\,n}$$

Using these definitions, we get:

$$F_{eb}^\infty(L) = \frac{C}{\Lambda}e^{-\Delta t/\tau}\left(1 - e^{-L/\lambda}\right)\left\{\frac{\Lambda e^{-L_{end}/\Lambda}}{L_{end}-L-a} - \frac{\Lambda e^{-\frac{L+l}{\Lambda}}}{l-a} - e^{-\frac{L+a}{\Lambda}}\left[E_1\left(\frac{L_{End}-L-a}{\Lambda}\right) - E_1\left(\frac{l-a}{\Lambda}\right)\right]\right\}$$

$$= \frac{C}{\Lambda}e^{-\Delta t/\tau}\left(1 - e^{-L/\lambda}\right)\left\{\frac{\Lambda e^{-\frac{L_{end}}{\Lambda}}}{L_{end}-L-a} - \frac{\Lambda e^{-\frac{L+l}{\Lambda}}}{l-a} - e^{-\frac{L+a}{\Lambda}}\left[\ln\left(\frac{l-a}{L_{end}-L-a}\right) + \sum_{k=1}^\infty \frac{(L_{end}-L-a)^k-(l-a)^k}{\Lambda^k k!k}\right]\right\}$$

$$\text{(S20)}$$

The total electrostatic force acting on drop number $n > 50$ is the sum of both contributions:

$$F_e^\infty(L) = F_{ea}^\infty(L) + F_{eb}^\infty(L) \quad \text{for } L < L_{end} - l. \quad \text{(S21)}$$

The different contributions to the total force are shown in Figure S15. Interestingly, the accelerating force of the charges ahead of the drop is stronger at the beginning before the

decelerating force of the charges behind the drop start to dominate. At the end of the slide path, there are no more charges ahead and the accelerating force contribution vanishes at $L_{end} - l$, leading to a steep increase in the drop force.
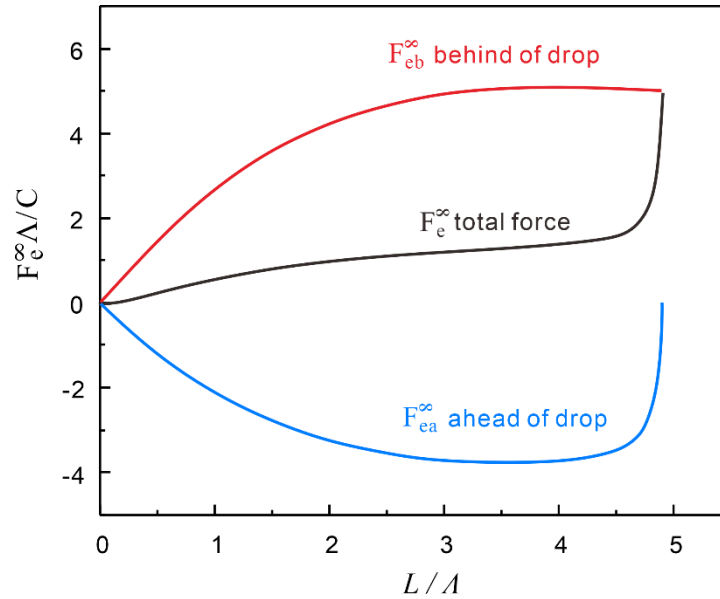

Figure S15. *Dimensionless force $F_e^{\infty}\Lambda/C$ on a drop after a long (>50) succession of drops as a function of slide length normalized with respect to the saturation slide length, L/Λ. The total force acting on the drop (black curve) consists of an accelerating force coming from charges ahead of the drop (blue curve) and a decelerating force from charges behind the drop (red curve). Parameters used in this example: Λ = 4 cm, w = 4 mm, l = 5 mm, a = 2 mm, L_{end} = 20 cm.*

SI 14. Numerical computation of the electrostatic force on a drop

One of the assumptions in Eq. (4) was to neglect the presence of the grounded back-electrode. To account, among other things, for the presence of the back electrode, we carried out numerical calculations of the electric field distribution based on Poisson's equation and the electrostatic force. As it turned out, by choosing the position of the center of charge in the drop appropriately we can account for the presence of the back electrode. In figure S16 the two-dimensional simulation domain and the mesh are displayed. The domain includes the substrate, the drop, and the surrounding air.
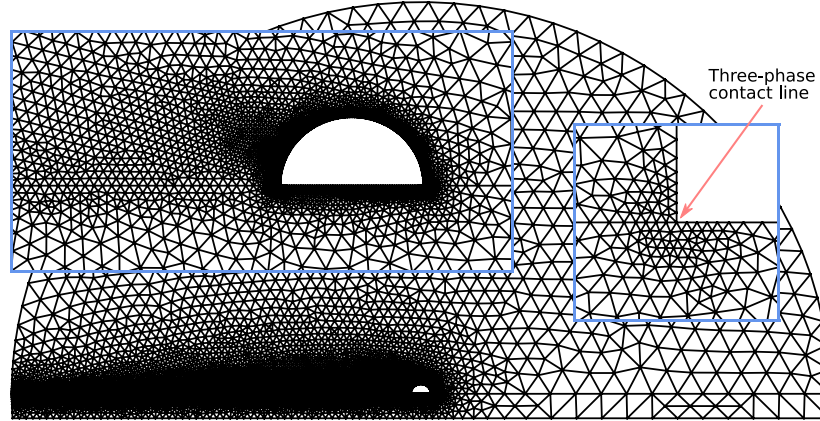
Figure S16. *Overview of the simulation domain and the grid including the substrate, the drop, and the surrounding air. The insets display the finer mesh around the drop and the highly refined mesh around the contact line (the physical height shown in the latter inset is 1 μm).*

The fundamental equation of electrostatics is Gauss's law. If the media are linear, isotropic, homogeneous and do not carry a space charge we end up with Poisson's equation $\Delta\varphi = 0$ in the surrounding air and in the substrate, with appropriate boundary conditions at the interfaces between different materials.

We assume that the drop is a conductor and can be modelled as a surface with a constant potential φ_{drop}. Even for non-conductive bodies with a dielectric permittivity much higher than their surrounding (such as water) this boundary condition is a good approximation. The value of φ_{drop} cannot be specified directly but is given implicitly by the total charge of the drop Q. Q and φ_{drop} are related by solving Poisson's equation and integrating $\int_{drop} \varepsilon_0 \vec{E} \cdot \vec{n} ds$ along the surface of the drop; here ε_0 is the vacuum permittivity and $\vec{n}$ and ds are the normal vector and the infinitesimal line element along the drop's surface, respectively. To fix the potential on the drop's surface, we iteratively vary φ_{drop} until the calculated drop charge is equal to the real drop charge.

At the interface between the substrate and air the electric field needs to fulfil the boundary condition $-(\varepsilon_s \vec{\nabla}\varphi_s - \vec{\nabla}\varphi_a) \cdot \vec{n} = \frac{\sigma(x)}{\varepsilon_0}$, where ε_s is the dielectric permittivity of the substrate, $\sigma(x)$ is the surface charge density on the substrate, $\vec{n}$ is the normal vector of the substrate,

and φ_s and φ_a are the electrostatic potentials infinitesimally away from the solid surface inside the substrate and inside air, respectively. To complete the set of boundary conditions, we assume that the surrounding circular boundaries are far away and that the normal component of the electric field vanishes in the far field, $\vec{\nabla}\varphi_{farfield} \cdot \vec{n} = 0$. We further assume that the electrode below the substrate is grounded, $\varphi_{electrode} = 0$. After the electric field fulfilling the equations and the boundary conditions above is obtained, the electrostatic force acting on the drop can be calculated from the integral of the Maxwell stress tensor on the drop's surface $F_e = \frac{\varepsilon_0}{2} \int_{drop} \vec{E}^2 \, \vec{n} \cdot \vec{n}_x ds$, where $\vec{n}_x$ is the normal vector pointing in sliding direction.

We implemented the equations and boundary conditions above in variational form into the open-source software package FEniCS [27]. The solution was obtained by the common finite-element method. To determine the potential on the drop surface φ_{drop} we solved a tracking-type optimal control problem utilizing *dolfin-adjoint* to automatically compute the gradient [28]. The finite-element mesh was generated with *Gmsh* (https://gmsh.info/). The mesh was systematically refined around the substrate-air interface as well as the drop-air interface with cell sizes as low as 50 µm. In the contact line region the minimal cell size was only 50 nm, see the right inset in figure S16.

The problem parameters include the drop shape and size, contact angle, slide length, charge distribution, substrate thickness, and dielectric permittivity of the solid. Here, we consider a fixed, circular-arc shaped drop with contact angles $\Theta_a = \Theta_r = 90°$ and diameter $w = 4$ mm on a substrate with $\varepsilon_s = 3.9$. The charge density behind the drop is supposed to be homogenous and constant at $\sigma = 5$ µC/m². There is no surface charge ahead of the drop. The resulting electrostatic force is plotted versus the sliding length L in figure S17 (symbols) for different substrate thicknesses. The electrostatic force scales linearly with slide length. With decreasing thickness of the substrate, the screening influence of the electrode becomes stronger, which results in lower overall electrostatic forces acting on the drop.

In figure S17 we also compare electrostatic forces calculated with the analytical model (black lines, Eq. S5) with the numerically calculated forces (symbols). The analytical model and the simulations predict the same linear scaling of the force with the slide length. As long as h is small the influence of h on the resulting force is negligible (lines, Figure S17); therefore, we set $h=0$. Furthermore, it turned out that, by shifting the effective drop charge away from the drop's center to different horizontal positions a, the analytical model can fit the simulations. Thus, phenomenologically we can take the presence of a back-electrode into account by choosing the right value of a. One reason for this could be that for a vanishing substrate thickness the charge on the drop surface is symmetrically distributed (which results in a vanishing horizontal force on the drop, compare the smaller forces for thinner substrates in Figure S17), whereas for larger thicknesses the charges on the substrate induce significant charges at the rear end of the drop. In addition, our simulations show that a large fraction of the charges is located in the utmost vicinity of the contact line.

In summary, the numerical calculations confirm the validity and scaling of Eq. (4). Good agreement was achieved when the center of charge of the drop was placed directly on the surface (h = 0). The choice of the parameter a is dictated by the thickness of the substrate. We find that for 1 mm and 5 mm thick substrates, setting $a = 2$ mm and $a = 0.8$ mm, respectively, can mimic the shielding effect of the back electrode.
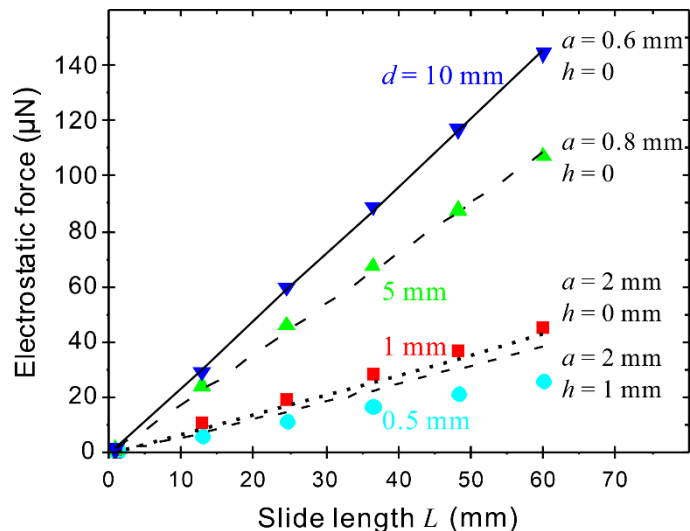

Figure S17. *Electrostatic force on a drop calculated from the solution of Poisson's equation (symbols) and the analytical model for different positions of the effective point charge (eq. S6, lines) as well as slide lengths L and substrate thicknesses d. Here we assumed a constant charge density for the deposited charge of $\sigma_1 = 5$ $\mu C/m^2$ behind the drop.*

SI 15. Drop velocity profiles on conducting and high-permittivity substrates of PS, Teflon, PDMS, and thiol-coated surfaces
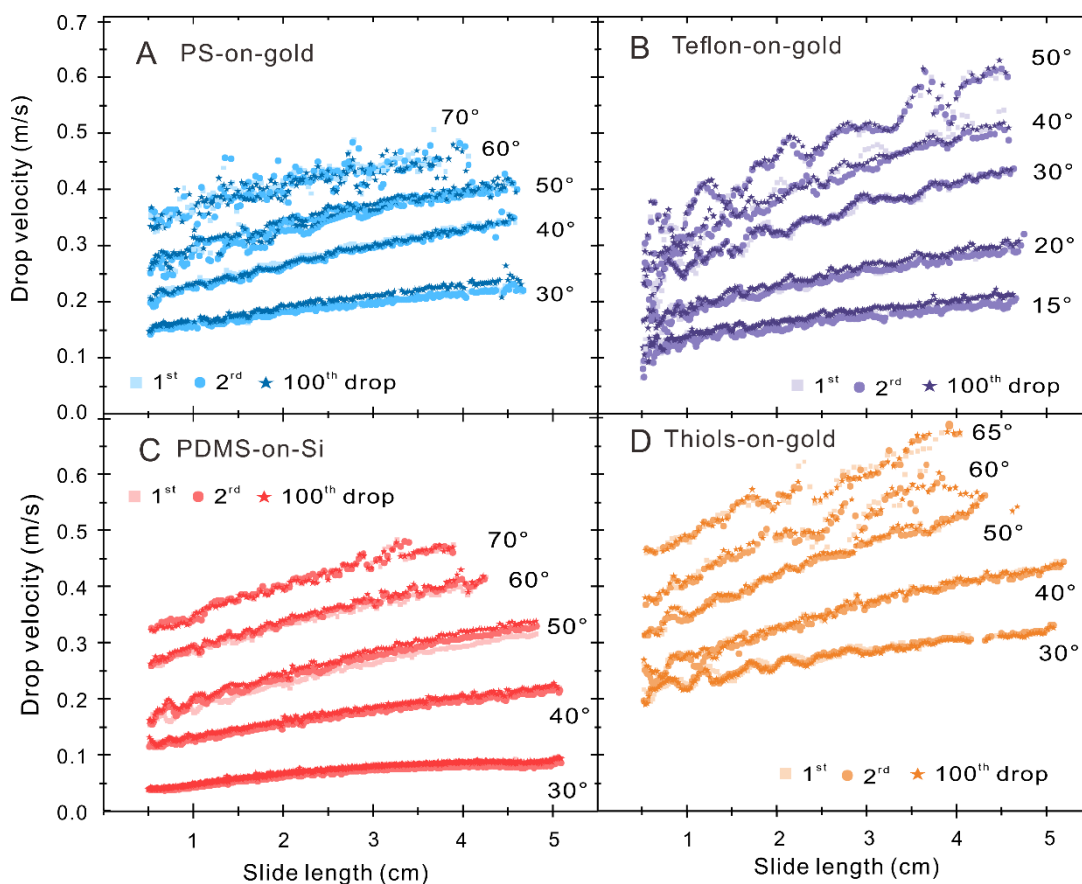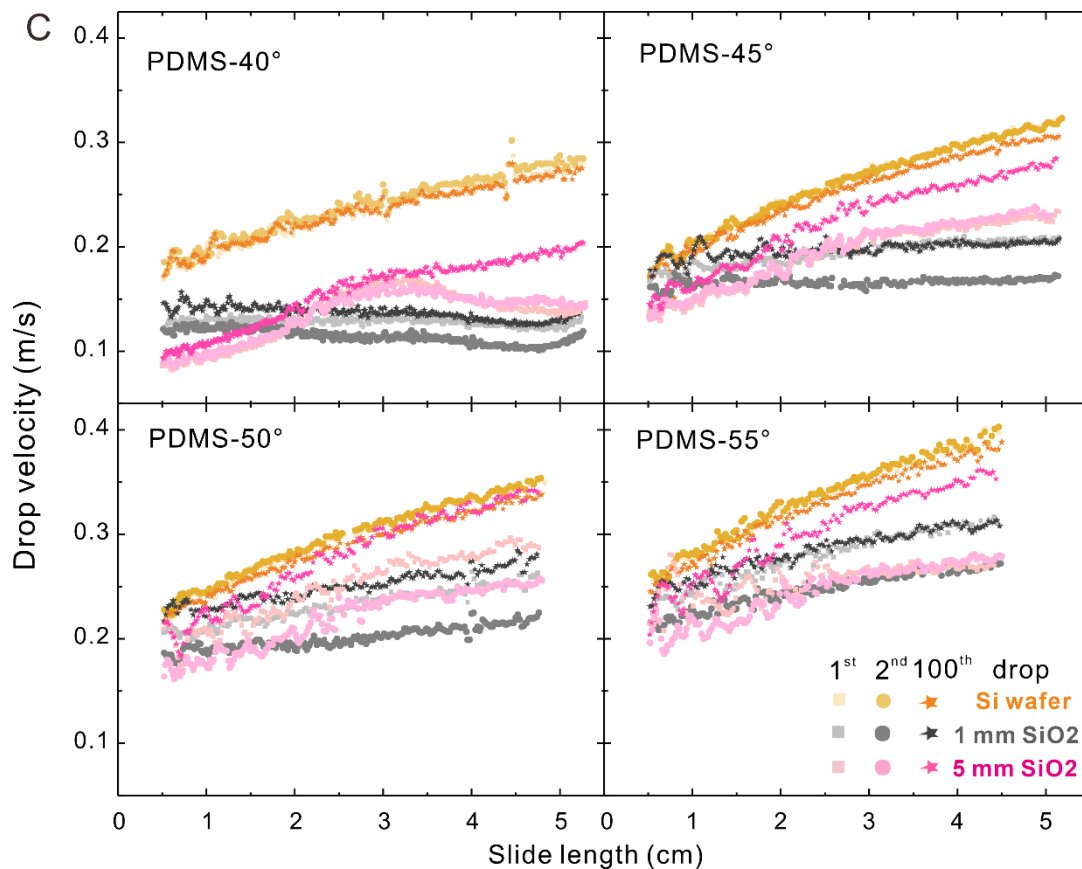

Figure S18*. Representative results for drop velocity-versus-slide length measured at different tilt angles. (A) 20 nm PS films on gold, (B) 60 nm thick Teflon films on gold, (C) PDMS on silicon wafers, and (D) Perfluorodecanethiol on gold. Results for drop number 1 (rectangle), 2 (circle), and 100 (star) are plotted. The lower tilt angle was given by the requirement that drops slide at all; at lower tilt angels the drops did not move. The maximal tilt angle was given by the requirement of having a stable steady state shape of the drop. At higher tilt angles and thus higher velocities the drop shape analysis started to fail.*
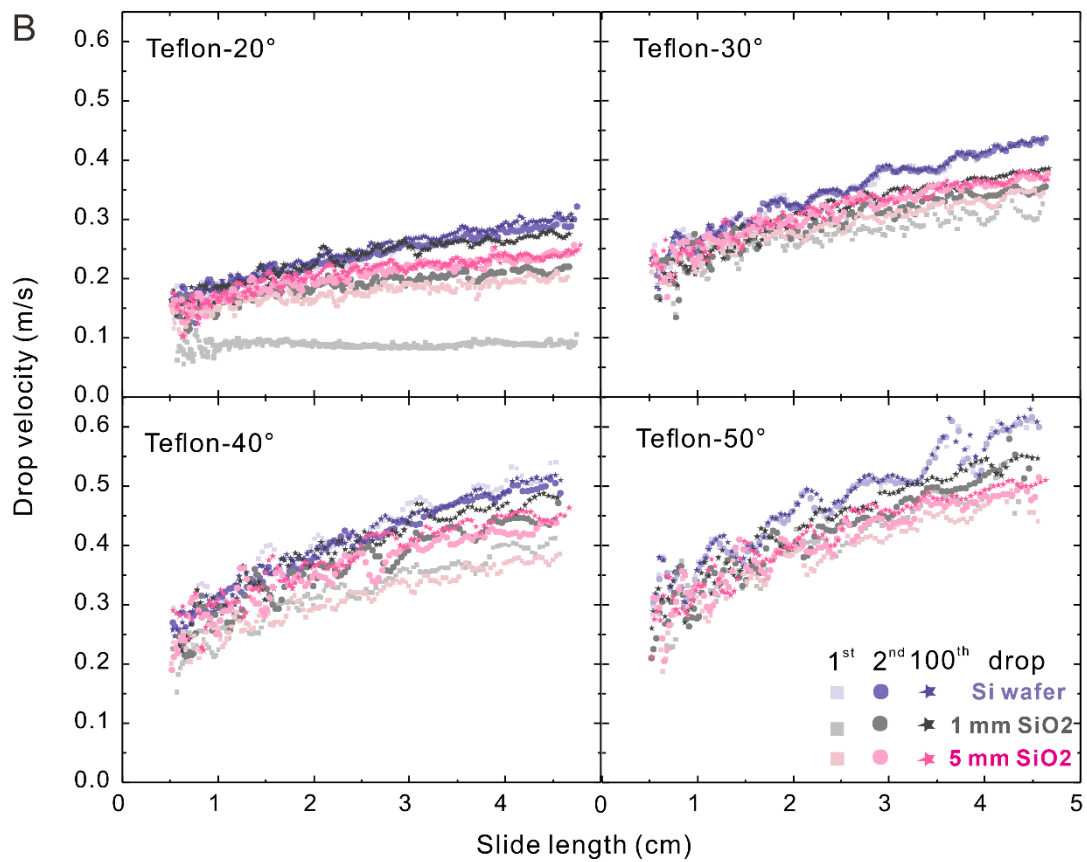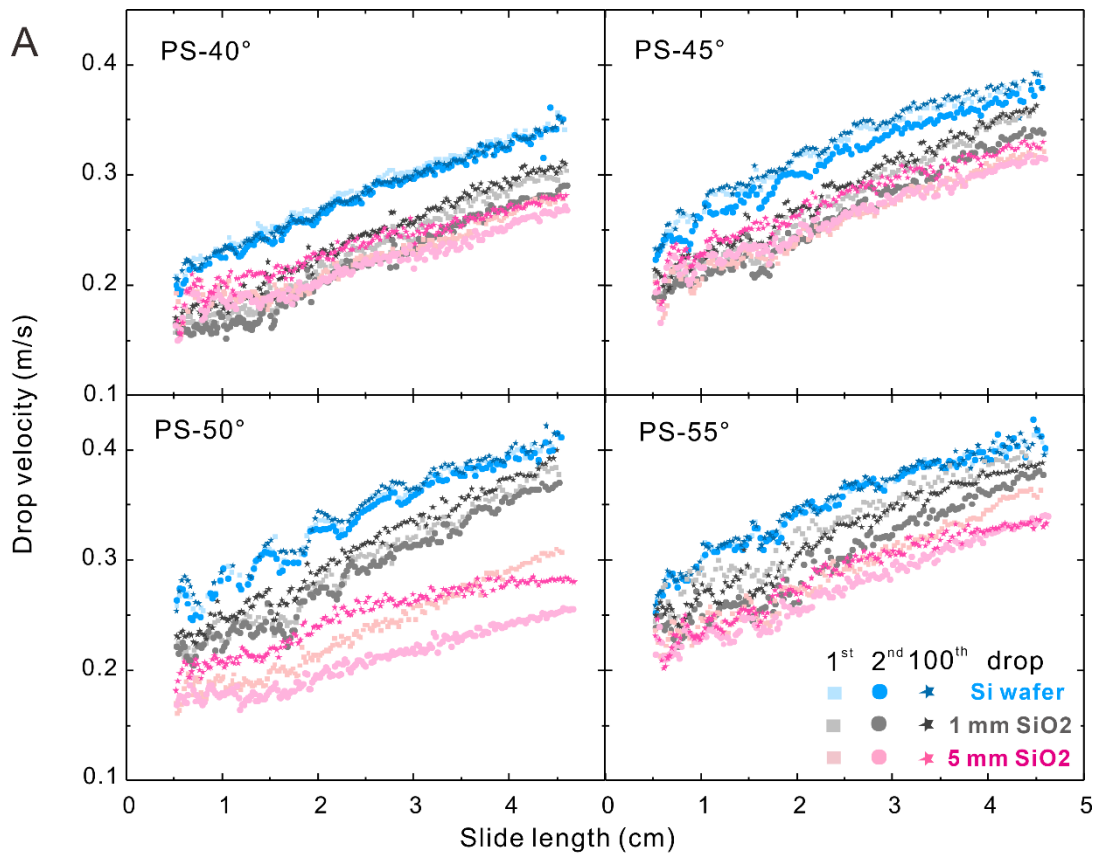
Figure S19. *Representative results for drop velocity-versus-slide length measured at different tilt angles. (A) 20 nm PS films, (B) 60 nm thick Teflon films, and (C) PDMS on 1 mm SiO₂ (blue symbols) and 5 mm SiO₂ (red symbols). For comparison also the results obtained on Si wafers (A) or gold (B, C) are plotted as black symbols. Results for drop number 1 (rectangle), 2 (circle), and 100 (star) are plotted.*

116

Figure S20*. Reference forces measured on different substrates and the linear fit (black lines) derived from velocities up to 0.4 m/s. (A) PS-on-gold fitted by $F_r = 74\ \mu N + 398\frac{\mu Ns}{m} \cdot U$, (B) Teflon-on-gold fitted with $F_r = 48\ \mu N + 175\frac{\mu Ns}{m} \cdot U$, (C) PDMS-on-Si fitted by $F_r = 141\ \mu N + 269\frac{\mu Ns}{m} \cdot U$, and (D) thiols-on-gold fitted with $F_r = 120\ \mu N + 103\frac{\mu Ns}{m} \cdot U$. The water drops of 33 µL volume were deposited at 1.3 s intervals. The results were obtained from the respective 2nd and 10th drop for tilt angles of between 15 and 70°. To complete the graph in particular at high velocity we added results obtained from 10-14 cm slide length, where the drops had reached or were close to their steady state velocity.*

## SI 17. Measured extra forces of drops on PS, Teflon, and PDMS-coated surfaces
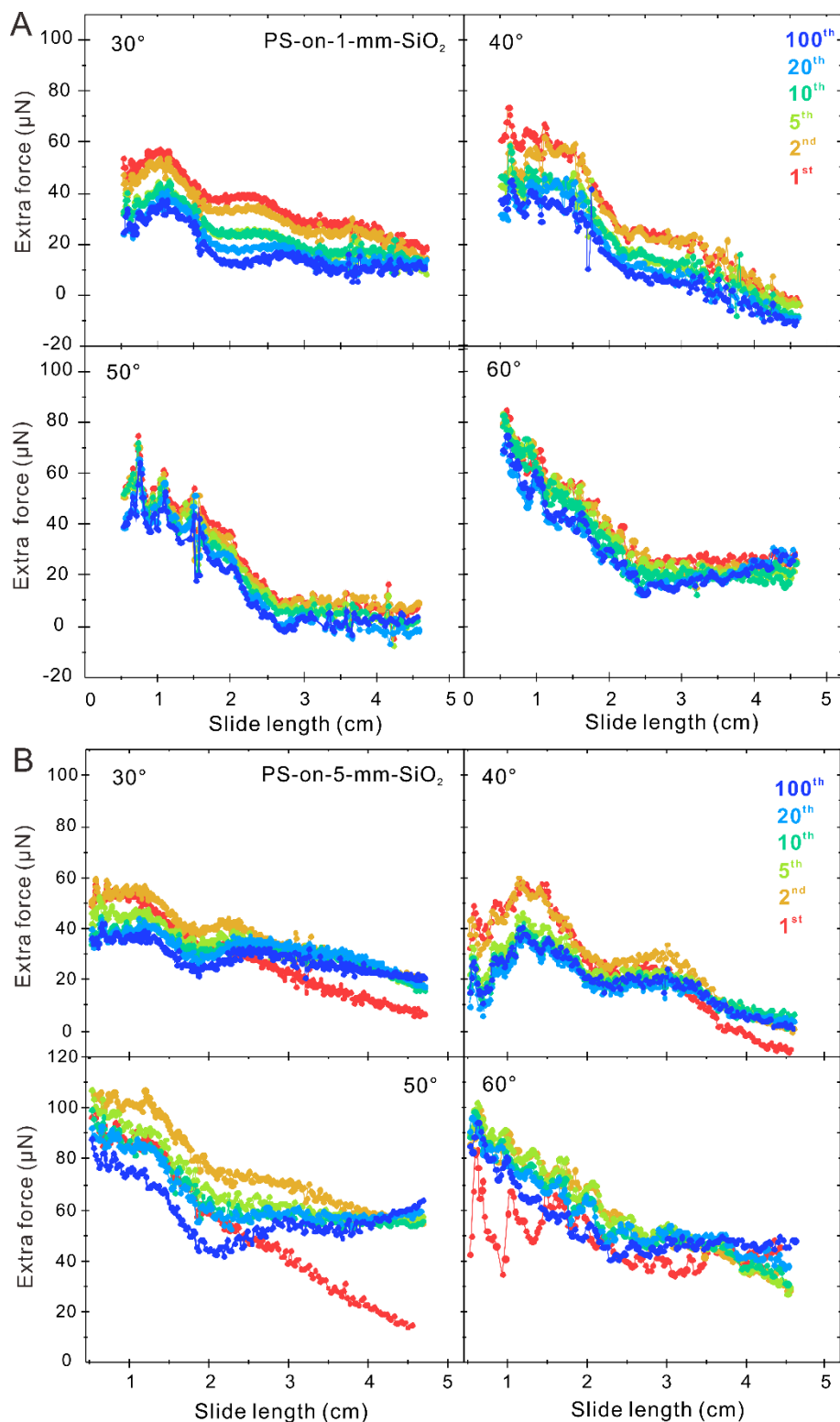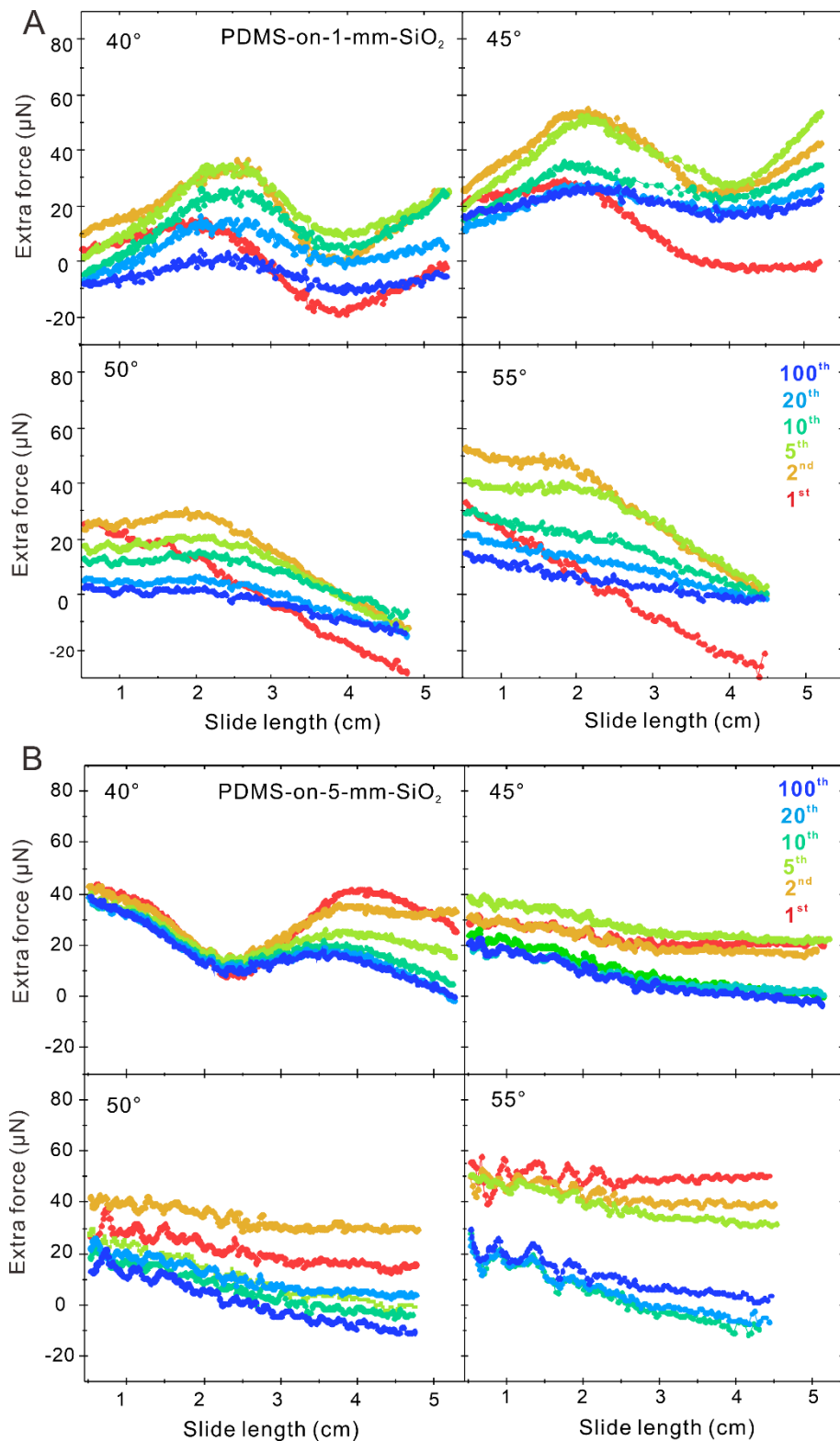

Figure S21. (A) Examples for extra forces acting on water drops sliding down PS-on-1-mm-SiO$_2$ and (B) PS-on-5-mm-SiO$_2$ for different tilt angles. Plotted are results for the 1st, 2nd, 5th, 10th, 20th, and the 100th drop. 33 µL drops were deposited at an interval of 1.3 s. Force were calculated with Eq. (3) using m*/m=1.05 and $F_r = 74$ µN $+ 398 \frac{\mu Ns}{m} \cdot U$.

118
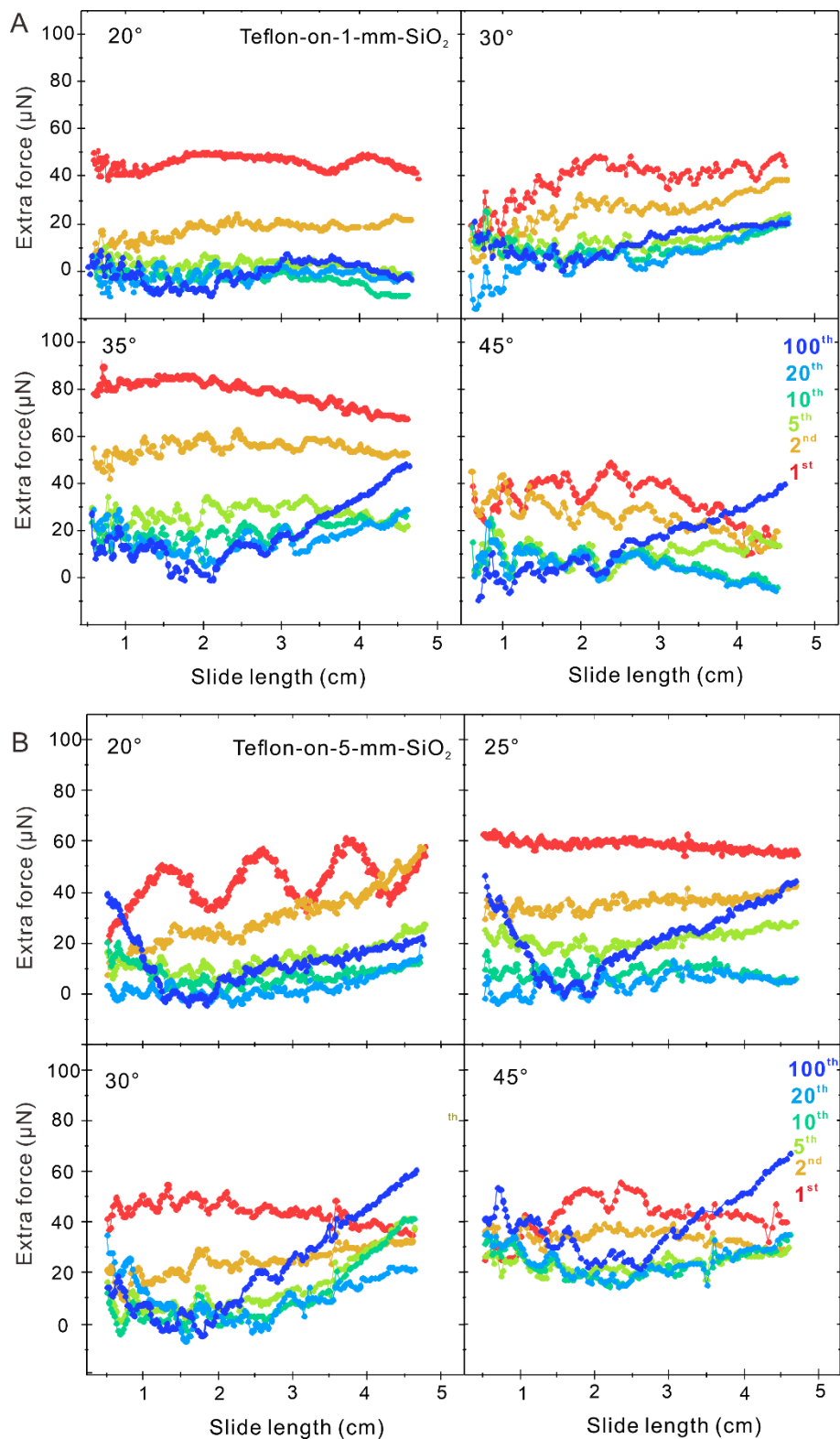
Figure S22. *(A) Examples for extra forces acting on water drops sliding down Teflon-on-1-mm-SiO₂ and (B) Teflon-on-5-mm-SiO₂. For different tilt angles. Plotted are results for the 1st, 2nd, 5th, 10th, 20th, and the 100th drop. 33 μL drops were deposited at an interval of 1.3 s. Force were calculated with Eq. (3) using m*/m=1.05 and $F_r = 48\ \mu N + 175 \frac{\mu Ns}{m} \cdot U$.*

Figure S23. *(A) Examples for extra forces acting on water drops sliding down PDMS-on-1-mm-SiO$_2$ and (B) PDMS-on-5-mm-SiO$_2$ for different tilt angles. Plotted are results for the 1st, 2nd, 5th, 10th, 20th, and the 100th drop. 33 μL drops were deposited at intervals of 1.3 s. Force were calculated with Eq. (3) using m*/m=1.05 and $F_r = 141$ μN $+ 269 \frac{μNs}{m} \cdot U$.*

120

SI 18. Measured extra forces of drops of aqueous NaCl solutions and ethylene glycol
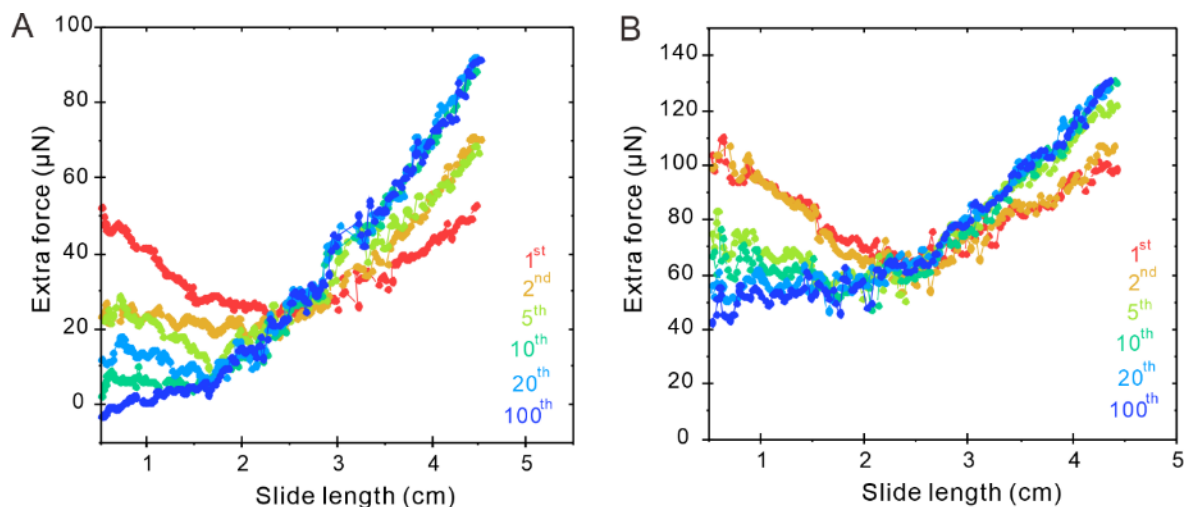
Figure S24. (A) Examples for extra forces acting on water drops containing 0.1 mM NaCl and (B) 1 M NaCl sliding down PFOTS-on-1-mm-SiO$_2$ at 65° tilt. Plotted are results for the 1st, 2nd, 5th, 10th, 20th, and the 100th drop. 33 μL drops were deposited at an interval of 1.3 s. Force were calculated with Eq. (3) using m*/m=1.05 and $F_r = 225$ μN $+ 89\frac{\mu Ns}{m} \cdot U$ for 0.1 mM and $F_r = 151$ μN $+ 178\frac{\mu Ns}{m} \cdot U$ for 1 M NaCl.
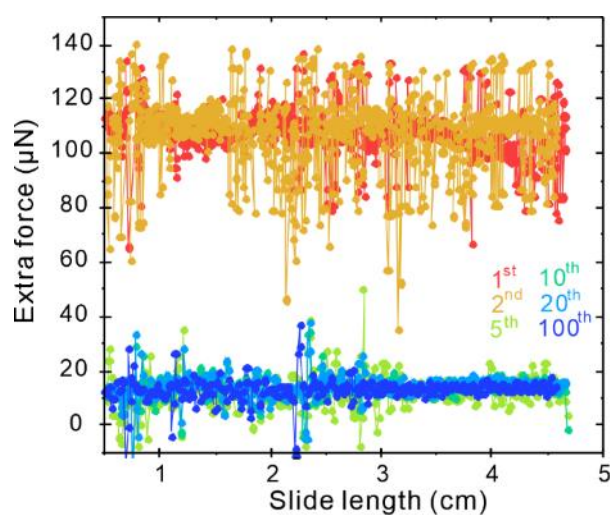
Figure S25. Examples for extra forces acting on drops of ethylene glycol sliding down Teflon-on-1-mm-SiO$_2$ at 55° tilt. Plotted are results for the 1st, 2nd, 5th, 10th, 20th and the 100th drop. 18.5 μL drops were deposited at an interval of 1.5 s. Force were calculated with Eq. (3) neglecting the acceleration term because the drops reached a steady state velocity even after 0.5 cm. The drops were exposed to air at ≈30% relative humidity and may have adsorbed water for the air.

SI 19: Video of water drops impacting on Teflon-coated surfaces

20 µL water drops falling 2.5 cm and impacting on Teflon-on-gold, Teflon-on-1-mm-SiO$_2$ and Teflon-on-5-mm-SiO$_2$. The impact velocity was U=0.70 m/s leading to a Weber number of $We = \rho U^2 d/\gamma = 23$, where d=3.4 mm is the drop diameter. In the first experiment the surfaces were held horizontally. In the second experiment they were tilted by 10°.

SI 20: The influence of polymer film thickness on drop mobility

To check how the thickness of the polymer film influences drop mobility, we measured drop velocities on PS-on-gold and PS-on-1-mm SiO_2 surfaces with film thicknesses of 20 nm and 200 nm, Teflon-on-gold surfaces and Teflon-on-1-mm SiO_2 surfaces with thickness of 60 nm and 400 nm (Figure S26). On high-permittivity substrates, the drop velocities for drop 1, 10 and 100 were almost the same independent on film thickness. Thus, the polymer film thickness has no effect on the drop mobility for PS and Teflon. On SiO_2 substrates, the dependence of drop velocity with drop number was more pronounced for thin polymer films than for thicker ones. AFM image showed that thick polymer films had a higher roughness than the thin films (Figure S27). Thus, in accordance with Helseth's report [29], we suspect that this slight change is caused by surface roughness.
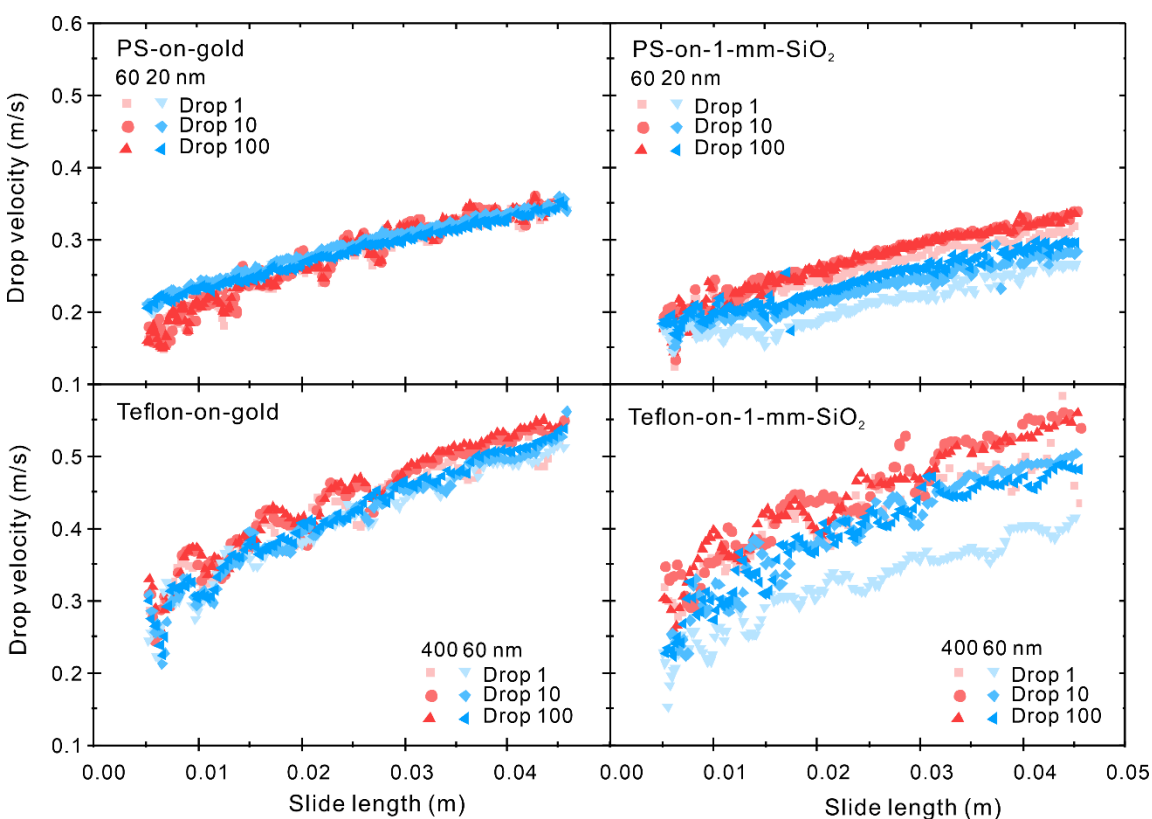

Figure S26. *Drop velocity-vs-slide length on PS and Teflon surfaces with different substrates and film thickness.*
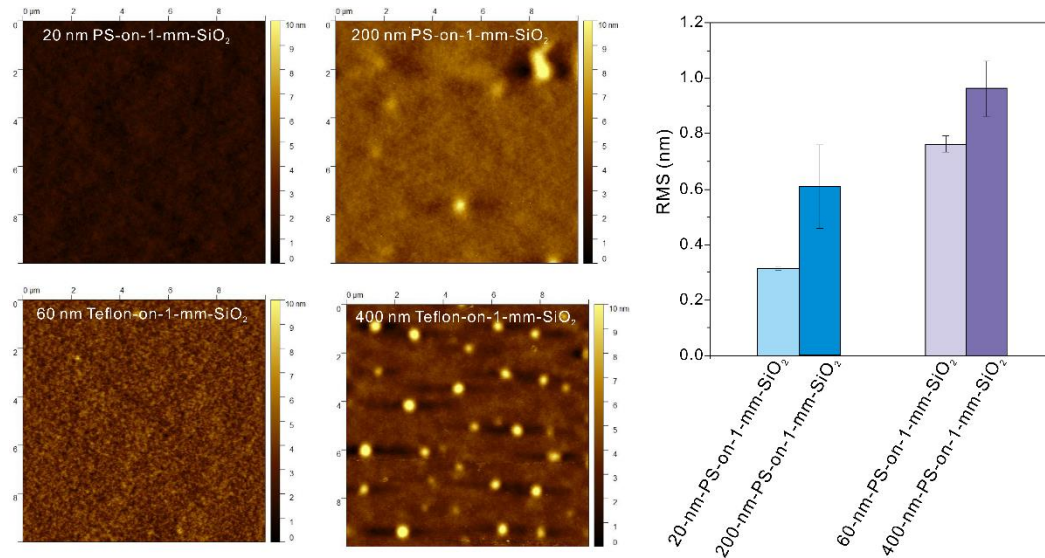
Figure S27. *Morphology and RMS of PS films and Teflon films with different thicknesses on 1 mm SiO₂ on an area of 10×10 μm² scale.*

References

1   Le Grand, N., Daerr, A. & Limat, L. Shape and motion of drops sliding down an inclined plane. *J. Fluid Mech.* **541**, 293-315, doi:10.1017/s0022112005006105 (2005).

2   Kim, H. Y., Lee, H. J. & Kang, B. H. Sliding of liquid drops down an inclined solid surface. *J. Colloid Interface Sci.* **247**, 372-380, doi:10.1006/jcis.2001.8156 (2002).

3   Huh, C. & Scriven, L. E. Hydrodynamic model of steady movement of a solid/liquid/fluid contact line. *J. Colloid Interface Sci.* **35**, 85-101, doi:10.1016/0021-9797(71)90188-3 (1971).

4   Voinov, O. V. Hydrodynamics of wetting. *Fluid Dynamics* **11**, 714-721, doi:DOI:10.1007/BF01012963 (1976).

5   Cox, R. G. The dynamics of the spreading of liquids on a solid surface. Part 1. Viscous flow. *J. Fluid Mech.* **168**, 169-194, doi:10.1017/S0022112086000332 (1986).

6   Dussan, E. B., Ramé, E. & Garoff, S. On identifying the appropriate boundary conditions at a moving contact line: an experimental investigation. *J. Fluid Mech.* **230**, 97-116, doi:10.1017/S0022112091000721 (1991).

7   Eggers, J. & Stone, H. A. Characteristic lengths at moving contact lines for a perfectly wetting fluid: the influence of speed on the dynamic contact angle. *J. Fluid Mech.* **505**, 309-321, doi:10.1017/S0022112004008663 (2004).

8   Eggers, J. Existence of receding and advancing contact lines. *Phys. Fluids* **17**, 082106, doi:10.1063/1.2009007 (2005).

9   Snoeijer, J. H. Free-surface flows with large slopes: Beyond lubrication theory. *Physics of Fluids* **18**, 021701, doi:10.1063/1.2171190 (2006).

10   Maglio, M. & Legendre, D. in *Computational and Experimental Fluid Mechanics with Applications to Physics, Engineering and the Environment Environmental Science and Engineering* (eds L. D. Sigalotti, J. Klapp, & E. Sira) 47-69 (2014).

11   Andersen, N. K. & Taboryski, R. Drop shape analysis for determination of dynamic contact angles by double sided elliptical fitting method. *Measurement Science and Technology* **28**, 047003, doi:10.1088/1361-6501/aa5dcf (2017).

12   Li, X. *et al.* Adaptation of a styrene-acrylic acid copolymer surface to water. *Langmuir* **37**, 1571–1577, doi:10.1021/acs.langmuir.0c03226 (2021).

13   Yarnold, G. D. The motion of a mercury index in a capillary tube. *Proceedings of the Physical Society* **50**, 540-552, doi:10.1088/0959-5309/50/4/307 (1938).

14   Frenkel, Y. I. On the behavior of liquid drops on a solid surface. 1. The sliding of drops on an inclined surface. *J. Exptl. Theoret. Phys. (USSR)* **18**, 659-669 (1948).

15   Dussan, E. B. & Davis, S. H. On the motion of a fluid-fluid interface along a solid surface. *J. Fluid Mech.* **65**, 71-95, doi:10.1017/S0022112074001261 (1974).

16   de Gennes, P. G. Wetting: Statics and dynamics. *Rev. Modern Phys.* **57**, 827-863, doi:10.1103/RevModPhys.57.827 (1985).

17   Shikhmurzaev, Y. D. The moving contact line on a smooth solid surface. *Int. J. Multiphase Flow* **19**, 589-610, doi:10.1016/0301-9322(93)90090-H (1993).

18   Olin, P., Lindstrom, S. B., Pettersson, T. & Wagberg, L. Water drop friction on superhydrophobic surfaces. *Langmuir* **29**, 9079-9089, doi:10.1021/la401152b (2013).

19   Yilbas, B. S., Al-Sharafi, A., Ali, H. & Al-Aqeeli, N. Dynamics of a water droplet on a hydrophobic inclined surface: influence of droplet size and surface inclination angle on droplet rolling. *RSC Advances* **7**, 48806-48818, doi:10.1039/c7ra09345d (2017).

20   Sartori, P. *et al.* Drop motion induced by vertical vibrations. *New J. Phys.* **17**, 113017, doi:10.1088/1367-2630/17/11/113017 (2015).

21   Ngan, C. G. & Dussan, E. B. On the dynamics of liquid spreading on solid surfaces. *J. Fluid Mech.* **209**, 191-226, doi:10.1017/s0022112089003071 (1989).

22   Yue, P. T. Thermodynamically consistent phase-field modelling of contact angle hysteresis. *J. Fluid Mech.* **899**, A15-41, doi:10.1017/jfm.2020.465 (2020).

23   Cai, X., Marschall, H., Wörner, M. & Deutschmann, O. Numerical simulation of wetting phenomena with a phase-field method using OpenFOAM. *Chemical Engineering & Technology* **38**, 1985-1992, doi:10.1002/ceat.201500089 (2015).

24   Jamshidi, F. *et al.* On suitability of phase-field and algebraic volume-of-fluid OpenFOAM (R) solvers for gas-liquid microfluidic applications. *Computer Physics Communications* **236**, 72-85, doi:10.1016/j.cpc.2018.10.015 (2019).

25   Stetten, A. Z., Golovko, D. S., Weber, S. A. L. & Butt, H. J. Slide electrification: charging of surfaces by moving water drops. *Soft Matter* **15**, 8667-8679, doi:10.1039/c9sm01348b (2019).

26   Blake, T. D., Clarke, A. & Stattersfield, E. H. An investigation of electrostatic assist in dynamic wetting. *Langmuir* **16**, 2928-2935, doi:10.1021/la990973g (2000).

27   Alnaes, M. S. *et al.* The FEniCS Project Version 1.5. *Archive of Numerical Software* **3**, 9-23 (2015).

28   Mitusch, S. K., Funke, S. W. & Dokken, J. S. dolfin-adjoint 2018.1: automated adjoints for FEniCSand Firedrake. *The Journal of Open Source Software* **4**, 1292 (2019).

29   Helseth, L. E. The influence of micro-scale surface roughness on water-droplet contact electrification. *Langmuir* **35**, 8268-8275, doi:10.1021/acs.langmuir.9b00988 (2019).

2.5. X. Li *et al. Submitted*, 2023

Surface charge deposition by moving drops reduces contact angles

Xiaomei Li [1] ∗, Aaron D. Ratschow[2]∗, Steffen Hardt[2], Hans-Jürgen Butt[1]†

1. Max Planck Institute for Polymer Research, Mainz, Mainz, Germany
2. Institute for Nano- and Microfluidics, Technische Universität Darmstadt, Darmstadt, Germany

Author contributions:

Xiaomei Li and Aaron D. Ratschow contributed equally. Hans-Jürgen Butt proposed and supervised the work, Xiaomei Li designed, conducted, evaluated, and interpreted the experiments, Aaron D. Ratschow developed the theoretical framework with input from Hans-Jürgen Butt and Steffen Hardt and derived the analytical model, Aaron D. Ratschow and Steffen Hardt worked out the simulation model and conducted the simulations, Xiaomei Li and Aaron D. Ratschow prepared the manuscript.

Surface charge deposition by moving drops reduces contact angles

Xiaomei Li,[1, *] Aaron D. Ratschow,[2, *] Steffen Hardt,[2, †] and Hans-Jürgen Butt[1, ‡]

[1] *Max Planck Institute for Polymer Research, Ackermannweg 10, 55128 Mainz, Germany*
[2] *Institute for Nano- and Microfluidics, TU Darmstadt,*
Alarich-Weiss-Straße 10, D-64237 Darmstadt, Germany
(Dated: April 6, 2023)

Slide electrification - the spontaneous charge separation by sliding water drops - can lead to an electrostatic potential of $1\,\mathrm{kV}$ and change drop motion substantially. To find out, how slide electrification influences the contact angles of moving drops, we analyzed the dynamic contact angles of aqueous drops sliding down tilted plates with insulated surfaces, grounded surfaces, and while grounding the drop. The observed decrease in dynamic contact angles at different salt concentrations is attributed to two effects: An electrocapillary reduction of contact angles caused by drop charging and a change in the free surface energy of the solid due to surface charging.

Introduction – The movement of liquid drops on solid surfaces plays a fundamental role in many natural and technological processes. Examples range from the spreading of raindrops on plant leaves or glass to processes like inkjet printing or coating [1–3]. The interaction between a liquid and a solid is largely determined by the contact angle near the three-phase contact line. Young's equation relates the contact angle (θ) to the interfacial energies of the liquid surface (L), solid surface (S), and the solid-liquid interface (SL) with [4],

$$\gamma_{\mathrm{L}} \cos(\theta) = \gamma_{\mathrm{S}} - \gamma_{\mathrm{SL}}. \tag{1}$$

A lower contact angle indicates a higher solid surface energy. Therefore, surface wettability can be controlled by choosing a high or low surface energy material, which leads to low or high contact angles, respectively. The composition of a smooth surface determines its contact angle. To control contact angles, electrowetting is a versatile tool. It is used in various microfluidic applications [5]. In electrowetting, the contact angle of a sessile drop on a dielectric substrate on top of an electrode decreases when a voltage (ΔU) is applied between the drop and the electrode. Microscopically, this effect is due to the electrostatic Maxwell stress acting on the liquid surface in the close vicinity of the contact line. Macroscopically, the effect can be attributed to a change in effective free surface energy of the solid-liquid interface because of the accumulation of charges [6, 7]. Intuitively, it is energetically favorable for counter-charges to accumulate at the solid-liquid interface under an applied potential, and thus its surface energy is reduced compared to the case without charges. The change in the solid-liquid interfacial energy can be expressed as

$$\Delta\gamma_{\mathrm{SL}} = \gamma_{\mathrm{SL}}^{\mathrm{eff}} - \gamma_{\mathrm{SL}} = -\frac{\varepsilon_0 \varepsilon_r}{2d} \Delta U^2. \tag{2}$$

It depends on the permittivity (ε_0 = vacuum permittivity, ε_r = relative permittivity) and the thickness of the substrate d [5] separating the liquid from an electrode. In the macroscopic description, the change in contact angle is given by the Young-Lippmann equation [6],

$$\cos(\theta) - \cos(\theta') = \frac{\Delta\gamma_{\mathrm{SL}}}{\gamma_{\mathrm{L}}}. \tag{3}$$

Here θ and θ' are the contact angles without and with an applied voltage.

Another physical phenomenon that involves drops and electrostatic charges is slide electrification [8–11]. A sliding aqueous drop on a hydrophobic surface can acquire a net charge while leaving behind an opposite charge on the dewetted surface. On low permittivity, hydrophobic surfaces, the drop is usually positively charged and negative surface charges are left behind [12–15]. Spontaneous charging of moving drops influences their motion substantially by direct Coulomb forces between the charges in the drop and the opposite charges on the solid surface [10, 16]. However, it is still not clear if spontaneous charging changes the contact angle. Here, we address the question: Do charges in the drop and/or surface charges generated by slide electrification change the advancing and receding contact angles? If yes, how does this effect depend on the salt concentration?

To answer these questions, we imaged sliding aqueous drops (Supporting information, S1) in a custom-made tilted plate setup (Fig. 1a) [10, 17]. Drops with a volume of $30\,\mu\mathrm{L}$ were placed onto a tilted surface by a peristaltic pump with a grounded syringe needle at fixed intervals of $1.5\,\mathrm{s}$. The surfaces used were flat, smooth, and hydrophobic, with an average roughness $<\ 1\,\mathrm{nm}$ within an area of $0.5 \times 0.5\,\mu\mathrm{m}^2$ (Supporting information: S2 and S3). Every drop moving down the surface first contacted a grounded electrode. We imaged the sliding drops from the side with a high-speed camera and set the slide length and time to zero when drops detach from the grounded electrode and enter the recording window. At this point, they already have an initial velocity. Based on the side-view images, the positions, velocities, and contact angles of the advancing and receding contact lines were determined automatically by an adapted image analysis MATLAB code [18]. The drop velocity for every drop position was defined as
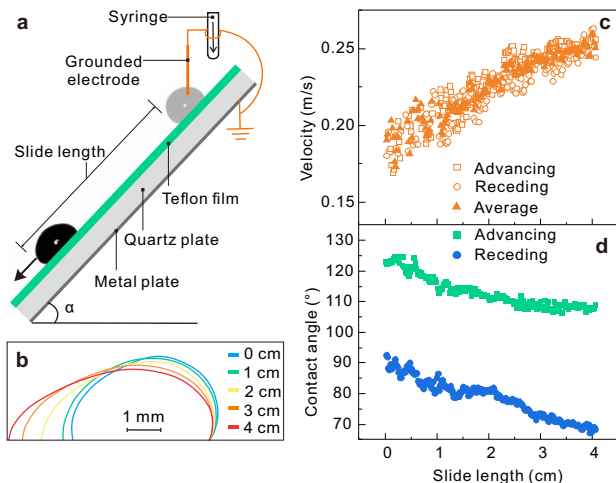
FIG. 1: Experiment for aqueous drops with 1 mM NaCl on a 40° tilted initially uncharged Teflon-quartz surface. The drop was grounded until it detached from the needle and ungrounded during the whole sliding. (a) Schematic of the experimental setup. (b) Drop profiles for different values of the slide length, (c) drop velocity, (d) dynamic advancing and receding contact angle over the slide length of the drop shown in (a).

the mean of the velocities of the front and rear contact lines [19]. As surfaces, we prepared 60 nm thick Teflon films on quartz plates (Teflon-quartz) by dip-coating (1 cm/min) from a solution of 1 wt% Teflon AF 1600 and annealing at 160 °C under vacuum for 24 h. The quartz plates were 1 mm thick and placed on a grounded metal plate.

When placing an aqueous drop containing 1 mM NaCl on a pristine, uncharged Teflon-quartz surface (Fig. 1a), the drop accelerates. Its shape becomes more elongated (Fig. 1b) while the velocity increases (Fig. 1c). In addition, the dynamic advancing and receding contact angles decrease with increasing velocity (Fig. 1d). Established theories, such as the Cox-Voinov hydrodynamic model [20, 21], the molecular kinetic model [22], combinations of both [23, 24], and the adaptation model [25] predict a decrease in receding, but an increase in advancing contact angle with increasing velocity. This prediction does not agree with our measurements. We conclude that there are additional effects influencing the contact angles and propose that the change in contact angle is due to charging of the drops.

To verify that charging of aqueous drops causes this change in contact angles, we sputter-coated the quartz plates with 5 nm chromium and 35 nm gold before coating Teflon films on top (Teflon-gold). In earlier experiments we had shown that in contrast to Teflon-quartz (Fig. 2a),

charging effects are negligible for 50 nm polymer films on grounded gold (Fig. 2b) [10, 16]. For Teflon-gold, the advancing contact angle indeed increase with velocity (Fig. 2e, orange symbols) and the decrease of the receding contact angle is weaker (Fig. 2f, orange symbols).

We propose that electrowetting reduces the contact angles of charged drops. The sliding drop on the Teflon-quartz surface spontaneously acquires positive charges, leaving negative surface charges behind. The related electrostatic potential leads to an electrowetting effect. To support this hypothesis, we calculate $\Delta\gamma_{\mathrm{SL}}$ and test, if the anticipated changes in contact angle (equation 3) are large enough. First, we convert measured drop charges Q to a potential $\Delta U = Q/C$ with the capacitance of the drop $C = (A\varepsilon_0\varepsilon_r)/d$ (Supporting information, S4). Here, A is the contact area of the drop. In previous measurements [10], after 4 cm sliding on a Teflon-quartz surface the drop charge was $Q \approx 0.7$ nC, $A \approx 17$ mm^2 and $\varepsilon_r = 4.5$, we estimate $\Delta U \approx 1$ kV, comparable to potentials reported by [26]. Based on equation 2, the changes in the solid-liquid interfacial tension are of the order of 10 mN/m leading to a decrease of $\approx 9°$ in contact angles. Since the potential continuously increases with increasing slide length, electrowetting can explain the decrease in advancing contact angle.

Are there other electrostatic effects influencing the contact angles? To isolate such effects, we use the same Teflon-quartz surfaces as previously but constantly ground the sliding drop with a tungsten wire to prevent drop charging and electrowetting effects (Fig. 2c). The grounded tungsten wire (25 μm diameter) was spanned parallel to the surface at ≈ 1 mm height along the path of the drop. Its influence on the drop velocity or contact angles was negligible (Supporting information, S5). With the grounded wire, the drop can still deposit negative surface charge at its rear, but the drop itself remains uncharged.

Fig. 2d-f shows the velocity, the dynamic advancing, and the dynamic receding contact angles versus slide length for the 1st and 100th consecutive grounded drop on the Teflon-quartz surface. We observe a distinct difference between the 1st (green circles) and 100th (blue triangles) drop. This observation indicates that the surface charge on the solid-liquid interface influences the contact angles and drop motion, even if the drop is uncharged. For comparison, the results of the reference measurement on the Teflon-gold surface (orange circles) are also plotted. There is no significant difference between the 1st and 100th drop on the gold substrate (Supporting information, S6).

Compared with the Teflon-gold reference (Fig. 2e-f, orange), the dynamic advancing contact angle of the 1st grounded drop on the Teflon-quartz surface was not affected. Only the dynamic receding contact angle was reduced by 10°. In comparison, the dynamic advanc-
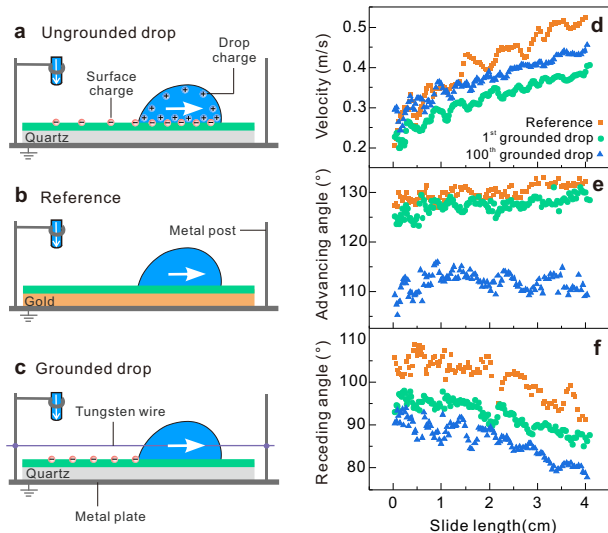
FIG. 2: Dynamic contact angles reduced by slide electrification. Schematics of a drop (30 µL drop with 1 mM NaCl) sliding down the 40° tilted (a) A Teflon-quartz surface and (b) a Teflon-gold surface without drop grounding (b), and (c) a Teflon-quartz surface with drop grounding during sliding. The corresponding drop velocity (d), dynamic advancing contact angle (e), and dynamic receding contact angle (f) over slide length for the 1st and 100th consecutive drop.

mentary charge on an already-charged surface. This energy depends on the size of the charged patch. As an example, we consider a circular patch of charges of radius R and a charge density σ. After area-averaging this energy, we obtain the change in free surface energy of the solid due to the presence of a charge density σ (Supporting information, S7):

$$\Delta\gamma_{\mathrm{S}} = \gamma_{\mathrm{S}}^{\mathrm{eff}} - \gamma_{\mathrm{S}} = \frac{\sigma^2 R}{\varepsilon_0(1 + \varepsilon_r)}. \tag{4}$$

The corresponding change in contact angle is given by

$$\cos(\theta) - \cos(\theta') = -\frac{\Delta\gamma_{\mathrm{S}}}{\gamma_{\mathrm{L}}}. \tag{5}$$

The surface energy increases quadratically with the charge and linearly with the length scale of the charged area R. For the 1st drop, there is only one characteristic scale of the problem that comes into consideration for R, which is the drop size, represented by its radius. With $R = \frac{2}{mm}$ and a charge density of $\sigma = 10\,\mu\mathrm{C/m}^2$ [10], we estimate an increase in solid surface energy of around $10\,\mathrm{mN/m}$, which would substantially change contact angles.

A macroscopic description with Young's equation and the effective solid surface energy $\gamma_{\mathrm{S}}^{\mathrm{eff}}$ is only viable above the characteristic length scale of the microscopic effects. On the microscopic scale, electrostatic forces, expressed by the Maxwell stress, and capillary forces balance at the liquid-gas interface. Mathematically, the electrostatic problem of an isopotential wedge, representing the liquid, next to a charged surface does not have an inherent length scale. Consequently, there is no apparent length scale over which the Maxwell stress is localized. It even becomes singular at the contact line [10, 27] for the model problem of an isopotential wedge. However, such mathematical singularities do not occur in nature. There are different mechanisms that could introduce a microscopic length scale close to the contact line. First, we have to consider that the treatment of the liquid surface as isopotential only applies on length scales above the Debye length, with $\lambda \approx 1 - 100\,\mathrm{nm}$ in aqueous solutions. Moreover, singularities of the electric field at the contact line would lead to electrostatic discharge [28, 29] above the limiting field strength of humid air, which is $\approx 2\,\mathrm{MV/m}$ [30]. Following this argument, the singularity is eliminated on the length scale where electrostatic discharge first occurs. With numerical simulations, we show that the introduction of such a microscopic length scale strongly localizes the Maxwell stress, which makes a macroscopic description with Young's equation viable. We estimate the limiting length scale for the macroscopic description of the effect to be of the order of $1\,\mu\mathrm{m}$ (Supporting information, S8), above which the contact angle should be well-defined by a change in the effective solid surface energy, as shown

ing contact angle of the ungrounded drop (Fig. 1d) decreases for slide lengths > 0 as the ungrounded drop charged and electrowetting commenced. For the 100th grounded drop on Teflon-quartz (Fig. 2e-f, blue), both the dynamic advancing and receding contact angles deviate from the Teflon-gold reference. The main difference was that the grounded drop continuously deposited charges at its receding contact line (Fig. 2b-c) while the drop on the Teflon-gold surface did not generate surface charges. Thus, in addition to electrowetting, surface charges cause a fundamentally new electrostatic effect that decreases contact angles.

We propose that charges on the solid-gas interface increase the surface energy and according to Young's equation reduce the contact angles. The surface energy is increased by two effects. The first is the self-energy of the charges on the surface, also referred to as Born energy. The corresponding change in the surface energy is of the order of $10\,\mu\mathrm{N/m}$ (Supporting information, S7) and is thus negligible. The second effect is that charges on the surface repel each other by Coulomb interaction. Thus, forming a layer of charges requires electrostatic work. To derive a theoretical scaling for this effect, we analytically calculate the work required to deposit an additional ele-
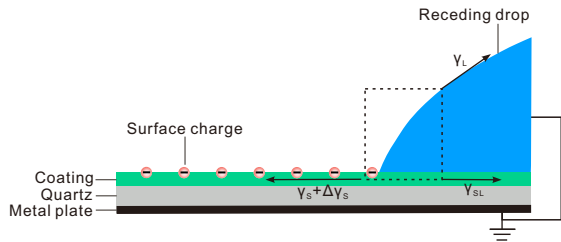
FIG. 3: Schematic representation of the discovered effect of contact-angle modification via electrostatic interaction with surface charges. The sliding drop deposits charges on the solid surface, which deform the liquid surface via electrostatic interactions. Above a characteristic length scale ('control' volume indicated by a dashed rectangle), the effect can be subsumed as a change in solid surface energy.

in Fig. 3.

To compare theory and experiments and explain the change of dynamic contact angles, we consider three effects: (i) Non-electrostatic contributions such as hydrodynamics described by the Cox-Voinov model, contact-line friction because of local pining and de-pining of contact line, and adaptation, (ii) surface charge-induced changes of the solid surface (equation 4), and (iii) electrowetting due to charging of the drop (equation 2). Our experiments are designed in such a way that the reference measurement on Teflon-gold substrates is only influenced by (i). On Teflon-quartz substrates the grounded drop is influenced by (i) and (ii), and the ungrounded drop is influenced by (i)-(iii). The initial decrease in receding contact angle between the reference and the grounded drop for the 1st drop was around 10° (Fig. 2f). To fully explain this with equation 4, the drop with a radius of 2 mm on quartz ($\varepsilon_r = 4.5$) would have to deposit a surface charge of $\sigma = 16\,\mu C/m^2$. This value agrees magnitude-wise with our previously published measurement of $10.3\,\mu C/m^2$ on the same substrate for the first drop [10].

For the 100th drop (blue) shown in Fig. 2e-f, also the advancing contact angle decreased. We attribute this to surface charges left behind by previous drops. Due to hydrodynamics, contact-line friction, and adaptation (effect i), receding contact angles are lower than advancing contact angles. We observe that dynamic receding contact angles are more affected by surface charge than advancing ones. In line with this observation, a calculation of the contact angle change as a function of surface charge density for different initial contact angles shows that lower contact angles are more affected (Fig. 4a). Note that the applicability of such models becomes questionable for contact angles of 20-30° due to electrostatic discharge [28].

To demonstrate the universality of the effect, we measured surfaces with different coatings and drops with different salts. For comparison, we calculated $\cos(\theta') - \cos(\theta)$. We observe it on 35 nm thick polystyrene (PS) films coated quartz plates, molecular layers of perfluoroctyltriethoxysilane (PFOTS), and polydimethylsiloxane (PDMS) grafted to quartz plates. The effect also occurs for all salts tested (Fig. 4b and Fig. S10a). The reduction of dynamic contact angles increase with increasing salt concentration up to $\approx 1\,mM$ followed by a decrease (Fig. 4c and Fig. S10b). This trend is consistent with the reported trends of drop/surface charges [31–33]. The initial increase of the effect with salt concentration can be explained by the Péclet number dependency of charge separation. In the drop there is a flow component directed upward at the receding contact line. It drives counterions away from the surface and extends the effective screening length. Assuming charge regulation at the solid-liquid interface, an extended screening length reduces the surface charge directly at the receding contact line which also reduces the surface charge transferred to the free solid surface. This effect is only effective if convective transport is stronger than diffusion of ions. The Péclet number $Pe = v\lambda/D$ ($v =$ drop velocity, $D =$ ion diffusivity) measures convective transport, which is more or less negligible up to $Pe = 1$ and causes a decrease of charge separation for $Pe > 1$. [34] For typical values $v = 0.3\,m/s$ and $D = 2 \times 10^{-9}\,m^2/s$, a transition between the two regimes is found at a salt concentration of $2\,mM$, which explains the reduced contact angle changes at $1\,mM$ and below. The experimental trends are in accordance with the theoretical scaling.

The theory also predicts a scaling of the effect with the length scale associated with the charged area, that for the first drop corresponds to the drop radius R. To confirm this scaling, we measured grounded drops of different volumes V and observe a clear increase of the effect for larger drops (Fig. 4d). We apply the theoretical scaling from the data point at $10\,\mu L$ on, which corresponds to a relationship $R^{(1/3)}$, and find an agreement up to $V \approx 30\,\mu L$. For larger volumes, the simple scaling breaks down as the drop height approaches the capillary length and the radius increases beyond the value it takes without the influence of gravity, which is reflected in the higher experimental values.

In addition to our own measurements, our theory helps to explain observations from the literature. For instance, Mugele et al. [35] reported that the contact angle of an aqueous solution on Teflon permanently decreased by 5-10° after the first wetting-dewetting cycle. This was likely caused by charges deposited onto the previously uncharged surface during the initial dewetting. Sun et al. [36] experimentally demonstrated that drops move along surface charge gradients towards higher charged regions and even do so against gravity. This phenomenon is eas-
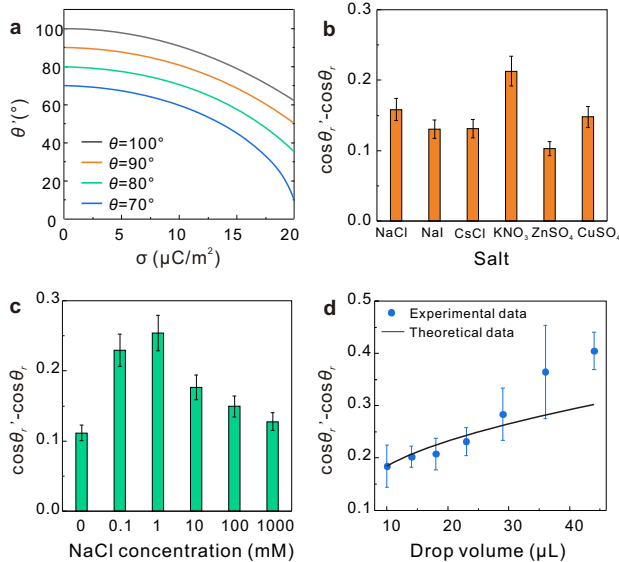
FIG. 4: Universality of the effect. (a) Theoretically expected contact angle as a function of surface charge density for different initial contact angles, calculated with equations (4) and (5). Experimentally determined $\cos(\theta_r') - \cos(\theta_r)$ for the first grounded drops with (b) different salt types, (c) salt concentrations, and (d) drop volumes of $1\,\mathrm{mM}$ NaCl aqueous solution on pristine Teflon-quartz surfaces in the velocity range $0.3 - 0.4\,\mathrm{m/s}$. θ_r and θ_r' are the dynamic receding contact angles without and with the influence of slide electrification.

ily conceivable with equation 4, as the higher charged regions have an increased free surface energy.

To conclude, we identified two mechanisms explaining how slide electrification can lead to a reduction in dynamic contact angles. Charges in the drop induce an electric field between the drop and the subsurface electrode, which via electrowetting causes a reduction of the advancing and receding contact angles. Charges on the solid surface effectively increase the surface energy and thus reduce the contact angle according to Young's equation. Depending on the distribution of surface charges the advancing or receding side can be affected. The latter effect can substantially reduce the dynamic contact angle, even when the drop itself is prevented from charging. We propose an analytical model based on Young's equation, which agrees well with our experimental data. The universality of the effect is supported by measurements with different salt types, salt concentrations, drop volume, and hydrophobic coatings. The discovered effect could help to explain contact angle hysteresis in many practical cases and facilitate the design of functional surfaces by focusing on the prevention of charge separation.

* X.L. and A.D.R. contributed equally to this work.
† hardt@nmf.tu-darmstadt.de
‡ butt@mpip-mainz.mpg.de

[1] P.-G. Gennes, F. Brochard-Wyart, and D. Quéré, *Capillarity and wetting phenomena: drops, bubbles, pearls, waves* (Springer, 2004).

[2] D. Bonn, J. Eggers, J. Indekeu, J. Meunier, and E. Rolley, Reviews of Modern Physics **81**, 739 (2009).

[3] D. Lohse, Annual Review of Fluid Mechanics **54**, 349 (2022).

[4] T. Young, Philosophical Transactions of the Royal Society of London , 65 (1805).

[5] F. Mugele and J. Heikenfeld, *Electrowetting: fundamental principles and practical applications* (John Wiley & Sons, 2018).

[6] J. Buehrle, S. Herminghaus, and F. Mugele, Physical Review Letters **91**, 086101 (2003).

[7] F. Mugele and J. Buehrle, Journal of Physics: Condensed Matter **19**, 375112 (2007).

[8] K. Yatsuzuka, Y. Mizuno, and K. Asano, Journal of Electrostatics **32**, 157 (1994).

[9] A. Z. Stetten, D. S. Golovko, S. A. Weber, and H.-J. Butt, Soft Matter **15**, 8667 (2019).

[10] X. Li, P. Bista, A. Z. Stetten, H. Bonart, M. T. Schür, S. Hardt, F. Bodziony, H. Marschall, A. Saal, X. Deng, R. Berger, S. A. L. Weber, and H.-J. Butt, Nature Physics **18**, 713 (2022).

[11] Y. Jin, C. Wu, P. Sun, M. Wang, M. Cui, C. Zhang, and Z. Wang, Droplet **1**, 92 (2022).

[12] J. K. Beattie, Lab on a Chip **6**, 1409 (2006).

[13] K. N. Kudin and R. Car, Journal of the American Chemical Society **130**, 3915 (2008).

[14] C. Tian and Y. Shen, Proceedings of the National Academy of Sciences **106**, 15148 (2009).

[15] T. Preočanin, A. Selmani, P. Lindqvist-Reis, F. Heberling, N. Kallay, and J. Lützenkirchen, Colloids and Surfaces A: Physicochemical and Engineering Aspects **412**,

120 (2012).

[16] D. Díaz, X. Li, P. Bista, X. Zhou, F. Darvish, H.-J. Butt, and M. Kappl, Physics of Fluids **35**, 017111 (2023).

[17] X. Li, F. Bodziony, M. Yin, H. Marschall, R. Berger, and H.-J. Butt, "Drop friction," (2023), submitted.

[18] N. K. Andersen and R. Taboryski, Measurement Science and Technology **28**, 047003 (2017).

[19] X. Li, S. Silge, A. Saal, G. Kircher, K. Koynov, R. Berger, and H.-J. Butt, Langmuir **37**, 1571 (2021).

[20] O. Voinov, Fluid Dynamics **11**, 714 (1976).

[21] R. Cox, Journal of Fluid Mechanics **168**, 169 (1986).

[22] T. Blake and J. Haynes, Journal of Colloid and Interface Science **30**, 421 (1969).

[23] F. Brochard-Wyart and P. De Gennes, Advances in Colloid and Interface Science **39**, 1 (1992).

[24] P. Petrov and I. Petrov, Langmuir **8**, 1762 (1992).

[25] H.-J. Butt, R. Berger, W. Steffen, D. Vollmer, and S. A. L. Weber, Langmuir **34**, 11292 (2018).

[26] W. Xu, Y. Jin, W. Li, Y. Song, S. Gao, B. Zhang, L. Wang, M. Cui, X. Yan, and Z. Wang, Science advances **8**, eade2085 (2022).

[27] L. Y. Yeo and H.-C. Chang, Modern Physics Letters B **19**, 549 (2005).

[28] M. Vallet, M. Vallade, and B. Berge, The European Physical Journal B-Condensed Matter and Complex Systems **11**, 583 (1999).

[29] J.-M. Löwe, V. Hinrichsen, I. V. Roisman, and C. Tropea, Physical Review E **102**, 063101 (2020).

[30] B. Li, X. Li, M. Fu, R. Zhuo, and D. Wang, Journal of Physics D: Applied Physics **51**, 375201 (2018).

[31] L. E. Helseth, Langmuir **36**, 8002 (2020).

[32] M. D. Sosa, M. L. M. Ricci, L. L. Missoni, D. H. Murgida, A. Cánneva, N. B. D'Accorso, and R. M. Negri, Soft Matter **16**, 7040 (2020).

[33] L. E. Helseth, Langmuir **39**, 1826 (2023).

[34] A. D. Ratschow, L. S. Bauer, P. Bista, S. A. L. Weber, H.-J. Butt, and S. Hardt, "How charges separate when surfaces are dewetted," (2023), submitted.

[35] F. Mugele, A. Klingner, J. Buehrle, D. Steinhauser, and S. Herminghaus, Journal of Physics: Condensed Matter **17**, S559 (2005).

[36] Q. Sun, D. Wang, Y. Li, J. Zhang, S. Ye, J. Cui, L. Chen, Z. Wang, H.-J. Butt, D. Vollmer, and X. Deng, Nature Materials **18**, 936 (2019).

Surface charge deposition by moving drops reduces contact angles -Supplemental Material-

Xiaomei Li,[1, *] Aaron D. Ratschow,[2, *] Steffen Hardt,[2, †] and Hans-Jürgen Butt[1, ‡]

[1]*Max Planck Institute for Polymer Research, Ackermannweg 10, 55128 Mainz, Germany*
[2]*Institute for Nano- and Microfluidics, TU Darmstadt,*
Alarich-Weiss-Straße 10, D-64237 Darmstadt, Germany
(Dated: April 6, 2023)

Contents

S1: Liquid preparation.

The chemicals used to prepare salt solutions include distilled water ($< 1\,\mu$S/cm; Gibco, Thermo Fisher Scientific), 1 M NaCl aqueous solution (Carl Roth, Germany), 1 M KNO_3 aqueous solution (Carl Roth, Germany), 0.1 M $ZnSO_4$ aqueous solution (Fluka, Germany), 1 M NaOH aqueous solution (VWR International, France), 37% HCl aqueous solution (Sigma-Aldrich), NaI (99.999%, Sigma-Aldrich), CsCl (99.9%, Sigma-Aldrich), $CuSO_4$ (99%, Sigma-Aldrich). Salt solutions were prepared by mixing appropriate amounts with distilled water.

S2: Surface preparation.

Substrates cleaning. Gold, glass slides ($76.2 \times 25.4 \times 1.0\,\text{mm}^3$, Paul Marienfeld), Si wafers ($< 0.005\,\Omega$cm; thickness, $525 \pm 25\,\mu$m, P++<100>, Silicon Materials) and quartz slides ($76.2 \times 25.4 \times 1.0\,\text{mm}^3$, Thermo Fisher Scientific) were used as substrates. Before use, they were cleaned in an ultrasonic bath in toluene and ethanol for 10 min each. After drying by N_2 blowing, they were O_2-plasma cleaned at 300 W for 10 min (Femto low-pressure plasma system, Diener electronic). Gold substrates with 5 nm chromium and 35 nm gold on glass slides were prepared by sputter coating and used immediately without further cleaning.

Surface preparation. (1) 60 nm Teflon coatings on gold and quartz substrates were prepared by dip-coating with a pulling speed of 10 mm/min from a solution of 1(wt)% Teflon AF 1600 ($\varepsilon_r = 1.9$; Sigma-Aldrich) in FC-43 (Sigma-Aldrich). Before use, we annealed the Teflon samples in the oven at 160 under vacuum for 24 h. (2) 35 nm PS coatings on gold and quartz substrates were prepared by dip-coating with a pulling speed of 90 mm/min from a solution of 1(wt)% PS (molecular weight, 192 kg/mol, $\varepsilon_r = 2.6$; Sigma-Aldrich) in toluene (99.8%, Sigma-Aldrich). Before use, we annealed the PS samples at 120 °C under vacuum for 24 h. (3) PFOTS coatings on Si wafers and quartz substrates were prepared by chemical vapor deposition. Cleaned Si wafers and quartz slides were put into a vacuum desiccator containing a tiny glass bottle with 0.5 ml 1H, 1H, 2H, 2H-perfluorooctadecyltrichlorosilane (97%, Sigma-Aldrich). The desiccator was evacuated to < 100 mbar. After 30 min, the samples were removed and cleaned by rinsing with ethanol to remove any unbound silanes. (4) PDMS layered costings were prepared by the "grafting to" method using silicone oil (molecular weight, 6 kg/mol; Alfa Aesar). A few drops of silicone oil were deposited on the cleaned Si wafer and quartz slides. The samples were stored at $22 - 23$ °C and 30–60% relative humidity for 24–48 hours after the PDMS drops spread and covered the substrates. Before use, they were cleaned using ultrasound in toluene, ethanol, and distilled water for 10 min each to remove the unbound silicone oil.

S3: SFM imaging.

We used tapping mode (Dimension Icon, Bruker) to measure the morphology of all surfaces within an area of $1 \times 1\,\mu\text{m}^2$ (Fig. S1). The cantilever had a nominal resonance frequency of 300 kHz and a spring constant of 26 N/m (160AC-NA, OPUS). The errors of root-mean-squared (RMS) roughness are the standard deviation of the RMS roughness from three measurements on different positions and different patches of samples.
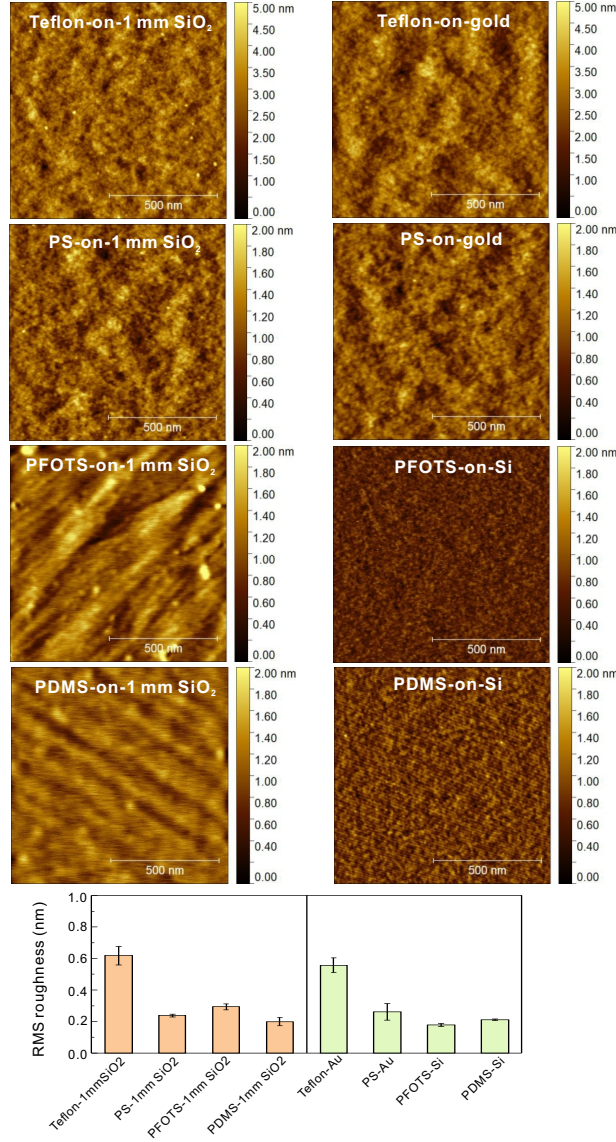
FIG. S1. Morphology and root-mean-square (RMS) roughness of all surfaces.

S4: Change of solid-liquid interfacial tension by electrowetting.

When a drop slides on the Teflon-quartz surface with a back electrode, the dielectric layer between the drop and the electrode comprises a 50 nm thick Teflon coating and 1 mm thick quartz. The capacitance (C) is

$$\frac{1}{C} = \frac{1}{C_p} + \frac{1}{C_q} = \frac{d_p}{A\varepsilon_0\varepsilon_p} + \frac{d_q}{A\varepsilon_0\varepsilon_q} \approx \frac{d_q}{A\varepsilon_0\varepsilon_q}. \tag{S1}$$

Here, C_p and C_q are the capacitance due to the polymer coating and the quartz substrate, respectively. The relative dielectric permittivity of the quartz is $\varepsilon_q = 4.5$. A is the contact area of the drop of $A \approx 17\,\text{mm}^2$. Thus, $C \approx 0.68\,\text{pF}$. In addition, the electrostatic voltage ΔU is given by

$$\Delta U = \frac{Q}{C}, \tag{S2}$$

where Q is the drop charge. In our previous measurements [S1], after 4 cm sliding on a Teflon-quartz surface with velocities of $0.2 - 0.5\,\text{m/s}$, the drop charge was $\approx 0.7\,\text{nC}$. From that, we obtain $\Delta U \approx 1.03\,\text{kV}$. According to equation

S2, the corresponding change of solid-liquid interfacial tension is $\Delta\gamma_{\mathrm{SL}} = -(C\Delta U^2)/2A \approx 10.6\,\mathrm{mN/m}$.

S5: Influence of tungsten wire on the sliding drop measurement.

A tungsten wire (diameter= 0.025 mm, from Alfa Aesar, USA) was spanned parallel to surfaces with a height of $\approx 1\,\mathrm{mm}$. We first recorded a 30 µL 1 mM NaCl aqueous solution drop sliding on a 40° tilted Teflon-gold surface in contact with the tungsten wire. To study the influence of the grounded tungsten wire on the drop motion, we then lifted the wire above the drop and recorded another drop sliding along the same path again without contact with the wire (Fig. S2a). The velocities, dynamic advancing contact angles, and dynamic receding contact angles of the two drops are almost the same (Fig. S2b-d). Thus, we conclude that the influence of the tungsten wire itself on the sliding drop measurement can be ignored.
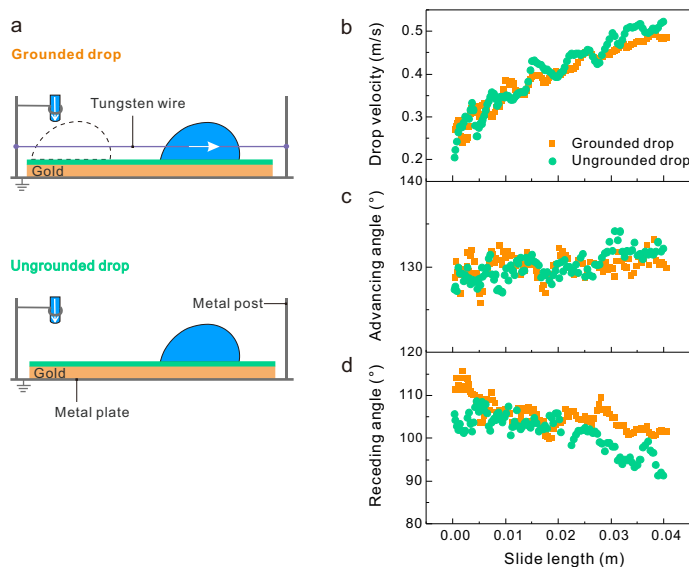
FIG. S2. Assessment of the influence of the grounded tungsten wire on the sliding drop measurement. (a) Schematics showing grounded and ungrounded drops on Teflon-gold surfaces. (b-d) Velocities, dynamic advancing contact angles, and dynamic receding contact angles versus slide length of grounded (orange) and ungrounded (green) drops sliding on the Teflon-gold surface.

S6: Drop-number dependence for ungrounded drops.

We measured multiple successive ungrounded drops as well. On the Teflon-gold surfaces, the sliding drops were not influenced by slide electrification. Thus, there is no drop-number dependence of the drop velocity and the dynamic contact angles (Fig. S3), further indicating that the Teflon-gold surface is a good reference system for experiments without charge accumulation. On the Teflon-quartz surface, both the drop velocity and the dynamic contact angles depend on the drop number (Fig. S4). Compared with the reference, the dynamic advancing angle for the 1st ungrounded drop decreases from 125° to 105° after 4 cm sliding, 20° lower than the reference, which is within the expectation based on the electrowetting theory. The dynamic receding angle of the 1st ungrounded drop decreases from 93° to 67° after 4 cm sliding, 30° lower than the reference. The reduction of the dynamic contact angle at the rear side is more than at the front side for the 1st ungrounded drop, supporting the idea that deposited surface charges affect the contact angle besides electrowetting. For the 100th ungrounded drop, a reduction of the dynamic advancing and receding contact angles occurs as well, which, however, is less than the reduction for the 1st drop. This is consistent with less charge accumulation inside the drop and therefore a reduced influence of electrowetting. Interestingly, the reduction of the dynamic contact angle for the 1st ungrounded drop is even less than the one of the 1st grounded drop. Based on this, we speculate that preventing drop from charging facilitates charge deposition on solid surfaces.
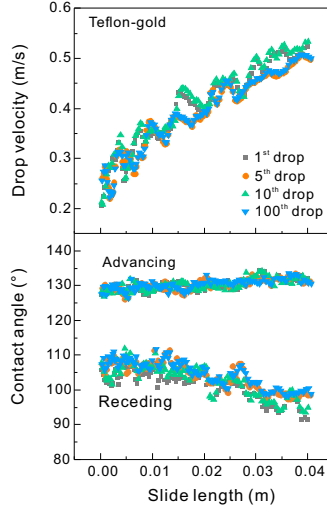
FIG. S3. Drop velocity, dynamic advancing angle, and dynamic receding contact angle versus slide length for the 1st, 5th, 10th, and 100th ungrounded drop sliding on the Teflon-gold surface.
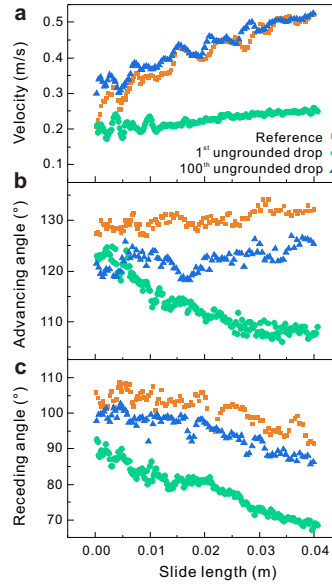

FIG. S4. Drop velocity, dynamic advancing angle, and dynamic receding contact angle versus slide length for the 1st and 100th ungrounded drop sliding on the Teflon-quartz surface.

S7: Change of solid surface energy by surface charges.

Here, we derive a scaling relationship for the electrostatic correction to Young's equation due to the charges deposited at the rear end of a drop sliding along a surface. Two electrostatic effects contribute to the increase in free surface energy when charges are present: the self-energy of the individual charges, and the Coulomb interaction energy between the charges. The self-energy of a single ion of charge q at the interface between two dielectrics is $q^2/[4\pi\varepsilon_0(\varepsilon_r+1)a]$, where a is the radius of the ion. Per unit area, this leads to an interfacial energy of $\Delta\gamma_{\text{S}} = q\sigma//[4\pi\varepsilon_0(\varepsilon_r+1)a]$. With a typical ionic radius of $a = 0.15\,\text{nm}$ and measured charge densities of $\sigma = 10\,\mu\text{C/m}^2$ [S1], the estimated increase in solid surface energy is only 17 µN/m. This is too small to cause a substantial change in contact angle.
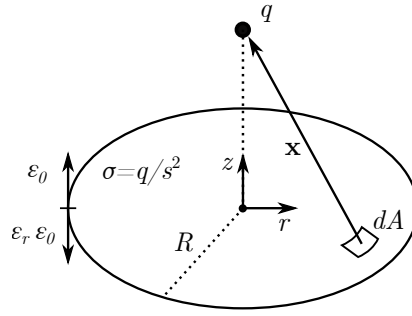
FIG. S5. Schematic representation of a charged circular area of radius R and surface charge $\sigma = q/s^2$ at the interface of air and a dielectric used in the analytical calculations. A single charge q is positioned centrally at a distance z. The distance from the single charge to an infinitesimal charged surface element dA is indicated.

To quantify the Coulomb interaction energy of the charges on the surface, we analytically compute the work required to deposit an additional charge q onto a surface carrying a charge density $d\sigma$. For an infinite charged plane, the electric field does not decay and the work becomes infinite. Consequently, the problem depends on the extension of the charged area. To this end, we consider a circular charged area of radius R located at the interface of air and a dielectric with relative permittivity ε_r (Fig. S5). The force $d\mathbf{F}$ between a single charge q located at a distance z above the center of the charged area and a differential surface element dA of charge $d\sigma dA$ is

$$d\mathbf{F} = \frac{q d\sigma}{2\pi\varepsilon_0(1+\varepsilon_r)} \frac{\mathbf{x}}{|\mathbf{x}|^3} dA, \tag{S3}$$

where $\mathbf{x}$ is the distance between the surface element and the single charge. The total force on the single charge points in a wall-normal direction and is found by integrating $d\mathbf{F}$ over the charged area,

$$\mathbf{F} = \int_S d\mathbf{F} = \frac{q d\sigma}{2\pi\varepsilon_0(1+\varepsilon_r)} \int_S \frac{\mathbf{x}}{|\mathbf{x}|^3} dA. \tag{S4}$$

We introduce cylindrical coordinates originating at the center of the charged area and obtain for the normal force $F_n = \mathbf{F} \cdot \mathbf{e}_z$

$$F_n = \frac{q d\sigma}{2\pi\varepsilon_0(1+\varepsilon_r)} \int_0^{2\pi} \int_0^R \frac{zr}{(r^2+z^2)^{3/2}} dr d\phi = \frac{q d\sigma}{\varepsilon_0(1+\varepsilon_r)} \left(1 - \frac{1}{\sqrt{1+R^2/z^2}} \right). \tag{S5}$$

The work required to deposit the additional single charge on the surface is found by integrating $dW = -F_n dz$ from $z = \infty$,

$$-W_0 = \int_0^\infty dW = -\int_0^\infty F_n dz,$$

$$\longrightarrow W_0 = \frac{q d\sigma}{\varepsilon_0(1+\varepsilon_r)} \int_0^\infty \left(1 - \frac{1}{\sqrt{1+R^2/z^2}} \right) dz = \frac{q d\sigma R}{\varepsilon_0(1+\varepsilon_r)}. \tag{S6}$$

The total Coulomb interaction energy on the surface is given by the integral over the surface charge density from zero to $\sigma = q/s^2$, where s is the characteristic spacing of surface charges,

$$E_0 = \int_0^{q/s^2} \frac{qR}{\varepsilon_0(1+\varepsilon_r)} d\sigma = \frac{q\sigma R}{\varepsilon_0(1+\varepsilon_r)}. \tag{S7}$$

Finally, we divide E_0 by s^2 to get the area-specific surface energy due to Coulomb interaction

$$\frac{E_0}{s^2} = \Delta\gamma_\mathrm{S} = \frac{\sigma^2 R}{\varepsilon_0(1+\varepsilon_r)}. \tag{S8}$$

Naturally, because the specific Coulomb interaction energy is $\propto \sigma^2$ and the specific self-energy is $\propto \sigma$, the Coulomb interaction energy dominates the increase in surface energy for $\sigma \gg q/(4\pi Ra) \approx 4\,\mathrm{nC/m}^2$.

S8: Electrostatic length scale.

In its simplest form, the electrostatic situation close to the receding contact line of a drop can be understood as an isopotential wedge next to a charged surface. The electrostatic potential distribution is governed by Laplace's equation, which does not contain an inherent length scale. Essentially, the observed change in contact angle is a consequence of Maxwell stresses deforming the liquid surface. However, from an equation without an intrinsic length scale, one would expect a deformation of the liquid surface that extends over the entire surface of the drop rather than a deformation occurring on such small scales that it only becomes visible as a change in contact angle. This raises the question about the mechanism that induces a sharp localization of the Maxwell stress in the close vicinity of the three-phase contact line.

This question is related to another problem, which is the singularity of the electric field strength at the tip of an isopotential wedge. It is well-known that the electric field strength diverges at this point, which raises the question about the physical mechanism that cuts off the singularity.

With respect to the latter question, different effects come into consideration. The idealized treatment of the liquid as a perfect conductor in the electrostatic problem implies that any Debye screening layers are regarded as infinitely thin. However, in an aqueous medium, counter charges are typically located in a diffuse layer with a thickness between 1 and 100 nm. Thus, treating the liquid surface as isopotential is only valid on length scales larger than the Debye length. This introduces an additional microscopic length scale that could resolve the singularity in the electric field.

A second effect that needs to be considered is dielectric breakdown. Humid air experiences dielectric breakdown at field strengths above about 2 MV/m. Electrostatic discharge thus constitutes a second mechanism that can screen the singularity in the electric field on the length scale where the breakdown field strength is exceeded. For relevant surface charges of the order of $\mu C/m^2$, both of these length scales are much smaller than the macroscopic length scale set by the drop radius and represent a scale that can no longer be resolved by optical imaging of a drop.
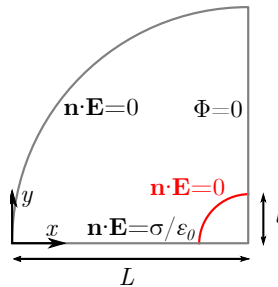

FIG. S6. Computational domain and boundary conditions. The horizontal boundary represents the charged solid surface and the vertical boundary the liquid surface. L and l are the macroscopic and microscopic length scales, respectively. The red circular boundary represents the implementation of the microscopic length scale.

To assess whether this microscopic length scale resolves the singularity in the Maxwell stress and localizes it microscopically in a narrow region around the contact line, we numerically solve the electrostatic Laplace equation,

$$\nabla^2 \Phi = 0, \tag{S9}$$

with the electric potential Φ and the electric field $\mathbf{E} = -\nabla\Phi$, in the computational domain shown in Fig. S6. It represents the gas phase around a charged surface next to an isopotential wedge, where we exemplarily set the contact angle to 90°. On the horizontal boundary, we specify the surface charge density , and on the vertical boundary we set the potential to zero, without loss of generality. The circular arc far from the contact line is assigned a homogeneous Neumann boundary condition, which corresponds to a vanishing normal component of the electric field. The radius L of the wedge represents the macroscopic length scale as set by the droplet radius. We introduce a microscopic length scale by removing a small section of radius l close to the contact line (red, Fig. S6) and compare the results to the situation without a microscopic length scale, $l \to 0$ (gray, Fig. S6). Processes within the excluded section, like electrostatic discharge, are beyond the validity of the governing equation. We use the finite element solver Comsol Multiphysics, version 6.0. We ensure grid independence of the results with a microscopic length scale by systematic refinement, monitoring the Maxwell stress at the coordinates (L, l). Naturally, the case without a microscopic length scale cannot be grid independent arbitrarily close to the singularity.
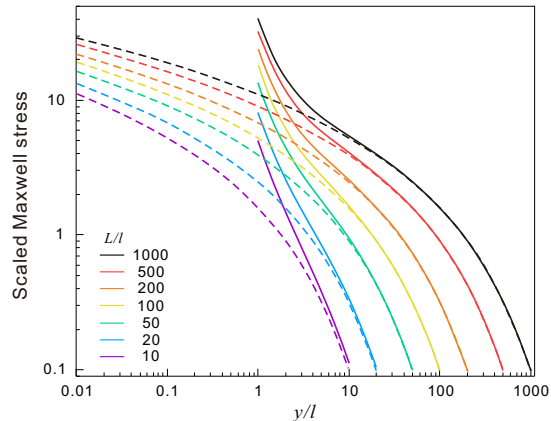
FIG. S7. Normal Maxwell stress scaled by σ^2/ε_0 along the liquid surface over the distance from the contact line y/l for various macroscopic length scales L/l, indicated by different colors. Solid lines correspond to simulations with and dashed lines to simulations without the inclusion of the microscopic length scale. The microscopic length scale eliminates the singularity and localizes the Maxwell stress near the contact line.

In Fig. S7 we show the normal Maxwell stress on the liquid surface, scaled by σ^2/ε_0, over the distance from the contact line, y/l, for various ratios of the length scales L/l. Dashed lines indicate the reference case without a microscopic length scale and solid lines the case with a microscopic length scale. Without a microscopic length scale, the Maxwell stress becomes singular at the contact line. Introducing the microscopic length scale resolves the singularity and focuses the Maxwell stress around the point $y/l = 1$ to an interval up to about $y/l < 10$. Thus, the introduction of a scale l has the effect that the forces deforming the liquid surface largely act in a region extending over a similar scale. This effect is roughly independent of the macroscopic length, as it is present across two orders of magnitude of L/l, which was the range considered in the simulations. We conclude that there is a microscopic length scale that eliminates the electrostatic singularity, for example the Debye length or the scale related to the onset of electrostatic discharge in air. The latter is of the order of $100\,\mathrm{nm}$ for relevant surface charge densities of $\approx 10\,\mu\mathrm{C/m^2}$. Due to the strong localization of the Maxwell stress on scales comparable to the microscopic length scale, the electrostatic forces result in a deformation of the liquid surface that is measurable as a contact angle change that can be modeled using Young's equation.

S10. The influence of different polymer coatings.

The reduction of dynamic contact angles occurs for quartz substrates with different hydrophobic coatings. We measured aqueous drops containing $1\,\mathrm{mM}$ NaCl sliding on a PS-quartz surface, PDMS-quartz surface, and PFOTS-quartz surface with velocities of $0.2 - 0.3\,\mathrm{m/s}$. The corresponding values $\cos(\theta') - \cos(\theta)$ range between 0.05 and 0.25 (Fig. S8).
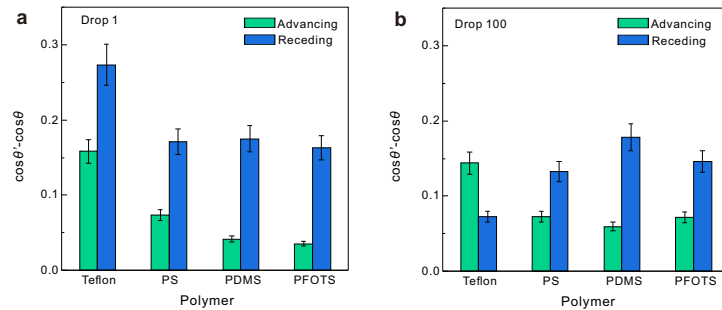
FIG. S8. $\cos(\theta') - \cos(\theta)$ for (a) the 1st and (b) the 100th ungrounded drop containing $1\,\text{mM}$ NaCl with velocities of $0.2 - 0.3\,\text{m/s}$ on quartz substrates with different hydrophobic coatings. θ and θ' are the dynamic contact angles without and with the influence of slide electrification.

S10: Influence of salt type, salt concentration, and drop volume.

We measured the dynamic advancing angles and the dynamic receding angles of ungrounded drops with different salts, different salt concentrations, and drop volumes on 40° tilted Teflon-gold surfaces. The velocity-dependent dynamic advancing and receding angles are similar for all drops (Fig. S10). Thus, we conclude that the influence of salt type, salt concentration, and drop volume on the dynamic contact angles for the Teflon-gold surfaces is ignorable.
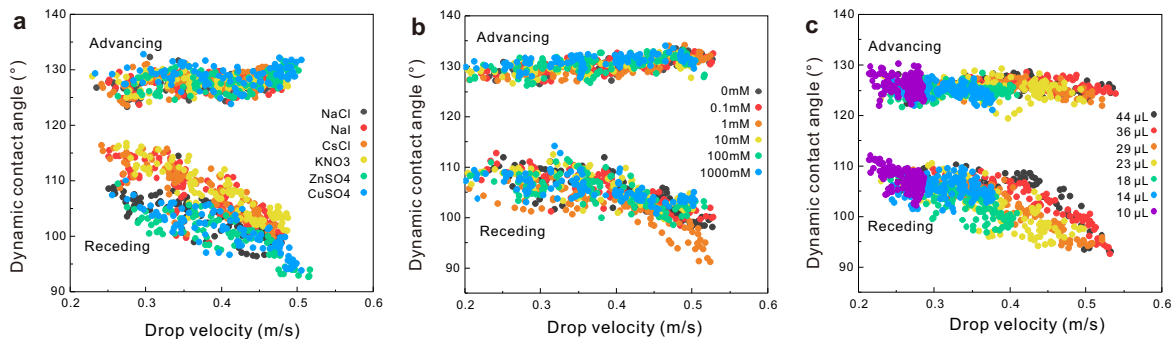
FIG. S9. Velocity-dependent dynamic contact angles for the 1st ungrounded drop for (a) different salts, (b) different NaCl concentrations, and (c) different drop volumes on 40° tilted Teflon-gold surfaces.

We measured ungrounded drops with different salts, NaCl concentrations, and volumes on the Teflon-quartz surface as well. For comparison, we calculated $\cos(\theta') - \cos(\theta)$ based on the Young-Lippmann equation at a velocity regime of $0.3 - 0.4\,\text{m/s}$ for the 1st ungrounded drop. Similar to grounded drops, both the dynamic advancing angle and the dynamic receding contact angle were reduced for drops with different salts (Fig. S10a). In addition, $\cos(\theta') - \cos(\theta)$ first increases and then decreases with the increase in salt concentration (Fig. S10b). $\cos(\theta') - \cos(\theta)$ stays almost constant as a function of drop volume for the dynamic advancing angle, while it increases for the dynamic receding angle (Fig. S10c). The dynamic advancing angle of the 1st ungrounded drop is influenced only by drop charging (electrowetting effect). Because of the compensation between contact area-dependent drop charge and contact area-dependent capacitance, the electrowetting effect is independent of drop volume. By contrast, on the receding side, both drop charging and surface charging affect the contact angle. The influence from surface charging is proportional to the drop radius, thus, $\cos(\theta') - \cos(\theta)$ increases with drop volume.
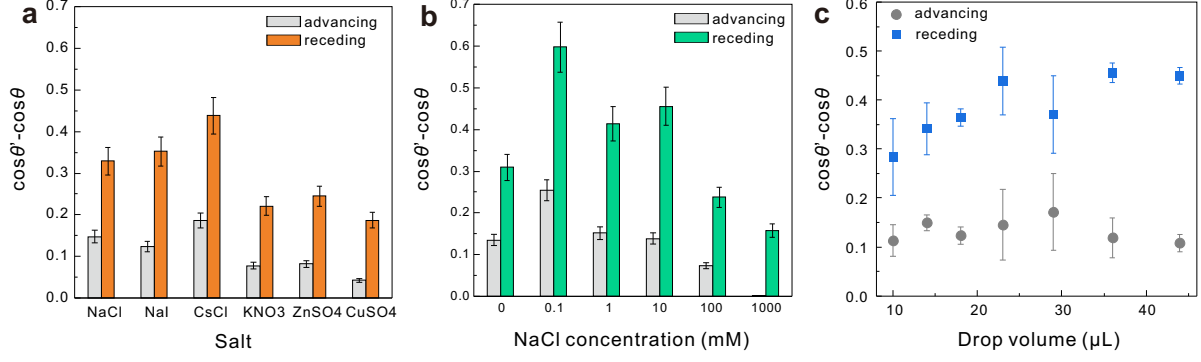
FIG. S10. $\cos(\theta') - \cos(\theta)$ for the 1$^{\text{st}}$ ungrounded drop with different salts (a), with different NaCl concentrations (b), and different volumes of 1 mM NaCl aqueous solution sliding on the Teflon-quartz surfaces with a velocity of $0.3 - 0.4$ m/s. θ and θ' are the dynamic contact angles without and with the influence of slide electrification.

[S1] X. Li, P. Bista, A. Z. Stetten, H. Bonart, M. T. Schür, S. Hardt, F. Bodziony, H. Marschall, A. Saal, X. Deng, R. Berger, S. A. L. Weber, and H.-J. Butt, Nature Physics **18**, 713 (2022).

2.6. X. Li *et al. Submitted*, 2023

Drop friction

Xiaomei Li[1], Francisco Bodziony[2], Mariana Yin[2], Holger Marschall[2], Rüdiger Berger[1], Hans-Jürgen Butt[1] *

1. Max Planck Institute for Polymer Research, Mainz, Mainz, Germany
2. Computational Multiphase Flows, Technische Universität Darmstadt, Darmstadt, Germany

Author contributions:

Xiaomei Li prepared the samples, performed the tilted-plate experiments, analysed and explained the data under Hans-Jürgen Butt and Rüdiger Berger's supervising. Francisco Bodziony and Mariana Yin carried out the numerical diffuse-interface simulations of drop motion under Holger Marschall's supervising. All the authors discussed and interpreted the results and wrote the manuscript.

Drop friction

Xiaomei Li[1], Francisco Bodziony[2], Mariana Yin[2], Holger Marschall[2], Rüdiger Berger[1], Hans-Jürgen Butt[1] *

[1] Max Planck Institute for Polymer Research, Ackermannweg 10, 55128 Mainz, Germany

[2] Computational Multiphase Flows, Technische Universität Darmstadt, Alarich-Weiss-Straße 10, 64287 Darmstadt, Germany

Abstract

Liquid drops sliding on tilted surfaces are an everyday phenomenon and are important for many industrial applications. Still, it is impossible to predict drop's sliding velocity. To make a step forward in quantitative understanding, we measured the velocity U, width w, length, advancing θ_a, and receding contact angle θ_r of liquid drops sliding down inclined flat surfaces made of different materials. We find the friction force acting on sliding drops of polar and non-polar liquids with viscosities (η) ranging from 10^{-3} to $1\,\mathrm{Pa\cdot s}$ can empirically be described by $F_f(U) = F_0 + \mu w \eta U$ for a velocity range up to 0.7 m/s. The dimensionless friction coefficient μ defined here varies between 20 to 200. It is an independent material parameter, specific for a liquid/surface combination. While static wetting is fully described by θ_a and θ_r, for dynamic wetting the friction coefficient is additionally necessary.

Introduction

When designing functional surfaces, people commonly use contact angles to characterize surface wettability[1, 2, 3]. A low contact angle indicates a high affinity between liquid and solid, and vice versa. In equilibrium, this relationship is expressed by Young's equation[4]. For many applications, it is important how drops slide over surfaces. However, a higher contact angle does not necessarily imply low friction between a drop and a solid. For example, rose petal and Salvinia leaves have high contact angles but also high lateral adhesion[5, 6, 7]. In these cases, the contact angle *hysteresis* better describes surfaces. Contact angle hysteresis is defined as the difference between the advancing contact angle and the receding contact angle. The static advancing and receding contact angles are measured at the front and rear, respectively, of sessile drop just before it starts sliding[8]. However, both contact angle and contact angle hysteresis are insufficient to describe the drop dynamics once a drop has started sliding over a surface. Due to the complex dynamics of sliding contact lines, there is no accessible parameter for the kinetic regime, which has a similar function like contact angle or contact angle hysteresis.

Drops sliding down inclined planes are ideal to study drop dynamics, because the external gravitational force driving the motion, $F_g = mg \sin \alpha$, can be adjusted by the tilt angle, α. Here, m is the mass of the drop and $g = 9.81$ m/s^2 is the acceleration of gravity[9, 10]. Despite many experimental and theoretical studies, it is still impossible to quantitatively predict the forces, which slow down drop motion. We call this force, which resists drop motion, "friction force"[11, 12, 13]. This friction force is caused by several dissipative processes. Possible dissipative forces in a sliding drop include hydrodynamic viscous force in the bulk and wedge[14], surface tension forces caused by thermal activation of liquid molecules near the contact line[15], pining/de-pinning by inhomogeneity's on the surface[16], elastocapillary deformation on soft surfaces[17], surface adaptation[18, 19, 20], electrostatic force from slide electrification[21, 22], and aerodynamic resistance[23] (Fig. 1a). Here, we focus on surfaces, which were as flat, smooth, homogenous, rigid, and inert as commonly possible. In this way, we minimize dissipation due to pining/de-pinning, elasto-capillary deformation, and adaptation. We chose high-permittivity or conductive substrates to get rid of electrostatic retardation. The aerodynamic resistance only becomes substantial for superhydrophobic surfaces, where drops reach velocities higher than 1 m/s. Thus, in our case, only dissipation from viscous and contact lines are relevant. The questions addressed were: How does drop friction depend on the velocity? Which material parameters influence drop friction?

How can we describe friction forces quantitatively? Which dissipation processes contribute how strongly to the friction of sliding drops? The aim is to quantitative predict drop sliding velocity.
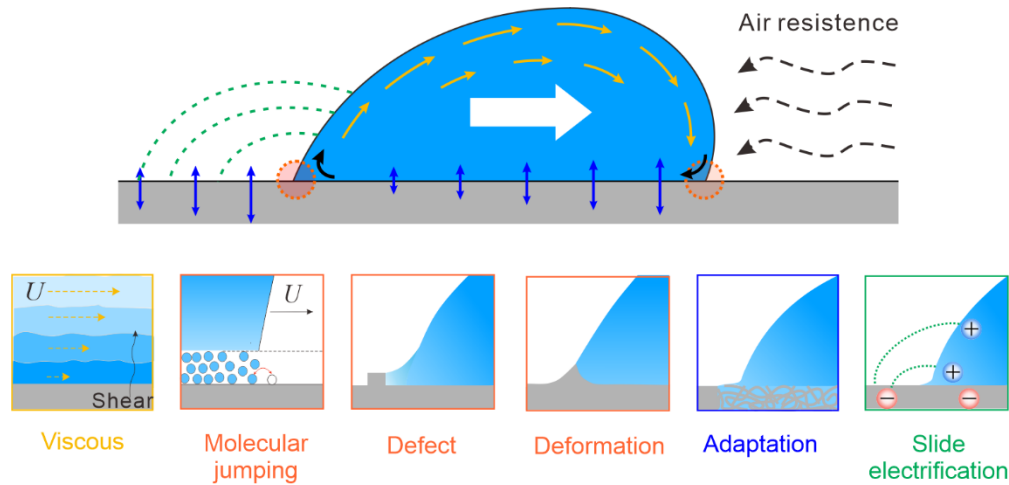

Figure 1. *Schematic of all energy dissipation processes of a sliding drop on a solid surface.*

To answer these questions, we let drops of 17 different liquids slide down 7 different types of planar solid surfaces. We measured their velocity, widths and lengths of their contact area, their advancing and receding contact angles. Using the equation of motion, we calculated the force resisting drop motion. By letting drops slide over few cm and by varying the tilt angle we were able to measure drop friction over drop velocity up to 0.7 m/s. In addition, we simulated the drop motion by direct numerical diffuse-interface simulations.

Results and discussion

Empirical description of friction forces

Drops sliding down tilted surfaces typically accelerate and then reach a steady state velocity. Depending on viscosity and tilt angle, a steady state is reached after a short or long slide distance. For example, water drops sliding down Teflon-gold surfaces showed a monotonically increasing velocity with sliding time and tilt angle (Fig. 2a). On our observation length of 4 cm, the acceleration phase was not over; only for very low tilt angles of 10°, water drops reached their steady-state velocity. Water has a viscosity of η = 0.92×10^{-3} Pas at 25°C (=0.92 cSt). In contrast, drops of silicone oil with a viscosity of 10 cSt slide down the Teflon-gold surface with the steady state velocity at all tilted angles (Fig. 2b).

The drop velocity (U) is defined as the average velocity of advancing contact-line velocity (U_a) and receding contact-line velocity (U_r), that is $U = \frac{U_a + U_r}{2}$ (Fig. 2c). For an increasing drop

velocity, the drops become longer and narrower. Due to the change in aspect ratio, the rear and front velocities were slightly different. The typical difference was, however, less than 8% (Fig. S1). The limitation at high velocity was given by two factors. One is the reachable highest tilt angle of the setup of 70°. The second one is pearl formation with tiny satellite droplets behind the primary drop[24]. In this regime, the drop loses its characteristic shape. For this reason, even water drops with their low viscosity did not exceed ≈0.7 m/s.

To obtain the friction force, we solved the equation of motion. After smoothening measured velocity-versus-time curves, the acceleration(dU/dt) of sliding drops was calculated. By applying the equation of motion[21],

$$F_f = mg \sin \alpha - m^* \frac{dU}{dt},$$ (1)

the friction force F_f on the sliding drop was extracted. Here, m^* is the effective mass with the consideration of the rolling component. We took $m^*/m = 1.05$ from direct numerical diffuse interface simulations[21]. We neglected the effect that m^*/m slightly changes with velocity, because the error from varying m^*/m is lower than the variation of velocity observed from sample to sample (Fig. S2). We also assumed that for every velocity the drop shape has reached its steady state. This assumption is not entirely true, since the drop is accelerating and the real drop shape slightly lags behind. In addition, the damped drop oscillations may cause a deviation from the steady-state drop shape.

We measured drops of 17 different liquids with viscosities ranging over three orders of magnitude (table 1). Seven different surfaces were studied: (1) naturally oxidized bare silicon wafers, (2) indium tin oxide (ITO) coated glass, (3) 1H, 1H, 2H, 2H-perfluorooctadecyltrichloro-silane (PFOTS) on a silicon wafer, (4) poly(dimethylsiloxane) (PDMS) brushes on silicon wafers, (5) 35 nm polystyrene (PS) on gold, (6) perfluorodecanethiol monolayer (thiols) on gold and (7) 60 nm Teflon on gold. The topography of the surfaces imaged by scanning force microscopy (SFM) showed a surface roughness between 0.1 and 2.5 nm (Fig. S3). The sliding details about drop shape, velocity, length and width, dynamic advancing contact angle, dynamic receding contact angles, and forces are summarized in Figs. S4-S25.
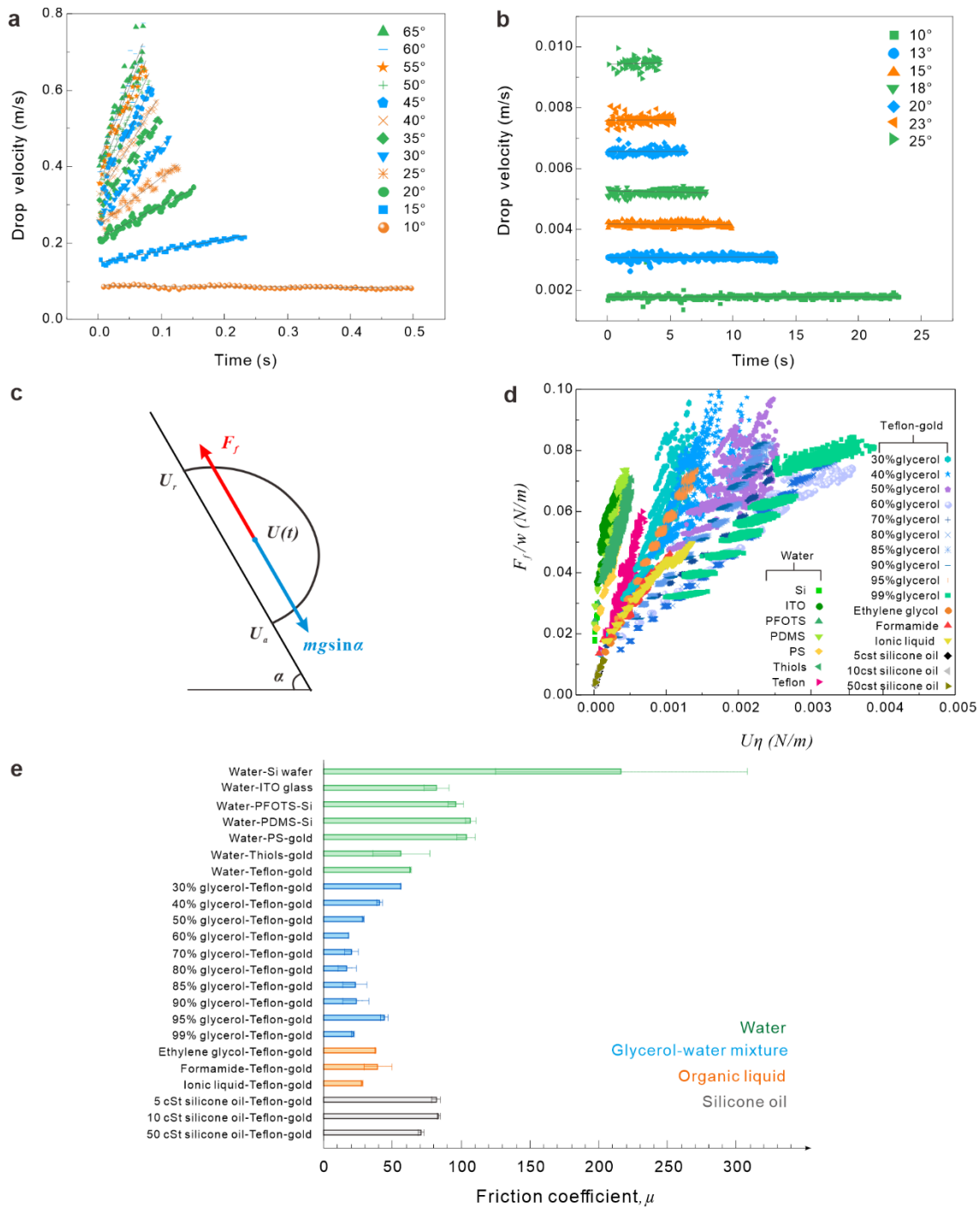
Figure 2. *Calculation and description of friction force. (a) Drop velocity-versus-time for a 30 μL water drop on Teflon-gold surfaces measured at different tilt angles (b) Drop velocity-versus-time for a 10 μL 10 cSt silicone oil drop on Teflon-gold surfaces measured at different tilt angles. (c) Schematic of forces acting on a sliding drop. In steady state, $F_f = mg \sin \alpha$. In the acceleration phase, $m^* \frac{dU}{dt}$ was taken into account in addition. (d) Friction forces per unit width versus velocity*

multiplied by viscous for 23 liquid/surface systems. (e) The friction coefficient of 23 liquid/surface systems.

For all liquid/surface combinations, the friction force increased with drop velocity. To find a universal empirical equation which describes the velocity-dependent friction force, we plotted friction force divided by drop width versus the velocity multiplied by viscosity (Fig. 2d). Normalization of the friction force by the drop width is reasonable because the capillary force is proportional to the width of the contact area of the drop (see below). In addition, a scaling with viscosity will allow the comparison of different liquids. All graphs in Fig. 2d exhibit a linear dependence. Then the friction force for all the liquid/surface combinations were accordingly fitted with the equation:

$$F_f = F_0 + \mu w U \eta \tag{2}$$

Here, F_0 is the friction force extrapolated to $U = 0$. We call the dimensionless term μ friction coefficient. This terminology is different from Bocquet and Barrat's[25], de Ruijter's[26] or McHale's definition[12]. Bocquet and Barrat defined it as the ratio of friction force to velocity by the hydrodynamic approach for the liquid/solid boundary with unit of Ns/m[25]. de Ruijter defined it based on the molecular kinetic theory for drop spreading in units of $Pa \cdot s$[26]. Similar to solid/solid system, McHale defined it as the ratio between drop friction and normal adhesion of a drop[12]. With the definition by equation (2), the friction coefficient depends on the specified liquid/solid surface combination (Fig. 3e). It indicates how the friction force increases with velocity during drop sliding.

The friction coefficient is a new independent material parameter characterizing drop sliding for a certain liquid/solid combination. It depends neither on the mean contact angle nor the contact angle hysteresis (Fig. S26). Equation (2) describes the friction force of all sliding drops over the whole velocity range (Fig. 3). It confirms that F_f increases proportional to the drop width, drop velocity, and viscosity. The proportionality to velocity and viscosity indicates that viscous dissipation is an important dissipation process. However, other dissipation channels like contact line friction and surface adaptation may also contribute to the velocity-dependent friction. They are certainly responsible for the velocity independent part, expressed by F_0.
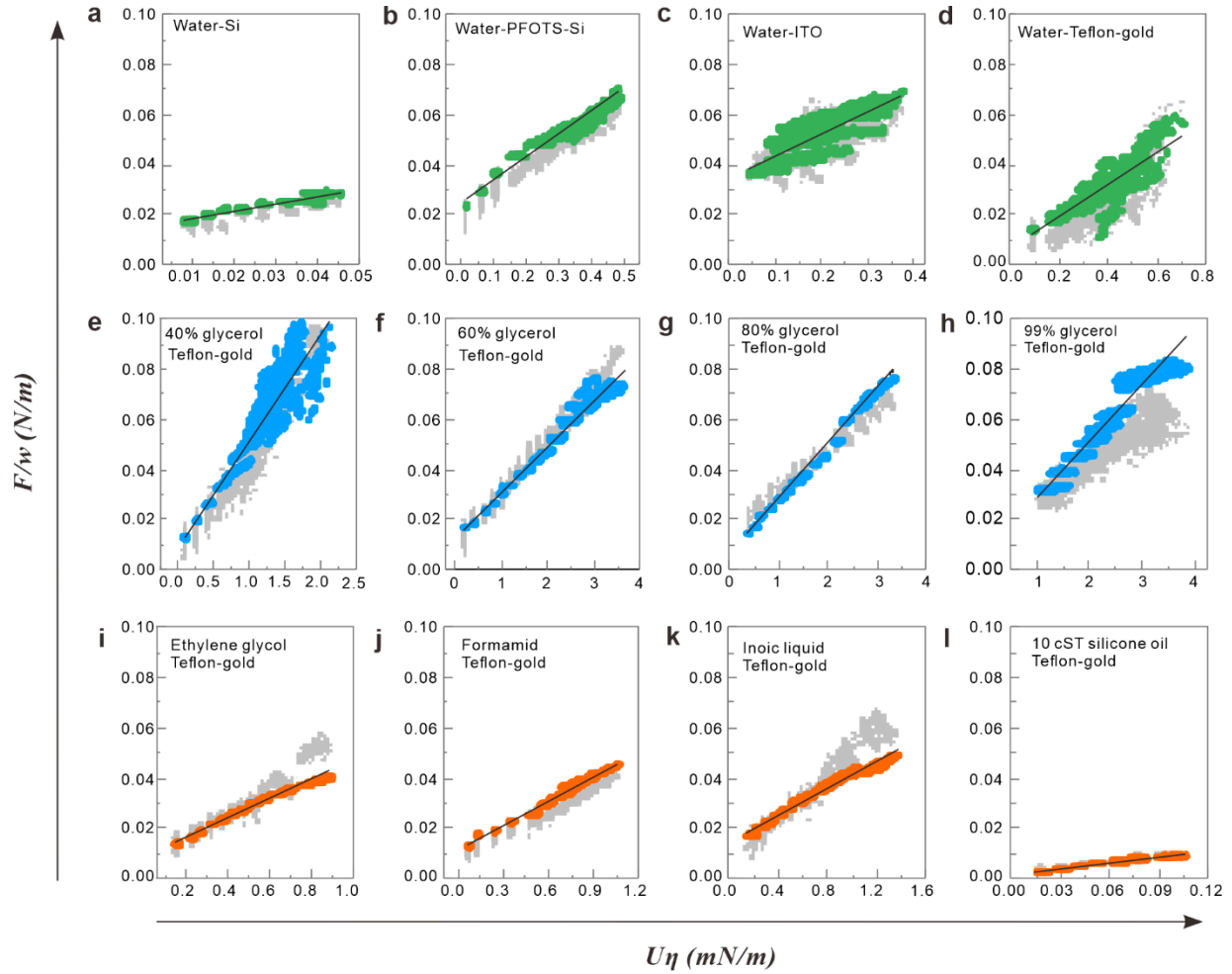
Figure 3. *Friction force (F_f, color) and apparent capillary force ($F_{c-apparent}$, grey) divided by the width $w(U)$ of the drop-versus-velocity multiplied by viscosity for different liquids on different surfaces. Black curves are linear fits with equation (1). The corresponding fitting parameters of μ and F_0/w are shown in table 1. Apparent capillary forces were calculated with equation (3) with measured $\theta_a(U)$, $\theta_r(U)$, and $k = 1$. In some cases like 60-95% glycerol-water mixture or silicone oil, the drop reached its steady state velocity within the first mm of sliding so that $dU/dt \approx 0$. As a results, the graph F_f/w-vs-$U\eta$ looks non-continuous. In contrast, for low-viscosity liquids such as water, drops accelerated within the whole recorded slide length, leading to continuous F_f/w-vs-$U\eta$ graphs.*

Contribution of apparent capillary force to the friction force

The force acting on a *static* sessile drop is given by the integral of the lateral surface tensional forces acting around the contact line (Fig. 4a) [27, 28, 29, 30]:

150

$$F_c = 2\gamma \int_0^\pi \xi \cos\theta \cos\varphi \, d\varphi \qquad (3)$$

Here, ξ is the radius describing the position of the contact line, φ is the azimuthal angle, θ is the contact angle, and γ is the surface tension of the liquid. After integration, one obtains

$$F_c = w\gamma k(\cos\theta_r - \cos\theta_a) \qquad (4)$$

in which, w is the width of the contact area, θ_r and θ_a are the receding and advancing contact angles. k is a geometric factor, whose precise value depends on the shape of the drop[31]. Equation (4) is often referred as the Furmidge-Kawasaki equation[19, 32, 33] and here we call it capillary force F_c.

The static force per unit width F_0/w on a sessile drop can be calculated by $k\gamma(\cos\theta_r^0 - \cos\theta_a^0)$. We obtained F_0/w with equation (2) by extrapolating measured dynamic friction forces to $U \rightarrow 0$. Using the static advancing and receding contact angles θ_a^0 and θ_r^0 which were measured by the in-/deflated drop (method section and table 1), we can calculate the static k-factor, k_s:

$$k_s = \frac{F_0/w}{\gamma(\cos\theta_r^0 - \cos\theta_a^0)} \qquad (5)$$

We find that k_s lies in the range of 0.5 to 1.5 for all the liquid/surface combinations within the error of the measurements (Fig. 4c). The average k-factor of all the liquid/surface systems was 0.88 ± 0.2 for the onset of sliding. This is consistent with ElSherbini and Jacobi's calculation[29] and Extrand's experimental results[34, 35]. For a hypothetical two-dimensional drop (Fig. 4b), the two parallel sides which are parallel to the external force do not contribute to the retentive force, resulting in $k = 1$[32, 33, 36, 37, 38]. In reality, k depends on the shape of the contact line, which varies depending on the azimuthal angle φ, and on how the actual contact angle varies along the contact line[29, 34, 35, 39]. Consequently, for sessile drops a k-factor < 1 is expected.
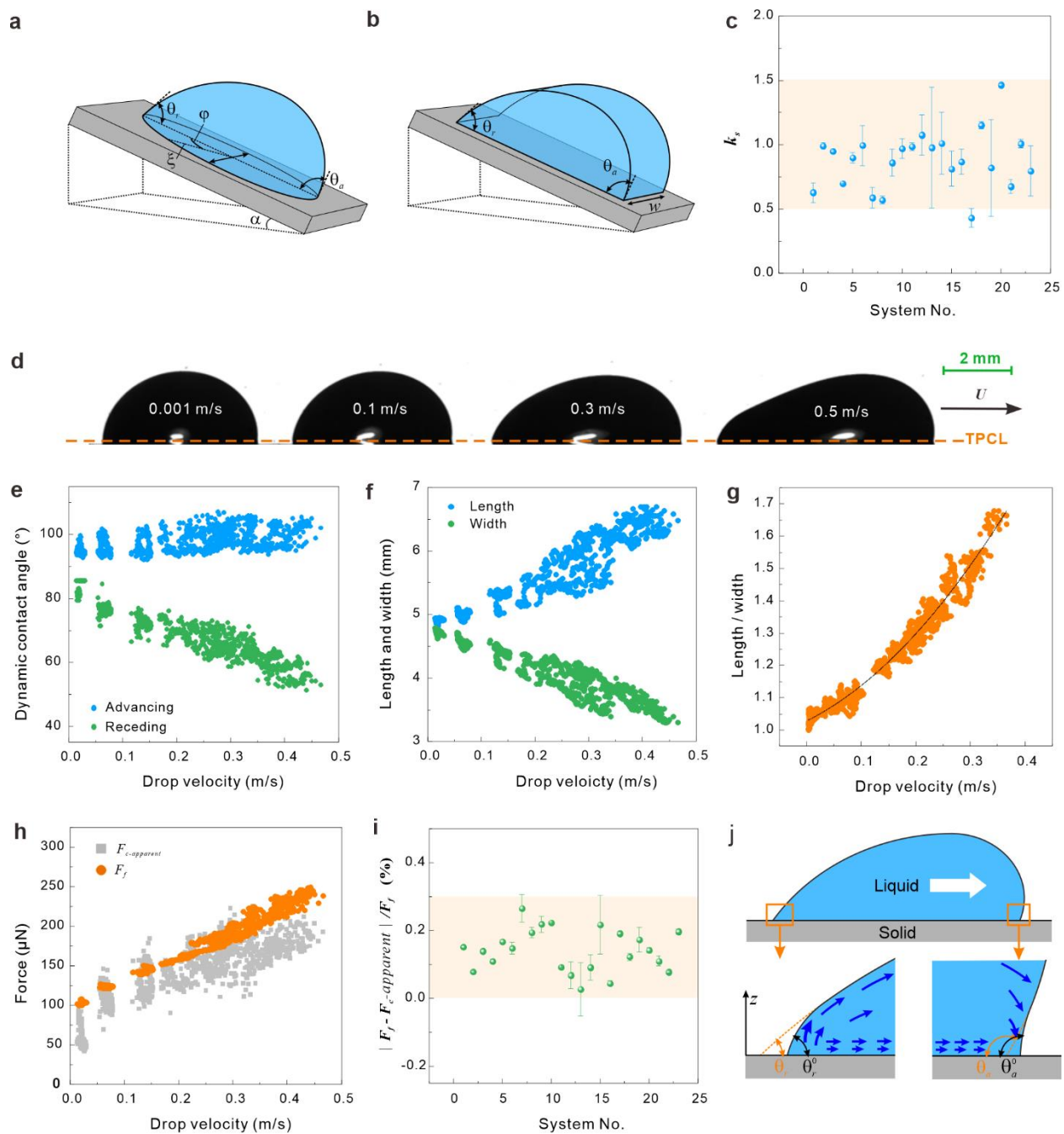
Figure 4. *Dynamic capillary force and its related parameters. (a) Schematic of a drop on a tilted plate and its two-dimensional counterpart (b). (c) Static k-factor (k_s) versus system number derived for the onset of sliding. k_s values were calculated by equation (4). (d) Side-view images of sliding water drops on the PS-gold surfaces at different velocities. Note: TPCL stands for a three-phase contact line. (e) Velocity-dependent dynamic advancing and receding contact angles for 30 µL water drops on PS-gold surfaces. (f) Velocity-dependent drop length, drop width, and length-to-width (g) for 30 µL water drops on PS-gold surfaces. The black curve in (g) is fitting by $\frac{L}{w} =$*

$2.049U^2 + 1.072U + 1.018$. *(h) Friction force and capillary force versus drop velocity for water drops sliding on PS-gold surfaces. (i) The percentage of the absolute difference between $F_{c-apperent}$ and F_f in F_f for 23 liquid/surface combinations. (j) Schematic of the shape of the drop close to the receding and advancing contact line.*

Can one apply equation (4) also in the kinetic regime? In the kinetic regime, sliding drops change their shape (unlike solid/solid systems). Sliding drops elongated with increasing velocity (Fig 4d, Fig. S4-S25). As a result, the contact length (L) increased while contact width (w) decreased (Fig. 4e, Fig. S4-S25), leading to an increasing aspect ratio (L/w) with increasing velocity. The velocity-dependent aspect ratio could be fitted by a 2nd-order polynomial (Fig. 4f, Fig. S4-S25). Knowing the relationship between aspect ratio and drop velocity, and by measuring drop velocity and contact length from the side view, we could determine the contact width. At the same time, the dynamic advancing contact angles increased while the dynamic receding contact angles decreased with drop velocity (Fig. 4g, Fig. S4-S25). By inserting $\theta_r(U), \theta_a(U)$, and $w(U)$ into equation (4), the apparent capillary force ($F_{c-apparent}$) was calculated. For simplicity, we assumed k = 1 and being independent of velocity. We call the force *apparent capillary force* because the apparent receding and advancing contact angles $\theta_r(U)$ and $\theta_a(U)$ were inserted. The apparent capillary forces as given by equation (4) are a good estimate for measured friction forces for all tested liquids and surfaces (Fig 4h, Fig S4-S25). The absolute error is around 5%-25% with k = 1 (Fig 4i). Thus, Eq. (4) is a good description of the friction force and holds even in the kinetic regime by taking an appropriate k-factor.

The above-mentioned proportionality of the friction force to viscosity indicates, that hydrodynamic dissipation plays a substantial role. For this reason, it is not a priori clear why equation (4) is able to describe the kinetic friction force of sliding drops A possible explanation is that relevant dissipating processes act close to the contact line. Then they influence the apparent contact angles, which enter into equation (4). With our setup, we measure the apparent contact angles on a length scale of 10-100 µm. Thus, energy dissipation occurring closer than 100 µm to the contact line are included. The processes include contact line friction as for example described by the molecular kinetic theory (MKT) proposed by Blake & Haynes[15]. It also includes viscous dissipation in the wedge. Cox-Voinov and others explain the change in dynamic contact angles due to viscous dissipation brought by shear flow in a hydrodynamic model near the contact line[40, 41, 42, 43]. Correspondingly, the force is wedge viscous force (F_{vw}). At a length scale of 100 µm, wedge viscous dissipation is already included in the slope of the liquid surface (Fig. 4j). Later, Brochard-Wyart and de Gennes proposed that total energy dissipation at the sliding contact line

153

comprises the viscous losses in the wedge plus processes related to contact line friction[44]. Meanwhile, Petrov and Petrov considered molecule hoping process affect the microscopic contact angle which further influence the apparent contact angles, microscopic contact angle and apparent contact angle are described by the MKT model and the hydrodynamic model individually[45]. At the end, both of them derived a similar formula. Thus, more than one process can contribute to energy dissipation near the contact line.

Assuming the contact line friction and wedge viscous dissipation enter via the dynamic advancing and receding contact angles leaves us with a total friction force

$$\text{F}_f = w\gamma k(\cos\theta_r - \cos\theta_a) + F_{bv} \tag{6}$$

Here, F_{bv} is the bulk viscous force. The good agreement between the forces calculated with the Furmidge-Kawasaki equation (4) and measured friction forces is thus most likely the effect of two compensating errors. On one hand, by setting $k = 1$, we most likely overestimated the capillary contribution. On the other hand, we neglected bulk viscous forces, leading to an underestimation of the friction force.

Table 1. *Properties of all the liquid/surface combinations. m, γ, and η are the drop mass, surface tension, and viscosity; θ_a^0 and θ_r^0 are the static advancing and receding contact angles. μ is the friction coefficient. $\frac{F_0}{w}$ is the dynamic friction force at zero velocity per unit width. (3). k_s is the static k-factor.*

System No.	Liquid-Surface	$m^{(3)}$ mg	γ mN/m	$\eta^{(4)}$ mPa·s	$\theta_a^{0(5)}$ °	$\theta_r^{0(5)}$ °	μ	F_0/w mN/m	$k_s^{(6)}$
1	Water-Si wafer	30	72	0.92	65	35	216±91	17.9±2	0.63±0.07
2	Water-ITO glass	30	72	0.92	111	83	82±9	34.3±1	0.99±0.03
3	Water-PFOTS	30	72	0.92	116	86	96±5	24.7±1	0.95±0.01
4	Water-PDMS	30	72	0.92	108	87	107±4	25.6±1	0.7±0.02
5	Water-PS	30	72	0.92	95	78	104±7	19.1±1	0.9±0.04
6	Water-Thiols	30	72	0.92	120	92	56±21	33.3±5	1±0.16
7	Water-Teflon	30	72	0.92	122	110	63±2	7.9±1	0.59±0.08
8	30% Glycerol-Teflon	30	69	2.5	112	102	56±2	6.6±1	0.57±0.1
9	40% Glycerol-Teflon	30	69	3.8	111	101	41±2	9.9±2	0.86±0.1
10	50% Glycerol-Teflon	30	68	6.9	109	100	29±2	13.3±1	0.97±0.08

11	60% Glycerol-Teflon	30	67	13.6	113	101	18±2	13.2±1	0.99±0.03
12	70% Glycerol-Teflon	30	66	27.1	112	101	20±5	13.1±1	1.08±0.16
13	80% Glycerol-Teflon	30	66	75.9	112	102	17±7	10.8±5	0.98±0.47
14	85% Glycerol-Teflon	30	65	93	111	100	23±9	12.2±3	1.01±0.24
15	90% Glycerol-Teflon	30	65	192	111	101	23±10	8.9±2	0.81±0.14
16	95% Glycerol-Teflon	30	65	265	109	99	44±3	10.5±2	0.87±0.1
17	99% Glycerol-Teflon [1]	30	64	943	111	98	22±2	6.1±1	0.43±0.07
18	Ethylene glycol-Teflon	21	48	16	98	88	38±2	9.6±1	1.15±0.03
19	Formamide-Teflon	32	58	4.6	105	94	40±10	9±4	0.82±0.38
20	Ionic liquid[2]-Teflon	30	51	22	101	90	28±2	14.3±1	1.46±0.07
21	5 cSt silicone oil-Teflon	10	21	5	55	45	82±3	1.9±1	0.68±0.05
22	10 cSt silicone oil-Teflon	11	21	10	56	49	84±2	2.1±1	1.01±0.07
23	50 cSt silicone oil-Teflon	12	21	50	58	47	71±2	2.5±1	0.8±0.19

Note: (1) 99% glycerol was purchased commercially, 30%-95% glycerol-water mixtures were made with 99% glycerol and distilled water. (2) The ionic liquid was 1-ethyl-3-methyl-imidazolium-thiocyanate. (3) The measurement error of drop mass was ±3 mg. (4) The error for the mixtures was around 15%. (5) The measurement error of static contact angle ($\theta_{a/r}^{\circ}$) was typically ±3°. (6) k_s is an average value over all the velocities.

Wedge and bulk viscous force in the simulation

Separating viscous dissipation from the wedge and bulk is a challenge as the transition between both is gradual[14]. Thus, to find out where viscous energy is dissipated inside a sliding drop, we carried out direct numerical simulations (DNS). The force caused by viscous dissipation can be accounted for by integrating the hydrodynamic shear stress (viscous force density in N/m^2) over the contact area of the drop. The simulations show that viscous dissipation is increased close to the three-phase contact line (Fig. 5a). Thus, we define the "wedge" region with a height of mesh height (37 μm) and a width (100-350 μm) equal to the double distance from the contact line to the peak of viscous dissipation (Fig. 5b). With this definition, the ratio between the wedge and bulk viscous dissipation was around 1/1 for water drops on PS-gold surfaces (Fig. 5c, green and blue triangles). For drops of 85% glycerol-water mixture on Teflon-gold surfaces, the wedge-to-bulk dissipation was 7/3 (Fig. S27). Both bulk and wedge dissipation forces increase roughly

linearly with velocity (Fig. 5c, green and blue triangle). Due to numerical errors, the linearly increasing viscosity forces deviate slightly at high velocity. Most importantly, bulk viscous forces in both systems are the lowest dissipated force and take up less than 20% of the friction force. This is in line with the deviation of apparent capillary force from friction force (Fig. 4i) and confirms our hypothesis that bulk viscous force is low.

The capillary force in the simulation was calculated by integrating the capillary stress, which is a function of the surface tension, over the contact area (eq. 9). The capillary force was almost constant for the glycerol-water mixture (Fig. S27, star). It increased linearly for pure water (Fig. 5c, star). The increasing capillary force for water can be attributed to the elongation of the drop with increasing contact area at high velocity (>0.1 m/s). The other reason could be that the shape of the interface degrades with fast dynamics at high velocity (details in the experimental section). This degradation could be reduced by implementing an interfacial relaxation method, like the one proposed in ref. 48. In contrast, the velocity for 85% glycerol-water mixture is so low that the shape of drops did not change much. Thus, drop-shape geometry affects the capillary force.

We further compared the apparent capillary force in the experiment with the sum of simulated wedge viscous force and simulated capillary forces (Fig. 5c and Fig. S27, circle). They match well, further confirming our hypothesis that apparent capillary force includes the wedge viscous dissipation.
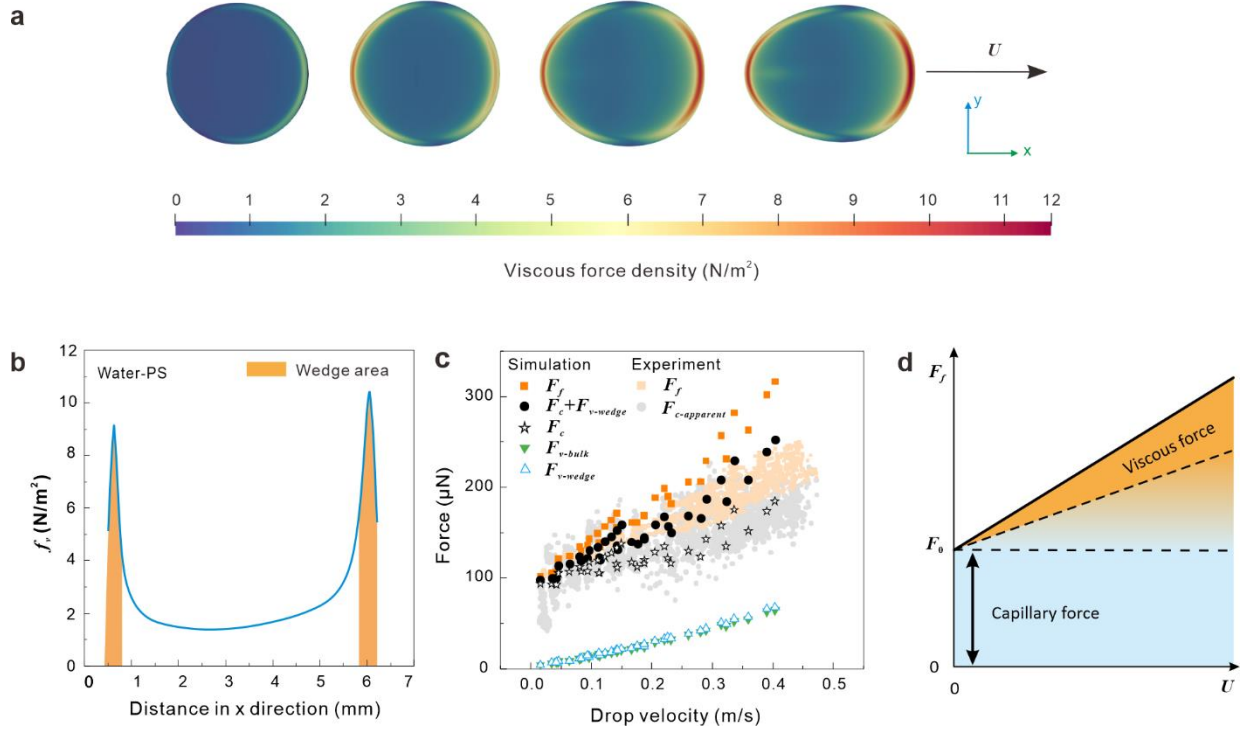
Figure 5. *Simulation of sliding drop by direct numerical simulations. (a) The distribution of viscous force density (f_v) at the solid-liquid interface of a water drop on a 50° tilted PS-gold surface at velocities at 0.06 m/s, 0.12 m/s, 0.18 m/s, and 0.25 m/s. (b) The definition of wedge region which is based on the viscous force density along x direction in (a). (c) Comparison of simulated force with the experimental force for water drops on PS-gold surface. (d) Schematic of friction force and its origin develop as the velocity of sliding drops.*

Conclusions

Friction forces of drops sliding on flat solid surfaces can empirically be described by $F_f = F_0 + \mu w U \eta$. The dimensionless friction coefficient μ depends on specific liquid/surface combination. This description is valid for polar and nonpolar liquids with viscosities in the range from 0.001 to 1 Pas. At least two different channels of energy dissipation occur: Capillary forces caused by contact angle hysteresis and viscous forces caused by shear flow. At low velocity, the capillary force dominates (Fig. 5d, blue region). It is given by $F_f(U \to 0) = F_0 = 0.88 w \gamma (\cos \theta_r^0 - \cos \theta_a^0)$. With increasing velocity, the linearly increasing part of the friction force, $\mu w U \eta$, contributes more and more (Fig. 5d, orange region). This increase is largely due to increasing wedge and bulk viscous dissipation. In addition, the capillary force may change due to the changes in drop shape and an increasing contact angles hysteresis. The Furmidge-Kawasaki

equation (4) is a good description of the friction force even for sliding drops, provided that the apparent dynamic receding and advancing contact angles are inserted. The shape factor for static friction is $k_s = 0.88 \pm 0.2$. With the above findings, a quantitative prediction of drop motion is achieved, which will facilitate the advancement in surface design, characterization, and drop manipulation.

Materials and Methods

Liquids. As liquids we used water (<1 µS/cm; Gibco, Thermo Fisher Scientific), glycerol (99%, AppliChem), water-glycerol mixtures, ethylene glycol ($\geq 99\%$ VWR), formamide (99.5%, AppliChem), the ionic liquid 1-ethyl-3-methyl-imidazolium-thiocyanate ($\geq 95\%$, Sigma-Aldrich) and silicon oil (Sigma-Aldrich).

Preparation of surfaces. We analysed 5 types of hydrophobic surfaces. To avoid electrostatic effects, all samples were on substrates with high dielectric permittivity. Gold substrates with 5 nm chromium and 35 nm gold on glass slides were prepared by sputter coating. After sputter coating, the gold substrates were used immediately without further cleaning. We used five different surfaces:

(1) Si wafer: Si wafer with native oxide layer of 1.6±0.3 nm as measured by ellipsometry, resistivity < 0.005 Ωcm, and thickness of 525±25 µm is from Silicon Materials (Germany). After cut into 25×100 mm^2, it was washed by ultrasonic cleaning with ethanol and then dried by nitrogen blowing.

(2) ITO glass: ITO glass ($24 \times 60 \times 0.175$ mm^3) is from Präzisions Glas & Optik (Germany) with resistivity of 20±5 Ohm/sq. It was used after purchase without further processing.

(3) PFOTS-Si surfaces: The PFOTS coating on Si wafer were prepared by chemical vapor deposition. The clean Si wafer were activated by 100% O$_2$ plasma for 10 min, then put into a vacuum desiccator containing a tiny glass bottle with 0.5 mL 1H, 1H, 2H, 2H-perfluorooctadecyl-trichlorosilane (97%, Sigma-Aldrich). The desiccator was evacuated to <100 mbar. After 30 min deposition, the samples were moved out and cleaned by rinsing with ethanol to remove unbound silanes.

(4) PDMS-Si surfaces: The poly(dimethylsiloxane) (PDMS) brushes coatings with thickness of around 5 nm were prepared by the "grafting to" method using PDMS (molecular weight, 6 kgmol^{-1}; Alfa Aesar) as described in[46]. Few drops of PDMS were deposited on a cleaned Si wafer.

The samples were stored at 22–23 °C and 30–60% relative humidity for 24–48 hours after the PDMS drops spread and covered the substrates. Before using, they were cleaned by ultrasonic in toluene, ethanol, and distilled water for 10 min each.

(5) PS-gold surfaces: 35 nm polystyrene coatings on gold substrates were prepared by dip-coating with the pulling speed of 90 mm/min from a solution of 1 wt% PS (molecular weight: 192 kgmol^{-1}, ε=2.6; Sigma-Aldrich) in toluene (99.8%, Sigma-Aldrich). Before using, the PS samples were annealed in the oven at 120°C under vacuum for 24 h.

(6) Thiols-gold surfaces were also prepared by "grafting to". Fresh gold substrates were immersed in 1 mM 1H,1H,2H,2H-perfluorodecanethiol/ethanol solution for 24 h. Then the surfaces were taken out and rinsed with fresh ethanol to remove unbound thiols.

(7) Teflon-gold surfaces: 60 nm Teflon coatings on gold substrates were prepared by dip-coating with the pulling speed of 10 mm/min from a solution of 1 wt% Teflon AF 1600 (ε=1.9; Sigma-Aldrich) in FC-43 (Sigma-Aldrich). Before using, the Teflon samples were annealed in the oven at 160°C under vacuum for 24 h.

Surface roughness was determined by SFM in tapping mode (Dimension Icon, Bruker) on an area of 0.5×0.5 μm^2 (figure S1). The cantilever had a nominal resonance frequency of 300 kHz and a spring constant of 26 N/m (160AC-NA, OPUS). The errors of root-mean-square roughness are from the deviation of three measurements on different positions and different samples.

Measurement of viscosity. The viscosity of the glycerol-water mixture was measured by a rolling ball viscometer LOVIS 2000 M (Anton Paar) with 600 μL solution at 25℃.

Static advancing and receding contact angles. Method of in-/deflated sessile water droplets was used to quantify the "static" advancing and receding contact angles (θ_r^0 and θ_a^0) by OCA 35, DataPhysics Instruments. First, an 8 μL liquid drop was deposited on the tested surfaces. Then 16 μL liquid was pumped into then pumped out of the drop with a flow rate of 1 $\mu L/s$ by a Hamilton syringe with a hydrophobic needle. Without pausing, the procedure was carried out three times. The inflation and deflation of drop were recorded from the side. By elliptical fitting to the drop contour, θ_r^0 and θ_a^0 were determined.

Measurement of sliding drop. The velocity and the dynamic contact angles, $\theta_r(U)$ and $\theta_a(U)$ were meaured by a home-built tilted plate setup[20, 21]. The drops were placed automatically on the tilted surfaces from a grounded syringe needle (1.5 mm outer diameter, Dosiernadel Vollmetal) connected to a peristaltic pump (MINIPULS 3, Gilson). Different liquids had slightly different drop sizes (table 1) because the drop volume depends on the surface tension and

density of the liquid. The height between the syringe needle and the surfaces was ≈5 mm, just enough to release the drop. Before starting to slide, the drops were neutralized by a grounded electrode. A high-speed camera (FASTCAM Mini UX100 (Photron) from the side recorded the drop sliding after the drops had detached from the grounded electrode. The lens (TitanTL telecentric lens, ×0.268, C-mount, Edmund Optics) had a resolution of ≈30 μm per pixel. Side view videos of the sliding drops were analysed by an adapted open drop-shape analysis code from MATLAB (DSAfM) version 9.5.0.944444 (R2018b). The dynamic advancing and receding contact angles were determined by applying a 4th polynomial fit to two-semic ellipse drop counters, which were divided in the middle of drops. The drop velocity was an average from the rear, U_r, and front, U_a, contact line velocity. All measurements were conducted at a temperature of 20 ± 1 °C and a humidity of 15–30%.

Direct numerical simulations (DNS) were based on a diffuse interface phase-field method. In this method, an initial hemispherical drop with a radius of $a = 2.5$ mm is placed on a 0.025×0.010 m^2 rectangular smooth inclined wall. The contact angle field of the numerical drop is computed directly from the wetting boundary condition using static contact angle as an input. We used the adaptive mesh refinement (AMR) technique with a mesh width of around 37 μm and a mesh density of 4000000. We have tried a higher mesh density of 7000000, but the influence of mesh density on numerical accuracy was negligible. The details about the schemes and solver in the simulation are referred to [F.Bodziony, M. Wörner, H. Marschall. The stressful way of droplets along single fibre strands – A computational analysis (accepted)]. To calculate the velocity and acceleration, the drop's barycentre positions were tracked for various inclination angles. Based on the velocity gradient, ∇U, the viscous stress tensor, $\tau = \mu(\nabla U + \nabla U^T)$, and the viscous force, F_v, in a contact area domain Ω was calculated:

$$F_v = \int f_v \, d\Omega = \int \tau \nabla U d\Omega \tag{8}$$

f_v is the viscous dissipation density per unit area in N/m^2. Based on the Saint Venant-Kirchho solid model[47], the capillary force was computed by integrating the surface tension stress in the contact area domain Ω with

$$F_c = \int \sigma \epsilon \partial_n C(x) \nabla C(x) d\Omega \tag{9}$$

σ relates to the surface tension γ by $\sigma = \frac{3}{2\sqrt{2}} \gamma$, ϵ is the capillary width indicating the thickness of the diffuse interface. $C(x)$ is the phase-field order parameter defined by volume fraction and x is

the local coordinate normal to the interface. $C(x) = \pm 1$ represents a pure phase, while $C(x) \in (-1,1)$ indicates a mixing phase. When $C(x)$ follows

$$C(x) = \tanh\left(\frac{x}{\sqrt{2}\epsilon}\right), \tag{10}$$

the drop shape has an equilibrium profile. We assume our numerical drop has an equilibrium profile to calculate the capillary force, which is not entirely true because the interface profile gets degraded with $C(x)$ deviating from eq. (10) at high velocity (> 0.1m/s).

Acknowledgment

References

1. Huhtamäki, T., Tian, X., Korhonen, J.T. & Ras, R.H. Surface-wetting characterization using contact-angle measurements. *Nature Protocols* **13**, 1521-1538 (2018).

2. Wang, D., Sun, Q., Hokkanen, M.J., Zhang, C., Lin, F.-Y., Liu, Q*., et al.* Design of robust superhydrophobic surfaces. *Nature* **582**, 55-59 (2022).

3. Li, X., Wang, D., Tan, Y., Yang, J., Deng, X. Designing transparent micro/nano re-entrant-coordinated superamphiphobic surfaces with ultralow solid/liquid adhesion. *ACS Applied Materials & Interfaces* **11**,29458-29465 (2019).

4. Young, T. III. An essay on the cohesion of fluids. *Philosophical Transactions of the Royal Society of London* **95**, 65-87 (1805).

5. Bhushan, B., Her, E.K. Fabrication of superhydrophobic surfaces with high and low adhesion inspired from rose petal. *Langmuir* **26**, 8207-8217 (2010).

6. Barthlott, W., Schimmel, T., Wiersch, S., Koch, K., Brede, M., Barczewski, M. *et al.* The Salvinia paradox: superhydrophobic surfaces with hydrophilic pins for air retention under water. *Advanced Materials* **22**, 2325-2328 (2010).

7. Li, X., Yang, J., Lv, K., Papadopoulos, P., Sun, J., Wang, D. *et al.* Salvinia-like slippery surface with stable and mobile water/air contact line. *National Science Review* **8,** 153-164 (2021).

8.   Butt, H.-J., Liu, J., Koynov, K., Straub, B., Hinduja, C., Roismann, I. *et al.* Contact angle hysteresis. *Current Opinion in Colloid & Interface Science*, 101574 (2022).

9.   Tadmor, R., Bahadur, P., Leh, A., N'guessan, H.E., Jaini, R., Dang, L. Measurement of lateral adhesion forces at the interface between a liquid drop and a substrate. *Physical Review Letters* **103**, 266101 (2009).

10.   Yoshida, N., Abe, Y., Shigeta, H., Nakajima, A., Ohsaki, H., Hashimoto, K*. et al.* Sliding behavior of water droplets on flat polymer surface. *Journal of the American Chemical Society* **128**, 743-747 (2006).

11.   Bormashenko, E., Bormashenko, Y., Oleg, G. On the nature of the friction between nonstick droplets and solid substrates. *Langmuir* **26**, 12479-12482 (2010).

12.   McHale, G., Gao, N., Wells, G.G., Barrio-Zhang, H., Ledesma-Aguilar, R. Friction coefficients for droplets on solids: The liquid–solid Amontons' Laws. *Langmuir* **38**, 4425-4433 (2022).

13.   Backholm, M., Molpeceres, D., Vuckovac, M., Nurmi, H., Hokkanen, M.J., Jokinen, V. *et al.* Water droplet friction and rolling dynamics on superhydrophobic surfaces. *Communications Materials* **1**, 1-8 (2020).

14.   Kim, H.-Y., Lee, H.J., Kang, B.H. Sliding of liquid drops down an inclined solid surface. *J. of Colloid Interface Sci.* **247**, 372-380 (2002).

15.   Blake, T., Haynes, J. Kinetics of liquidliquid displacement. *Journal of Colloid and Interface Science* **30**, 421-423 (1969).

16.   Joanny, J., De Gennes, P.-G. A model for contact angle hysteresis. *The Journal of Chemical Physics* **81**, 552-562 (1984).

17.   Andreotti B, Snoeijer JH. Statics and dynamics of soft wetting. *Annual Review of Fluid Mechanics* **52**, 285-308 (2020).

18.   Butt, H.-J., Berger, R., Steffen, W., Vollmer, D., Weber, S.A. Adaptive wetting—adaptation in wetting. *Langmuir* **34**, 11292-11304 (2018).

19.   Tadmor, R. Open problems in wetting phenomena: pinning retention forces. *Langmuir* **37**, 6357-6372 (2021).

20.   Li, X., Silge, S., Saal, A., Kircher, G., Koynov, K., Berger, R. *et al.* Adaptation of a styrene–acrylic acid copolymer surface to water. *Langmuir* **37**, 1571-1577 (2021).

21.   Li, X., Bista, P., Stetten, A.Z., Bonart, H., Schür, M.T., Hardt, S. *et al.* Spontaneous charging affects the motion of sliding drops. *Nature Physics* **18**, 1-7 (2022).

22.   Díaz, D., Li, X., Bista, P., Zhou, X., Darvish, F., Butt, H.-J. *et al.* Self-generated electrostatic forces of drops rebounding from hydrophobic surfaces. *Physics of Fluids* **35**, 017111 (2023).

162

23. Mouterde, T., Raux, P.S., Clanet, C., Quéré, D. Superhydrophobic frictions. *Proceedings of the National Academy of Sciences* **116**, 8220-8223 (2019).

24. Le Grand, N., Daerr, A., Limat, L. Shape and motion of drops sliding down an inclined plane. *Journal of Fluid Mechanics* **541**, 293-315 (2005).

25. Bocquet, L., Barrat, J.-L. Hydrodynamic boundary conditions, correlation functions, and Kubo relations for confined fluids. *Physical Review E* **49**, 3079 (1994).

26. De Ruijter, M.J., Blake, T., De Coninck, J. Dynamic wetting studied by molecular modeling simulations of droplet spreading. *Langmuir* **15**, 7836-7847 (1999).

27. Brown, R., Orr Jr, F., Scriven, L. Static drop on an inclined plate: analysis by the finite element method. *Journal of Colloid and Interface Science* **73**, 76-87 (1980).

28. Dimitrakopoulos, P., Higdon, J. On the gravitational displacement of three-dimensional fluid droplets from inclined solid surfaces. *Journal of Fluid Mechanics* **395**, 181-209 (1999).

29. ElSherbini, A., Jacobi, A. Retention forces and contact angles for critical liquid drops on non-horizontal surfaces. *Journal of Colloid and Interface Science* **299**, 841-849 (2006).

30. Semprebon, C., Brinkmann, M. On the onset of motion of sliding drops. *Soft Matter* **10**, 3325-3334 (2014).

31. Ravazzoli, P.D., Cuellar, I., González, A.G., Diez, J.A. Contact-angle-hysteresis effects on a drop sitting on an incline plane. *Physical Review E* **99**, 043105 (2019).

32. Furmidge, C. Studies at phase interfaces. I. The sliding of liquid drops on solid surfaces and a theory for spray retention. *Journal of Colloid Science* **17**, 309-324 (1962).

33. Kawasaki, K. Study of wettability of polymers by sliding of water drop. *Journal of Colloid Science* **15**, 402-407 (1960).

34. Extrand, C, Gent, A. Retention of liquid drops by solid surfaces. *Journal of Colloid and Interface Science* **138**, 431-442 (1990).

35. Extrand, C.W., Kumagai, Y. Liquid drops on an inclined plane: the relation between contact angles, drop shape, and retentive force. *Journal of Colloid and Interface Science* **170**, 515-521 (1995).

36. Buzágh, A., Wolfram, E. Bestimmung der Haftfähigkeit von Flüssigkeiten an festen Körpern mit der Abreißwinkelmethode. II. *Kolloid-Zeitschrift* **157**, 50-53 (1958).

37. Olsen, D.A., Joyner, P.A., Olson, M.D. The sliding of liquid drops on solid surfaces. *The Journal of Physical Chemistry* **66**, 883-886 (1962).

38. Dussan, E. On the ability of drops or bubbles to stick to non-horizontal surfaces of solids. Part 2. Small drops or bubbles having contact angles of arbitrary size. *Journal of Fluid Mechanics* **151**, 20 (1985).

39. Humayun, S., Maynes, R.D., Crockett, J., Iverson, B.D. Retention forces for drops on microstructured superhydrophobic surfaces. *Langmuir* **38**, 15960-15972 (2022).

40. Voinov, O. Hydrodynamics of wetting. *Fluid Dynamics* **11**, 714-721 (1976).

41. Cox, R. The dynamics of the spreading of liquids on a solid surface. Part 1. Viscous flow. *Journal of Fluid Mechanics* **168**, 169-194 (1986).

42. Hocking, L. Rival contact-angle models and the spreading of drops. *Journal of Fluid Mechanics* **239**, 671-681 (1992).

43. Petrov, J.G., Petrov, P.G. Forced advancement and retraction of polar liquids on a low energy surface. *Colloids and Surfaces* **64**, 143-149 (1992).

44. Brochard-Wyart, F., De Gennes, P. Dynamics of partial wetting. *Advances in Colloid and Interface Science* **39**, 1-11 (1992).

45. Petrov, P., Petrov, I. A combined molecular-hydrodynamic approach to wetting kinetics. *Langmuir* **8**, 1762-1767 (1992).

46. Teisala, H., Baumli, P., Weber, S.A., Vollmer, D., Butt, H.-J. Grafting silicone at room temperature—a transparent, scratch-resistant nonstick molecular coating. *Langmuir* **36**, 4416-4431 (2020).

47. Van Brummelen, E., Shokrpour-Roudbari, M., Van Zwieten, G. Elasto-capillarity simulations based on the Navier–Stokes–Cahn–Hilliard equations. *Advances in Computational Fluid-Structure Interaction and Flow Simulation*, 451-462 (2016).

48. Bagheri, M., Stumpf, B., Roisman, I.V., Tropea, C., Hussong, J., Wörner, M. et al. Interfacial relaxation – crucial for phase-field methods to capture low to high drop–film impacts. *International Journal of Heat and Fluid Flow* **94**, 108943 (2022).

Supporting information

Drop friction

Xiaomei Li[1], Francisco Bodziony[2], Mariana Yin[2], Holger Marschall[2], Rüdiger Berger[1], Hans-Jürgen Butt[1] *

[1] Max Planck Institute for Polymer Research, Ackermannweg 10, 55128 Mainz, Germany

[2] Computational Multiphase Flows, Technische Universität Darmstadt, Alarich-Weiss-Straße 10, 64287 Darmstadt, Germany
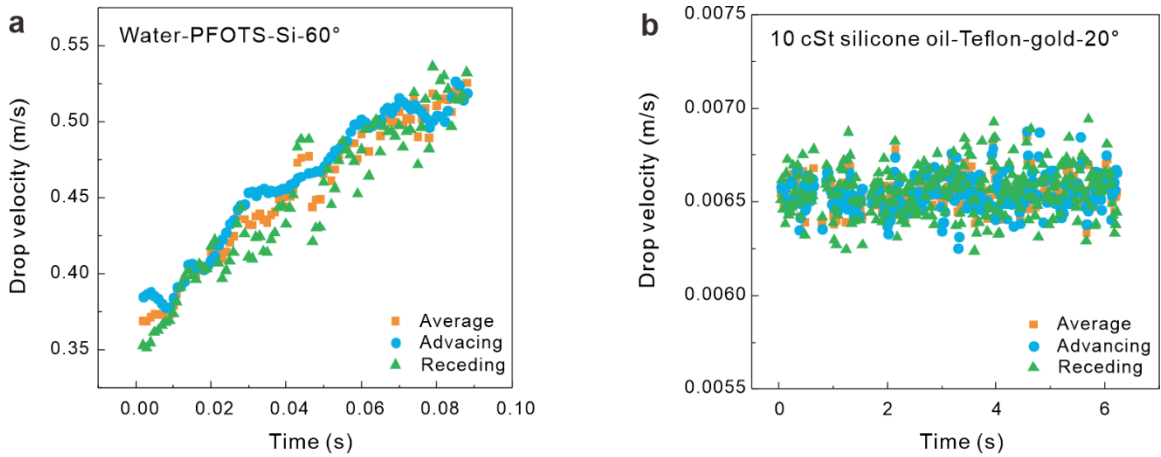
Figure S1. Average velocity, advancing velocity, and receding velocity versus time for water drop on a 60° tilted PFOTS-Si surface and 10 cSt silicone oil drop on a 20° tilted Teflon-gold surface. For example, the average deviation of U_a and U_r from U for water drops sliding down the PFOTS-Si surface at 60° and for 10 cSt silicone oil drops sliding down Teflon-gold surfaces at 20° were (4±3) % and (3±5)%, respectively.
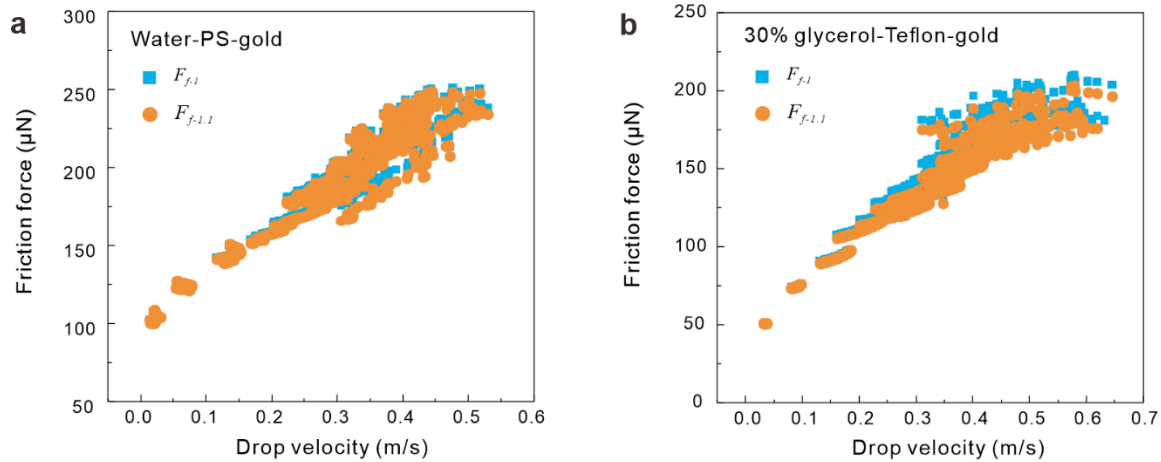
Figure S2. Deviation of friction force when m^*/m changes from 1 to 1.1. The deviation percentage is calculated by $\frac{2(F_{f-1}-F_{f-1.1})}{(F_{f-1}+F_{f-1.1})} \times 100\%$. The friction forces deviated within $\approx 1\%$ of water drop on the PS-gold surface and $\approx 2.5\%$ for 30% glycerol-water mixture on the Teflon-gold surface when we change m^*/m from 1.0 to 1.1.

166
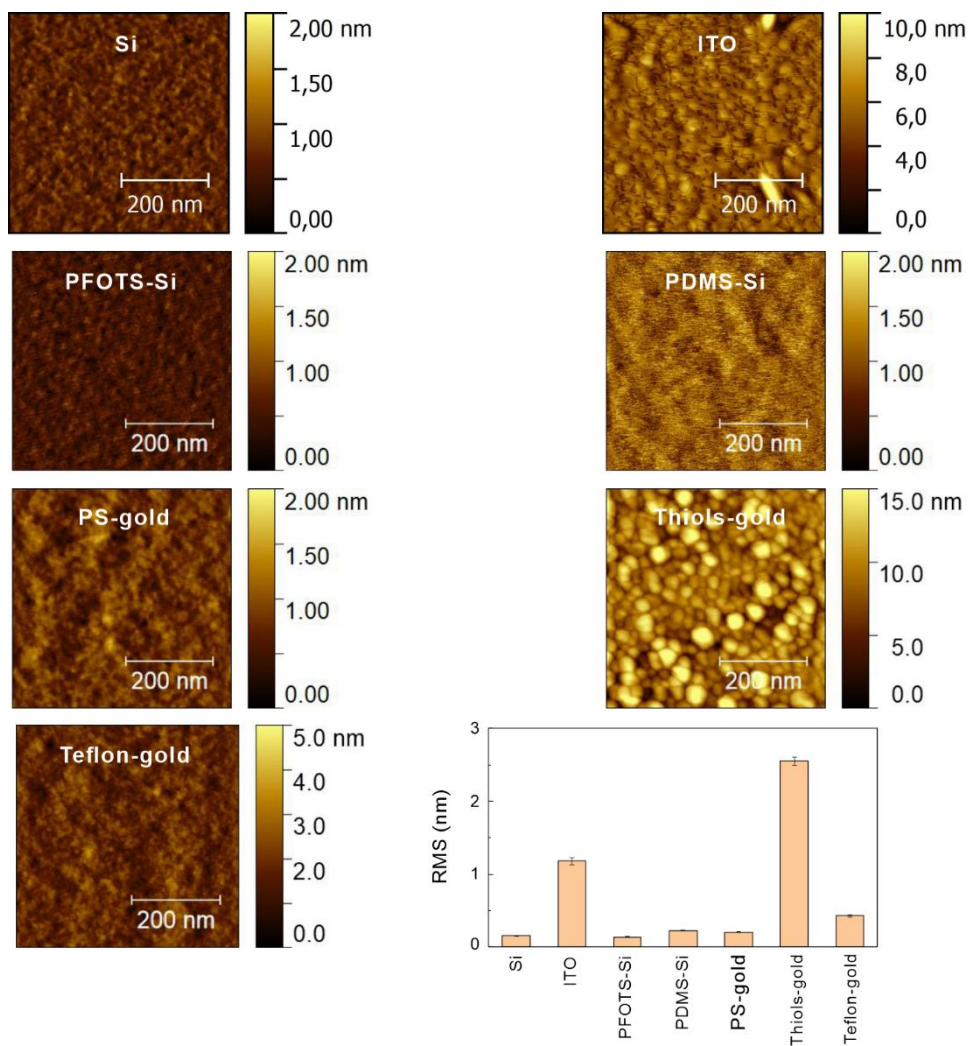
**Figure S3.** Topography and average RMS of all the surfaces measured by AFM over 0.5 x 0.5 μm^2.
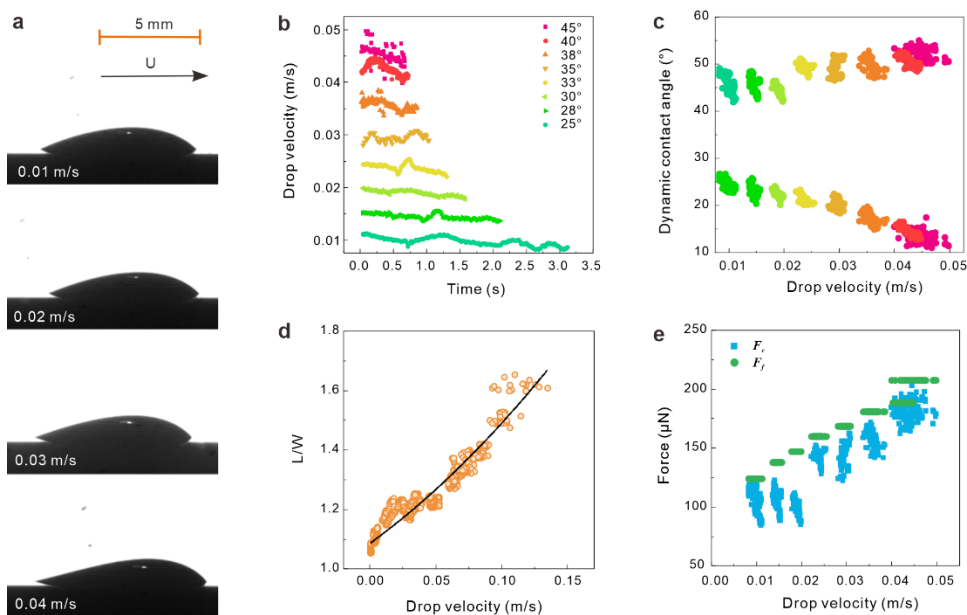
Figure S4. Water drops on a Si wafer. (a) Drop profile; (b) velocity; (c) velocity-dependent dynamic contact angle (upper is the advancing side, below is the receding side); (d) velocity-dependent aspect ratio (length-to-width: L/W,) with the fitting curve: $\frac{L}{w} = 8.312U^2 + 3.21U + 1.086$, U in m/s; (e) velocity-dependent friction force and capillary force of 30 ± 2 μL sliding water drops.
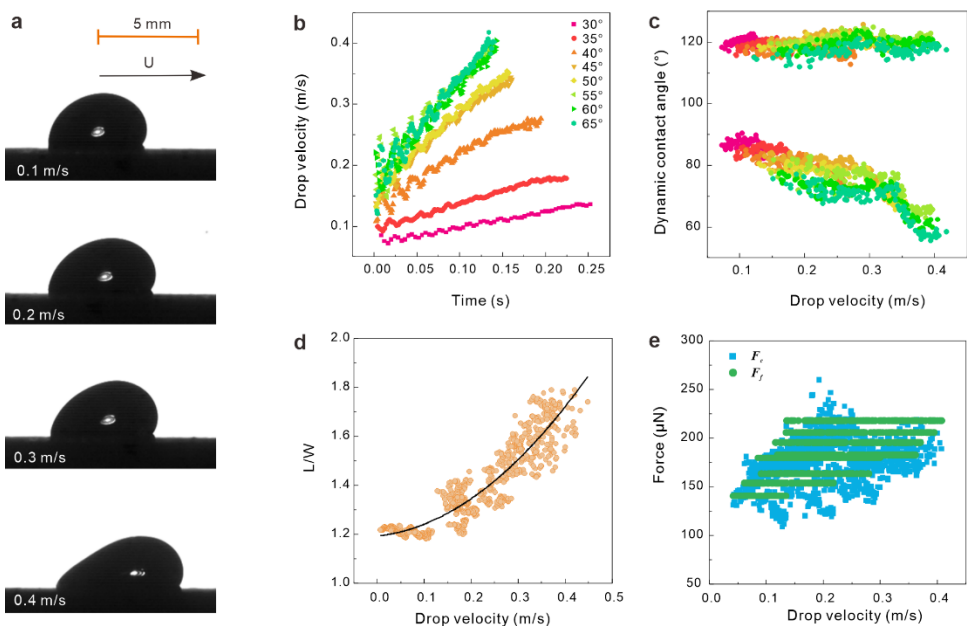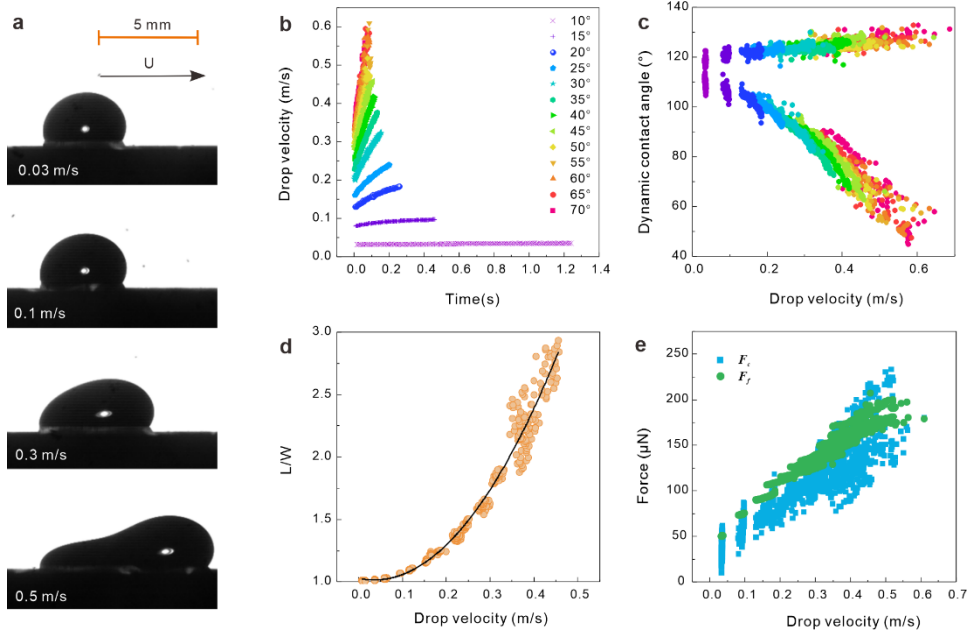

Figure S5. Water drops on ITO glass. (a) Drop profile; (b) velocity; (c) velocity-dependent dynamic contact angle (upper is the advancing side, below is the receding side); (d) velocity-dependent aspect ratio (length-to-width: L/W,) with the fitting curve: $\frac{L}{w} = 2.782U^2 + 0.205U + 1.194$; (e) velocity-dependent friction force and capillary force of 30 ± 2 μL sliding water drops.
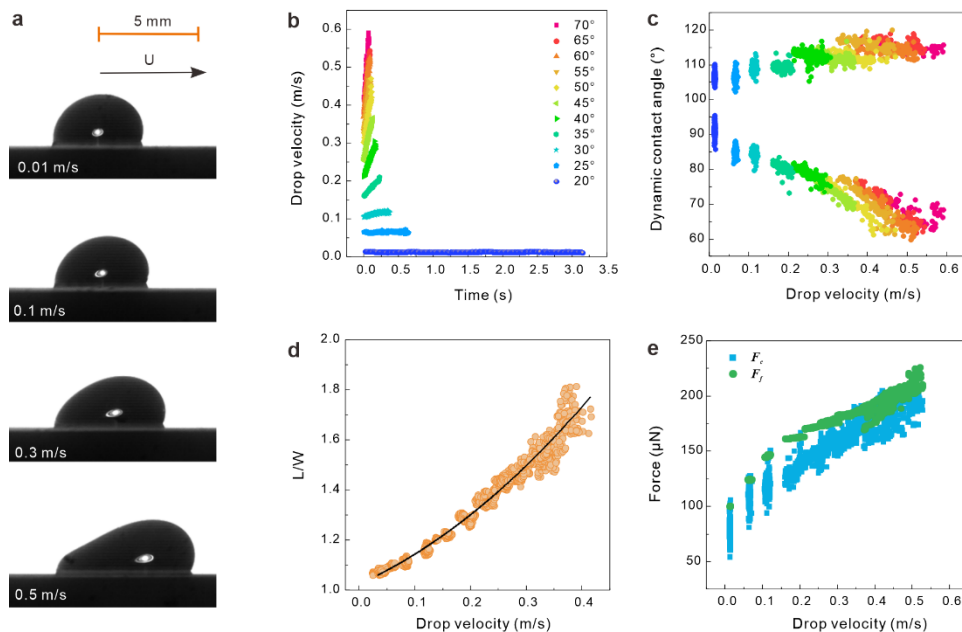
Figure S6. Water drops on PFOTS-Si surfaces. (a) Drop profile; (b) velocity; (c) velocity-dependent dynamic contact angle (upper is the advancing side, below is the receding side); (d) velocity-dependent aspect ratio (length-to-width: L/W,) with the fitting curve: $\frac{L}{w} = 1.931U^2 + 0.993U + 1.026$; (e) velocity-dependent friction force and capillary force of 30$\pm$2 μL sliding water drops.
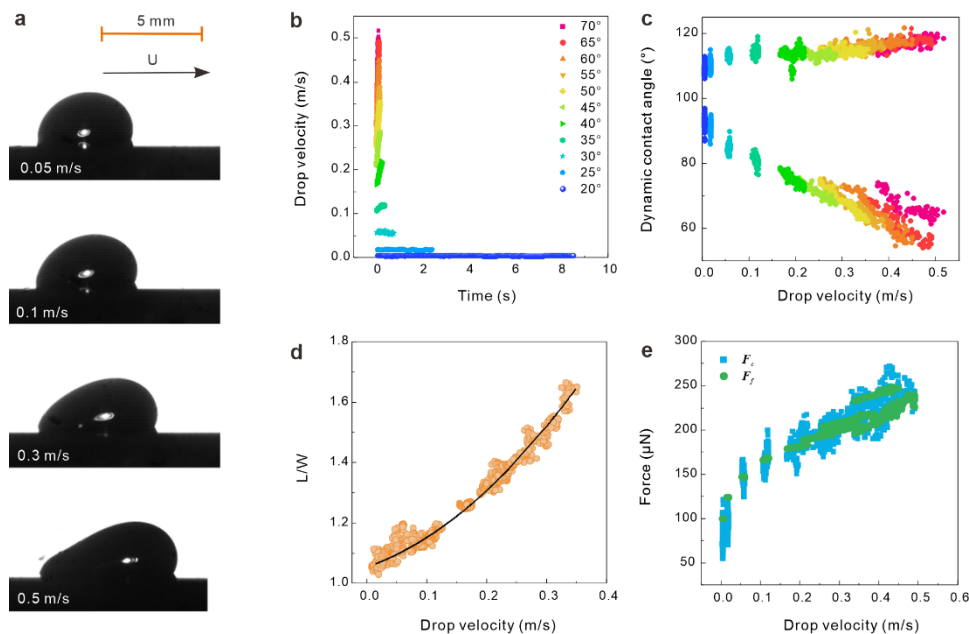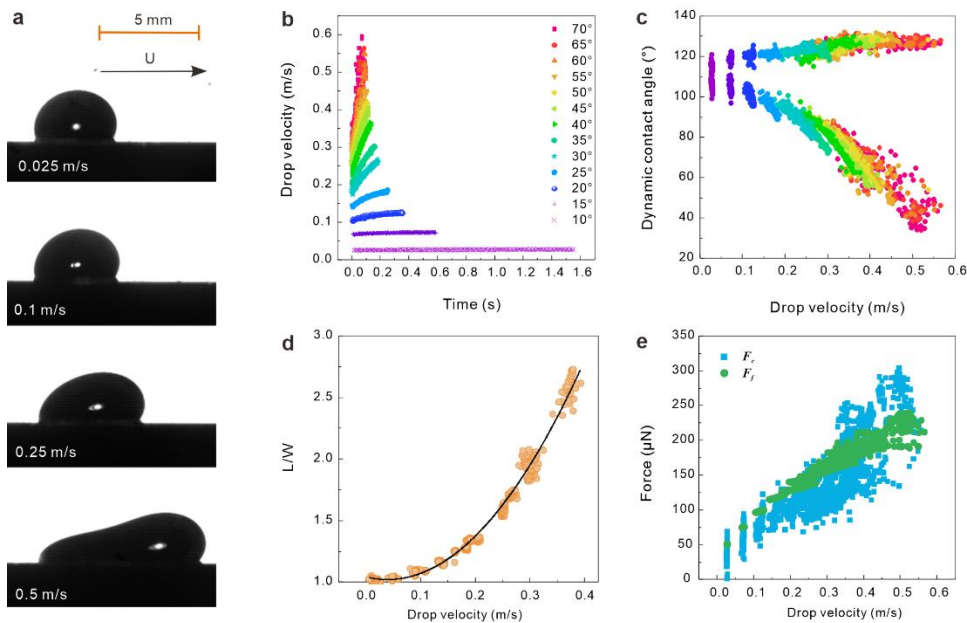

Figure S7. Water drops on PDMS-Si surfaces. (a) Drop profile; (b) velocity; (c) velocity-dependent dynamic contact angle (upper is the advancing side, below is the receding side); (d) velocity-dependent aspect ratio (length-to-width: L/W,) with the fitting curve: $\frac{L}{w} = 2.951U^2 + 0.697U + 1.054$; (e) velocity-dependent friction force and capillary force of 30$\pm$2 μL sliding water drops.

169
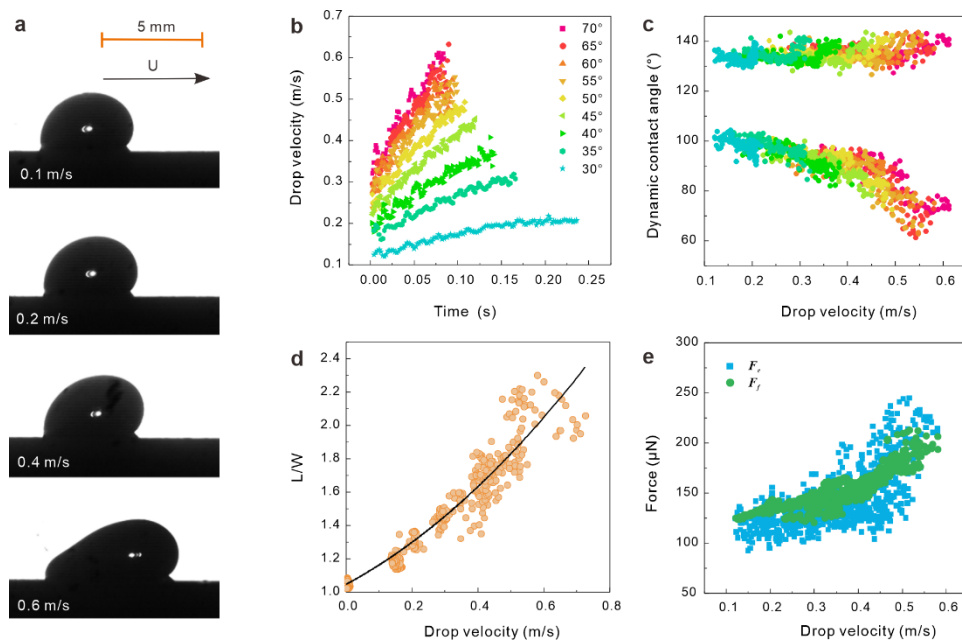
Figure S8. Water drops on thiols-gold surfaces. (a) Drop profile; (b) velocity; (c) velocity-dependent dynamic contact angle (upper is the advancing side, below is the receding side); (d) velocity-dependent aspect ratio (length-to-width: L/W,) with the fitting curve: $\frac{L}{w} = 1.013U^2 + 1.058U + 1.048$; (e) velocity-dependent friction force and capillary force of 30 ± 2 μL sliding water drops.
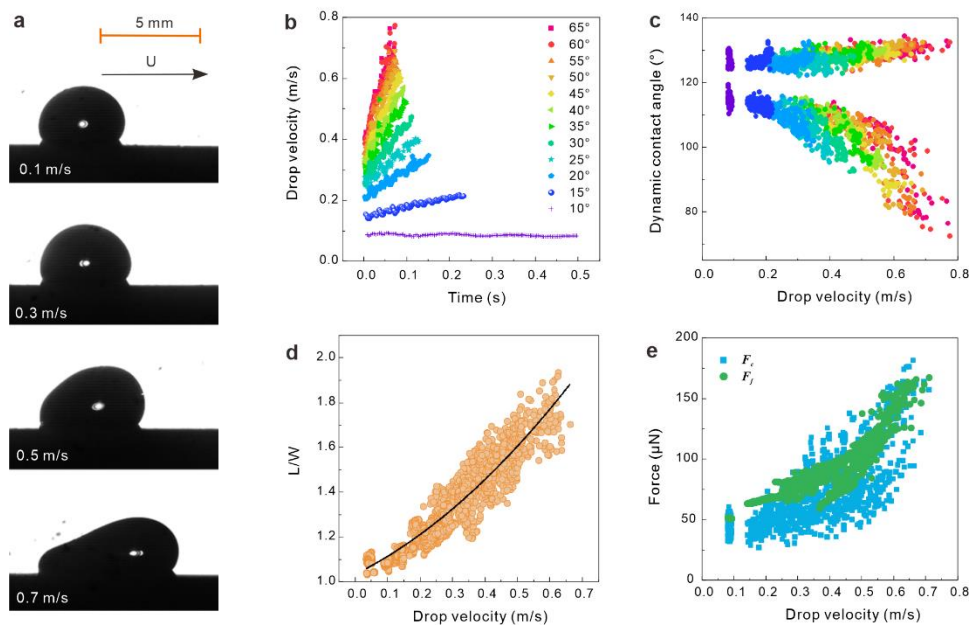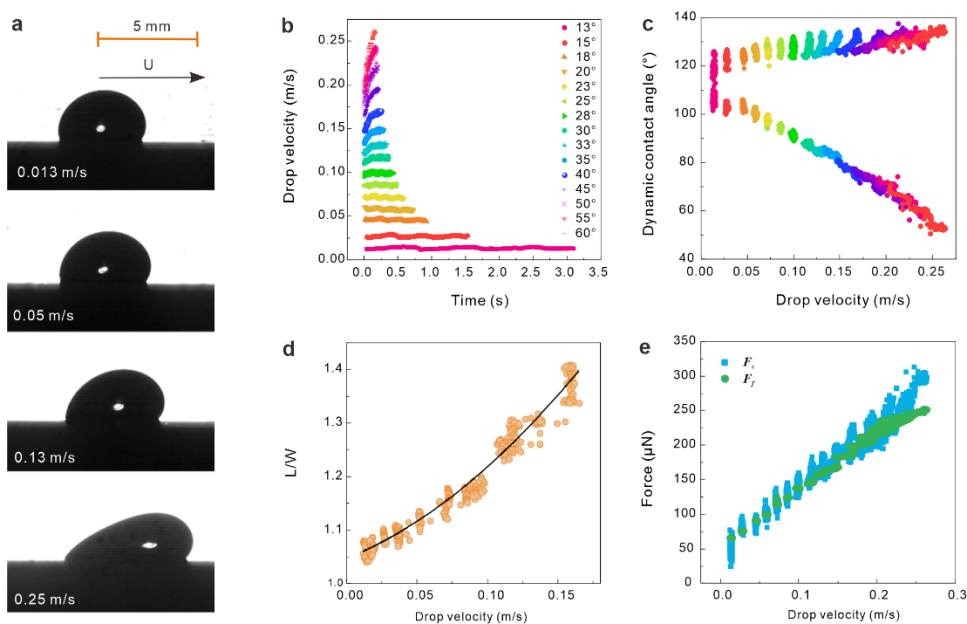

Figure S9. Water drops on Teflon-gold surfaces. (a) Drop profile; (b) velocity; (c) velocity-dependent dynamic contact angle (upper is the advancing side, below is the receding side); (d) velocity-dependent aspect ratio (length-to-width: L/W,) with the fitting curve: $\frac{L}{w} = 0.856U^2 + 0.715U + 1.034$; (e) velocity-dependent friction force and capillary force of 30 ± 2 μL sliding water drops.

170

Figure S10. 30% glycerol-water mixture drops (30±2 μL) on Teflon-gold surfaces. (a) Drop profile; (b) velocity; (c) velocity-dependent dynamic contact angle (upper is the advancing side, below is the receding side); (d) velocity-dependent aspect ratio (length-to-width: L/W,) with the fitting curve: $\frac{L}{w} = 10.33U^2 - 0.729U + 1.03$; (e) velocity-dependent friction force and capillary force.
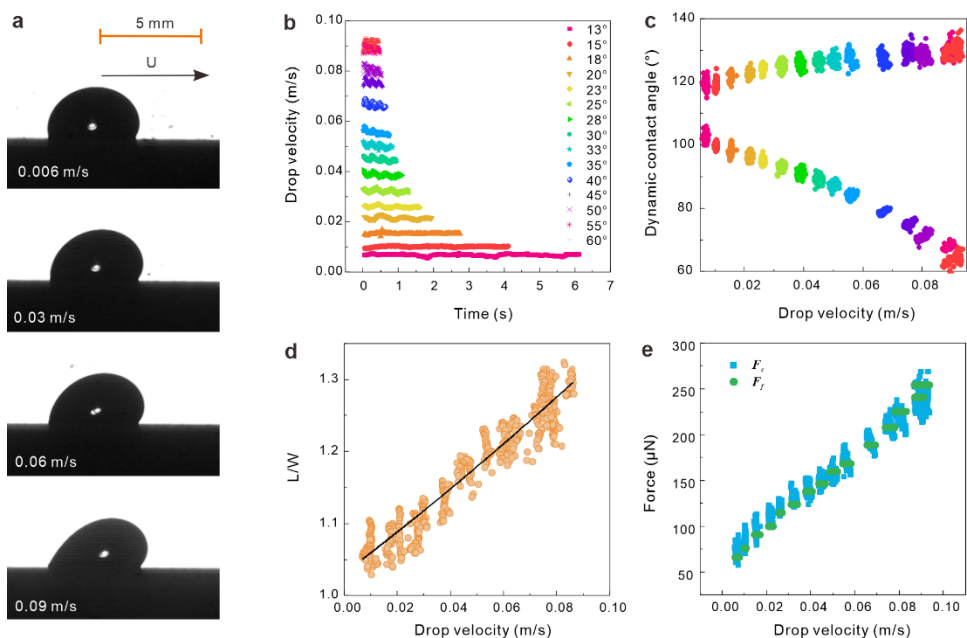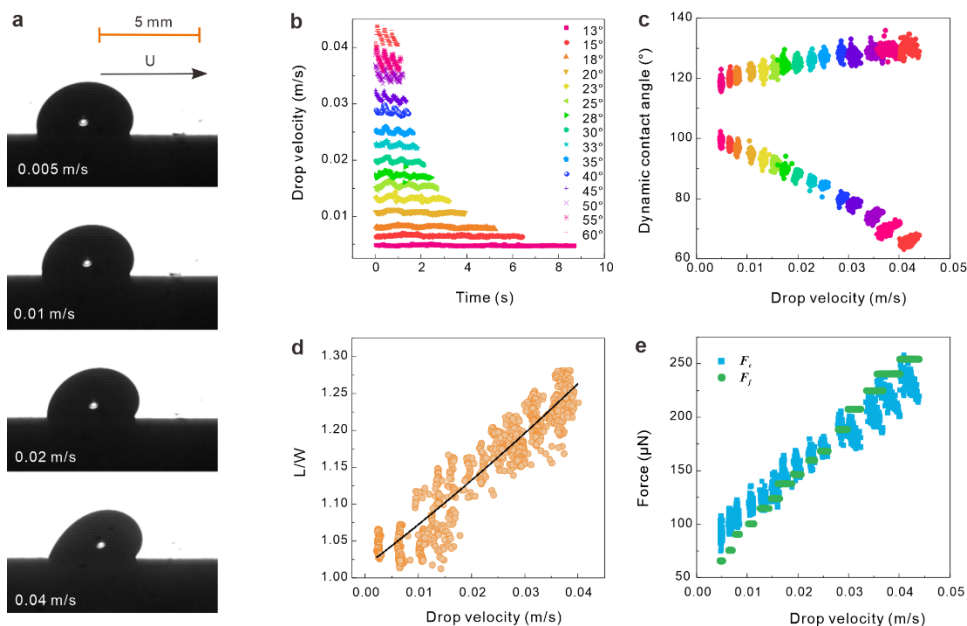

Figure S11. 40% glycerol-water mixture drops on Teflon-gold surfaces. (a) Drop profile; (b) velocity; (c) velocity-dependent dynamic contact angle (upper is the advancing side, below is the receding side); (d) velocity-dependent aspect ratio (length-to-width: L/W,) with the fitting curve: $\frac{L}{w} = 13.68U^2 - 1.087U + 1.043$; (e) velocity-dependent friction force and capillary force of sliding drops with 30±2 μL.
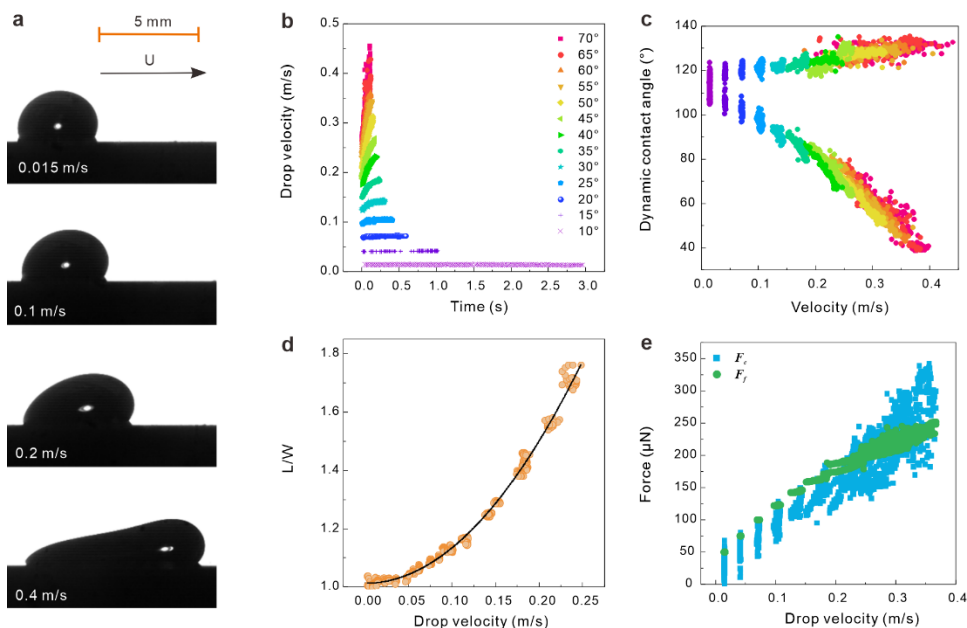
Figure S12. 50% glycerol-water mixture drops (30$\pm$2 µL) on Teflon-gold surfaces. (a) Drop profile; (b) velocity; (c) velocity-dependent dynamic contact angle (upper is the advancing side, below is the receding side); (d) velocity-dependent aspect ratio (length-to-width: L/W,) with the fitting curve: $\frac{L}{w} = 12.12U^2 - 0.001U + 1.013$; (e) velocity-dependent friction force and capillary force.
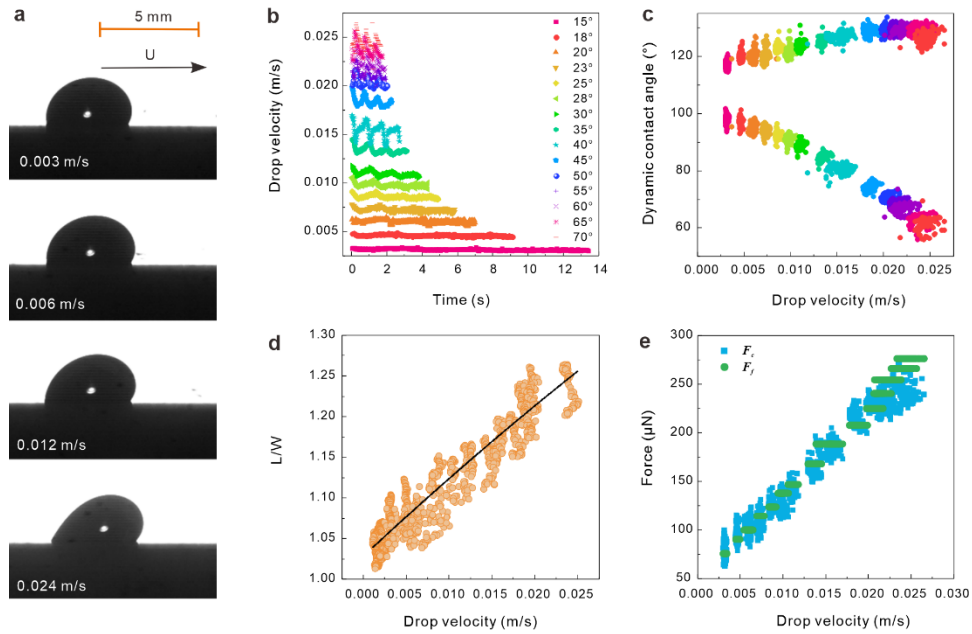

Figure S13. 60% glycerol-water mixture drops on Teflon-gold surfaces. (a) Drop profile; (b) velocity; (c) velocity-dependent dynamic contact angle (upper is the advancing side, below is the receding side); (d) velocity-dependent aspect ratio (length-to-width: L/W,) with the fitting curve: $\frac{L}{w} = 6.406U^2 + 1.076U + 1.047$; (e) velocity-dependent friction force and capillary force of sliding drops with 30$\pm$2 µL.
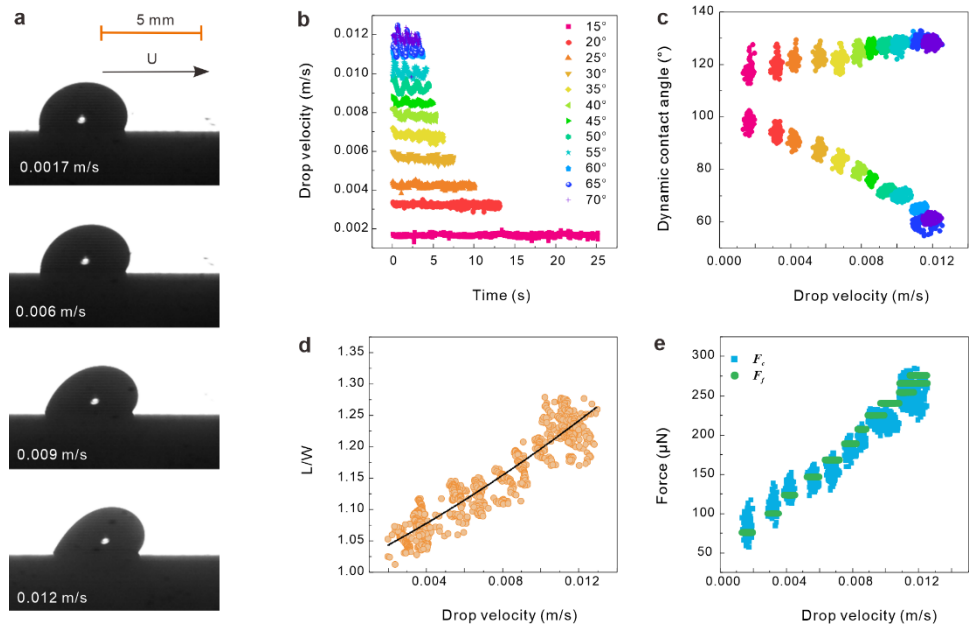
Figure S14. 70% glycerol-water mixture drops on Teflon-gold surfaces. (a) Drop profile; (b) velocity; (c) velocity-dependent dynamic contact angle (upper is the advancing side, below is the receding side); (d) velocity-dependent aspect ratio (length-to-width: L/W,) with the fitting curve: $\frac{L}{w} = 3.17U^2 + 2.80U + 1.03$; (e) velocity-dependent friction force and capillary force of sliding drops with 30$\pm$2 µL.

Figure S15. 80% glycerol-water mixture drops on Teflon-gold surfaces. (a) Drop profile; (b) velocity; (c) velocity-dependent dynamic contact angle (upper is the advancing side, below is the receding side); (d) velocity-dependent aspect ratio (length-to-width: L/W,) with the fitting curve: $\frac{L}{w} = 17.85U^2 + 5.46U + 1.02$; (e) velocity-dependent friction force and capillary force of sliding drops with 30$\pm$2 µL.
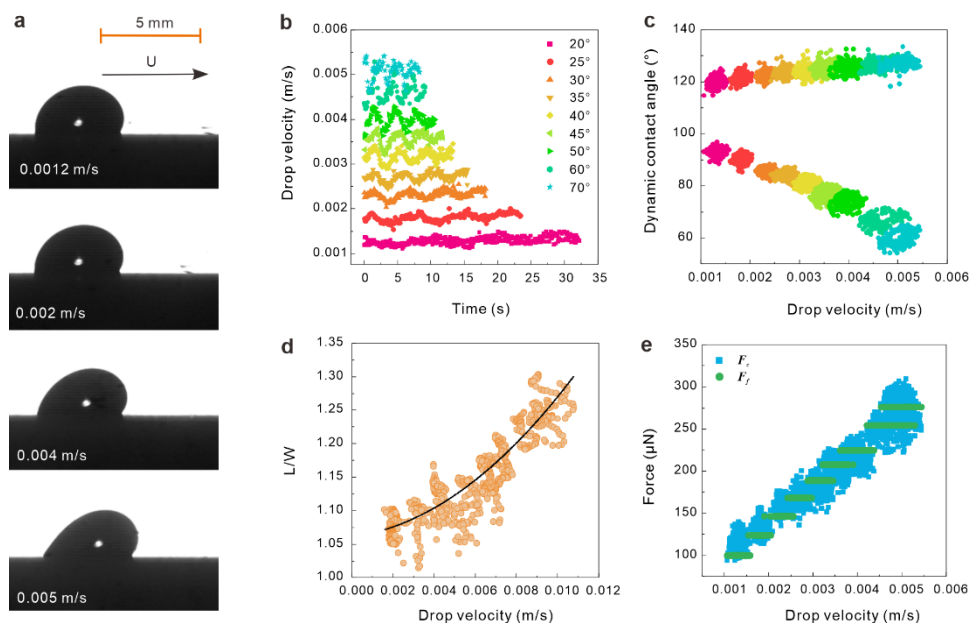
Figure S16. 85% glycerol-water mixture drops on Teflon-gold surfaces. (a) Drop profile; (b) velocity; (c) velocity-dependent dynamic contact angle (upper is the advancing side, below is the receding side); (d) velocity-dependent aspect ratio (length-to-width: L/W,) fitted with $\frac{L}{w} = -29.44U^2 + 9.83U + 1.03$; (e) velocity-dependent friction force and capillary force of sliding drops with 30 ± 2 μL.
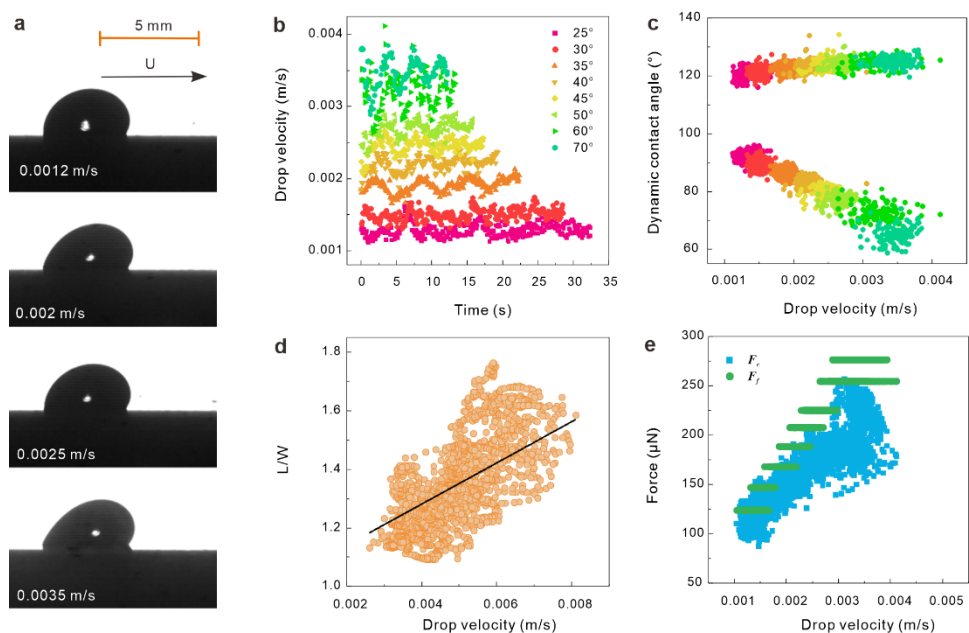

Figure S17. 90% glycerol-water mixture drops on Teflon-gold surfaces. (a) Drop profile; (b) velocity; (c) velocity-dependent dynamic contact angle (upper is the advancing side, below is the receding side); (d) velocity-dependent aspect ratio (length-to-width: L/W,) fitted with $\frac{L}{w} = 315.2U^2 + 15.38U + 1.01$; (e) velocity-dependent friction force and capillary force of sliding drops with 30 ± 2 μL.

Figure S18. 95% glycerol-water mixture drops on Teflon-gold surfaces. (a) Drop profile; (b) velocity; (c) velocity-dependent dynamic contact angle (upper is the advancing side, below is the receding side); (d) velocity-dependent aspect ratio (length-to-width: L/W,) fitted with $\frac{L}{w} = 1696U^2 + 3.87U + 1.06$; (e) velocity-dependent friction force and capillary force of sliding drops with 30 ± 2 μL.

Figure S19. 99% glycerol-water mixture drops on Teflon-gold surfaces. (a) Drop profile; (b) velocity; (c) velocity-dependent dynamic contact angle (upper is the advancing side, below is the receding side); (d) velocity-dependent aspect ratio (length-to-width: L/W,) fitted with $\frac{L}{w} = 70.25U + 1$; (e) velocity-dependent friction force and capillary force of sliding drops with 30 ± 2 μL..
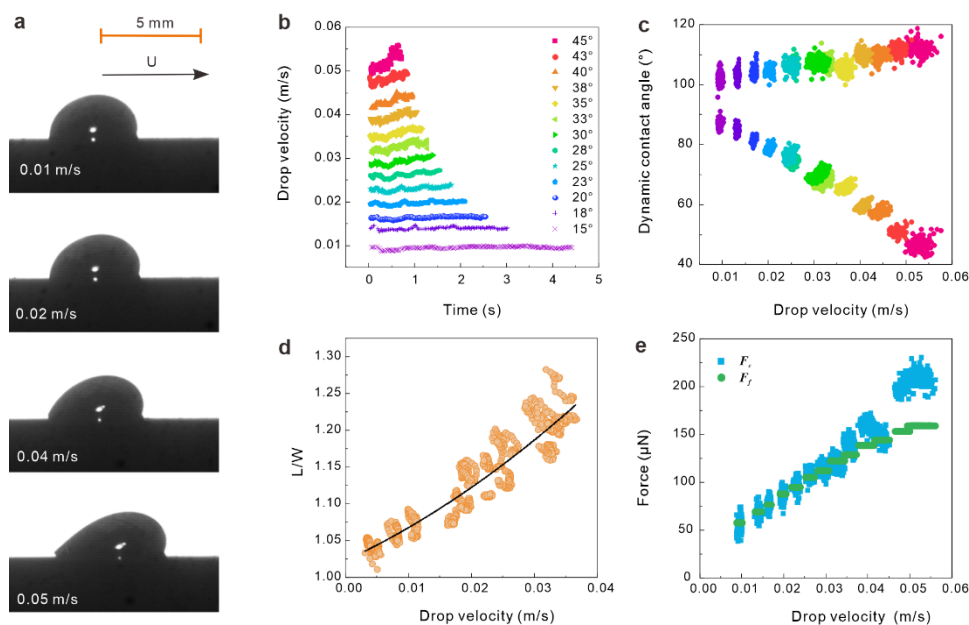
Figure S20. Ethylene glycol drops on Teflon-gold surfaces. (a) Drop profile; (b) velocity; (c) velocity-dependent dynamic contact angle (upper is the advancing side, below is the receding side); (d) velocity-dependent aspect ratio (length-to-width: L/W,) fitted with $\frac{L}{w} = 49.04U^2 + 3.99U + 1.02$; (e) velocity-dependent friction force and capillary force with 21 ± 2 μL drops.
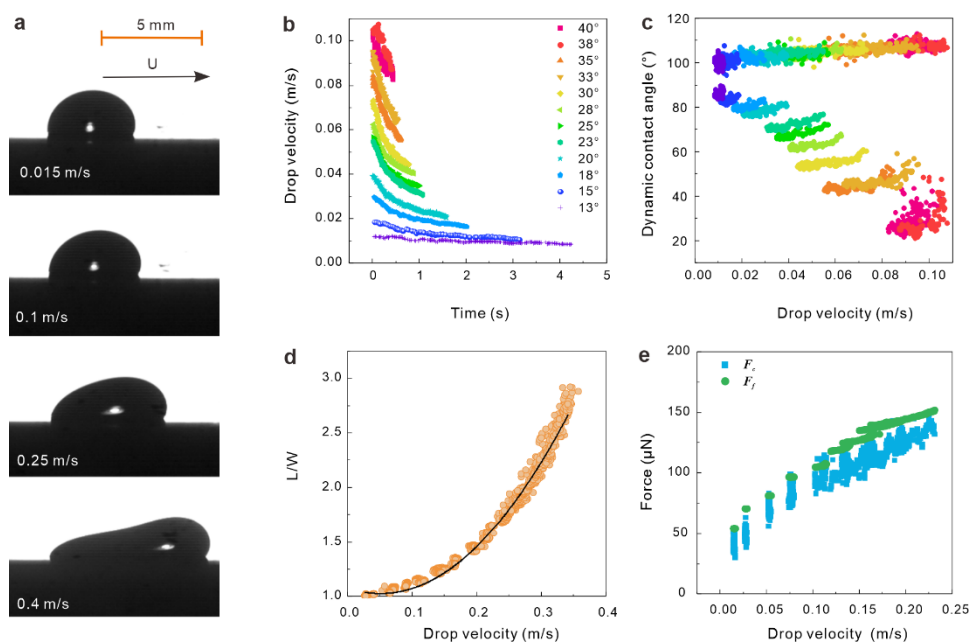

Figure S21. Formamide drops on Teflon-gold surfaces. (a) Drop profile; (b) velocity; (c) velocity-dependent dynamic contact angle (upper is the advancing side, below is the receding side); (d) velocity-dependent aspect ratio (length-to-width: L/W,) fitted with $\frac{L}{w} = 19.46U^2 - 2.00U + 1.08$; (e) velocity-dependent friction force and capillary force of 32 ± 2 μL drops.
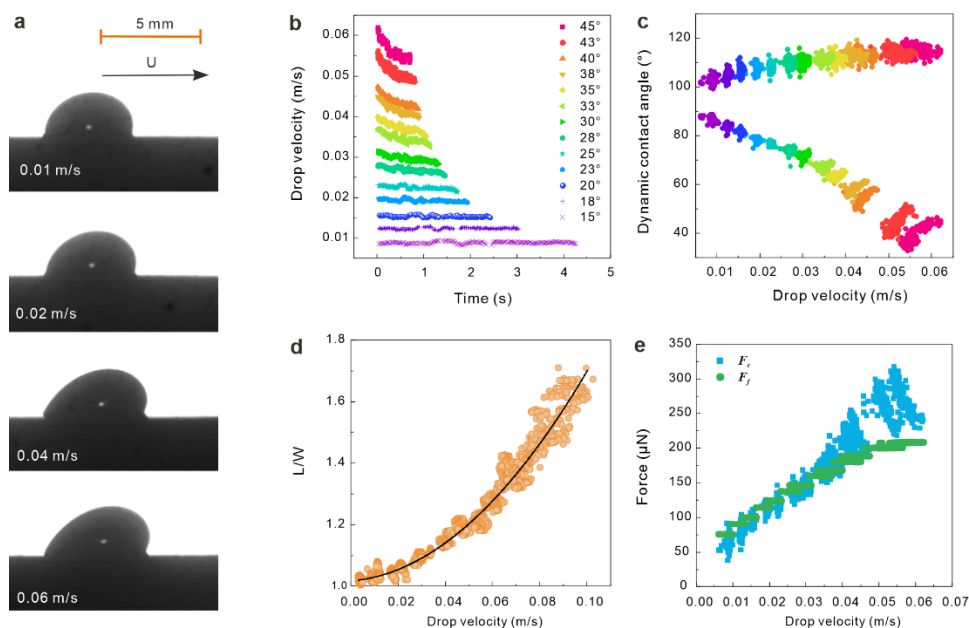
176

Figure S22. Ionic liquid drops on Teflon-gold surfaces. (a) Drop profile; (b) velocity; (c) velocity-dependent dynamic contact angle (upper is the advancing side, below is the receding side); (d) velocity-dependent aspect ratio (length-to-width: L/W,) fitted with $\frac{L}{w} = 62.06U^2 + 0.599U + 1.02$; (e) velocity-dependent friction force and capillary force of 30 ± 2 μL drops.
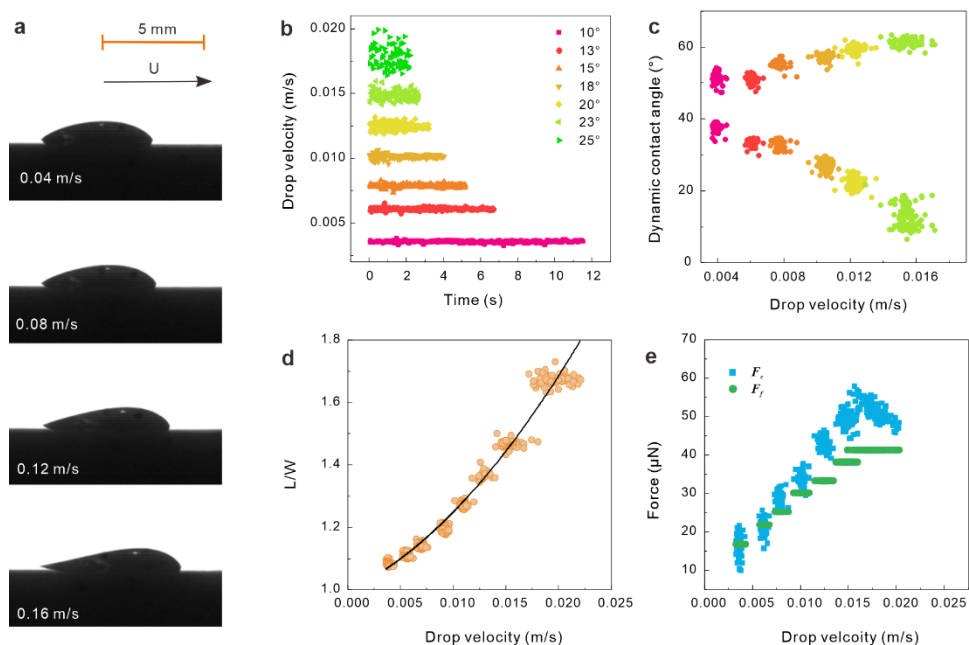

Figure S23. 5 cSt silicone oil drops on Teflon-gold surfaces. (a) Drop profile; (b) velocity; (c) velocity-dependent dynamic contact angle (upper is the advancing side, below is the receding side); (d) velocity-dependent aspect ratio (length-to-width: L/W,) fitted with $\frac{L}{w} = 921.2U^2 + 16.02U + 0.997$; (e) velocity-dependent friction force and capillary force of 10 ± 2 μL drops.
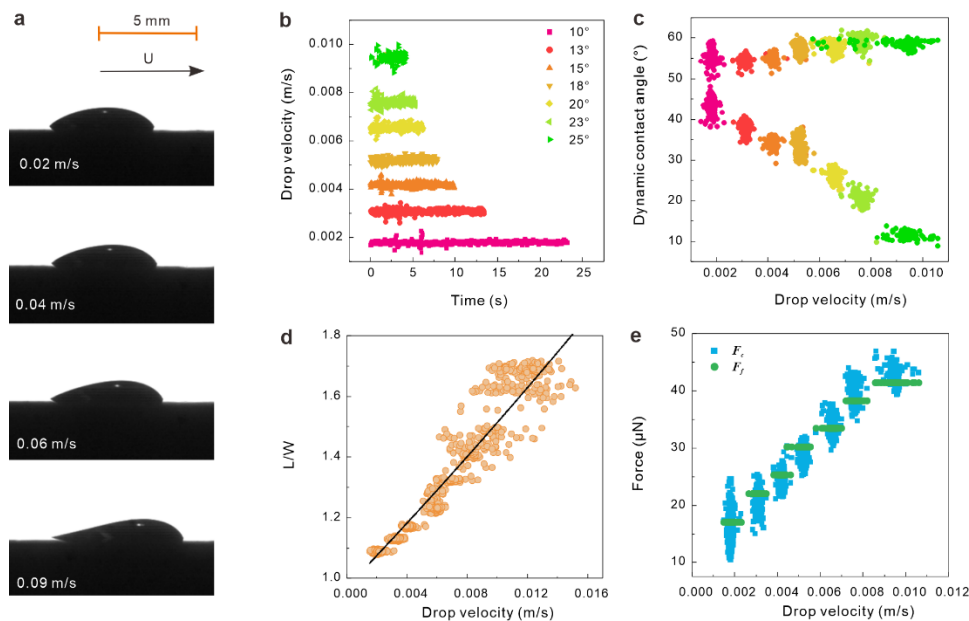
Figure S24. 10 cSt silicone oil drops on Teflon-gold surfaces. (a) Drop profile; (b) velocity; (c) velocity-dependent dynamic contact angle (upper is the advancing side, below is the receding side); (d) velocity-dependent aspect ratio (length-to-width: L/W,) fitted with $\frac{L}{w} = 256.4U^2 + 51.7U + 0.971$; (e) velocity-dependent friction force and capillary force of 11 ± 2 µL drops.
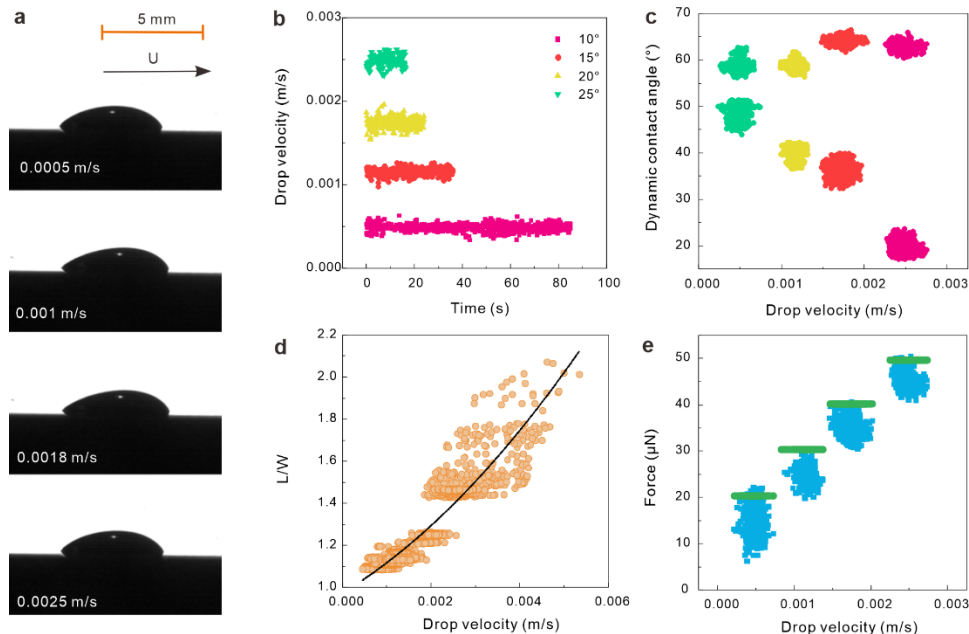

Figure S25. 50 cSt silicone oil drops on Teflon-gold surfaces. (a) Drop profile; (b) velocity; (c) velocity-dependent dynamic contact angle (upper is the advancing side, below is the receding side); (d) velocity-dependent aspect ratio (length-to-width: L/W,) fitted with $\frac{L}{w} = 16420U^2 + 127.3U + 0.974$; (e) velocity-dependent friction force and capillary force of 12 ± 2 µL drops.
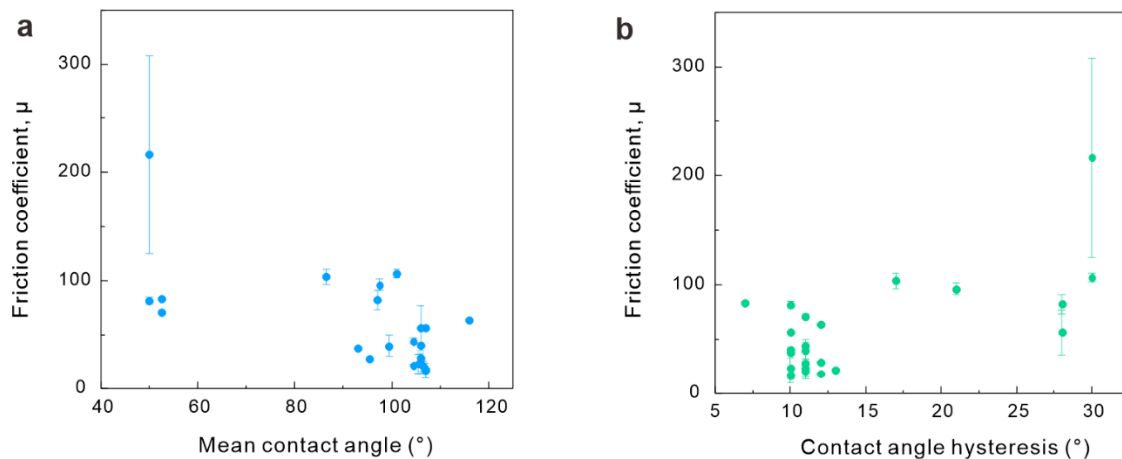
Figure S26. Friction coefficient versus mean contact angle (a) and contact angle hysteresis (b). The mean contact angle was calculated by averaging static advancing contact angle and static receding contact angle.
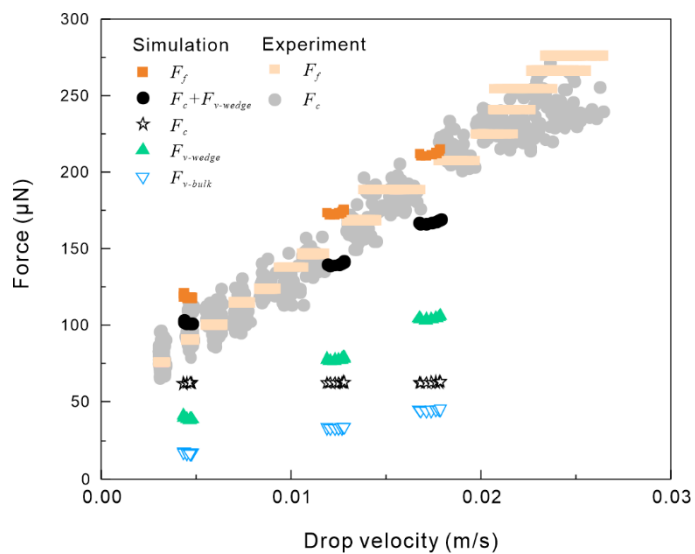

Figure S27. Comparison between experimental force and simulated force for sliding drops with 85% glycerol-water mixture on Teflon-gold surfaces.

3. Conclusions and Outlook

The projects included in the thesis continued and extended the development of dynamic wetting. Using a home-built tilted plate setup and two homemade random copolymer systems: PS/PAA and P(MMA-*co*-HQSEA), we verified the adaptation model experimentally for the first time. Meanwhile, applying the adaptation model to dynamic contact angles enables us to enter new territory for studying adaptation kinetics in situ and in time scales down to milliseconds and microseconds. In addition, we found a new energy dissipation channel of sliding drop—slide electrification, which resists drop motion and reduces dynamic contact angle on insulated surfaces substantially. The discovery that surface permittivity influences drop motion opens new avenues toward engineering surfaces with desired wetting properties. Moreover, the explanation that the influence of charging of surfaces and sliding drops by slide electrification on contact angle is equivalent to a change in interfacial energy not only helps to understand reported interesting phenomena in literature but also inspired a way to manipulate drop motion. Finally, we find out a universal empirical equation to predict drop friction. In which a dimensionless and material-specific parameter—friction coefficient is a new empirical property and should be considered in surface engineering.

4. Personal Publications

Journal Articles

1. **X. Li**, F. Bodziony, M. Yin, H. Marschall, R. Berger, H.-J. Butt. Drop friction. *Submitted* (2023).

2. **X. Li**, A. D. Ratschow, S. Hardt, H.-J. Butt. Surface charge deposition by moving drops reduces contact angles. *Submitted* (2023).

3. **X. Li**, K. Auepattana-Aumrung, H.-J. Butt, D. Crespy, R. Berger. Fast-release kinetics of a pH-responsive polymer detected by dynamic contact angles. *J. Chem. Phys.* 158, 144901 (2023).

4. D. Díaz D, **X. Li**, P. Bista, X. Zhou, F. Darvish, H.-J. Butt, M. Kappl. Self-generated electrostatic forces of drops rebounding from hydrophobic surfaces. *Physics of Fluid* 35, 1, 017111 (2023).

5. S. Shumaly, F. Darvish, **X. Li**, A. Saal, C. Hinduja, W. Steffen, O. Kukharenko, H.-J. Butt, R. Berger. Deep learning to analyze sliding drops. *Langmuir* 39, 3, 111-1122 (2023).

6. **X. Li**, P. Bista, A. Z. Stetten, H. Bonart, M. T. Schür, S. Hardt, F. Bodziony, H. Marschall, A. Saal, X. Deng, R. Berger, S. A. L. Weber, H.-J. Butt. Spontaneous charging affects the motion of sliding drops. *Nature Physics* 18, 713-719 (2022).

7. **X. Li**, M. Encheva, H.-J. Butt, E.H.G. Backus, R. Berger. Adaptation and recovery of a styrene-acrylic acid copolymer surface to water. *Macromol. Rapid Commun.* 2100733 (2022).

8. W.S.Y. Wong, P. Bista, **X. Li**, L. Veith, A. Sharifi-Aghili, S.A.L. Weber, H.-J. Butt. Tuning the charge of sliding water drops. *Langmuir* 38, 19, 6224-6230 (2022).

9. Y. Tan, J. Yang, Y. Li, **X. Li**, Q. Wu, F. Fan, F. Yu, J. Cui, L. Chen, D. Wang, X. Deng. Liquid-pressure-guided superhydrophobic surfaces with adaptive adhesion and stability. *Adv. Mater.* 38, 19, 6224 (2022).

10. H.-J. Butt, J. Liu, K. Koynov, B. Straub, C. Hinduja, I. Roismann, R. Berger, **X. Li**, D. Vollmer, Steffen W, M. Kappl. Contact angle hysteresis. *Current Opinion in Colloid & Interface Science*, 101574 (2022).

11. **X. Li**, S. Silge, A. Saal, G. Kircher, K. Koynov, R. Berger, H.-J. Butt. Adaptation of a styrene-acrylic acid copolymer surface to water. *Langmuir* 37, 4, 1571–1577 (2021).

12. J. Liu, Y. Sun, X. Zhou, **X. Li**, M. Kappl, W. Steffen, H. Butt. One‑Step Synthesis of a Durable and Liquid‑Repellent Poly (dimethylsiloxane) Coating, *Adv. Mater.* 33, 2100237 (2021).

13. **X. Li**, J. Yang, K. Lv, P. Papadopoulos, J. Sun, D. Wang, Y. Zhao, L. Chen, D. Wang, Z. Wang, X. Deng. Salvinia-like slippery surface with stable and mobile water/air contact line. *National Science Review* 8, 5, 153 (2021).

14. **X. Li**, D Wang, Y. Tan, J. Yang, X. Deng. Designing transparent micro/nano re-entrant-coordinated superamphiphobic surfaces with ultralow solid/liquid adhesion. *ACS Appl. Mater. Interfaces* 11, 32 (2019).

Oral Presentations

1. **X. Li**. How friction develops during the sliding of drops. SPP Winter Workshop in Göttingen, Germany, 5th-8th December 2022.

2. **X. Li**. How spontaneous charging in sliding drops affects their motion. 36th European Colloid & Interface Society Conference, Chania, Greece, 4th-9th September 2022.

3. **X. Li**. Additional contribution to contact angle hysteresis. Max Planck Center workshop, Enschede, Netherlands, 14th-16th March 2022.

4. **X. Li**. Dynamic wetting and dewetting process on adaptive surfaces. SPP Winter Workshop, Freiburg, Germany, 8th-11th November 2021.

5. **X. Li**. Dynamic wetting and dewetting process on adaptive surfaces. SPP Friday Colloquium, online, 16th July 2021.

6. **X. Li**. How fast copolymer surface adapts to water? Wetting Dynamic Conference, Bonn, Germany, 28th-30th September 2020

Poster Presentations

1. **X. Li**. Adaptation and recovery of a PS/PAA copolymer surface to water. 36th European Colloid & Interface Society Conference, Chania, Greece, 4th-9th September 2022. (Win the poster award)

2. **X. Li**. Adaptation of Polymer Surfaces. SPP Winter Workshop, Freiburg, Germany, 8th-11th November 2021.

3. **X. Li**. Adaptation of PS/PAA copolymer to water. 5. 5th Droplet Conference, online, 17th-20th August 2021.